THE UNIVERSITY OF QUEENSLAND

AUSTRALIA

Modelling of mechanical and electrochemical interspecies interactions in microbial communities

Tomas Storck
Bachelor of Science (TU Delft)
Master of Science (TU Delft)

A thesis submitted for the degree of Doctor of Philosophy at
The University of Queensland in 2015
School of Chemical Engineering
Advanced Water Management Centre

ABSTRACT

Microbial interactions play an important role in environmental processes, both beneficial (e.g., production of methane through anaerobic digestion) and detrimental (e.g., bulking of sludge). By better understanding microbial interactions, conditions can be optimised to either make the microbial processes more effective or limit the negative effects caused by the microbial community. This thesis mathematically investigates physical and chemical microbial interspecies interactions in order to determine the impact of elementary controlling mechanisms. Research is focused on basic mechanical interactions and chemical-electrochemical interspecies interactions, with application to key systems where the physical, electrical, and chemical elements are linked. To enable description of the physical components, an extendible individual-based modelling framework is presented that predicts the movement, growth and development of single cells, as well as their interactions with surfaces and other cells in the microbial community (chapter 2). This extends previous approaches to consider physics at the level of individual cells and enables the use of non-spherical cell geometries. Using this model it is shown that (i) in a biofilm consisting of rod-shaped cells, inclusion of cell-substratum anchoring links cause biofilms to rapidly grow in thickness instead of surface area, and (ii) inter-floc bridging in activated sludge is related to the relative growth rates of floc forming and filament forming microorganisms. A microbial community where direct interspecies electron transfer occurs is evaluated by modelling both the physical organisation of cells and interspecies links, along with diffusion-migration transport, electrochemistry and biochemical reactions. This allows comparison of the external limitations of a recently reported direct interspecies electron transfer (IET) mechanism to classical, mediated IET through formate or hydrogen (chapter 3). This work shows that direct IET through nanowires is more strongly limited by thermodynamics than formate-mediated IET. Redox complex activation losses encountered during cell-nanowire transfer govern the system (93% of total losses). A sensitivity analysis shows that only when the redox complex transfer rate is an order of magnitude higher or the redox complex count is five times higher does nanowire resistance play a role, yet the feasibility of direct IET remains lower than formate-mediated IET. However, a minor metabolic advantage, as reported in recent literature, is sufficient to explain why direct IET can outcompete formate-mediated IET in some systems despite the limitations governing electron transfer. The techniques developed in chapter 2, as well as reaction-diffusion as applied in chapter 3 are further developed to consider the shell-shaped aggregates mediating anaerobic oxidation of methane in deep sea sediments (chapter 4). Extremely low reaction rates, acid dissociation and polysulfide precipitation cause diffusion to be non-limiting even in the largest reported aggregates, which explains why the aggregate continues to grow despite the thermodynamically suboptimal cell organisation. Using cell-cell EPS links and anti-collision as the sole cell-cell interactions, a shell-shaped morphology analogous to that observed in *in vitro* experiments can be grown from a small microbial inoculum.

DECLARATION BY AUTHOR

This thesis is composed of my original work, and contains no material previously published or written by another person except where due reference has been made in the text. I have clearly stated the contribution by others to jointly-authored works that I have included in my thesis.

I have clearly stated the contribution of others to my thesis as a whole, including statistical assistance, survey design, data analysis, significant technical procedures, professional editorial advice, and any other original research work used or reported in my thesis. The content of my thesis is the result of work I have carried out since the commencement of my research higher degree candidature and does not include a substantial part of work that has been submitted to qualify for the award of any other degree or diploma in any university or other tertiary institution. I have clearly stated which parts of my thesis, if any, have been submitted to qualify for another award.

I acknowledge that an electronic copy of my thesis must be lodged with the University Library and, subject to the policy and procedures of The University of Queensland, the thesis be made available for research and study in accordance with the Copyright Act 1968 unless a period of embargo has been approved by the Dean of the Graduate School.

I acknowledge that copyright of all material contained in my thesis resides with the copyright holder(s) of that material. Where appropriate I have obtained copyright permission from the copyright holder to reproduce material in this thesis.

PUBLICATIONS DURING CANDIDATURE

Peer-reviewed papers

- **Storck, T.**, Picioreanu, C., Virdis, B., and Batstone, D.J. (2014). Variable cell morphology approach for individual-based modelling of microbial communities. Biophysical Journal *106*, 2037-2048. doi:10.1016/j.bpj.2014.03.015
  Supplementary material: cell.com/biophysj/biophysj/supplemental/S0006-3495(14)00291-4
- **Storck, T.**, Virdis, B., and Batstone, D. J. Modelling extracellular limitations for mediated versus direct interspecies electron transfer. *Accepted for publication in The ISME Journal*

Conference presentations

- **Storck, T.**, Picioreanu, C., Virdis, B., and Batstone, D. J. Modelling of mediated versus direct interspecies electron transfer in microbial communities. *Proceedings of 13th World Congress on Anaerobic Digestion: Recovering (bio) Resources for the World*, 25-28 June 2013 Santiago de Compostela, Spain
- **Storck, T.**, Virdis, B., Picioreanu, C., and Batstone, D. J. Effect of direct versus indirect interspecies electron transfer in microbial communities through individual based, variable morphology modelling. *Book of Abstracts: 4th Microbial Fuel Cell Conference*, 1-4 September 2013 Cairns, Australia

PUBLICATIONS INCLUDED IN THIS THESIS

- **Storck, T.**, Picioreanu, C., Virdis, B., and Batstone, D. J. (2014). Variable cell morphology approach for individual-based modelling of microbial communities. Biophysical Journal *106*, 2037–2048. doi:10.1016/j.bpj.2014.03.015

	Contribution		
Contributor	Developed model	Designed model	Wrote/edited paper
Tomas Storck	100%	50%	60%
Cristian Picioreanu	-	20%	20%
Bernardino Virdis	-	10%	10%
Damien Batstone	-	20%	10%

Paper extended and incorporated in chapter 1 and chapter 2.

- **Storck, T.**, Virdis, B., and Batstone, D. J. Modelling extracellular limitations for mediated versus direct interspecies electron transfer. *Accepted for publication in The ISME Journal*

	Contribution		
Contributor	Developed model	Designed model	Wrote/edited paper
Tomas Storck	100%	60%	80%
Bernardino Virdis	-	20%	10%
Damien Batstone	-	20%	10%

Paper extended and incorporated in chapter 1 and chapter 3.

CONTRIBUTIONS BY OTHERS TO THE THESIS

My advisory team, consisting of Prof. Damien Batstone, Dr. Bernardino Virdis and Dr. Cristian Picioreanu, has provided valuable feedback on the work presented in this thesis.

This thesis contains work done as part of a larger research project on interspecies electron transfer (Australian Research Council - DP0985000). Researchers working on this project have made valuable indirect contributions to the thesis in the form of presentations and discussions. Most notably, I would like to recognise contributions made by Mr. Keelan Fischer and Dr. Natacha Juste-Poinapen.

As a result of my three-month visit to TU Delft, a MSc thesis has been written by Mr. Bas Cockx on the mechanical model presented in chapter 2. Parts of his thesis have been implemented in chapter 5.

STATEMENT OF PARTS OF THE THESIS SUBMITTED TO QUALIFY FOR THE AWARD OF ANOTHER DEGREE

None.

ACKNOWLEDGEMENTS

My principal advisor, Damien Batstone, your diverse knowledge combined with your incredible efficiency inspired me to work in a different way from what I was used to. During my PhD you gave me opportunities to explore and to take the time to figure things out by looking at the fundamentals of the problem. During the PhD you have enabled me to be more independent and persistent than I thought I could be.

My advisor, Bernardino Virdis, your kindness, patience, honesty as well as your hands-on experience with electrochemistry has kept me happy when working on topics I sometimes found difficult to understand. You are one of the nicest and most approachable people I have worked with. When talking to you I feel I can say "I still don't get it" as often as needed.

My advisor, Cristian Picioreanu, your strife for excellence and captivating writing style have taught me a lot about writing papers. Thank you for introducing me to the people in AWMC, it was you who after completing my masters lured me out of my comfort zone that is "cold and dark Western Europe" and allowed me to have this learning opportunity in Australia.

My mathematical modelling colleagues, particularly Keelan Fischer and Emma Thompson, thank you for the valuable modelling discussions we have had. Enjoy the wealth of computing time you will now have on the server, you deserve it.

My thesis reviewers and milestone committee, Dr. Amelia-Elena Rotaru, A/Prof. Daniel Bond, A/Prof. Tony Howes and Dr. Stefano Freguia, thank you for your time and feedback on my work. Your kind words and down-to-earth view on research have really improved the quality of my work.

I would also like to thank the fantastic people I have met here in Brisbane. My current and previous office mates, my house mates and their families, the Hawken Gang, the Gehrmann level 6 West Side, Waffles & Friends, the French OTs from 2013, my Dutch and spare-Dutch friends, the AD13 Spain road trip companions, the people I have tutored Statistics with and everybody in AWMC, your friendship has made this one of the most amazing experiences of my life.

My friends back in the Netherlands, who have remained in touch despite the changes in your lives and mine, I am looking forward to seeing you soon.

My family, thank you for your support. We have a lot of catching up to do, wine to drink and pistachio nuts to eat.

And finally, Linda de Waal, thank you for the love and support you have given me these past three and a half years I have been on the other side of the world. I remember when I told you for the first time about the PhD project, you immediately said "awesome" and that I should go for it. You have never doubted me, always allowed me to chase my dreams. Now, finally, I am done, and I am coming back to you.

KEYWORDS

Anaerobic digestion, anaerobic oxidation of methane, biofilm, electron transfer, microbial communities

AUSTRALIAN AND NEW ZEALAND STANDARD RESEARCH CLASSIFICATIONS (ANZSRC)

ANZSRC code 060106	Cellular Interactions	70%
ANZSRC code 060504	Microbial ecology	20%
ANZSRC code 090702	Environmental Engineering Modelling	10%

FIELDS OF RESEARCH (FOR) CLASSIFICATION

FoR code: 0904	Chemical Engineering	50%
FoR code: 0907	Environmental Engineering	30%
FoR code: 0605	Microbiology	20%

TABLE OF CONTENTS

3 Mediated versus direct interspecies electron transfer 53

4 Modelling of shell-shaped aggregates in zero-valent sulfur mediated anaerobic oxidation of methane 71

5 Conclusions and recommendations 90

LIST OF FIGURES

LIST OF TABLES

LIST OF ABBREVIATIONS USED IN THE THESIS

Ac^-	Acetate
ADP	Adenosine diphosphate
ANME	Anaerobic methanotroph
AOM	Anaerobic oxidation of methane
API	Application programming interface
ATP	Adenosine triphosphate
DEET	Direct EET
DIET	Direct IET
DLVO	Derjaguin–Landau–Verwey–Overbeek
DNA	Deoxyribonucleic acid
DSS	*Desulfosarcina*, *Desulfococcus* or Desulfobulbaceae
EPS	Extracellular polymeric substances
FISH	Fluorescence *in-situ* hybridisation
For^-	Formate
H_2S	Hydrogen sulfide
H_2S_2	Hydrogen disulfide
H_2S_n	Hydrogen polysulfide
HAc	Acetic acid
HFor	Formic acid
HS^-	Bisulfide
HS_2^-	hydrodisulfide
HS_n^-	hydropolysulfide
IET	Interspecies electron transfer
K^+	Potassium ion
MIET	Mediated IET
NAD+	Nicotinamide adenine dinucleotide (oxidised form)
NADH	Nicotinamide adenine dinucleotide (reduced form)
ODE	Ordinary differential equation
Pro^-	Propionate
HPro	Propionic acid
RNA	Ribonucleic acid
S^-	Sulfide
S_2^-	Disulfide
S_n-	Polysulfide
SEM	Scanning electron microscopy
SR	Sulfate reduction
TEM	Transmission electron microscopy
VFA	Volatile fatty acid

Chapter 1

INTRODUCTION

1.1 RESEARCH MOTIVATION

A microbial cell is one of the simplest manifestations of life, yet a large community of microorganisms can show highly complex behaviour. Natural microbial communities consist of a number of different species interacting on a biochemical level, often to the mutual benefit of the involved microorganisms (symbiotic mutualism). For example, some communities of microbial species thrive by cooperatively consuming compounds a single species is unable to utilise (syntrophy). Besides biochemical interactions, microbial communities often show a particular and reproducible spatial organisation. This morphology often has a strong effect on the system as a whole, for example via substrate availability or membrane fouling. These macroscopic effects can be traced back to microscopic origins, namely the behaviour of individual cells. By changing external variables of a system (food source, mixing, anti-flocculant, etc.) or of the cells (cell types in the inoculum, inoculum organisation), the inter-species interactions and thereby the resulting community can change completely.

By investigating the interactions in microbial communities on a microscopic level, a better understanding can be obtained of what causes microbial communities to show certain macroscopic properties. In turn, this information can be used to improve desirable processes or limit detrimental effects. Mathematical models are described and applied in this thesis to analyse the role of mechanical and biochemical interactions on various microbial communities. The fundamental theory required to understand microbial systems, an overview of particularly interesting microbial communities and previous work done is summarised in this chapter. Based on the literature review, key research challenges are identified and the approach taken to address these challenges is discussed.

1.2 LITERATURE REVIEW

1.2.1 Fundamentals of microbial life

In its simplest form, a microorganism is a self-replicating entity that obtains chemical material and energy through the conversion of a substrate to a product. To study how microorganisms facilitate reactions, accumulate mass and energy, grow, divide and finally have a critical impact on their environment, an understanding of the fundamental physics, chemistry and biology behind these processes must be obtained.

Thermodynamics

Reaction thermodynamics determine how much energy can be obtained from a chemical or biological reaction and, therefore, if it proceeds. In particular, the second law of thermodynamics states that the total entropy or disorder of a system and its surroundings must be equal to (reversible) or greater than zero (irreversible process):

$$\Delta S_{total} = \Delta S + \Delta S_{surr} \geq 0 \tag{1.1}$$

with S denoting the entropy. If the temperature remains constant, the entropy change of the surrounding heat reservoir is related to the heat flow from the system into the surroundings ($-Q$) via $\Delta S_{surr} = -\frac{Q}{T}$ (Smith et al., 2001, chapter 5). If the process also takes place at constant pressure, the heat flow into the system (Q) is equal to the increase in enthalpy of the system, $Q = \Delta H$. Substituting these two equations into equation 1.1, multiplying by T and reorganising the terms yields the equation for the Gibbs free energy change of the system:

$$\Delta G = \Delta H - T\Delta S \leq 0 \tag{1.2}$$

Therefore, a reaction is feasible only if the Gibbs free energy change of the reaction under the actual conditions is less than zero, $\Delta G'_r < 0$. This is true as long as pressure and temperature changes are small, which is generally the case for biochemical systems.

The Gibbs energy change of reaction under standard conditions (ΔG^0_r) is calculated as the Gibbs free energy of the products minus the Gibbs free energy of the substrates. Therefore, given Gibbs energy of formation (ΔG^0_f) for all involved compounds and stoichiometry coefficients (ν) for the reaction (negative for substrates, positive for products), the Gibbs energy change of reaction under standard conditions is calculated as:

$$\Delta G^0_r = \sum_i \nu_i \Delta G^0_f \tag{1.3}$$

Standard conditions in this thesis refer to 298.15 K, an effective partial pressure of 1 bar for gaseous compounds and an effective concentration of 1 $\mathrm{mol\,L^{-1}}$ for aqueous solutions (pH 0). The Gibbs energy of formation is well tabulated for most compounds (for example, see section 5 in Haynes (2014)).

From the Gibbs energy change of reaction under standard conditions, ΔG_r can be adjusted for the concentration (for aqueous solutions) or partial pressure (for gases) of the compounds involved in the reaction using the reaction quotient Q:

$$\Delta G'_r = \Delta G^0_r + RT \ln Q \qquad \text{where } Q = \prod_{i \text{ is (aq)}} \left(c_i/c_{ref}\right)^{\nu_i} \prod_{i \text{ is (g)}} \left(p_i/p_{ref}\right)^{\nu_i} \tag{1.4}$$

ΔG^0_r is calculated using equation 1.3. The value of c_i/c_{ref} for pure components (e.g., water or solids) is 1. c_{ref} is the reference concentration (standard 1 $\mathrm{mol\,L^{-1}}$) and p_{ref} is the reference pressure (standard 1 bar). In some cases, especially if c_i or p_i is high, the non-ideality of the mixture is taken into account in equation 1.4 by replacing these quantities with activity a (effective concentration) and fugacity f (effective partial pressure).

Biological reactions

Cellular biomass is accumulated via the anabolic reaction. Because of the chemical complexity of cells, the amount of biomass is usually denoted in mol carbon (Cmol). A commonly used composition is $CH_{1.8}O_{0.5}N_{0.2}$ (neglecting elements that make up smaller fractions of biomass, such as P, S, K, Mg and various trace elements). In order to produce biomass, compounds containing these elements are consumed, which in itself is generally a highly unfeasible reaction ($\Delta G'_r > 0\ \mathrm{kJ\,mol^{-1}}$). To allow the anabolic reaction to proceed, energy is consumed by the cells in the form of adenosine triphosphate (ATP), which releases useful energy when it is converted to adenosine diphosphate (ADP).

Living cells require energy in the form of ATP not only to grow, but also to repair deteriorating cell components and maintain a feasible intracellular environment, for example by pumping out Na^+ ions leaking into the cell (Heijnen and Kleerebezem, 2009). This process is called maintenance and can take up a large fraction of the available energy, especially for slow-growing microorganisms.

In order to take up and store energy in the form of ATP, cells perform catabolic reactions. By coupling the oxidation of an electron donor to the reduction of an electron acceptor an excess of Gibbs free energy is released. Through a complex pathway, the energy released by the catabolic reaction is coupled to the generation of ATP which is later used to make non-spontaneous reactions feasible.

Aerobic versus anaerobic growth

The amount of energy available to microorganisms via the catabolic reaction depends strongly on the environment in which cells grow, in particular on the presence or absence of free oxygen (O_2). Oxygen is a strong electron acceptor and releases a large quantity of energy when coupled to an electron donor in the catabolic reaction, which in turn is readily used to generate ATP. Microorganisms grow-

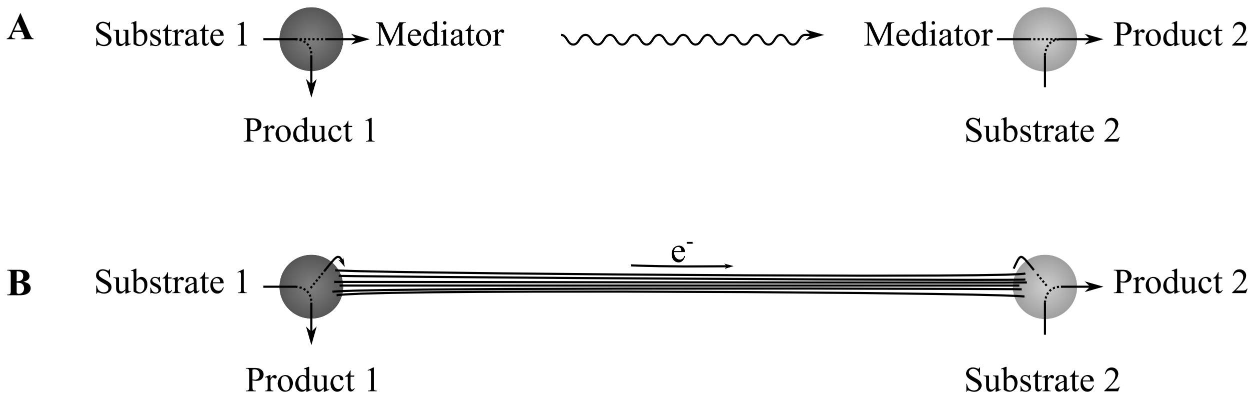

Figure 1.1: Schematic representation of the different interspecies electron transfer (IET) modes investigated in the thesis, (A) mediated IET; (B) nanowire direct IET.

ing in aerobic environments generally have enough energy available for anabolism and maintenance through the conversion of free oxygen, allowing them to grow at high rates.

Microorganisms growing in the absence of oxygen (anaerobic microorganisms) use alternative electron acceptors (e.g., carbon dioxide) and therefore have less energy available per mol substrate consumed in the catabolic reaction. The metabolism of these cells is often very specialised, with cells utilising energy in a very efficient manner. One technique used by cells is syntrophy. Mixed species microbial communities allows cells to specialise and efficiently consume one substrate, producing an intermediate that can be used by another species.

A commonly used form of syntrophy is interspecies electron transfer (IET). It allows one species (electron-donating species) to dispose of the electrons produced through its metabolic reactions by transferring the reducing equivalent to another species (electron-accepting species), which consumes the electrons to drive its metabolism. IET plays an important role in bioelectrochemical systems and in thermodynamically limited processes, such as syntrophic organic acid and ethanol oxidation in anaerobic digestion.

Mediated interspecies electron transfer

Mediated interspecies electron transfer (MIET) is the most frequently described mode of IET, whereby electrons are transported from electron-donating cells to electron-consuming cells using a mediator compound (figure 1.1). In MIET, the electron-donating species releases Gibbs free energy by oxidising the substrate while disposing of the released electrons by reducing another compound, thereby producing the mediator. Another microbial species releases energy by reducing one compound while oxidising the mediator. The product at the electron-donating species is removed, while the electron-accepting species is supplied a substrate, making MIET a mutually beneficial process for the species involved.

Hydrogen-mediated interspecies electron transfer (hydrogen-MIET) has been generally proposed as the dominant transfer mechanism in for example syntrophic propionate oxidation via acetogenesis and methanogenesis in anaerobic digestion. The electrons released at the electron-donating species are transferred to protons form hydrogen, which can store 2 mol electrons per mol H_2 ($H_2 \longrightarrow 2\,H^+ + 2\,e^-$).

The thermodynamic feasibility of hydrogen-MIET is generally low and highly sensitive to the mediator concentration, in some cases too low to explain the observed metabolic rates. Alternative mediated IET modes such as formate-MIET have since been suggested, allowing an increased metabolic rate due a larger concentration range under which the thermodynamic reactions are feasible (Boone et al., 1989; Batstone et al., 2006). While many microorganisms encode for genes important to formate utilisation, they fail to utilise formate in pure culture (e.g., methanogenic archaea (Hedderich and Whitman, 2013)), leaving hydrogen as default, presumably less favourable electron transfer mode for many systems (e.g., anaerobic digestion, anaerobic oxidation of methane coupled to sulfate reduction).

Direct interspecies electron transfer

Direct interspecies electron transfer (DIET) has been recently proposed as a more feasible IET mode that is not limited by the diffusion rate of the mediator (Summers et al., 2010). Unlike mediated IET, no electron carrying compound is transported. Instead, cell-cell electron transfer occurs via an electron-conducting matrix such as conductive pili called nanowires (Reguera et al., 2005), as depicted in figure 1.1B.

Direct IET is analogous to direct extracellular electron transfer (DEET), which describes electron transfer between cells and solid-state electron acceptors (e.g., iron or manganese oxides, electrodes). Outer membrane cytochromes play an important role in extracellular electron transfer to insoluble minerals such as Fe(III) oxides in *Geobacter* (Mehta et al., 2005), as well as in *Shewanella* species (Shi et al., 2009; Okamoto et al., 2011). If electrons during direct IET follow a pathway similar to that observed in respiration of Fe(III)/Mn(IV) oxides, then reduced intracellular redox carriers such as NADH would transfer electrons through the extracellular environment via c-type cytochromes and conductive pili (Lovley, 2012). At the receiving end of the conductive pili, electrons needs to be transferred to the methanogen via another redox complex.

DEET research has revolved mainly around studies of bacteria belonging to the genera *Shewanella* and *Geobacter* (Stams et al., 2006), which are proven to be highly efficient in engaging with solid extracellular electron acceptors. Cell-to-cell DIET has been observed mainly in defined co-culture IET systems of these organisms (e.g., for *Geobacter metallireducens* and *G. sulfurreducens*) (Summers et al., 2010; Liu et al., 2012; Shrestha et al., 2013), as well as in *Geobacter* dominated mixed-culture performing ethanol oxidation (Morita et al., 2011). Recently, it was shown that DIET can occur in methanogenic systems and between microbial species commonly found in environmental biological aggregates (e.g., between *Methanosaeta* and *Geobacter* species) (Rotaru et al., 2014b). Use of DIET over MIET can even enhance the metabolic capability of methanogens such as *Methanosarcina barkeri* to allow methanogenesis simultaneously from CO_2 reduction and acetate cleavage (Rotaru et al.,

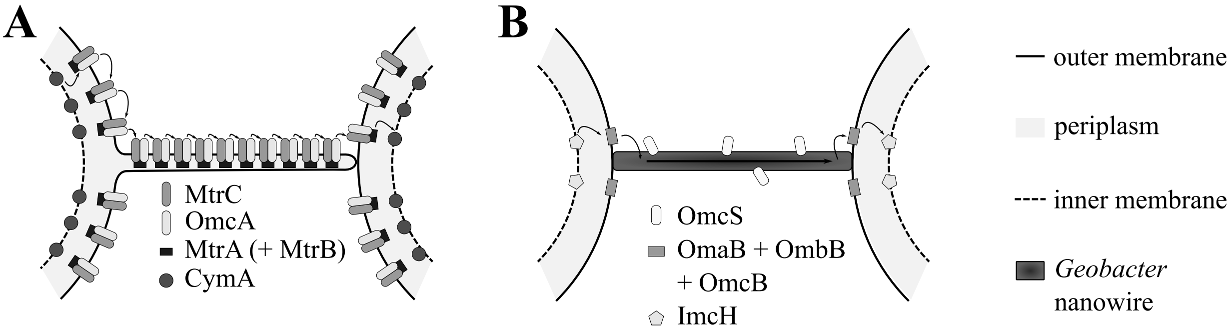

Figure 1.2: Schematic representation of the hypothesised protein complexes and electron import/export pathways used in direct interspecies electron transfer (direct IET) for (A) *Shewanella*; and (B) *Geobacter*, based extracellular electron transfer (DEET) mechanisms reported in literature. Note that this is a simplified overview and the role of these and other proteins is being debated.

2014a). Although bacteria belonging to the genus *Shewanella* have been frequently reported to transfer electrons to electrodes or Fe(III) or Mn(IV) oxides, their role in interspecies interaction remains to be reported and the role of direct electron transfer is still disputable (Marsili et al., 2008; Kotloski and Gralnick, 2013).

Assuming that the external pathway for direct IET is analogous to that of DEET to insoluble metal oxides, two main processes are defined in which protein complexes could play a role in direct IET: transfer from the cell interior to the exterior and transport along the nanowire. It is believed that transfer and transport occur via different pathways for *Shewanella* and *Geobacter* (Shi et al., 2007).

Various studies have tried to characterise the DEET mechanism pathways. New information based on proteomic studies are rapidly being published, identifying new proteins involved or refuting previously published findings. Below is a summary of conclusions drawn in recent literature, proposing a possible but highly speculative and incomplete pathway for DIET between similar microorganisms (*Shewanella*-*Shewanella* and *Geobacter*-*Geobacter*).

For *S. oneidensis*, an electron present in the inner membrane quinone/quinol pool is transferred via CymA across the periplasm (Myers and Myers, 2000). Here, MtrA facilitates transfer across the periplasm (Pitts et al., 2003) (most likely via MtrB, see Myers and Myers (2002)) to OmcA and MtrC cytochrome complexes located all along the outer membrane (Shi et al., 2009). Recent work has suggested that the nanowires observed in *S. oneidensis* are extensions protruding from the periplasm and outer membrane (Pirbadian et al., 2014), suggesting that long-range electron transport in *Shewanella* takes place via hopping between the OmcA/MtrC sites located along the nanowire (Pirbadian and El-Naggar, 2012). To extend the DEET pathway for *Shewanella* to direct IET, the electron must be transferred from the nanowire initiated by one species to the cell interior of the partner species. A possibility is that this occurs via the same pathway in reverse (i.e., the electron transfers from an OmcA/MtrC site on the nanowire to an outer membrane cytochrome complex of the partner species). This pathway is shown in figure 1.2A.

Even less is known about electron transfer from the interior to the exterior of *G. sulfurreducens* (Shi et al., 2007). Electrons are believed to be transferred across the inner membrane via ImcH (Levar et al., 2014). OmcB is believed to be present in the outer membrane (Qian et al., 2007) as part of an OmaB/OmbB/OmcB protein complex (Liu et al., 2014), although its role in electron transfer is yet to be confirmed. OmcS is located along the nanowire and possibly plays a role transferring electrons from solid metal oxides to the nanowire in DEET (Mehta et al., 2005; Leang et al., 2010), but its role in DIET is unknown. Transfer between the nanowire and the partner cell's inner membrane is assumed to occur via this pathway in reverse. A schematic representation of this pathway is given in figure 1.2B.

Unlike the *Shewanella* nanowire, the *Geobacter* nanowires were found to be pili showing metallic-like conductivity (Malvankar et al., 2011; Vargas et al., 2013; Malvankar et al., 2014). For *Geobacter*, proteins PilA and OmcS play an important role in the conductivity of the nanowire, but are not directly used for long-range electron transport (Leang et al., 2010; Veazey et al., 2011; Malvankar et al., 2012b; Vargas et al., 2013), providing further evidence that electrons are transported using different mechanisms in *Geobacter* and *Shewanella*.

In the last few years, the mechanism for electron transport along the nanowire has been frequently debated (for example, see Strycharz-Glaven et al. (2011), Malvankar et al. (2012a) and Strycharz-Glaven and Tender (2012)). The relative feasibility of the proposed mechanisms (electron hopping and metallic-like conductivity) is not further investigated in the thesis. Because literature provides parameters required to model metallic-like conductivity as observed in *Geobacter* this mechanism is presumed when examining the relative feasibility of direct and mediated IET.

In chapter 3, the feasibility of direct versus mediated IET is evaluated for the acetogenesis and methanogenesis steps in anaerobic digestion by analysing the extracellular limitations of these mechanisms.

1.2.2 Microbial communities in nature

Interspecies interactions allow cells of different species to influence each other (symbiosis), either with a beneficial effect for some or all of the involved species (mutualism), a beneficial effect for one of the species without significantly affecting others (commensalism) or with a beneficial effect for one species, while harming one or multiple others (parasitism). Through biochemical and bio-electrochemical interactions described in subsection 1.2.1 and through mechanical interactions (e.g., cell-cell EPS and filial links, displacement of newly formed cells resulting from anti-collision forces, etc.), microorganisms have an effect on each other and the microbial community as a whole.

Four types of microbial communities that are important for environmental, industrial or medical reasons have been identified and are described in this chapter.

Biofilms

A biofilm is a collection of microbial cells on a surface, often held in place by extracellular polymeric substances (EPS) and cell-cell or cell-substratum pili connections. Biofilms are formed naturally in many environments where enough substrate is available and conditions are feasible (for example, relatively high humidity and temperature). By definition, biofilms grow on a surface (substratum). Sometimes this surface also functions as the food source (e.g., microbially induced corrosion, Picioreanu and van Loosdrecht (2002)).

EPS plays an important role in biofilms and other microbial aggregates. Most microbial cells secrete various polysaccharides, proteins and other compounds, forming the "microbial glue" that makes up 50-90% of the organic matter in biofilms, thereby allowing cells and other biomass to agglomerate through the formation of hydrogen bonds or exerting cell-cell DLVO (Derjaguin–Landau–Verwey–Overbeek) forces (Hermansson, 1999; Evans, 2000, chapter 2). Besides cell-cell interactions, cell-substratum interactions are known to play an important role in biofilm formation (Donlan, 2001).

Biofilm development is generally described by three stages (figure 1.3):

1. Initial attachment
2. Maturation
3. Quasi-steady state due to biomass detachment

When a cell or a small cluster of cells suspended in the medium approaches a substratum, van der Waals forces allow the cells to attach to and remain on this surface (figure 1.3A). Given enough time the cell divides or more cells attach (B). Often connections are formed between the cell and surface (C), either making a connection to a fixed location (pili anchor the cell to a position on the surface) or maintaining a constant distance to the surface (EPS is secreted by the cells, allowing them to glide over the surface).

When the initial cells are attached to the substratum it becomes easier for the biofilm to grow due to the increasing number of cell-cell and cell-substratum links, allowing rapid growth of the biofilm (figure 1.3D). If a moving medium is present (dotted line in the figure), the cells shield each other from mechanical stress exerted by the flow. Eventually, further cell attachment and division (maturation) results in the biofilm becoming thicker (E and F).

Tall, finger-shaped extrusions are often formed when biomass detachment rates are low (figure 1.3G) and can break off in their entirety due to forces exerted by the flow (sloughing, H). The thicker biofilm becomes more exposed and shear stress start to detach small amounts of the biofilm (erosion, H). Biomass detachment due to mechanical stress causes the biofilm to become more uniform, as has been demonstrated in experiments (van Loosdrecht et al., 1995) and using mathematical modelling (Xavier et al., 2005a). As detachment becomes more dominant, the amount of biomass over a longer time period remains constant (dynamic steady state, H).

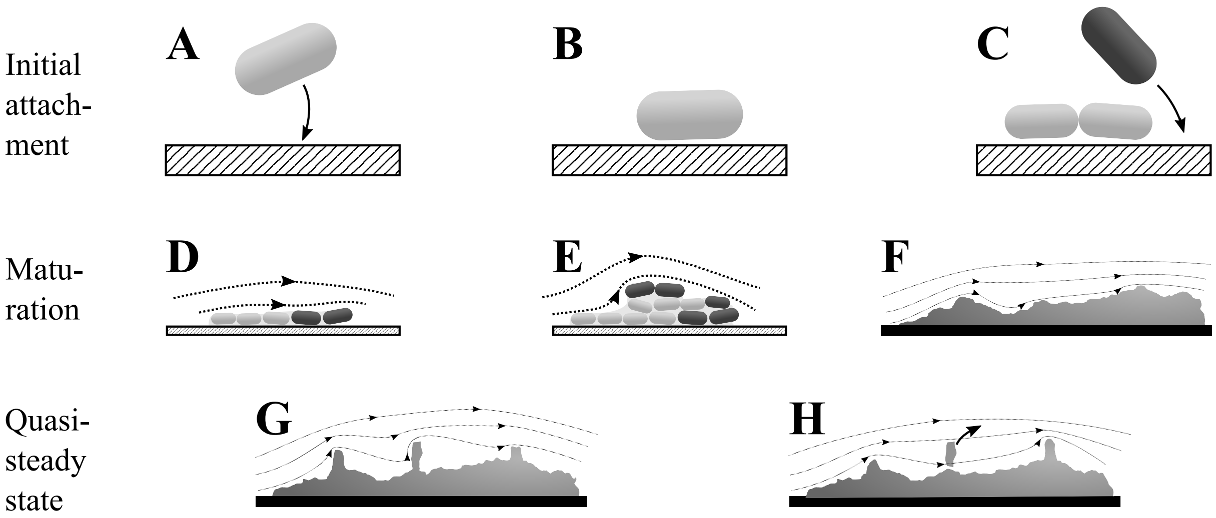

Figure 1.3: Schematic representation of the three stages of biofilm development. (A) Initial cell approaches surface; (B) cell is suspended above the surface due to electrostatic and other cell-surface forces; (C) cells divide, new cells attach; (D) division and attachment continues to form a monolayer, only slightly influencing fluid flow (dotted line); (E) cell stacking causes biofilm to become thicker; (F) biofilm continues to grow and forms small extrusions; (G) extrusions become tall, finger-like structures, obstructing flow; (H) erosion (first finger) and sloughing (second finger) cause detachment while new extrusions form (third finger).

Besides protection from mechanical stress, biofilms provide an evolutionary advantage for microbial cells by allowing cells to exchange material, either as syntrophic interactions (e.g., interspecies electron transfer, subsection 1.2.1), DNA (Evans, 2000, chapter 6), or cell-cell signalling (Nadell et al., 2008).

Biofilm growth and development without medium flow is studied in chapter 2. Inclusion of stresses induced by medium flow is discussed in Outlook and future work (section 5.3).

Activated sludge flocs

The activated sludge treatment process is applied in sewage treatment in order to remove biological material and various contaminants present in wastewater. In an aeration tank, a complex microbial community uses the organic and inorganic contaminants present in the sludge together with the supplied oxygen to grow, thereby removing the soluble pollutants. Afterwards, the mixture of biomass and treated water is pumped into a settling tank, where the biomass flocs sink to the bottom, separating the activated sludge from the water. Part of the biomass is recycled to the aeration tank, while the water is further treated or returned to rivers or seas.

Although the process occurs naturally in wastewater, industrial applications of the activated sludge process are carefully monitored and adjusted in order to minimise odour and amount of biomass washed out, while maximising the conversion of waste. How cost-efficient a treatment plant is depends strongly on how well the microbial growth processes are controlled.

Within the microbial communities, the distinction can be made between floc-forming and filamentous microorganisms. In the sludge, floc formers, filament formers, EPS and other types of biomass form dense heterogeneous aggregates commonly referred to as flocs. Floc-forming microorganisms tend to form dense aggregates, while filament formers grow as long strands of cells. Many mathematical models make this distinction and model the microorganisms in the sludge as such (Seviour and Nielsen, 2010, chapter 5).

Which type of organisms dominate the microbial communities is governed by the nutrients in the water, the oxygen availability, solid and hydraulic retention time, temperature, pH and various other conditions that can be directly or indirectly controlled in the wastewater treatment plant. It is generally assumed that the floc formers have a higher maximum growth rate than the filament formers but a lower affinity for oxygen and nutrients (kinetic selection theory) (Seviour and Nielsen, 2010, chapter 5). This means that floc formers generally have higher specific growth rates when sufficient substrate is available, while filament formers dominate the floc if oxygen availability is limited or dissolved nutrient concentrations are low.

Depending on the relative abundance of the various types of microbes, various floc morphologies can be obtained. When a healthy balance of floc formers and filament formers grows in the sludge, ideal flocs are formed that consist of an internal matrix of filaments providing structure and support on which floc formers grow. These flocs settle readily in activated sludge processes and thereby minimise biomass wash-out. If too few filaments are formed, the resulting pinpoint flocs can be easily broken up as a result of turbulence, which is detrimental to the settleability of the sludge. When excessive amounts of filaments are formed, the filaments "escape" the floc interior, which results in large, sparse flocs and can result in interfloc bridging, in turn causing sludge bulking and foaming (Sezgin et al., 1978; Madigan et al., 2009).

In chapter 2 the effect of relative growth rates and resulting activated sludge floc structure is studied.

Anaerobic digestion

Anaerobic digestion describes a collection of processes in which an organic substrate is broken down by microorganisms under oxygen-poor conditions. It is a common process in natural environments such as wetlands, where a low diffusion rate limits the oxygen availability and methane is produced by microorganisms in the resulting anaerobic subsurface. Methanogenesis in wetlands is responsible for significant amounts of the greenhouse gas emitted into the atmosphere (Bridgham et al., 2013). Anaerobic digestion is frequently applied in industry, for example to convert harmful organics into less harmful compounds (wastewater treatment plants) or to produce energy in the form of biogas (a mixture mostly consisting of methane and carbon dioxide) from organic material. In recent years, applications are steered towards combining waste treatment with energy generation and resource recovery. Wastewater treatment plants are focusing on the recovery of fertiliser and energy, while biogas production utilises waste streams from other industries as a (co-)substrate.

Anaerobic digestion converts complex organic compounds into a mixture of methane and carbon dioxide in four steps, as shown in figure 1.4.

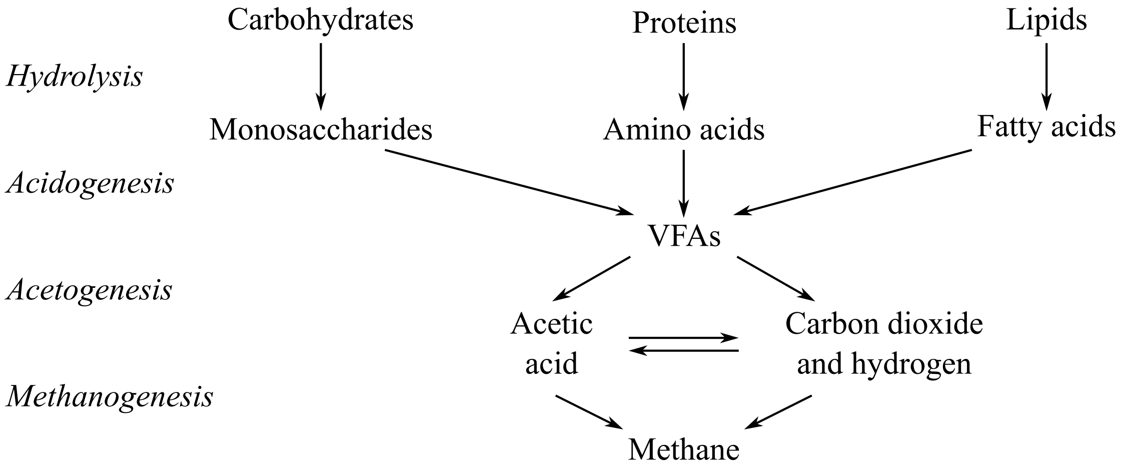

Figure 1.4: Schematic representation of the different steps in an anaerobic digestion process. Only major reactions are shown and hydrogen is assumed as the default mediator in acetogenesis/methanogenesis. Conversion from acetic acid to carbon dioxide and vice-versa occurs via homoacetogenesis and microbial acetate oxidation. VFAs is short for volatile fatty acids.

Organic substrate fed to the digester is generally a mixture of various organic compounds, each of which consists of units linked together into polymer chains (e.g., multiple glucose units form a polysaccharide compound). In the hydrolysis step, these chains are cleaved through the addition of water, in turn producing monomers of simple sugars, amino acids, and fatty acids that can more easily be consumed by microorganisms in successive steps. Smaller compounds, such as volatile fatty acids (VFAs), acetate and hydrogen are produced in small amounts as well.

In the acidogenesis step, fermentative bacteria further break down the monomers produced by hydrolysis into VFAs such as butyrate and propionate. These products function as substrates for acetogenesis and methanogenesis.

Acetogenesis converts the VFAs into acetate or acetic acid (Ac^-, HAc), carbon dioxide (as CO_2 or bicarbonate, $HCO_3{}^-$) and hydrogen, such that for propionate (Pro^-) and butyrate (But^-) this step is described by the following reactions:

$$\mathrm{Pro^- + 3\,H_2O \longrightarrow Ac^- + HCO_3{}^- + 3\,H_2 + H^+} \tag{1.5a}$$

$$\mathrm{But^- + 3\,H_2O \longrightarrow 2\,Ac^- + 2\,H_2 + H^+} \tag{1.5b}$$

After this phase of the anaerobic digestion, the digestible organic compounds in the substrate have largely been converted into acetate, carbon dioxide and hydrogen.

In the final step of anaerobic digestion, methanogenesis converts the mixture into methane (CH_4) and carbon dioxide. For hydrogen, this yields the reactions:

$$\mathrm{Ac^- \longrightarrow CH_4 + HCO_3{}^-} \tag{1.6a}$$

$$\mathrm{HCO_3{}^- + 4\,H_2 + H^+ \longrightarrow CH_4 + 3\,H_2O} \tag{1.6b}$$

Syntrophic interactions are important especially for the acetogenesis and methanogenesis steps. The thermodynamic feasibility of reactions 1.5a, 1.5b and 1.6b is low, as only a few kilojoule of energy is released per mol reaction under natural conditions. Because of the low hydrogen concentration in acetogenesis/methanogenesis, small changes in the concentration govern the feasibility of these reactions, as further discussed in chapter 3. Despite the relatively feasible acetoclastic methanogenesis (equation 1.6a) being responsible for the majority of the methane produced in common anaerobic digestion communities (2 to 3 times higher than hydrogenotrophic methanogenesis (Batstone et al., 2002)), accumulation of hydrogen is problematic for the community as it can inhibit acetogenesis. Even with fast consumption of the intermediate hydrogen, thermodynamic calculations have shown that hydrogen would not be a feasible intermediate for the acetogenesis/methanogenesis reactions (Boone et al., 1989). Alternative intermediates and transfer modes for propionate oxidation coupled to methanogenesis have been proposed to try and explain the experimentally observed reaction rates, as is discussed in more detail in chapter 3.

Anaerobic oxidation of methane in deep sea sediments

Vast quantities of methane are continuously released from seeps in the ocean floor and contribute strongly to the greenhouse effect, with recent discoveries suggesting that the number of methane seeps is much higher than previously assumed (Skarke et al., 2014). Before it reaches the atmosphere, a large fraction of the gas released is biologically converted through anaerobic oxidation of methane coupled to sulfate reduction (AOM/SR) (Boetius et al., 2000):

$$\mathrm{CH_4(aq) + SO_4{}^{2-} \longrightarrow HS^- + HCO_3{}^- + H_2O} \tag{1.7}$$

Fluorescent in-situ hybridisation (FISH), isotopic and phylogenetic analysis have shown that the anaerobic methanotrophs (ANME, clades ANME-1, -2 and -3) and species of the genus *Desulfosarcina*, *Desulfococcus* or family Desulfobulbaceae (for simplicity all abbreviated to DSS) play an important role in AOM/SR (Boetius et al., 2000; Orphan et al., 2001; Milucka et al., 2012). For some years it was commonly assumed that AOM occurs at the ANME species while SR occurs at the DSS (in some work therefore often called sulfate-reducing bacteria, SRB) with some unknown interspecies electron carrier. However, most proposed electron carriers have been disproved with thermodynamic calculations or lack supporting evidence (Sø rensen et al., 2001; Nauhaus et al., 2002; Orcutt and Meile, 2008; Knittel and Boetius, 2009). Recent work has investigated syntrophy between the ANME-2/DSS species with another approach and presented strong evidence that both sulfate ($SO_4{}^{2-}$) and methane (CH_4) are converted at the ANME-2 cells in order to produce elemental sulfur (S_0), which is exported as polysulfide (Milucka et al., 2012). The role of the DSS is then to scavenge energy by disproportionating the polysulfides produced at the ANME-2 to sulfide and elemental sulfur. Experimental evidence suggests hydrodisulfide ($HS_2{}^-$) is the dominant intermediate in the ANME-2/DSS aggregates (Milucka et al., 2012). Based on these findings, equation 1.7 can be split up into catabolic reactions 1.8 and 1.9:

$$7\,CH_4(aq) + 8\,SO_4{}^{2-} + 5\,H^+ \longrightarrow 4\,HS_2{}^- + 7\,HCO_3{}^- + 11\,H_2O \tag{1.8}$$

$$4\,HS_2{}^- + 4\,H_2O \longrightarrow SO_4{}^{2-} + 7\,HS^- + 5\,H^+ \tag{1.9}$$

Microscopic analysis of AOM/SR communities has shown that ANME-2 and DSS are usually in close proximity, further suggesting that a syntrophic interaction takes place between ANME-2 and DSS. It was found that 60 to 70% of the total biomass present in the reported systems is contained in well-organised shell-shaped aggregates, with an inner layer of ANME-2 and an outer layer of DSS (Orphan et al., 2002; Nauhaus et al., 2007). Alperin and Hoehler (2010) has shown that shell-shaped aggregates are thermodynamically considerably less feasible than interspersed ANME-2 and DSS (for a diffusion-reaction interspecies hydrogen transfer system, which should translate well to the disulfide mechanism from Milucka et al. (2012)). The reason for aggregates developing a shell-shaped morphology has thus far only been investigated using a rule-based division numerical model (Nauhaus et al., 2007), which is limited in that (i) division rules are enforced on a natural system, (ii) the effect of thermodynamics is not considered and (iii) the morphology seems to change for aggregates larger than 5 µm in diameter.

In chapter 4, the driving force behind the typical shell-shaped morphology observed in ANME-2/DSS deep sea sediments is investigated using thermodynamic calculations, diffusion-reaction simulations and Lagrangian-based mechanical modelling.

1.2.3 Analysis of microbial communities

In order to get a better understanding of development and workings of microbial communities, a range of analytical techniques is available, both theoretical and experimental. Work presented in this thesis has a strong focus on mathematical modelling, which allows detailed and easily obtainable insights to be obtained that would be limited or difficult to observe directly through experimental work. Mathematical modelling, however, requires experimental verification. Modelling results obtained as part of this thesis have been verified with experimental observations made by specialised researchers where possible. One of the most important experimental techniques used for verification of microbial aggregate properties is microscopy.

Microscopy

A wide range of microscopy techniques is available to study microorganisms, each of which is suited to investigate different properties of individual cells or of the community as a whole. Microscopy techniques that are frequently used to study different properties relevant for the work presented in this thesis are discussed.

Visualisation of community organisation and protein complex distribution

In order to get an estimate of the types of cells present in a community, fluorescence *in-situ* hybridisation (FISH) is frequently applied. By binding fluorescent probes to complimentary parts of the genome and analysing the samples using fluorescence microscopy, specific parts of the community light up. By overlaying images obtained using different probes, a map can be built with information on the spatial organisation of the different targets. Specific targets are related to certain microbial species, allowing visualisation of the microbial species distribution in samples such as shell-shaped aggregates facilitating anaerobic oxidation of methane/sulfate reduction (Orphan et al., 2002; Nauhaus et al., 2007). An alternative technique to visualise community properties (e.g., cytochrome presence) is Raman microscopy. Here, Raman scattering (a phenomenon where a photon is emitted of a wavelength typical for the sample material) to identify the presence of a certain compound in a defined state. In particular, Raman microscopy can be used to identify the redox state of cytochromes believed to be involved in direct electron transfer (Virdis et al., 2012, 2014), providing quantitative information about the transfer mechanism (Ly et al., 2013).

Analysis of individual cells, cell appendices and protein complex distributions

Electron microscopy techniques such as scanning electron microscopy (SEM) and transmission electron microscopy (TEM) are readily applied to study the morphology of microbial aggregates (Shapiro, 1987; Donlan, 2001), or to visualise individual cell appendices such as nanowires (Gorby et al., 2006; Pirbadian and El-Naggar, 2012) and redox complexes (Malvankar et al., 2011; Inoue et al., 2011). Through a combination of lenses, a beam of electrons is projected on a sample. Transmitting (primary) electrons (in TEM) or scattering (secondary) electrons (in SEM) are detected, allowing visualisation of the inner structure (using TEM) or surface (using SEM) of the sample. TEM is particularly useful for the visualisation of extracellular cytochromes using immunogold labelling (Leang et al., 2010).

Investigation of individual proteins and protein complexes

Diffraction limits the techniques used for subcellular microscopic analysis. Electron microscopy is one of few techniques that can investigate cells and subcellular organelles on the nanometre scale. Besides TEM, scanning tunnelling microscopy is frequently applied to study individual protein complexes and nanowire structures (Gorby et al., 2006; Veazey et al., 2011). Scanning tunnelling microscopy utilises the quantum tunnelling effect by setting a voltage difference between the tip and sample surface. The resulting current is affected by the sample-tip distance and the biological material, interpretation of which provides information on the surface morphology of the sample. Atomic force microscopy is another technique used to investigate individual nanowires. By using a conductive tip and applying a voltage difference, the charge propagation through *Shewanella* (El-Naggar et al., 2010; Pirbadian and El-Naggar, 2012) and *Geobacter* (Malvankar et al., 2015) nanowires has been investigated.

Mechanical modelling

Modelling of mechanical interactions in biological aggregates is a very powerful method to analyse the role of fundamental controlling factors in the structure and function of mixed microbial populations. Mechanical models help predict different structural and functional aspects like the shape and size of the aggregate, the development of a certain spatial distribution of microbial populations and EPS and are readily extended to model the impact of specific mechanisms such as gene transfer, microbial motility or cell-cell signalling.

The two basic approaches taken for modelling of mechanical interactions in microbial aggregates are based on a continuum or on an individual representation of the microbial community. Continuum based models use a volume-averaged description of the biomass composing the biofilm. Starting from the now widely applied one-dimensional continuum models (Wanner and Gujer, 1986), more complex two- and three-dimensional continuum multispecies biofilm models have been proposed (e.g., Alpkvist and Klapper (2007a); Merkey et al. (2009)). Alternatively, in individual-based models, biofilms are represented as a collection of individual microbes or functional elements (agents), whereas substrate transport/reaction and hydraulic flow are solved separately in a continuum field (e.g., Kreft et al. (2001); Lardon et al. (2011)). Models combining continuum (for EPS) with individual (for microbial cells) representations have also been developed (Alpkvist et al., 2006). Both approaches are suitable to investigate mixed population aggregates, with individual-based models generally being superior for investigating the impact of interactions at microbe level, while the continuum-based approach is still more applicable at larger geometric scales (Wood and Whitaker, 1998).

Individual-based modelling of microbial populations has allowed the spatial investigation of the role of intra- and extracellular polymer substances (Xavier et al., 2005a; Xavier and Foster, 2007; Lardon et al., 2011), gene transfer (Seoane et al., 2011; Rudge et al., 2012), cell-cell communication and quorum sensing (Nadell et al., 2008, 2010; Melke et al., 2010), microbial motility (Picioreanu et al., 2007; Janulevicius et al., 2010; Harvey et al., 2011), antibiotic resistance and survival of persister cells (Chambless, 2006) and substrate transfer effects on many different microbial ecology interactions (competition, mutualism, parasitism, toxicity, cross-feeding, *etc.*) (Picioreanu et al., 2004; Batstone et al., 2006; Xavier et al., 2007; Picioreanu et al., 2010).

A key challenge in individual-based modelling has been determining how position of the agents (the cells and parts thereof) change over time, which at higher level determines how the microbial colonies spread and change in shape, size and microbial ecology. In approaching this essential mechanical problem, the existing microbial community models are often limited in their complexity in one or more of the following ways:

1. Only simple microbial geometries are applied, either spheres or cylinders
2. Structural properties of the aggregate are not determined by the action of individual agents, but are imposed on a collection of agents

3. Rigid connections are used for intra- or intercellular links.

Microbial morphology contains essentially two elements: the primary morphology refers to cell shape (e.g., cocci are spherical cells, bacilli are rod-shaped, *etc.*), while the secondary morphology is related to division mode and subsequent sibling connections (e.g., strings of streptococci, grape-like staphylococci colonies, sarcina tetrads, filamentous bacilli, branched filamentous streptomyces, *etc.*). The simplest shape (i.e., sphere in three or circle in two dimensions) for a microbial cell allows for ready computation of division and anti-collision (Kreft et al., 1998, 2001), but it brings serious limitations when describing a series of other aspects numerically, as it can be easily observed that cells have a wide variety of morphologies (Madigan et al., 2009). For example, bacilli (rod-shaped cells) may have a different response to substrate concentrations as compared to cocci (sphere-shaped cells) as rods have a larger surface-to-volume ratio than spheres. Rod-shaped cells also transfer genes differently when side-to-side than when perpendicular to each other (Seoane et al., 2011). Cell-cell and cell-surface electron transfer can also be influenced by the cell shape and the way cells connect in a filamentous micro-colony (Pfeffer et al., 2012). It is also hypothesised that specific co-aggregation between cells with different morphology (e.g., filamentous actinomycetes with streptococci and with lactobacilli) is essential in the formation of complex food webs such as in dental plaque (Kolenbrander, 2000)). Cell morphology also strongly affects the shape of the aggregate. For example, an array of filamentous rod-shaped cells can form a longer, more slender and more rigid filament than the equivalent amount of spherical cells. Therefore, understanding how filamentous microorganisms influence aggregates is very important in formation of activated sludge flocs used in water treatment (Martins et al., 2004; Seviour and Nielsen, 2010, chapter 5). Real world functionality of morphology infers that different cell shapes should also be included in agent based modelling, particularly where interactions between individual cells are being investigated.

In a coarse-grain representation of the biofilm microbial structure, grouping of cells as a collection (cluster) and modelling only the interactions between different clusters would remove interactions between individual cells that could otherwise have a crucial effect on the aggregate structure. Nitrifying biofilms are one typical example where clustering is important, with ammonium and nitrite oxidizing organisms are typically organized in spherical clusters (Okabe et al., 1999; Alpkvist et al., 2006). This clustering would be more easily modelled using structural elements (e.g., strong adhesion forces between sibling cells).

In a mechanical model of microbial aggregates, the function of extracellular polymers is mainly to act as an elastic link between particles. Including biofilm structural components such as EPS as hard spherical objects (Xavier et al., 2005b; Matsumoto et al., 2010; Lardon et al., 2011) or rigid links (Popławski et al., 2008) may introduce artifacts related to the volumetric occupation and to the actual rheological properties of the polymeric matrix. Rather, in concordance with the particle-spring representation of microbial cells, the EPS matrix could be described by a collection of springs connecting a series of cells.

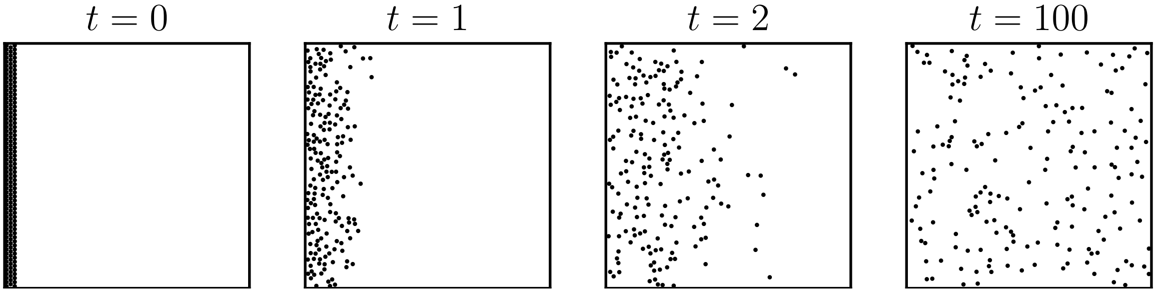

Figure 1.5: Example of the diffusion process on molecular level. Each box contains 179 circles.

In-depth numerical methods for microbial growth and resulting structures at cell level and cluster level (e.g. cellular Potts, (Popławski et al., 2008; Izaguirre et al., 2004)) are readily available in literature. Particle-spring approaches have already long been used in chemistry to model molecular interactions, for example in proteins using amino acid sub-units (Windisch et al., 2006). Particle-spring models have also been used before for maintaining an elastic cell shape and allowing for deformable cell-cell and cell-particulate connections in biofilms (Dillon et al., 1996; Harvey et al., 2011). More recently, these models have been constructed to explain patterns developed during the social movement of myxobacteria (Janulevicius et al., 2010; Harvey et al., 2011) where populations of flexible gliding rod-shaped cells were shown to form specific patterns as a function of the various forces acting on each bacterial body, subjected to multiple cell-cell interactions. By a similar method, large populations of long flexible filamentous cells of gliding cyanobacteria were modelled and the effectiveness of photophobic responses in this population was quantified (Tamulonis et al., 2011). Recently, growth and colony formation of zigzagged Diatoma chains in contrasting flow environments have also been modelled with a particle-spring model (Celler et al., 2014). However, the approach of modelling heterogeneous biofilms with growing microorganisms of variable morphology has not been previously addressed. A particle-spring, individual-based model in which cells of different morphologies are modelled is presented in chapter 2.

Transport and reaction modelling

Given the spatial organisation of cells in a microbial community, transport and reaction rates can be determined. Transport of chemical compounds through a medium (in biochemistry usually water) takes place via diffusion, migration and advection.

Diffusion

Diffusion is a transport process where a compound is transferred along a concentration gradient. It is a result of spontaneous movement of the solute (molecules) in the medium, where an initially organised system (e.g., figure 1.5, $t = 0$) reaches a state of higher entropy through random movement of the individual molecules ($t = 1$ and $t = 2$) until a dynamic steady state is achieved ($t = 100$). Although on a microscopic scale the molecules still move, the system on a macroscopic scale does not change.

Fick's first law describes the rate at which diffusive transport takes place on a macroscopic level. It states that the flux at which a diluted chemical species *i* in a stationary medium is transported is proportional to the concentration gradient via a diffusion coefficient:

$$J_i = -D_i \nabla c_i \tag{1.10}$$

The minus sign is needed because diffusion takes place from a high to a low concentration. The diffusion coefficient D_i depends on the chemical species that is being transported (e.g., an electron carrier), the medium in which diffusion takes place (usually water in biological systems) and the temperature of the system. Diffusion constants in water are well tabulated for common chemical compounds (e.g., in the CRC Handbook of Chemistry and Physics, Haynes (2014)) and can be estimated using empirical methods for compounds for which no experimentally determined values are available (e.g., Wilke-Chang relation (Wilke and Chang, 1955), with the molar volume estimated using LeBas additive volumes method (Albright, 2008)).

Through mass conservation principles, Fick's first law can be rewritten to describe a stationary or transient system. Mass conservation states that concentration change (accumulation) equals the production rate minus the gradient of the flux:

$$\frac{\partial c_i}{\partial t} = r_i - \nabla J_i \tag{1.11}$$

By substituting equation 1.10 for J_i, Fick's second law is obtained:

$$\frac{\partial c_i}{\partial t} = r_i + \nabla \left(D_i \nabla c_i \right)$$

The diffusion constant does not change significantly throughout the domain for biochemical processes and by factoring out D, Fick's second law can be written as:

$$\frac{\partial c_i}{\partial t} = r_i + D_i \nabla^2 c_i$$

Systems described in the thesis are generally considered to be stationary (i.e., in steady state), either because the steady state feasibility is compared (chapter 3) or because transport equilibrium occurs much faster than other phenomena (chapter 4). For a stationary system, $\frac{\partial c_i}{\partial t}$ is set to zero and Fick's second law is written as:

$$0 = r_i + D_i \nabla^2 c_i \tag{1.12}$$

Although diffusive transport is often slow (diffusion constants are generally in the order 1×10^{-9} $\mathrm{m^2\,s^{-1}}$), it is important for systems where medium transport is limited, such as sediments, microbial biofilms, aggregates, but also microscopic systems such as cell membranes.

Migration

The transport of charged particles (ions) is related to the potential gradient through the medium. The Nernst-Planck equation is used to model transport of diluted chemical compounds when both a diffusion gradient and a potential gradient are present. By adding a migration term to Fick's law (equation 1.10), the flux is described by:

$$J_i = -D_i \nabla c_i - \frac{z_i D_i F}{RT} c_i \nabla \Phi \tag{1.13}$$

Here, z_i denotes the charge of the ion, F Faraday's constant, R is the ideal gas constant (8.3145 $\mathrm{J\,mol^{-1}\,K^{-1}}$), T is the temperature and Φ is the electric potential (such that the electric field is represented by $E = -\nabla\Phi$).

Analogous to Fick's law, the stationary Nernst-Planck equation is obtained by substituting equation 1.13 for J_i in the equation for mass conservation (equation 1.11), assuming the term $\frac{z_i D_i F}{RT}$ is constant and setting $\frac{\partial c_i}{\partial t} = 0$:

$$0 = r_i + D_i \nabla^2 c_i + \frac{z_i D_i F}{RT} \nabla \left(c_i \nabla \Phi \right) \tag{1.14}$$

In order to model a diffusion-migration system on a macroscopic scale, an additional equation is required to fully define the system. This can be done by implementing the Poisson equation to model the effect of charge imbalance on the electric field:

$$\nabla^2 \Phi = -\frac{\rho_f}{\varepsilon} \qquad \text{where } \rho_f = F \sum_i \left(z_i c_i \right) \tag{1.15}$$

ρ_f is the charge distribution and ε is the permittivity of the medium. The Poisson-Nernst-Planck equations are commonly used in ion transport modelling and electrodialysis (Kurnikova et al., 1999; Nikonenko et al., 2014).

A disadvantage of the Poisson-Nernst-Planck equations is the increased complexity of the numerical methods, resulting in a mathematical model that is numerically more difficult to solve. Instead, a simplification is commonly applied by combining the Nernst-Planck equation with the local electroneutrality condition:

$$\sum_i c_i z_i = 0 \tag{1.16}$$

By fixing the concentration of one ion in order to satisfy the electroneutrality condition, the system can be solved. If an ion is chosen that is present in a sufficiently high concentration (e.g., potassium or sodium), the transport rate of the balancing ion is usually low enough to justify this simplification.

The Nernst-Planck equation is useful for modelling transport in diffusion-migration systems where an electric field is present (e.g., through the Poisson-Nernst-Planck equations in electrodialysis membranes (Nikonenko et al., 2014)), but is also relevant for systems where an electric potential can be formed as a result of an ion imbalance (e.g., by assuming local electroneutrality in direct interspecies electron transfer (chapter 3)).

Advection

Advection describes the transport of a compound dissolved in a bulk medium that is in motion. Depending on the system, advection can transport chemical compounds at high rates, for example in stirred reactors or gas seeps in oceans.

Given the velocity field **u** of the bulk medium and assuming (i) the medium is incompressible (generally a valid assumption for liquid flows, especially in low pressure biochemical systems), (ii) the system is stationary and (iii) migration is negligible, the equation for advection-diffusion-reaction systems is given by:

$$0 = r_i + D_i \nabla^2 c_i - \mathbf{u} \cdot \nabla c_i \tag{1.17}$$

The key challenge in calculating the advection rate is to determine the velocity field of the bulk medium, **u**. In the simplest case a laminar flow is present, which happens when the ratio of the inertial forces to the viscous forces (Reynold number, *Re*) is low. When this ratio is high, the medium flow is turbulent, causing the bulk medium to flow in chaotic patterns. Using computational fluid dynamics, the fluid flow can be simulated by evaluating the Navier-Stokes equation.

As stated in subsection 1.2.2, transport is studied in anaerobic oxidation of methane/sulfate reduction and anaerobic digestion (interspecies electron transfer). Advective transport and medium flow is neglected in these microbial systems due to the formation of dense aggregates. Diffusion and (for direct interspecies electron transfer) migration sufficiently describe transport in these systems. Implementation of fluid flow and advective transport is discussed in Outlook and future work, section 5.3.

Biological reactions

It is easily observed that the amount of biomass increases exponentially when thermodynamics remain feasible (i.e., enough substrate is available, no significant inhibition takes place). This is because the macroscopic rate at which living cells grow depends recursively on the mass of cells in the system, or in mathematical form:

$$\frac{dm}{dt} = m\mu \tag{1.18}$$

Here, μ is defined as the specific growth rate (often in units $\mathrm{kg\,kg^{-1}\,h^{-1}}$ simplified to $\mathrm{h^{-1}}$) and is related to the biomass doubling time via $\frac{\ln(2)}{\mu}$. Through integration of ordinary differential equation 1.18, the amount of biomass at any time t can be determined given the initial mass m_0:

$$m(t) = m_0 e^{\mu t} \tag{1.19}$$

For a simple system, the specific growth rate μ increases with the concentration until it approaches a plateau value μ_{max} (i.e., growth is a hyperbolic function of the substrate concentration). A frequently used model equation for μ is the Monod equation, which in its simplest form (single substrate, no inhibition, negligible biomass maintenance) is written as:

$$\mu = \mu_{max} \frac{c_s}{K_s + c_s} \tag{1.20}$$

μ_{max} and half-saturation constant K_s are empirically determined.

The Monod equation is an empirical form of the Michaelis-Menten equation. Analogous to the Michaelis-Menten equation, it can be extended to include various forms of inhibition. Non-competitive inhibition can be implemented as having an impact on μ_{max}:

$$\mu = \frac{\mu_{max}}{1 + c_i/K_i} \frac{c_s}{K_s + c_s} \tag{1.21}$$

Similarly, competitive inhibition modifies the substrate affinity:

$$\mu = \mu_{max} \frac{c_s}{K_s\left(1 + c_i/K_i\right) + c_s} \tag{1.22}$$

Uncompetitive inhibition is modelled through changing the effective substrate concentration in the denominator:

$$\mu = \mu_{max} \frac{c_s}{K_s + c_s\left(1 + c_i/K_i\right)} \tag{1.23}$$

Given the amount of biomass, the yield of biomass over substrate and the maintenance rates, the substrate consumption rate can be calculated from the specific growth rate. Empirical methods for estimating the biomass yield and maintenance energy are readily available in literature, such as the Herbert-Pirt relation (Heijnen, 2010).

Because for some microbial systems little is known about the kinetics, an equation based on reaction thermodynamics and transport limitations can be preferred to describe the rates at which biological reactions can take place. Here, a simple relation is derived suitable to model systems that are:

- Limited by thermodynamics ($\Delta G'_{r,cat}$ is close to a minimum value $\Delta G'_{min}$ and sensitive to small changes in concentration, as dictated by equation 1.4) and
- Characterised by a low transport rate (e.g., diffusion-based systems, Boone et al. (1989))

For these systems, the catabolic rate and therefore the energy availability is constrained by $\Delta G'_{r,cat} \leq \Delta G'_{min}$, where in turn $\Delta G'_{r,cat}$ is governed by the transport rate of the involved compounds. For a well-adapted anaerobic microbial community converting propionate or butyrate to methane, a value of $\Delta G'_{min}$ between -15 and -25 kJ (mol reaction)$^{-1}$ is assumed, giving microorganisms enough energy to generate ATP required to perform anabolic and maintenance reactions (Stams and Plugge, 2009).

A reaction limited only by thermodynamics will proceed at the highest possible rate for at which the driving force $\Delta G'_{r,cat} - \Delta G'_{min} < 0\ \mathrm{kJ\,mol^{-1}}$. The value of $\Delta G'_{r,cat}$ is constrained by the substrate and product concentrations (equation 1.4). In combination with the boundary concentrations or the allowed concentrations at other cells, a maximum concentration gradient is imposed by the thermodynamics. As a result, the diffusion transport rates are limited. Because the concentration gradient is as high as thermodynamically possible, an inhibition function based on the principle described here provides a limit to the biochemical rate that could possibly be achieved by the cell:

$$f_{inh} = 1 - \exp\left(\left(\Delta G'_r - \Delta G'_{min}\right)/RT\right) \tag{1.24}$$

The thermodynamic rate equation uses the inhibition factor f_{inh} to describe the biological rate:

$$r_X = r_X^{max} f_{inh} \tag{1.25}$$

In this equation, r_X^{max} is set to an arbitrary high value. As long as $\Delta G'_r < \Delta G'_{min}$, the inhibition factor f_{inh} is between 0 and 1. When the Gibbs free energy change of reaction approaches the threshold value ($\Delta G'_r \rightarrow \Delta G'_{min}$), the inhibition factor approaches 0 ($f_{inh} \rightarrow 0$). This mathematical solution is stable and non-zero when $\Delta G'_r \approx \Delta G'_{min}$, thereby providing the maximum rate that can be achieved while thermodynamics are still feasible. Similar equations have been used to model reaction rates by Orcutt and Meile (2008) as well as Hoh and Cord-Ruwisch (1996) and Batstone et al. (2006) by including a Michaelis-Menten term.

In chapter 2 the exponential growth of a biofilm is modelled using equation 1.19. The impact of substrate and oxygen concentration on the relative growth rates of filament formers and floc formers in activated sludge is explained using equation 1.20. The thermodynamic rate equations (1.24 and 1.25) presented here are used in chapter 3 to compare the thermodynamic feasibility of different electron transfer modes.

Acid dissociation and precipitation reactions

Besides biological reactions, chemical reactions can play an important role in transport-reaction systems. Acid dissociation reactions are described by the following general reaction:

$$\mathrm{HA} \rightleftharpoons \mathrm{A^-} + \mathrm{H^+} \tag{1.26}$$

Here, HA denotes an acid, $\mathrm{A^-}$ is its conjugate base. An important effect of acid dissociation equilibrium is the buffering effect on pH (e.g., for $\mathrm{CO_2/HCO_3^-}$).

Precipitation reactions result in a similar equilibrium between a dissolved compound and a solid. The solid can function as a substrate or product source or sink, but also as an intermediate for other precipitation reactions (Kamyshny, Jr. et al., 2004).

Acid dissociation reactions are generally much faster than biological reactions and are therefore often modelled as being in equilibrium at all times (Batstone et al., 2002). Precipitation reactions are often slower than acid dissociation reactions, but if biological reaction rates are slow enough these also can be modelled being at equilibrium concentrations.

Bioelectrochemical modelling

When electrons transfer in redox reactions such as acetogenesis and methanogenesis occurs in a way other than immediate transfer to another chemical compound, this reaction is classified as a bioelectrochemical reaction. In these reactions, electric charges move through a system without being coupled to a reducing equivalent, which results in additional losses. To model the feasibility of electrochemical systems, an extension is made to the thermodynamics described in subsection 1.2.1.

Bioelectrochemical reactions occur when electrons are transferred between redox active cell components. The feasibility of an electrochemical reaction is generally presented as a potential difference, or voltage. The voltage is a measure for how much energy can be released when a reaction proceeds, where a positive voltage corresponds to a feasible forward reaction. A voltage is an alternative representation of Gibbs free energy change ΔG. The two are related via equation 1.27:

$$V = -\Delta G' / (F \nu_{e^-}) \tag{1.27}$$

Here, F is Faraday's constant ($F = 96485\ \mathrm{C\,mol^{-1}}$) and ν_{e^-} is the stoichiometry coefficient for electrons in the reaction.

The voltage is described for a system consisting of an oxidation and a reduction half-reaction. How readily a half-reaction occurs at standard temperature and pressure (as with Gibbs free energy, 298.15 K, effective concentration $1\ \mathrm{mol\,L^{-1}}$ and partial pressure 1 bar) depends on the standard reduction potential, where a strong positive standard reduction potential means the reduction will readily occur compared to a standard hydrogen electrode reaction, and a strong negative standard reduction potential corresponds to a feasible oxidation reaction compared to a standard hydrogen electrode. The standard reduction potential is tabulated for common reactions, for example in section 5 of Haynes (2014).

By subtracting the standard reduction potential of the oxidation reaction taking place at the anode from the standard reduction potential of the reduction reaction taking place at the cathode, the voltage or potential difference under standard conditions is obtained:

$$V_0 = E_{0,cathode} - E_{0,anode} \tag{1.28}$$

In order to calculate the voltage for reaction conditions from the voltage at standard conditions, the

Nernst equation is used to take into account differences in concentration and partial pressure:

$$V = V_0 - \frac{RT}{F\nu_{e^-}} \ln Q \qquad \text{where } Q = \prod_{i \text{ is (aq)}} \left(c_i/c_{ref}\right)^{\nu_i} \prod_{i \text{ is (g)}} \left(p_i/p_{ref}\right)^{\nu_i} \tag{1.29}$$

The Nernst equation is analogous to the relation for $\Delta G_r'$, equation 1.4. As before, the concentration can be replaced by activity and partial pressure by fugacity to account for non-ideality.

Bioelectrochemical modelling is combined with transport and reaction modelling in chapter 3 to evaluate the feasibility of direct interspecies electron transfer. Besides the effect of concentration, other losses are encountered in the form of ohmic losses in the nanowire, activation losses due to cell-redox complex transfer and solution resistance (migration losses).

Ohmic losses

One of the simplest relations between voltage (electric potential energy, thermodynamics) and current (flow of electrons, kinetics) is given for metallic-like conductivity by Ohm's law. Ohm's law states that the current I and voltage are directly proportional via a resistance R, which is formulated as:

$$V = RI \tag{1.30}$$

The term voltage loss (symbol η) is used interchangeably for voltage in this equation.

Equation 1.30 is often used in electrical engineering, but can be applied for any system showing ohmic resistance (e.g., conductive pili showing metallic-like conductivity formed between *Geobacter* species in direct interspecies electron transfer, see Malvankar et al. (2014) and chapter 3).

A measured R is specific for a resistance that has a certain length L and cross-sectional area A. The variable structure of the resistance in microbiological systems (pili of different lengths) can be accounted for by defining R as a function of a resistivity ρ that depends only on the material, while accounting for L and A:

$$R = \frac{\rho L}{A} \tag{1.31}$$

The resistivity can be readily measured for electrical systems, but the variable, complex structure and small scale of microbiological communities makes direct measurement of ρ in these systems difficult. Still, the resistivity of some biological materials has been determined in some experiments, see for example El-Naggar et al. (2010) and Malvankar et al. (2011).

As multiple resistances can be involved in a system (e.g., multiple conductive pili present between two cells), electrical circuits with parallel and series resistances are formed. For multiple resistances in parallel, the current is distributed such that the potential difference over each resistance is equal. For resistances in series, the current through each resistance is the same, while the potential difference depends on the resistance:

$$I = \begin{cases} I_1 + I_2 + ... + I_N & \text{for circuit in parallel} \\ I_1 = I_2 = ... = I_N & \text{for circuit in series} \end{cases} \tag{1.32}$$

$$V = \begin{cases} V_1 = V_2 = ... = V_N & \text{for circuit in parallel} \\ V_1 + V_2 + ... + V_N & \text{for circuit in series} \end{cases} \tag{1.33}$$

An example of a circuit in parallel is a cell pair (subscript cp) consisting of an electron-donating cell and an electron-accepting cell, connected through multiple conductive pili (nanowires). Because these nanowires have the same length and cross-sectional area and are made of the same biological material, equation 1.31 states the resistance R_{nw} for each nanowire must be the same. Therefore, if N_{nw} nanowires are present, the current through a nanowire must be $I_{nw} = \frac{I_{cp}}{N_{nw}}$ in order to get the same voltage drop $\eta_{nw} = \eta_{cp}$ through each nanowire.

Many losses are not described by Ohm's law. For example, losses encountered when electrons are transferred to a redox complex on the cell surface is found to be non-linear.

Redox complex activation losses

For electrode kinetics, various equations have been described relating the voltage loss η (sometimes called overpotential) to the electrochemical kinetics. It has been observed experimentally that an exponential relationship exists between the voltage loss and the current:

$$\eta = k_T \ln\left(\frac{i}{i_0}\right) \tag{1.34}$$

Here, k_T is the Tafel coefficient (in V). i is the current density (in $\mathrm{A\,m^{-2}}$), describing how much current flows through the available area. i_0 is the exchange current density (in $\mathrm{A\,m^{-2}}$), which is the current density at zero overpotential. The exchange current density is depends on the electrode material (e.g., redox complex) and the concentration of the electroactive species. This equation is usually referred to as the Tafel equation.

It was later found that when the voltage loss η is low, the Tafel equation does not accurately describe the current. This has led to derivation of the Butler-Volmer equation. In the form used in the thesis, it is assumed that a single-electron, single-step equilibrium redox reaction takes place at the electrode using a mediating redox complex that is therefore either in a reduced form (R) or oxidised form (subscript O):

$$\mathrm{R} \underset{red}{\overset{ox}{\rightleftharpoons}} \mathrm{O^+} + \mathrm{e^-} \tag{1.35}$$

The oxidation and reduction reactions take place at reduced and oxidised sites, respectively, and are first-order dependent on the available surface redox complex concentration c^s_R and c^s_O (in $\mathrm{mol\,m^{-2}}$). A reduced site becomes oxidised by transferring an electron to another compound and *vice versa*, such that the total concentration of sites remains constant ($c^s_{total} = c^s_R + c^s_O$). Therefore, the forward surface-specific reaction rate is given by:

$$r^s = r^s_{ox} - r^s_{red} = k_{ox}c^s_R - k_{red}c^s_O \tag{1.36}$$

where r^s is the surface-specific electron production rate (in $\mathrm{mol\,m^{-2}\,s^{-1}}$) and k is a rate coefficient (in $\mathrm{s^{-1}}$).

The absolute rate r^sA at which electrons are transferred is related to the net current via F, allowing equation 1.36 to be written as a current through inclusion of the electrode surface A:

$$I = FA\left(k_{ox}c^s_R - k_{red}c^s_O\right) \tag{1.37}$$

By assuming the rate coefficients follows Arrhenius' law and considering the effect of the potential on the activation energy, the following relations can be set up for the rate coefficients (Bard and Faulkner, 1980):

$$k_{ox} = k_{A,ox}\exp\left(\frac{-E_{a,ox}}{RT}\right)\exp\left(\frac{(1-\alpha)F}{RT}\eta\right) \tag{1.38a}$$

$$k_{red} = k_{A,red}\exp\left(\frac{-E_{a,red}}{RT}\right)\exp\left(\frac{-\alpha F}{RT}\eta\right) \tag{1.38b}$$

where k_A is the pre-exponential factor used in Arrhenius' equation, E_a is the activation energy, α is the symmetry factor and η the voltage loss (sometimes called overpotential).

At equilibrium, no net current flows ($I = 0$) and no voltage loss is present ($\eta = 0$). If it is assumed that the surface concentrations c^s are equal, equation 1.37 states that the equations for the rate coefficients 1.38a and 1.38b can be simplified by introducing k_0:

$$k_0 = k_{A,ox}\exp\left(\frac{-E_{a,ox}}{RT}\right) = k_{A,red}\exp\left(\frac{-E_{a,red}}{RT}\right) \tag{1.39}$$

Substituting equation 1.39 into equations 1.38a and 1.38b and the resulting equations into equation 1.37, the Butler-Volmer equation is obtained:

$$I = FAk_0\left(c^s_R\exp\left(\frac{(1-\alpha)F}{RT}\eta\right) - c^s_O\exp\left(-\frac{\alpha F}{RT}\eta\right)\right) \tag{1.40}$$

For applications of the Butler-Volmer equation in this thesis, a simplified version is used. First, it is assumed that the oxidised and reduced redox complex surface concentrations are the same, thereby setting $c^s_O = c^s_R = c^s_{act}$. Furthermore, it is assumed that the rate-determining step is the electron transfer (the H^+ concentration was found to be buffered therefore non-limiting) such that the reaction is simple enough for the transfer coefficient α to be replaced by the simpler symmetry factor β (Bockris and Nagy, 1973). With these assumptions, equation 1.40 simplifies to:

$$I = FAk_0 c^s_{act} \left(\exp\left(\frac{(1-\beta)F}{RT}\eta \right) - \exp\left(-\frac{\beta F}{RT}\eta \right) \right) \tag{1.41}$$

The symmetry factor β is often taken to be 0.5, in which case an explicit relation between I and η can be obtained using an inverse hyperbolic sine approximation of the Butler-Volmer equation (Noren and Hoffman, 2005). Occasionally, instead of a surface-specific standard rate constant and concentration, a volumetric concentration value c_{act} and $k_{0,vol}$ is reported in literature (e.g., Bowden et al. (1982) and Reed and Hawkridge (1987)). Furthermore, the exchange current density $i_0 = Fc^s_{act}k_0$ is sometimes used in the Butler-Volmer equation (Picioreanu et al., 2010).

At high overpotential, the Butler-Volmer equation simplifies to the Tafel equation, 1.34. The Butler-Volmer equation cannot be solved explicitly (except in the special case $\alpha = 0.5$ (Noren and Hoffman, 2005)), but can be solved implicitly with ease.

Solution resistance

Bioelectrochemical reactions can result in a local imbalance of ions, which via the Nernst-Planck equation (equation 1.14) results in a potential gradient opposing the electron flow. By integrating the potential gradient, the losses between two points A and B is obtained, or mathematically:

$$V = \int_A^B (\nabla V) \qquad \text{with } \nabla V \text{ via equation 1.14} \tag{1.42}$$

A bioelectrochemical model describing extracellular losses and implementing ohmic losses, activation losses and solution resistance is described in chapter 3.

1.3 RESEARCH OBJECTIVES AND APPROACH

The literature review has shown that there are knowledge gaps in relation to the role of mechanical and (electro)chemical interspecies interactions in various microbial communities. Specifically, a mathematical tool to model microbial systems accounting for cell flexibility, variable cell morphologies and interactions with other cells and the environment via EPS or pili connections is not available in literature. A model taking into account mechanical forces as a result of intercellular and cell-substratum interactions could provide new insights into the role of individual cells and specific links on systems where mechanical interactions play an important role (e.g., biofilms and activated sludge flocs). Furthermore, the extracellular limitations of a novel syntrophic electrochemical interaction (direct interspecies electron transfer via a network of nanowires) and the resulting feasibility of this process are not known. Finally, an explanation for the formation of typical shell-shaped aggregates facilitating anaerobic oxidation of methane coupled to sulfate reduction is not available, and the feasibility of a recently proposed syntrophic mechanism (Milucka et al., 2012) in these aggregates has not been investigated.

The main goal of this thesis is to improve understanding of mechanical and electrochemical interactions between microorganisms in mixed-culture systems. By developing and applying an extendible modelling toolset, biological systems discussed in subsection 1.2.2 are analysed in this thesis. Comparing the mathematical modelling outcomes to experimental observations published by various researchers provides insight into the mechanisms and limitations at work in these microbial communities. Based on the identified knowledge gaps, the following research objectives have been formulated:

Research objective 1: Modelling physical microbial interactions in biofilms and flocs

Microbial aggregates show complex behaviour which can be attributed to simple cell-cell interactions. By modelling cell growth and division, intracellular, intercellular and interspecies connections, cell-cell and cell-substratum collisions, the aggregate morphology can be predicted based on Lagrangian properties of individual cells. A biofilm of *E. coli* cells growing on a planar substratum and an inoculum of floc formers and filament formers in activated sludge are modelled to investigate the effect of the different cell-cell interactions on the shape of the resulting microbial community in chapter 2.

Because of limitations to existing modelling frameworks described in subsection 1.2.3, a novel individual-based modelling framework is described that can simulate the development of variable cell morphology communities.

Research objective 2: Predicting theoretical feasibility of mediated versus direct interspecies electron transfer

The lack of a strong electron acceptor limits the feasibility of many anaerobic processes. To overcome these thermodynamic limitations some microbial communities share reduced metabolites, a process called interspecies electron transfer (IET). Recent work (Summers et al., 2010) has shown that besides mediated (*i.e.,* diffusion-limited) IET a novel mechanism called direct IET exists where electrons are transferred between cells through conductive pili. In chapter 3 the thermodynamic rate limit of direct IET is compared to hydrogen- and formate-mediated IET for an acetogenesis/methanogenesis system.

An electrochemical model based on the Nernst-Planck equation (equation 1.14) is implemented in a finite element analysis modelling tool in order to model extracellular: limitations in a cell pair and a multicellular system.

Research objective 3: Understanding syntrophy and aggregate formation in marine anaerobic oxidation of methane

Anaerobic oxidation of methane (AOM) is coupled to sulfate reduction (SR) in marine environments. By evaluating mechanics and reaction thermodynamics and kinetics, the development of the typical shell-shaped aggregate morphology observed in experiments is simulated (chapter 4).

For this research objective, a diffusion-based model similar to the model in chapter 3 is used together with the mechanical model described in chapter 2, thereby investigating both biochemical and mechanical interspecies interactions.

Chapter 2

MECHANICAL INTERACTIONS IN MICROBIAL BIOFILMS AND ACTIVATED SLUDGE

ABSTRACT

An individual-based, mass-spring modelling framework has been developed to investigate the effect of cell properties on the structure of biofilms and microbial aggregates through Lagrangian modelling. Key features distinguishing this model are variable cell morphology described by a collection of particles connected by springs, and a mechanical representation of deformable intracellular, intercellular and cell-substratum links. A first case study describes the colony formation of a rod-shaped species on a planar substratum. This case shows the importance of mechanical interactions in a community of growing and dividing rod-shaped cells (i.e., bacilli). Anchoring cell-substratum links promote formation of mounds as opposed to single-layer biofilms while gliding cell-substratum links impede mound formation. Head-to-tail filial links formed during division decrease the roundness of the biofilm. A second case study describes the formation of flocs and development of external filaments in a mixed culture activated sludge community. It was shown by modelling that distinct cell-cell links, microbial morphology and growth kinetics can lead to excessive filamentous proliferation and interfloc bridging, possible causes for detrimental sludge bulking. This methodology has been extended to more advanced microbial morphologies such as filament branching and proves to be a very powerful tool in determining how fundamental controlling mechanisms determine diverse microbial colony architectures.

2.1 INTRODUCTION

The nature of cell-cell and cell-substratum interactions influences the morphology of the microbial community as a whole. It was described in subsection 1.2.2 that in biofilms cell-cell forces (e.g., filial links or EPS) and cell-substratum forces (e.g., EPS or pili) have a strong effect on how well biofilms adhere to a surface. By better understanding how biofilm characteristics such as spread and homogeneity are determined by the properties of individual cells, valuable knowledge applicable to for example medicine (Donlan, 2001) and biofouling (Le-Clech et al., 2006) can be obtained. In this chapter a biofilm consisting of rod-shaped cells is modelled to investigate how cell-cell and cell-substratum links affect the biofilm morphology.

In activated sludge processes the mixed population dynamics are known to play an important role in the formation of long filaments extending from the microbial flocs. The formation of these filaments can result in interfloc bridging, which in turn leads to sludge bulking, as was discussed in subsection 1.2.2. The impact of individual cell properties on the morphology of flocs is investigated in this chapter to get a better understanding of what causes these detrimental bulking effects.

In subsection 1.2.3 it was explained that existing models used to investigate mechanical interspecies interactions are limited in that they cannot simulate complex cell geometries, deforming cells and cell-cell or cell-substratum connections, or that structural properties are imposed on the aggregate. In order to address some of the restrictions in existing individual-based models, a new variable-morphology physics-based approach for modelling microbial communities is described in this chapter. The cell shape, as well as the cell aggregate morphology, is provided by a particle-spring approach in an overall Lagrangian approach, allowing inheritance of morphological and other properties.

This approach has been applied to simple single- and mixed population systems. In the first part of this chapter, a detailed description of the mathematical model is given, introducing the model processes, the components making up the cells and links, the various forces taken into account and the cell growth and division mechanism. The model is then applied to investigate how deformable cell-cell sticking (e.g., EPS) and filial links as well as anchoring and gliding cell-substratum links affect the morphology of a biofilm formed from a single-cell inoculum growing on a flat surface. The importance of electrostatic forces and naturally occurring cell radius variation is briefly discussed. Furthermore, the model is used to examine how the development of an activated sludge floc is affected by the relative growth rates of the dominant microbial species and properties of the filial links and sticking links. The impact of filament branching and the importance of individual cell morphology on the floc morphology is analysed.

2.2 MODEL DESCRIPTION

The mathematical model is designed to simulate formation of complex microbial community structures (e.g., biofilms, biological flocs) based on mechanical interactions between cells with variable primary, secondary and tertiary morphology (e.g., cocci, bacilli, filaments). This section describes the modelling approach for the elemental components (subcellular agents) as well as for primary (cellular), secondary (cell-descendants) and tertiary (intercellular/environmental) relationships between microbial cells.

2.2.1 Components and structure

Elemental components: particles and springs

The basic model elements are particles (mass agents), connected by massless springs. Each particle is characterized by three state variables: mass (m), velocity (v), and position (p). Springs join particles to each other or to fixed reference points (e.g., a biofilm substratum) and have a characteristic spring constant k_s and a rest length L_s^{rest}. A microbial cell can consist of one particle (in case of spherical cells), or of multiple particles connected by intracellular springs (for rods and more complicated geometries). Cells can also be linked by intercellular springs into filaments. Further links connect cells and filaments into higher level structures such as aggregates, biofilms or flocs. All springs used in this model are linearly elastic, following Hooke's law. The force in a spring connecting two particles is described by Hooke's law:

$$\mathbf{F}_s = k_s \frac{\mathbf{L}_s}{L_s}\left(L_s - L_s^{rest}\right) \tag{2.1}$$

where $\mathbf{F}_s$ is the force acting on particle a, k_s is the spring constant, $\mathbf{L}_s$ is a vector describing relative position of particle a with respect to position of particle b (i.e., $\mathbf{L}_s = \mathbf{p}_b - \mathbf{p}_a$), L_s is the length (norm) of vector $\mathbf{L}_s$ and the rest length L_s^{rest} of the spring. The force acting on particle b is $-\mathbf{F}_s$.

Primary structures: cell types

The primary structure defines the shape of individual cells. Different cellular geometries can be defined by connecting particles with springs. Cocci are spherical microbes, represented in the model by single particles with diameter D_s. Bacilli are rod-shaped cells, represented by two particles with fixed diameter D_r connected by a stiff spring with variable rest length $L_{s.i}^{rest}$ (see figure 2.1A). If flexible cell bodies or other shapes (e.g., bacteria with different aspect ratios $\frac{L_r}{D_r}$, helical, spirochetes, *etc.*) are of interest, these could be modelled by multiple particles connected by different settings of elastic and angular springs (Windisch et al., 2006; Janulevicius et al., 2010; Harvey et al., 2011).

Microbial cells have an inherent density ρ, but their mass changes during cell growth, leading to a change in cell shape or size. The spherical cell diameter D_s can be calculated as $D_s = \sqrt[3]{6m/\pi\rho}$. Rod-shaped cells are assumed to have a diameter D_r that does not change as the cell grows and an internal spring rest length changing as a function of the current microbial mass, maintaining a constant cell density. A rod-shaped cell consists of two half spheres and an open-ended cylinder, such that the internal spring rest length is set by the mass via $L_{s,i}^{rest} = 4m/\left(\rho\pi\left(D_r\right)^2\right) - 2D_r/3$. A stiff internal spring (high $k_{s,i}$ value) keeps the actual spring length ($L_{s,i}$) approximately to the desired spring length ($L_{s,i}^{rest}$), such that the cell length can be described by $L_r = L_{s,i}^{rest} + D_r$.

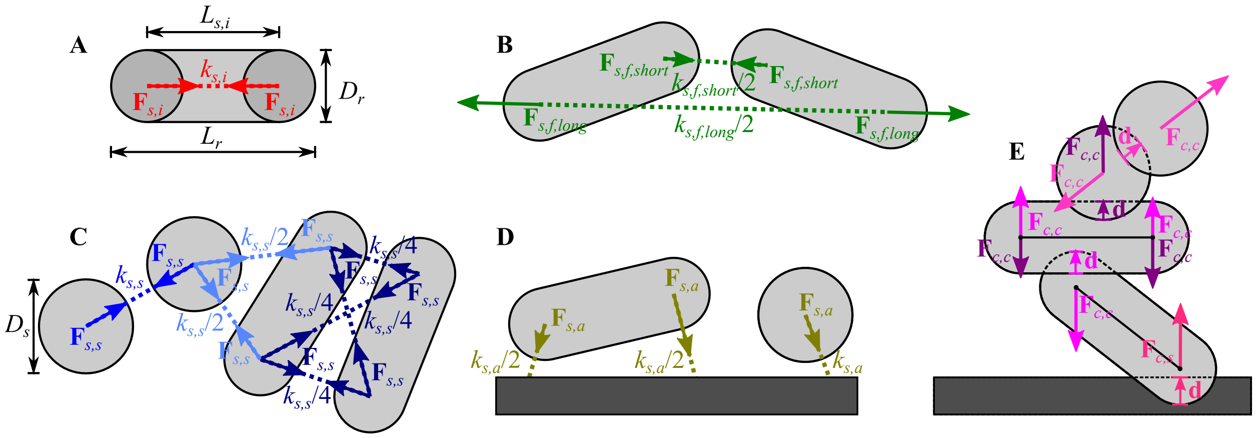

Figure 2.1: Forces acting on the mass particles. (A) Internal spring forces, $\mathbf{F}_{s,i}$, in rod-shaped cells; (B) short and long filial spring forces, $\mathbf{F}_{s,f}$, in rod-shaped cells; (C) sticking spring forces, $\mathbf{F}_{s,s}$, using four springs between rod-shaped cells, two springs between a rod-shaped and a spherical cell and one spring between spherical cells; (D) anchoring forces, $\mathbf{F}_{s,a}$; (E) collision response forces, $\mathbf{F}_{c,c}$, between rod-shaped cells, spherical cells, rod-shaped and spherical cells and collision response forces between cells and substratum, $\mathbf{F}_{c,s}$. In addition to the forces shown in the figure, drag acts on all particles opposing the direction of movement. Force vectors are added to a resultant force vector for each mass particle. Spring constants (k_s) are scaled for the number of springs in that link.

Secondary structures: filial links

The secondary structure defines microbial assemblies related by filial links between immediate siblings. Examples include diplococci and diplobacilli (pairs of spheres or rods), streptococci and streptobacilli (filaments of spheres or rods through division along a single plane) or sarcina and tetrads (square or cubic structures through division of cocci along two and three planes, respectively (Rothfield and Zhao, 1996)). Less structured links lead to staphylococci clusters (grape-like structures) and palisade bacilli. In this thesis, only modelling of straight and branched rod filaments is illustrated, but filaments of spherical cells can easily be implemented using sets of filial springs.

Straight filaments of rods can be created in several ways. Short head-to-tail springs ensure that cells will remain connected by inducing the elastic force $\mathbf{F}_{s,f,short}$ (function of $k_{s,f,short}$ and $\mathbf{L}_{s,f,short}$, see equation 2.1 and figure 2.1B). The angle between cells can be controlled by adding longer range springs with the elastic force $\mathbf{F}_{s,f,long}$. By changing the difference in rest length of the two springs, the filament rigidity (i.e., the resistance to chain bending) and the gap between two bacilli in a filament can be readily controlled. The rest length for filament springs between two cells A and B is a function of the internal spring rest lengths of the cells ($L^{rest}_{s,i,A}$, $L^{rest}_{s,i,B}$) and diameter D_r. In addition, spring length factors ($l_{s,short}$ and $l_{s,long}$) control the gap size between cells. For straight filaments the rest length is given by $L^{rest}_{s,f,short} = l_{s,f,short}D_r$ and $L^{rest}_{s,f,long} = l_{s,f,long}D_r + L^{rest}_{s,i,A} + L^{rest}_{s,i,B}$.

Filament branching is implemented in a similar way. In a branch joint, two sets of springs are created from the newly branched cell A to the neighbouring cells B and C. Joints between cell A and cell B

are described by a set of springs with rest lengths:

$$L^{rest}_{s,f,short} = l_{s,f,branch} D_r \tag{2.2}$$

and

$$L^{rest}_{s,f,long} = l_{s,f,branch} \sqrt{\left(L^{rest}_{s,i,A} + 0.5 L^{rest}_{s,f,short}\right)^2 + \left(L^{rest}_{s,i,B} + \sqrt{0.75} L^{rest}_{s,f,short}\right)^2} \tag{2.3}$$

where $l_{s,f,branch} = 0.5\left(l_{s,f,short} + l_{s,f,long}\right)$. By substituting the internal spring rest length of cell C for B, the springs in the joint between A and C can be described.

The set of a short and long spring is very similar to the use of an angular spring. By setting the relative spring length, the stiffness of the filaments and branches can be maintained, thus allowing a high versatility in defining and maintaining secondary structures.

Tertiary structures: sticking and anchoring links

Non-filial cell-cell, as well as cell-substratum links are in this model called tertiary links and include in first instance sticking (cell-cell) and anchoring (cell-substratum) connections. These links may describe the adhesive forces created by EPS (see Burdman and Jurkevitch (1998) and references there), thus enabling aggregation of biomass.

Sticking links form an elastic matrix by creating cell-cell bonds with a number of springs depending on cell morphology. One spring is needed for sphere to sphere, two springs for sphere to rod, and four springs for rod to rod connection (figure 2.1C) to fully satisfy geometric degrees of freedom. This approach allows for implicit modelling of elasticity and strength of the sticking link matrix, without actually defining the mass of the EPS. Tertiary structure linear springs generate forces $\mathbf{F}_{s,s}$ with rest length defined by $L^{rest}_{s,s}$ (equation 2.1). The spring constants $k_{s,s}$ are scaled for the number of springs involved in the link ($k_{s,s}/N_{s,s}$).

Cell-substratum bonds play an important role in the tertiary biofilm structure. These links are modelled using anchoring forces $\mathbf{F}_{s,a}$, characterized by $k_{s,a}/N_{s,a}$ and $L^{rest}_{s,a}$. A sphere is fixed using a single spring, while rods require two springs to be immobilized such that all rotational degrees of freedom are eliminated (figure 2.1D). The locations on the substratum to which the springs are fixed are determined by projecting the position of the cell particles along the vertical axis onto the horizontal plane.

Collision response

During growth and division, cells will collide with each other and with the substratum. In order to avoid overlapping cells, a collision detection mechanism has been implemented and collision response forces are applied on overlapping particles.

Collision detection is handled by factorial checking of all cell pairs, with proximity and factorial elimination used to minimize checks. Routines detect collision events (Ericson, 2005) by calculating the distance δ for point-point (two spherical cells), line segment-point (a spherical and a rod-shaped cell), line segment-line segment (two rod-shaped cells) and point-plane (particle-substratum). For two cells A and B, the collision detection functions return the overlap vector $\mathbf{d} = (D_A + D_B)/2 - \delta$, which provides distance and direction of overlap. Collision response is based on elastic repulsion of colliding objects, by adding forces $\mathbf{F}_{c,c} = k_{c,c}\mathbf{d}$ whenever overlap is detected, where $k_{c,c}$ is the cell-cell collision coefficient. For spherical cells, the collision response force $\mathbf{F}_{c,c}$ will act in the sphere center. For rod-shaped cells, $\mathbf{F}_{c,c}$ is distributed proportionally between the two particles according to the inverse of the distance between collision point and particle (figure 2.1E).

Similarly, for cell-substratum collision the force $\mathbf{F}_{c,s}$ is introduced with a coefficient $k_{c,s}$.

DLVO force

Cells in proximity of a planar substratum encounter an attractive van der Waals force ($F_{vdW} \propto -d^{-2}$, where d is the distance between cell surface and substratum) and a repulsive electrostatic force ($F_R \propto \kappa e^{-\kappa d}$ with κ the inverse Debye length) (Hermansson, 1999). The combination of the van der Waals and electrostatic force is called the DLVO force ($\mathbf{F}_{DLVO} = C_{ES}\kappa e^{-\kappa \mathbf{d}} - C_{vdW}\mathbf{d}^{-2}$, with key constants C_{ES} and C_{vdW}), after the surnames initials of the researchers who independently formulated the theory. DLVO forces allow cells to maintain a fixed stable distance from the substratum, usually in the order of a few nanometers (reversible adhesion). If a cell overcomes the repulsive force and further approaches the substratum, the attractive force becomes dominant again and pulls the cell onto the substratum (irreversible adhesion). Because other forces in the model operate on the micrometer scale, the DLVO forces can make the mathematical model stiff. To minimize model stiffness, the norm of $\mathbf{d}$ in the DLVO force is set to have a lower limit of $6/\kappa$, even if the actual distance between cell surface and substratum is smaller.

2.2.2 Model processes

The major processes included in the model are (i) cell growth and division and (ii) particle movement and link reorganization to achieve mechanical relaxation. When needed, other processes could be introduced in this framework (see Results and discussion).

Cell growth

In the model, increase in cell size is driven by an increase in cell mass, assuming constant cell density. Spherical cells can only grow in diameter, while rod-shaped cells grow only in length, maintaining a fixed diameter (Shapiro and Hsu, 1989; Stewart et al., 2005).

Mass change for a single cell is the result of specific microbial growth rate (μ) (Harvey et al., 1967), such that the increase in mass is described by $\frac{\mathrm{d}m}{\mathrm{d}t} = \mu m$. For rod-shaped cells, the mass is distributed equally over the two particles comprising a cell. For this study, the specific growth rate is generated randomly for each growth step and for each cell, following a normal distribution around the mean with a standard deviation (see table 2.1). Because the scope of this framework is the microbial community structure, other factors affecting the net growth rate are not taken into account in the present study (e.g., biomass decay and starvation leading to cell mass decrease, substrate limitation and product/substrate inhibition, *etc.*).

Cell division

Division is biochemically a very complex process, with one of the key issues being the division plane (Madigan et al., 2009). Prokaryotic bacilli such as *E. coli* will normally divide longitudinally along a plane in the central cross-section of the rod, while cocci may divide in one, two, three, or any number of planes to form filaments, tetrads, sarcina, or staph structures, respectively (Rothfield and Zhao, 1996). For rods, the division plane is inherent in the geometry of the cell.

In the model, a cell divides when a critical mass has been reached. Apart from determining divisional plane and cell-sibling orientation, the other major issue is sharing of links in secondary and tertiary structures. Secondary links are redistributed to maintain a straight filament by inserting newly formed cells in the array (branching excluded), while tertiary links are distributed between mother and daughter according to the proximity of the cell.

Mechanical relaxation

The initial collection of cells is made of a system of particles and springs in mechanical equilibrium. When new cells are formed as a result of microbial growth and division, this equilibrium is perturbed. The model takes a physics-based approach to compute the new location for each particle by relaxing the momentum balances towards the equilibrium of forces:

$$\frac{\mathrm{d}\mathbf{v}}{\mathrm{d}t} = \frac{\sum_j \mathbf{F}_j}{m} \tag{2.4}$$

where $\mathbf{v} = [v_x, v_y, v_z]$ is the particle velocity and $\sum_j \mathbf{F}_j$ the sum of all forces acting on the particle. Position $\mathbf{p} = [p_x, p_y, p_z]$ is then calculated from the velocity:

$$\frac{\mathrm{d}\mathbf{p}}{\mathrm{d}t} = \mathbf{v} \tag{2.5}$$

Each particle will contribute with six equations (equation 2.4 and equation 2.5 in a three-dimensional Cartesian coordinate system) to the system of ordinary differential equations, which describes the redistribution of the microbial community.

Included in the current model are elastic forces $\mathbf{F}_s$ due to intracellular, intercellular or cell-substratum springs, and collision response forces $\mathbf{F}_c$. In addition, velocity damping forces $\mathbf{F}_d = -k_d\mathbf{v}$ prevent

Table 2.1: Model parameters for *E. coli* and activated sludge simulations. Parameters without a reference are arbitrarily chosen.

Parameter	Symbol	Default value	Units	Reference and notes
Internal springs				
Spring constant	$k_{s,i}$	5×10^{-11}	$\mathrm{N\,m^{-1}}$	
Filial links (*E. coli*)				
Short spring spring constant	$k_{s,f,short}$	5×10^{-13}	$\mathrm{N\,m^{-1}}$	
Long spring spring constant	$k_{s,f,long}$	5×10^{-13}	$\mathrm{N\,m^{-1}}$	
Stretch limit	$d_{f,break}$	1	µm	
Short spring relative length	$l_{f,short}$	0.5	–	
Long spring relative length	$l_{f,long}$	1.7	–	
Filial links (activated sludge)				
Short spring spring constant	$k_{s,f,short}$	2×10^{-11}	$\mathrm{N\,m^{-1}}$	
Long spring spring constant	$k_{s,f,long}$	2×10^{-11}	$\mathrm{N\,m^{-1}}$	
Stretch limit	$d_{f,break}$	2	µm	
Short spring relative length	$l_{f,short}$	0.5	–	
Long spring relative length	$l_{f,long}$	1.7	–	
Sticking links (activated sludge)				
Spring constant	$k_{s,s}$	1×10^{-11}	$\mathrm{N\,m^{-1}}$	Same for all cell types
Formation limit	$d_{s,form}$	0.5	µm	
Stretch limit	$d_{s,break}$	1	µm	
Anchoring links (*E. coli*)				
Spring constant	$k_{s,a}$	1×10^{-11}	$\mathrm{N\,m^{-1}}$	
Formation limit	$d_{a,form}$	0.5	µm	
Stretch limit	$d_{a,break}$	1	µm	
DLVO forces (*E. coli*)				
Electrostatic force grouped constants	C_{ES}	1×10^{-22}	$\mathrm{N\,m}$	
Van der Waals force grouped constants	C_{vdW}	1×10^{-31}	$\mathrm{N\,m^{2}}$	
Inverse Debye length	κ	5×10^{7}	$\mathrm{m^{-1}}$	
Collission response				
Cell-cell collision spring constant	$k_{c,c}$	1×10^{-10}	$\mathrm{N\,m^{-1}}$	
Cell-substratum collision spring constant	$k_{c,s}$	1×10^{-10}	$\mathrm{N\,m^{-1}}$	
Other relaxation parameters				
Relaxation time step	Δt_{rel}	1	s	
Velocity damping coefficient	k_d	1×10^{-13}	$\mathrm{N\,s\,m^{-1}}$	

Table 2.1 (continued): Model parameters for *E. coli* and activated sludge simulations. Parameters without a reference are arbitrarily chosen.

Parameter	Symbol	Default value	Units	Reference and notes
Bacilli geometry (*E. coli*)				
Cell diameter	D_r	0.75 ± 0.0375	µm	Pierucci (1978)
Initial cell length	$L_{r,0}$	3	µm	
Final cell length	$L_{r,div}$	5.75	µm	Pierucci (1978)
Cell mass at division	$m_{r,div}$	2.45×10^{-15}	kg	
Fil. former geometry (activated sludge)				
Cell diameter	D_r	0.5	µm	Lau et al. (1984)
Initial cell length	$L_{r,0}$	1.67	µm	
Final cell length	$L_{r,div}$	4	µm	Lau et al. (1984)
Cell mass at division	$m_{r,div}$	3.70×10^{-15}	kg	
Floc former geometry (activated sludge)				
Cell diameter	D_r	0.35	µm	Lau et al. (1984)
Initial cell length	$L_{r,0}$	0.317	µm	
Final cell length	$L_{r,div}$	1.1	µm	Lau et al. (1984)
Cell mass at division	$m_{r,div}$	6.09×10^{-16}	kg	
Growth (*E. coli*)				
Growth rate coefficient for bacilli	μ	1.23 ± 0.277	h^{-1}	Koch and Wang (1982); Képès (1986)
Growth (activated sludge, low O_2 conc.)				
Growth time step	Δt_{growth}	540	s	
Growth rate coefficient for fil. form.	μ	0.217 ± 0.0434	h^{-1}	
Growth rate coefficient for floc form.	μ	0.153 ± 0.0306	h^{-1}	
Growth (activated sludge, high O_2 conc.)				
Growth time step	Δt_{growth}	240	s	
Growth rate coefficient for fil. form.	μ	0.271 ± 0.0542	h^{-1}	Lau et al. (1984)
Growth rate coefficient for floc form.	μ	0.383 ± 0.0766	h^{-1}	Lau et al. (1984)
Other parameters				
Biomass density	ρ	1010	$kg\,m^{-3}$	

large oscillations and stabilize the movement of particles towards the mechanical equilibrium. For simulations involving a planar substratum, the DLVO force and normal forces act on cells as well.

During each time step of mechanical relaxation, cell-cell and cell-substratum distances are checked and tertiary links are formed or broken. Formation of a new set of springs between two cells A and

B (a sticking link) occurs when the distance d between the cell center (for a spherical cell) or the cell axis (for rod-shaped cells) and the center or axis of the other cell is $d < d_{s,form}$. An existing link is broken when the actual spring length exceeds the maximum length, $L_{s,s} > L_{s,s}^{rest} + d_{s,break}$. Similarly, anchoring links are formed and broken, with d the distance between cell and substratum. The spring constants are set such that the springs are stiff enough for the cell structures to be rigid under weak stress and to mitigate overall model stiffness. Intracellular springs have relatively high stiffness compared to intercellular springs as also suggested in literature (Volle et al., 2009). Values for spring constants, formation and stretch limits are given in table 2.1.

2.2.3 Model implementation and solution

As cell growth and division are orders of magnitude slower than the mechanical relaxation (minutes/hours versus seconds (Picioreanu et al., 2000)), it is computationally advantageous to use a model solution that splits time-stepping algorithm in two phases. During the growth phase, executed with time steps in the order of hours, cell masses increase. When the cell mass exceeds a critical value after the growth step, the cell divides. Filial links may be created between the involved cells. In a second phase, a partially relaxed state is calculated by moving the particles according to the ordinary differential equation (ODE) momentum balances (equation 2.4 and 2.5), solved over a much shorter time interval. Sticking and anchoring links can be created or removed during this phase. For the small-size microbial aggregates simulated, 1 s of mechanical relaxation was in general sufficient. After relaxation, the state variables for each particle and cell links are stored and a new growth/division phase begins, as is schematically represented in figure 2.2.

A preliminary version of the Diatoma model described by Celler et al. (2014) was used as the basis for this model when coding started in 2011. The new individual-based modelling solution algorithm

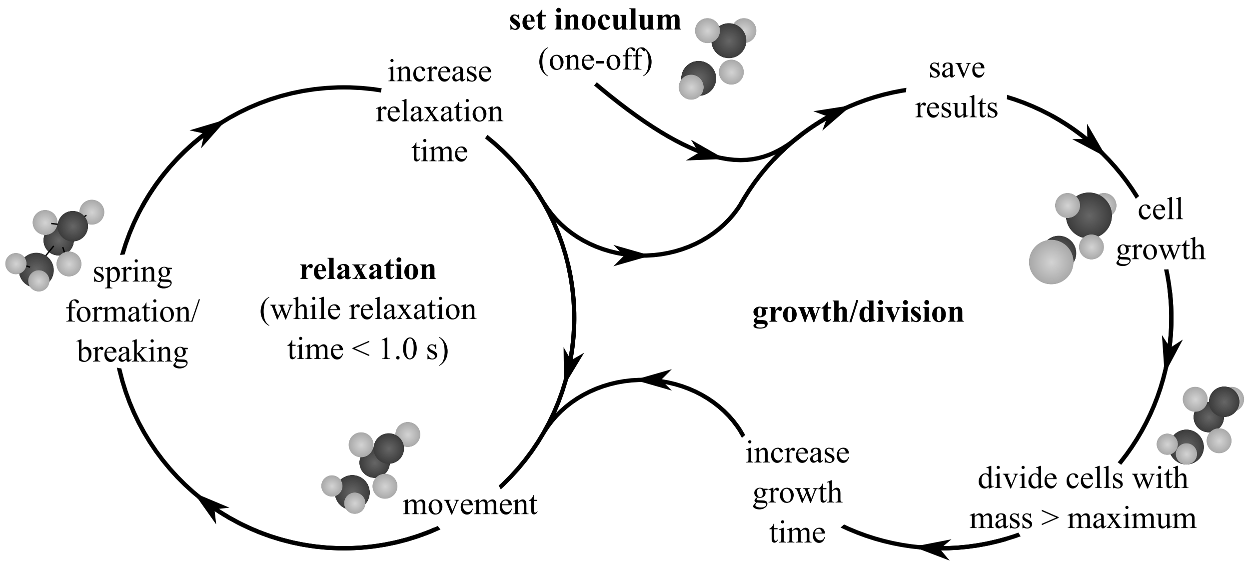

Figure 2.2: Schematic representation of the individual-based model implementation.

Table 2.2: Overview of model version used to obtain results.

Figure	Model version
2.3	2015
2.4	2014
2.5	2014
2.6	2015
2.7	2014
2.8	2015
2.9	2014

has been rewritten from scratch as object-oriented Java code. Through the JMatIO library (December 2012-December 2014, sourceforge.net/projects/jmatio), results are exported from Java to MATLAB data files (R2012b-R2014b, The MathWorks, Natick, MA) for data analysis and rendering.

Model versions used in the thesis

Throughout the project, the model presented in this chapter has been continuously improved to allow for a greatly improved simulation speed (chapter 4). The conclusions drawn in the paper have not changed, but the exact organisation of the specific community structure is slightly different because of code structure changes, the switch to a more efficient ODE solver algorithm and updates made to the seeded random number generator in the Java language. An overview of the model version used for each figure in this chapter is given in table 2.2. Results in chapter 4 are generated using the 2015 version.

For simulations published in Storck et al. (2014) (denoted version 2014 in table 2.2), a Dormand-Prince Runge-Kutta ODE solver (Press et al., 2007) has been written in Java and is used to determine relaxation. In simulations published in later work or only in the thesis, a more efficient implementation of the same algorithm is used (Apache Commons Mathematics Library 3.3, The Apache Software Foundation). Furthermore, improvements to binary space partitioning have been made. These changes have led to orders of magnitude improvements in computational speed (for example, the results in figure 2.4A have been obtained in 14 hours of computation time, a similar cell count for the simulation described in figure 2.3B was obtained in less than 2 minutes. A tenfold higher cell count (at 6.67 h) was obtained in less than 2.5 hours). Further optimisations have been made through parallelisation of the relaxation step (Cockx, 2014), and will be further improved upon in the future, as is discussed in chapter 5.

Visualisation of results

For version 2014 of the individual-based model, MATLAB was used in combination with POV-Ray (3.7 Beta, www.povray.org, Persistence of Vision Pty. Ltd., Williamstown, Victoria, Australia) for rendering the community organisation. More recent results are rendered using Blender (version 2.72-2.74, Blender Foundation, Amsterdam, The Netherlands), which has the advantage that it allows inspection of the community by providing a graphical interface without having to render the structure. Definition of the cell community in Blender was done through the Python 3 (www.python.org) application programming interface (API). Two-dimensional images have been created using the latest versions of Matplotlib (Hunter, 2007) in combination with SciPy (www.scipy.org) and NumPy (www.numpy.org).

2.3 RESULTS AND DISCUSSION

Two case studies are discussed in this chapter to illustrate the potential of the mechanical modelling approach. In the first case colony growth of rod-shaped cells (e.g., *E. coli*, *B. subtilis*, *etc.*) on a planar surface is simulated. Secondly, a mix of two cell morphologies is used (spherical cells and chains of rod-shaped cells) to simulate communities of floc forming and filamentous bacteria in mixed population systems, as encountered both in activated sludge flocs and in anaerobic biofilms.

2.3.1 Rod-shaped cells on a planar surface

Growth of a pure culture containing rod-shaped cells is simulated on a planar substratum, which may represent an agar surface. Cell diameter and final length are taken from earlier experimental work (Pierucci, 1978) assuming *E. coli* growth on glucose. The specific growth rate of a cell is generated randomly at each time step from a normal distribution, with parameters as found in Koch and Wang (1982); Képès (1986). The cell is modelled by two particles connected by a stiff spring.

Importance of cell radius variation and DLVO forces

In a mathematical model without cell-cell and cell-substratum links, rod-shaped cells initially positioned at the same height and parallel above a horizontal substratum plane encounter no vertical forces. Therefore, a community formed as a result of an initial cell growing on a flat substratum, without anchoring or filial links will remain a monolayered biofilm if variations in the vertical position or variations in the cell diameter are not included. After a number of iterations, either numerical round-off and truncation errors will accumulate and push cells away from the substratum, or the model will be unable to find a valid numerical solution.

In real world biofilms, imperfections in the cell shape, different cell diameters or irregularities of the substratum surface would cause the community to eventually push cells into the third dimension, away from the substratum. These imperfections are simulated in the model by implementing slight variations in the cell diameter when a cell divides. The diameter of cells formed during the cell division step is determined by random sampling from a normal distribution with a standard deviation 5% of the mean diameter (table 2.1). The cell diameter remains constant for the rest of the simulation and the cell length is set to satisfy the equations described in subsection 2.2.1. A simulation with only

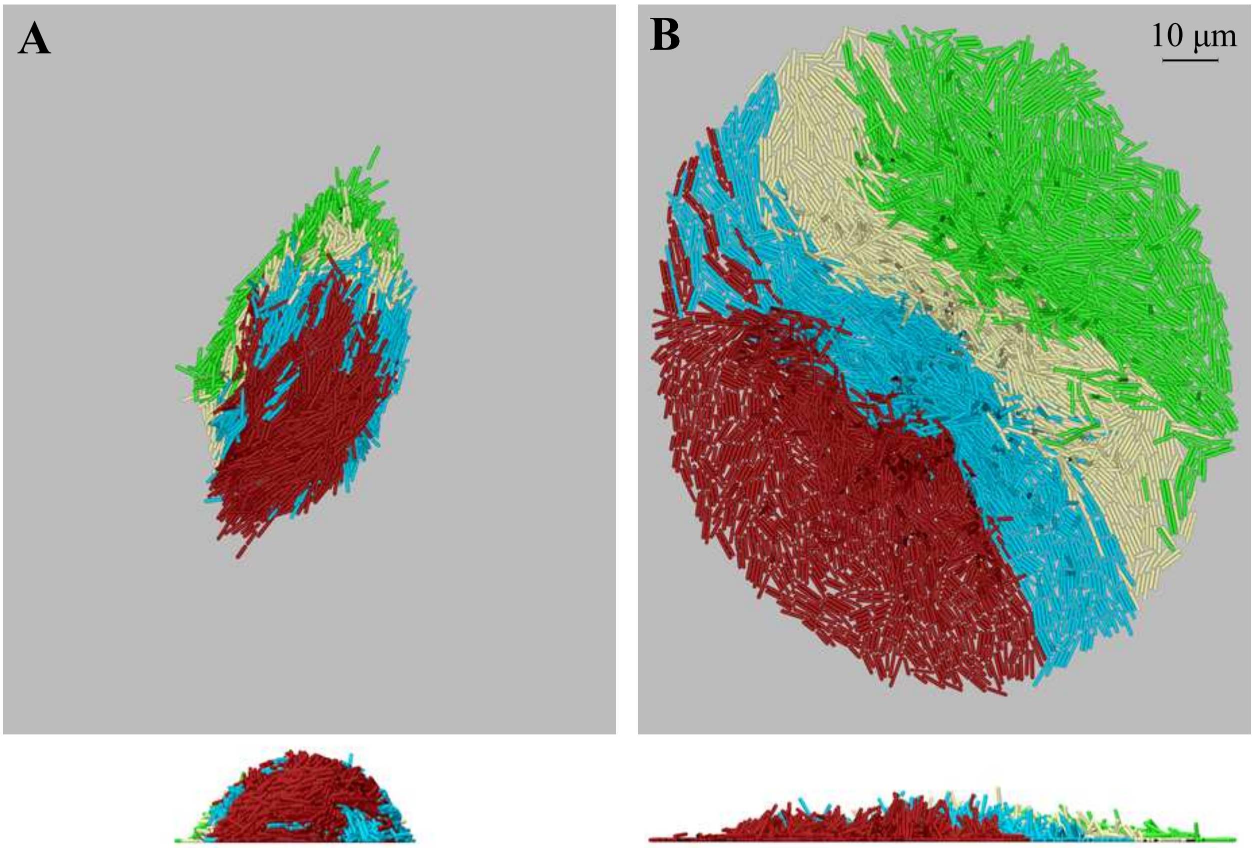

Figure 2.3: Colony development for a pure culture of rod-shaped cells on a planar substratum (top and lateral views) after 6.67 h. (A) no anchoring, no filial, no DLVO forces; (B) no anchoring, no filial, DLVO forces (as in figure 2.4A). Note that the inoculum of A and B are the same, but different from the inoculum used in figure 2.4.

velocity damping and anti-collision forces is shown in figure 2.3A and shows that without DLVO forces, a steep mound of cells is formed.

DLVO forces acting on the cells allow the cells to maintain a constant distance from the substratum plane by exerting weakly attractive forces when cells are further away from the substratum and repulsive forces when a cell approaches the substratum, thereby stimulating growth of a monolayered biofilm (figure 2.3B). This effect becomes more pronounced as the biofilm grows. Because DLVO forces play such an important role, they are included by default for the remainder of the rod-shaped community simulations in this chapter.

Colony formation without cell-substratum, without filial links

Primarily, collision response, DLVO and velocity damping forces act on the cells. Additional forces are introduced when investigating the effect of cell-substratum (anchoring) and filial links. Ten simulations with different initial states are run for each case.

Without anchoring links to bind the cells to the substratum, cells can move along the surface and encounter only a drag force relative to the cell velocity (introduced as damping in this model). Although the differences in diameter cause cells to displace each other slightly in the vertical dimension, DLVO

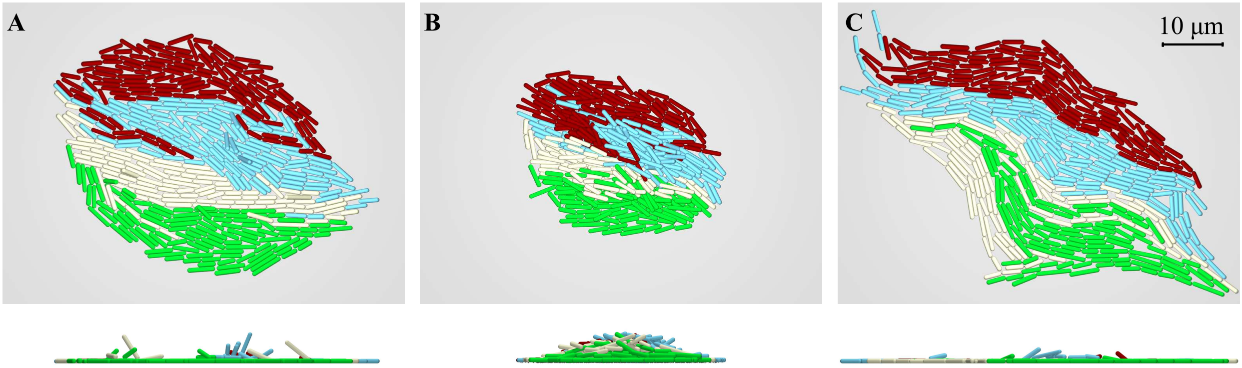

Figure 2.4: Colony development for a pure culture of rod-shaped cells on a planar substratum (top and lateral views) after 4.67 h. (A) no cell-substratum and no filial links; (B) with cell-substratum anchoring; (C) with filial links only. Colors denote the first four cell generations: red, yellow, blue and green, respectively. Animations of these simulations are presented in appendix A.

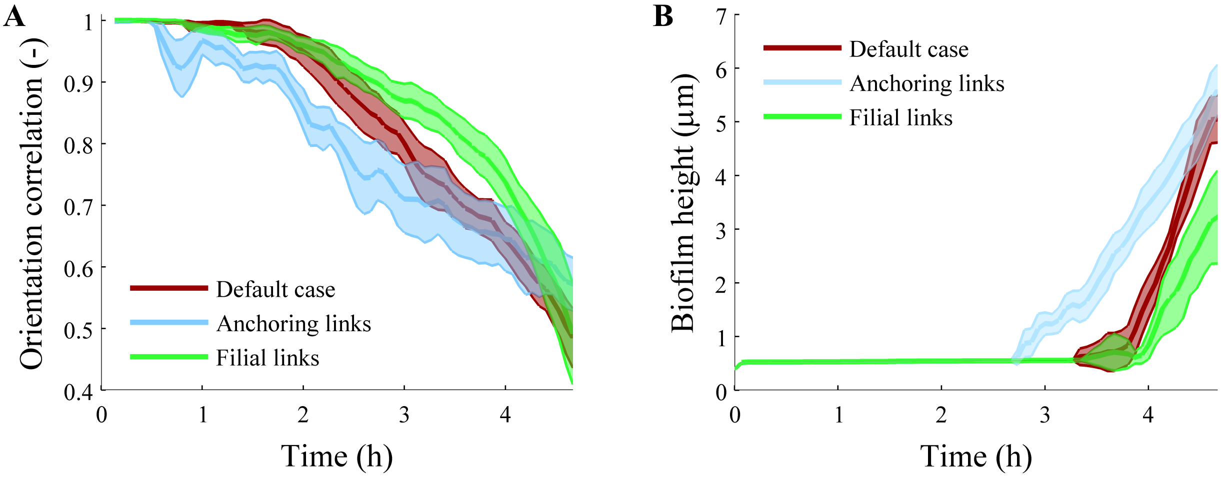

Figure 2.5: (A) Orientation correlation coefficient; (B) biofilm thickness, for simulated colonies of rod-shaped cells growing on a planar substratum. The shaded regions represent the 95% confidence interval for mean, based on 10 simulations (two-tailed t-test).

forces prevent cells from stacking for an average of 3.8 h (figure 2.4A, figure 2.5B, Supplementary movie 3). By fitting an ellipse to enclose all cells, the mean area of the biofilm at which stacking occurs is for this particular case found to be 730 ± 80 μm^2 (95% CI).

Simulation results suggest that the cells remain aligned during colony expansion, as observed in figure 2.4A. The overall orientation of cells in the colony can be quantified with the orientation correlation coefficient (Janulevicius et al., 2010), $C(t) = (1/K)\sum_{j\neq k}^{K}\left(2\cos^2\theta\left(\mathbf{o}_j(t),\mathbf{o}_k(t)\right)-1\right)$ with $\mathbf{o}$ being the orientation vector for the cell (equivalent to $\mathbf{L}_{s,i}$).

From a parallel alignment of cells in the early stage of colony formation, a more random orientation develops over time (see figure 2.5A). The initial parallel positioning can be explained by the cell division mechanism. Directly after division, both cells are aligned head-to-tail. The internal springs then relax, displacing the cells slightly while maintaining strong alignment. After several division and relaxation steps the alignment is lost.

The spread of different generations throughout the biofilm can be observed by labeling the first four generations of cells with different colors. After 70 divisions (4.67 h), cell generations are generally grouped (i.e., phase separation occurs, figure 2.4A), but some cell clusters have moved into cell collections of a different generation.

These simulations suggest that when rod-shaped cells with parameters as in table 2.1 grow on a flat, smooth substratum to which no EPS links can be formed, the biofilm may grow as a monolayer for a limited period of time . The simulated colony formation is very similar to the experimental observations of *E. coli* growth presented as time lapse microscopy movies by Stewart et al. (2005). Colonies of *B. subtilis* have also been observed to develop the same morphology (de Jong et al., 2011).

Effect of cell-substratum links

Observational work also shows that multiple layers of cells can form when rod-shaped bacteria grow on a planar substratum (Shapiro and Hsu, 1989). The underlying mechanism for this mounding of cells is not well understood, and one factor that can contribute to cell stacking is the formation of anchoring links between cell and a fixed point on the substratum, which would impede the movement along the surface. In this way, the newly formed cells could meet more resistance to movement along the substratum plane and be forced to escape towards the top of the colony. The anchoring links can be seen as strong cell bonds with substratum due to pili, or as a result of sticky EPS.

During simulations of this scenario, anchoring links are formed, stretched, broken and formed again as new cells displace their neighbours. Simulations show that initially the colony can expand along the plane, similar to the two-dimensional development without anchoring forces. However, as the colony increases in size, the amount of opposing force met by a cell growing far from the colony edge increases until DLVO and its anchoring forces are overcome, the cell is pushed up into the third dimension and the anchoring link is broken. If the cell is close enough to the substratum, a new cell-substratum link is formed, but this link is quickly broken as well because of the excessive upward force. This process repeats until eventually the cell is pushed too far from the substratum to form new anchoring links and where DLVO force is weaker, thereby escaping the substratum (figure 2.4B and Supplementary movie 4). Cells not anchored to the substratum continue to grow freely and eventually form stacks and mounds. Similar to experimental observations (Shapiro and Hsu, 1989), this mound is highest around the colony center. The first cells that break away from the substratum are positioned around the middle of the colony, where the forces required to displace neighbouring cells are the highest.

The model biofilm thickness (colony height) has been quantified and compared to that of a biofilm without anchoring links (figure 2.5B). Without anchoring links, the biofilm can remain flat for almost four hours. Including cell anchoring leads to three-dimensional colonies after on average 2.9 h for the set of parameters described in table 2.1. The mean surface area at which cell stacking is first observed is 210 ± 30 μm^2. This area is much smaller than the default case due to anchoring links limiting the horizontal expansion of the biofilm as well as a lower cell count at which cells first stack.

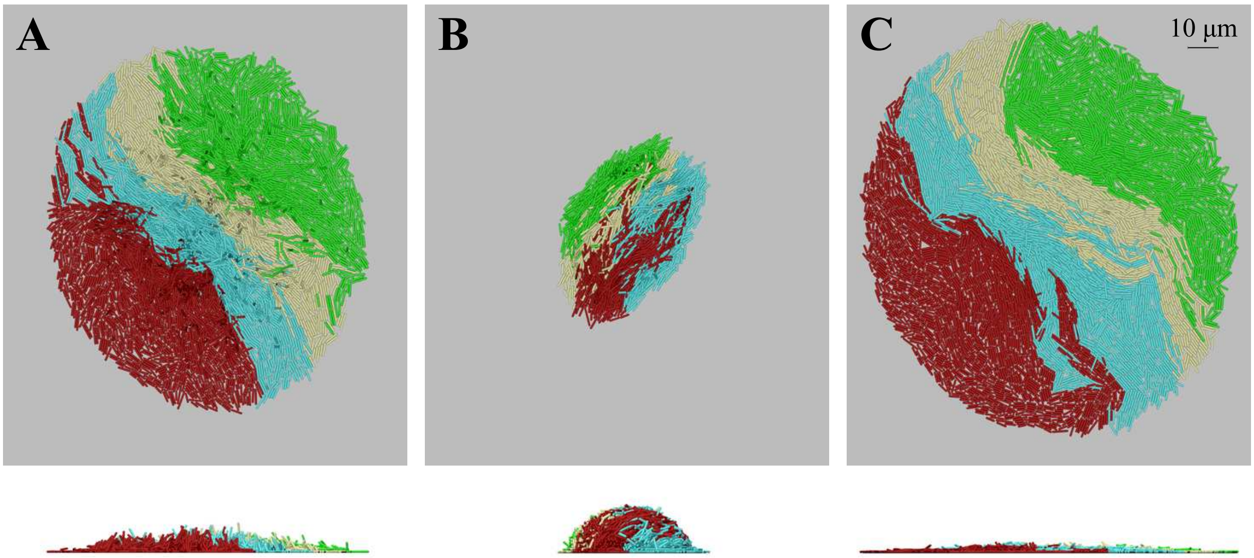

Figure 2.6: Colony development for a pure culture of rod-shaped cells on a planar substratum (top and lateral views) after 6.67 h. (A) no anchoring cell-substratum links; (B) anchoring cell-substratum links; (C) gliding cell-substratum links. Animations of these simulations are presented in Supplementary movies 2-7.

By increasing or decreasing the strength of the anchoring links (via $d_{a,break}$), the moment at which stacking occurs can be advanced or delayed. For example, setting $d_{a,break}$ to twice the default length causes cells to stack after on average 1.9 h, while halving $d_{a,break}$ results in cell stacking after 3.08 h.

Cell-substratum links also appear to disrupt the parallel alignment of rod-shaped cells in the biofilm. Anchored cells respond to displacement with an opposing force, pushing away other cells in different directions, eventually causing the biofilm to lose the parallel cell alignment (i.e., the orientation correlation quickly decreases, see figure 2.5A).

An alternative to anchoring links is the use of a slime capsule cell-substratum link (Harvey et al., 2011). Although both the anchoring and gliding approaches maintain a constant distance between cell and substratum, the slime allows the cells to freely glide along the plane, whereas anchoring links exert horizontal and vertical forces and eventually break when cells are displaced. Forces exerted by gliding cell-substratum links only have a vertical component. The mathematical model shows that compared to a non-anchoring, non-gliding simulation (figure 2.6A), anchoring links promote cell stacking (figure 2.6B and figure 2.5), whereas gliding links delay cell stacking (until 5.13 h for the simulation shown in figure 2.6C).

In conclusion, it is expected that biofilms able to form anchoring cell-substratum connections will become thicker and much less spread out than biofilms less able to bind to a substratum or dominated by gliding EPS links. Gliding cell-substratum links impede the formation of a multilayered biofilm for longer compared to when cell-substratum links are absent. The effect of cell-substratum links can be investigated experimentally by inoculating substrata with different surface roughness and observing the biofilm spread and thickness through microscopy.

Effect of filial links

Independent of the presence of anchoring links the model consistently produces colonies with rounded edges (figure 2.4A and B), in contrast to some experimental observations (Stewart et al., 2005; de Jong et al., 2011), which show also elongated or irregularly shaped colonies. One possible explanation is that elongated colonies could be the result of cells maintaining a head-to-tail connection after division, which was implemented in the model through the use of filial links.

Simulations with filial links and no anchoring to substratum indeed resulted in irregularly shaped monolayer colonies, with less circularity (figure 2.4C and Supplementary movie 5). Initially, the alignment of cells is better maintained in the presence of filial links, but near the end of the simulation (3.67 h) the alignment is lost completely (figure 2.5A).

From figure 2.5B it can be seen that filial links have no significant effect on the moment at which cell stacking first occurs (4.02 h with filial links). For these simulations, the area of the biofilm when mound formation is first observed is 1100 ± 200 μm^2, much larger than in the default case. A possible explanation for this increase is that due to the decreased colony roundness a larger ellipse is needed to envelop the cells.

The simulations show that the colony roundness can be largely determined by the ability of the species to form head-to-tail connections: cells capable of forming chains show more irregularity in their colony shape. A relation between mound formation and filial links was not observed. One way to further assess this is to biofilm morphology for species that have similar cell morphology but differ in ability to form filial links (either through manipulation or strain selection). Through image processing, the effect of filial links on cell orientation can be quantified experimentally.

2.3.2 Activated sludge floc structure and bulking

Wastewater treatment extensively uses activated sludge processes, where the microorganisms aggregated in flocs are retained in the treatment system by use of gravity clarifiers. One of the main problems of this technology is that bulking of sludge causes flocs with poor settleability and dewaterability. Sludge bulking is a result of flocs forming long, external filaments and thereby connecting to other flocs. The occurrence of interfloc bridging is found to be related to the shape and density of flocs, with a key factor being the formation of excessive filaments (see subsection 1.2.2).

The analysis here focuses on the balance between two characteristic organisms, a filament former *Sphaerotilus natans* and a floc former from the *Citrobacter* genus, growing together in the same floc. *S. natans* is a rod-shaped organism known to form relatively rigid filaments and widely found in wastewater treatment plants with bulking sludge problems (Bitton, 2011). Growth parameters are readily available for both pure culture (Seviour and Nielsen, 2010, chapter 12) and growth in co-culture with a floc former (Lau et al., 1984). Because they do not affect the results for a system with a multicellular inoculum, variation in rod cell diameters has been neglected. By varying some

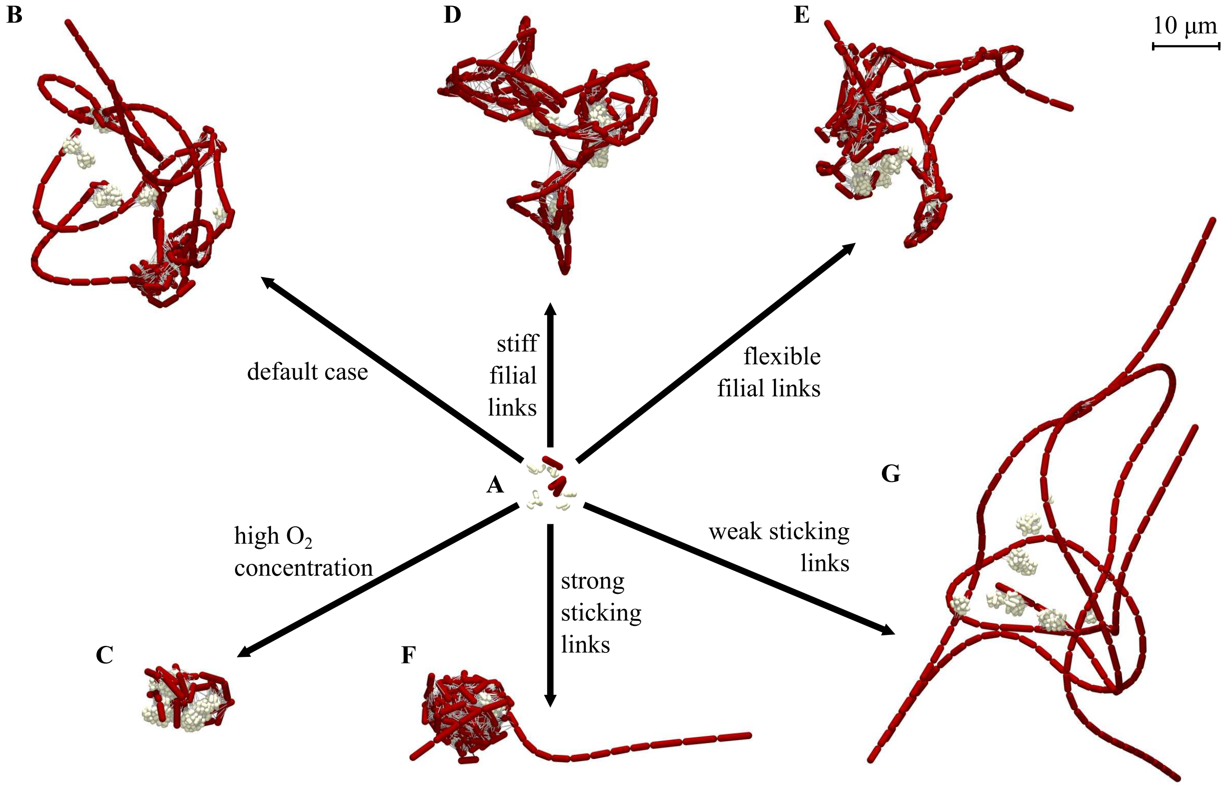

Figure 2.7: Simulated activated sludge floc structures made of floc former and filament former rod-shaped cells, showing the effect of different types of intercellular links. (A) initial state for all simulated flocs; (B) The standard case (low O_2 concentration, ($l_{s,f,short} = 0.5$, $l_{s,f,long} = 1.7$) and $d_{s,break} = 1$ µm); (C) Increased relative floc former growth rate (high O_2 concentration parameter set from table 2.1); Different filament stiffness is generated by changing ($l_{s,f,short}, l_{s,f,long}$): (D) stiff filaments $(0.1, 2.1)$; (E) flexible filaments $(0.9, 1.3)$; Sticking link strength was changed through $d_{s,break}$: (F) strong sticking (5 µm); (G) weak sticking (0.2 µm). States A, B, D-G are shown after 16.80 h (369 cells), C after 7.67 h (362 cells). Animations of aggregate development for all simulations are available in Supplementary movie 8-13.

of the microbial properties (e.g., relative growth rates, filament stiffness, sticking strength, presence of branching, floc former cell shape), effects on the structure of the resulting flocs are investigated below.

Relative growth rate of floc and filament formers

Floc formers have a higher maximum growth rate compared to filament formers, but a lower affinity for both oxygen and soluble carbon (Seviour and Nielsen, 2010, chapter 5). Therefore, at low substrate concentrations the filament formers can dominate the floc. While the model currently does not calculate substrate concentration fields, the ratio of the average growth rates of both species can be scaled by assuming fixed bulk concentrations. Two sets of parameters were used (table 2.1), corresponding to low and high oxygen concentration. In the initial floc, the same total mass of floc and filament formers was taken. That is, the inoculum contains six times as many floc former cells as filament former cells due to different cellular masses (figure 2.7A).

At low concentrations, starting from an initial state (figure 2.7A), the filament former grows faster

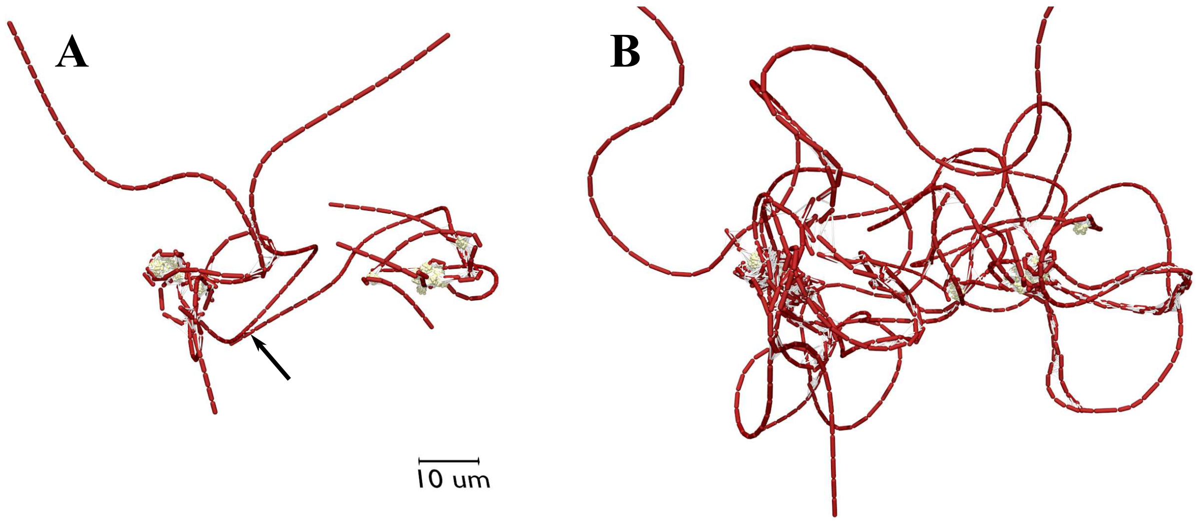

Figure 2.8: Simulated activated sludge floc structure showing interfloc bridging under low O_2 concentration growth conditions. (A) After 16.80 h and (B) after 22.50 h of growth. The arrow in A shows the first interfloc link formed. Parameters are identical to other simulations, with double the number of initial cell. A movie showing floc development is available as Supplementary movie 14.

than the floc former (figure 2.7B). The developed floc is disperse, with small colonies of floc formers attached at different positions to filaments extending freely into the bulk liquid. This behavior has frequently been reported in literature, see e.g. Martins et al. (2004) and references therein. The faster filament growth quickly puts filament formers out of reach of floc formers, which mainly occupy the floc interior. The chains of filament formers can then quickly expand into the bulk liquid and form interfloc bridges, in turn making sludge bulking possible.

Interfloc bridging can be reproduced in the model by growing two flocs simultaneously under low O_2 concentrations, initially separated by 50 μm. Similar to the floc in figure 2.7B, external filaments rapidly form and the first interfloc connection is formed within 16.80 h (figure 2.8A, arrow). The external filaments continue to grow and curl due to intercellular interactions, forming more interfloc cell-cell links until both flocs are strongly intertwined after 22.50 h of growth (figure 2.8B), similar to has experimentally been visualised by Yang et al. (2012) in figure 2.9F.

The model predicts that at high substrate concentrations (starting from the same initial state), an ideal floc is formed (Seviour and Nielsen, 2010, chapter 5). The filaments are present inside the floc but do not extend into the bulk liquid because they are “captured” by the floc formers before they escape from the floc (figure 2.7C). The dividing filamentous cells are very likely to connect through sticking springs with the more abundant floc formers that grow faster at high O_2 concentrations, preventing the filament growing away from the dense floc kernel. In time, however, the filaments will still be able to escape the floc (Supplementary movie 9) pushing other cells away and breaking cell-cell links as they grow away from the floc.

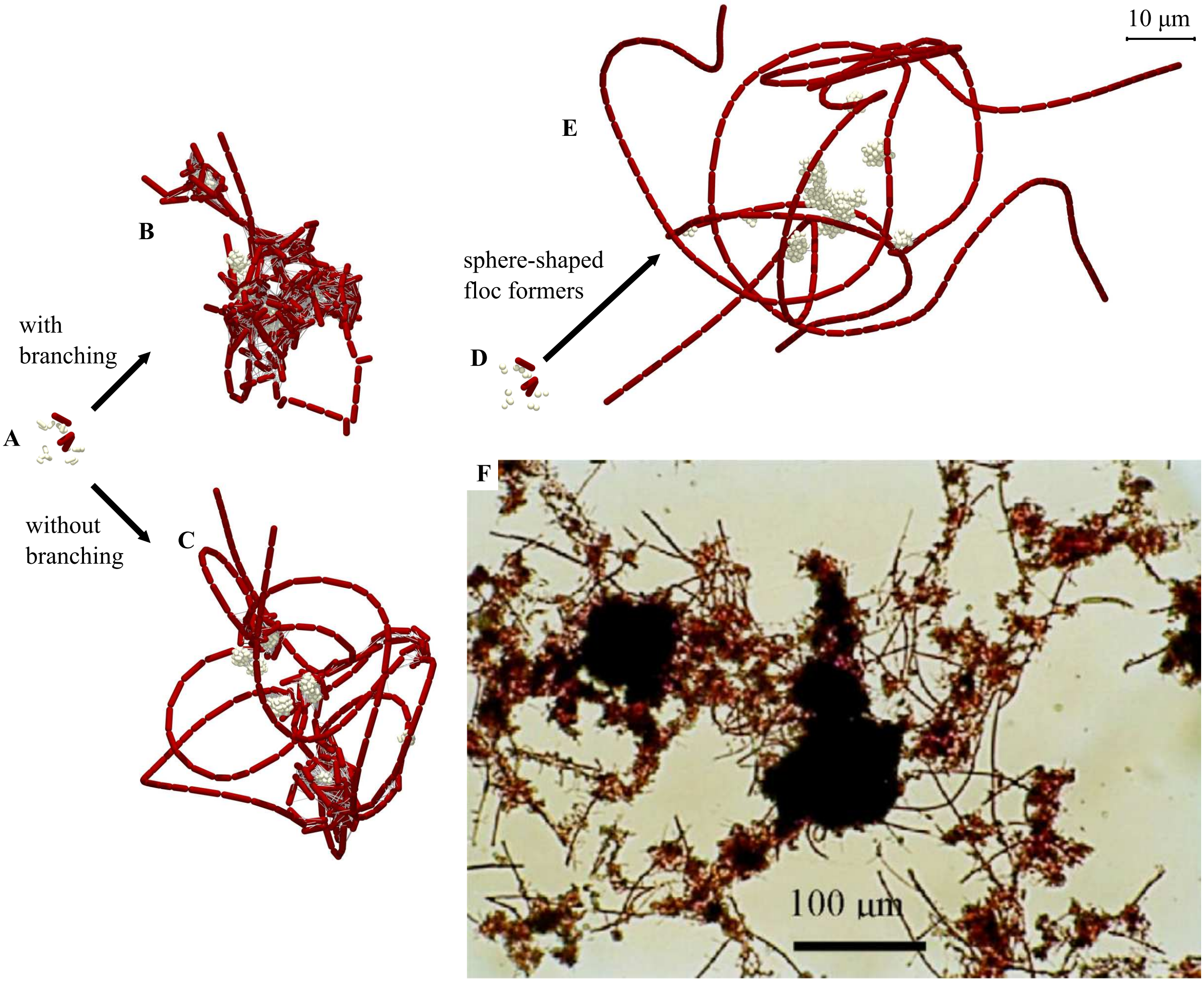

Figure 2.9: Simulated activated sludge floc structures showing the effect of filament branching and spherical floc formers. (A) Initial state for rod-shaped floc former; (B) 30% filament branching; (C) Strictly straight (non-branching) filament former; (D) initial state for spherical floc former; (E) spherical floc former; (F) Interfloc bridging observed in a Gram-stained visible light micrograph (from Xie et al. (2007)). Simulation results are shown after 19.65 h. Animations of aggregate development resulting in structures B, C and E can be found in Supplementary movie 15, Supplementary movie 8 and Supplementary movie 16, respectively.

Stiffness of filaments

Filament stiffness (resistance to filament buckling) can be tuned by changing relative spring rest lengths for filial links, e.g., a shorter $l_{s,f,short}$ and longer $l_{s,f,long}$ lead to stiffer filaments. Three parameter sets were used here for ($l_{s,f,short}$, $l_{s,f,long}$): standard (0.5, 1.7), flexible (0.9, 1.3) and stiff (0.1, 2.1), together with the low concentration growth parameters (table 2.1). The gap size between cells is identical for these parameter sets.

The simulation results suggest that filial link stiffness in the range tested does not play a major role in interfloc bridging, as all three cases resulted in a similar floc structure (figure 2.7B, D, E). Note that the stretch limit $d_{f,break}$ was not increased with increasing stiffness, so filaments already under tension (stiff) could break under a lower force than flexible filaments. For these parameters, however, filament link breakage occurred only rarely.

Strength of sticking links

The influence of sticking links on floc formation (e.g., due to different EPS strength) was investigated by varying the sticking spring stretch limit ($d_{s,break}$): normal (1 µm), strong (5 µm) and weak (0.2 µm). It was found that sticking springs play an essential role in the formation of floc structure and therefore in interfloc bridging (figure 2.7B, F, G). Strong sticking links allow floc formers to capture and maintain links with filament formers, resulting in a compact floc with only few outreaching filaments (figure 2.7F). For weaker sticking links the floc breaks up as it grows (figure 2.7G), resulting in a very disperse structure. These simulations suggest that the strength of EPS in activated sludge communities is a major factor in sludge bulking. It might even be possible that by adding chemicals to degenerate EPS, sludge bulking can increase where EPS structure is weakened instead of broken down completely. This is a challenge to assess experimentally in simple experiments, since methods to reduce EPS strength (e.g., ion exchange resins or EDTA) also can have an impact on environmental factors.

Branching of filaments

Although the modelled organism *S. natans* does not show true branching, many other filament formers do (e.g., *Nocardia* (Seviour and Nielsen, 2010, chapter 12)). To model filament branching effects on the floc bridging, a 30% chance is set to form a new branch at division instead of inserting the new cell in the straight filament. Model simulations show how the branching filament former sprouts numerous side chains, at the expense of filament length (figure 2.9B). The filaments of a branching floc are not long enough to extend far into the bulk liquid and a denser floc develops compared to the floc made of straight filaments growing at similar rate (figure 2.9C), thereby attenuating the bulking tendency of filamentous sludge, as also observed experimentally (Picioreanu et al., 2000).

Sphere-shaped versus rod-shaped floc formers

While for this study most simulations included rod-shaped floc formers, spherical cells are also widespread in activated sludge (Seviour and Nielsen, 2010, chapter 12). Simulations have been run to investigate the effect of floc former morphology on the floc structure. All parameters (i.e., mass, growth rate, spring constants) for spherical cells were the same as the rod-shaped floc formers, except the maximum diameter set to obtain the same maximum mass ($D_{s,div} = 0.52$ µm). The same initial number of cells and a similar initial cell distribution were created (compare figure 2.9A to figure 2.9D).

Simulated flocs including spherical floc formers (figure 2.9E) were more disperse than those created with rod-shaped cells (figure 2.9C). The most notable difference is that the spherical cells do not capture filaments as well as the rod-shaped cells. The denser packing of spherical cells in a colony leads to a smaller cluster volume for the spherical floc formers. This means that the chance to encounter a filament former is smaller when spherical floc formers are present instead of rod-shaped cells, resulting in less dense flocs.

2.3.3 Context and Applications

While both simple (single-population) and more complex (mixed population, mixed morphology) applications have been demonstrated here on a largely physical basis, the method allows for obvious extension to applications where substrate fields are also solved (i.e., solute transport and reaction are included). This would allow more realistic growth based on substrate and product concentration fields and would make the model available to investigate biochemical phenomena such as interspecies electron transfer on an aggregate scale.

Another key application is physical dynamics in the presence of a convective field, with two-way coupling through computational fluid dynamics (Alpkvist and Klapper, 2007b). Rather than imposing a specific geometry and set of mechanical properties on the biofilm, these can be dynamically developed in the presence of the flow field. The model proposed here is well suited to this application due to its fundamental mechanical basis.

There is a wide range of possible extensions, including microbial motility, implementation of inert and substrate particles and imposition of planar axes and division rules which allow formation of packets such as tetrads. The main negative of this approach is the computational requirements, particularly with large numbers of agents, but this can be addressed in a number of ways including solver optimization and code parallelization.

Another key issue is experimental or observational verification of model based analysis. In this thesis, the focus lies on the development and application of a variable morphology technique in order to identify possible controlling mechanisms on a basic level that drive apparently complex colony behaviour. This highlights the application of model based analysis to develop experimental hypotheses that can be then further investigated, with application to both simple and complex systems. One of the strengths of identifying experiments based on model analysis is that specific experiments can be observed and modelled under dynamic conditions to provide a complete picture of how morphology is derived from basic properties.

2.4 CONCLUSIONS AND FUTURE WORK

A variable morphology, individual-based model has been described and applied to investigate how the geometric and mechanical properties of elemental agents (microbes and EPS) can influence larger aggregates. Specifically, application of the model towards a pure culture biofilm of rod-shaped cells and a mixed community in an activated sludge floc has shown that (i) anchoring cell-substratum links promote cell stacking, while gliding links impede the formation of mounds; (ii) filial links cause biofilm roundness to decrease; (iii) interfloc bridging resulting in sludge bulking can be reproduced by changing the relative growth rates of floc formers and filament formers and (iv) filament branching and cell morphology have a strong effect on the floc morphology.

The described modelling approach can readily be extended to model a wide range of potential microbial communities, with particular applicability to problems where mechanical properties of the aggregate are important or coupled to the growth environment. Particularly, in chapter 4, the model is applied to describe the formation methane oxidising anaerobic granules present in deep-sea sediments. Further extensions to and applications of the modelling framework have been made by other researchers and are discussed in chapter 5.

Chapter 3

MEDIATED VERSUS DIRECT INTERSPECIES ELECTRON TRANSFER

ABSTRACT

Interspecies electron transfer (IET) is important for many anaerobic processes, but is critically dependent on mode of transfer. In particular, direct interspecies electron transfer (DIET) has been recently proposed as a metabolically advantageous mode compared to mediated interspecies electron transfer (MIET) via hydrogen or formate. The relative feasibility of these IET modes is analysed by modelling external limitations using a reaction-diffusion-electrochemical approach in a three-dimensional domain. For otherwise identical conditions and using parameters estimated from literature, the model indicates external electron transfer rates per cell pair (cp) are considerably higher for formate-MIET (317×10^3 $e^-\,cp^{-1}\,s^{-1}$) compared with DIET (44.9×10^3 $e^-\,cp^{-1}\,s^{-1}$) or hydrogen-MIET (5.24×10^3 $e^-\,cp^{-1}\,s^{-1}$). MIET is limited by the mediator concentration gradient at which reactions are still thermodynamically feasible, while DIET is limited through redox complex (e.g., cytochromes) activation losses. Model outcomes are sensitive to key parameters for external electron transfer including complex transfer rate constant and redox complex area, concentration or count per cell, but formate-MIET is generally more favourable for reasonable parameter ranges. Extending the analysis to multiple cells shows that the size of the network does not strongly influence relative or absolute favourability of IET modes. Similar electron transfer rates for formate-MIET and DIET can be achieved in the reported case with a slight ($0.7\ kJ\,mol^{-1}$) thermodynamic advantage for DIET. This indicates that close to thermodynamic feasibility, external limitations can be compensated for by improved metabolic efficiency when using direct electron transfer.

3.1 INTRODUCTION

Interspecies electron transfer (IET) is a vital process for microbial communities present in energetically limited processes, such as anaerobic digestion (subsection 1.2.2). Through syntrophy, two or more species are able to cooperatively utilise substrates that individually they cannot convert. Specifically, IET describes the transfer of a strongly reduced compound produced by one species to another species that is able to utilise it as a substrate. This conversion mutually benefits the species involved, as one species is able to prevent accumulation of product while the other is supplied a substrate.

In this chapter, a model is described and applied to study the thermodynamic feasibility of a recently discovered mode of IET called direct IET (DIET). In DIET, the reducing equivalent (i.e., electrons) are transferred directly through a conductive matrix, instead of via a mediator such as hydrogen or formate (mediated IET, MIET). The advantage of DIET over MIET is that diffusion limitation is less likely to occur, which is known to be the controlling mechanism for MIET (Boone et al., 1989). However, transfer of the electron to the conductive matrix via a redox complex, transport through the matrix and ion migration result in electrochemical losses, as discussed in subsection 1.2.1.

By calculating the maximum rate that can be achieved by the electron transfer mechanism based on extracellular losses and limitations, the feasibility of DIET is compared to conventional mediated IET (MIET) via hydrogen or formate. The model considers the conversion of propionate to methane via acetogenesis and hydrogenotrophic methanogenesis. For hydrogen-MIET, reactions 1.5a and 1.6b are balanced for hydrogen to yield the reactions:

$$\mathrm{Pro^- + 3\,H_2O \longrightarrow Ac^- + HCO_3{}^- + 3\,H_2 + H^+} \tag{3.1a}$$

$$\mathrm{0.75\,HCO_3{}^- + 3\,H_2 + 0.75\,H^+ \longrightarrow 0.75\,CH_4 + 2.25\,H_2O} \tag{3.1b}$$

Formate-MIET is an alternative to hydrogen-MIET with the advantage that the process is feasible over a higher range of concentrations (Boone et al., 1989):

$$\mathrm{Pro^- + 2\,HCO_3{}^- \longrightarrow Ac^- + 3\,For^- + H^+} \tag{3.2a}$$

$$\mathrm{3\,For^- + 0.75\,H^+ + 0.75\,H_2O \longrightarrow 0.75\,CH_4 + 2.25\,HCO_3{}^-} \tag{3.2b}$$

In direct IET the electrons are not transferred via a reduced component, but directly through an external matrix such as a network of electron conducting nanowires (Reguera et al., 2005):

$$\mathrm{Pro^- + 3\,H_2O \longrightarrow Ac^- + HCO_3{}^- + 7H^+ + 6\,e^-} \tag{3.3a}$$

$$\mathrm{0.75\,HCO_3{}^- + 6.75\,H^+ + 6\,e^- \longrightarrow 0.75\,CH_4 + 2.25\,H_2O} \tag{3.3b}$$

The different pathways for mediated and direct IET result in distinct differences in extracellular limitations.

3.1.1 Limitations in mediated versus direct IET

Metabolic modelling of *Geobacter*-mediated ethanol oxidation with fumarate as terminal electron acceptor has suggested that DIET has a metabolic advantage over MIET (hydrogen or formate) (Nagarajan et al., 2013). However, the analysis considered only intracellular metabolism, without taking into account external voltage losses inherent to long-range electron transport. Although DIET does not depend on a mediator to transfer electrons (and is therefore less likely to be limited by diffusion), transport of electrons between the cells through a conductive matrix results in multiple electrochemical losses unique to DIET. These include:

1. activation losses (overpotentials) for transfer from a terminal membrane-bound redox complex to the nanowire (and the inverse),
2. electrical resistance of the nanowire and
3. solution resistance caused by migration of ions between the cells.

Indirect, secondary limitations may also develop due to development of a p*H* gradient caused by saline ion migration, and due to accumulation of non-mediator intermediates. A single factor may control, or multiple factors may combine in order to govern feasibility of DIET. External limitations in nanowire-DIET have not been previously analysed, particularly in relation to well-understood MIET systems. In this work, a mechanistic framework is proposed that enables direct assessment of the relative feasibility of DIET and MIET in a thermodynamically restricted system (specifically, propionate conversion to acetate and methane).

By evaluating the extracellular limitations for hydrogen-mediated, formate-mediated and direct IET, the thermodynamic feasibility of the three modes is compared and bottlenecks are identified. A sensitivity study is conducted to determine the impact of uncertainties of DIET parameters estimated from literature on the relative feasibility of the IET modes. Finally, a multicellular DIET model is presented that can simulate IET in complex cell networks to analyse how interactions change on a larger scale.

3.2 MODEL DESCRIPTION

3.2.1 Model geometry and components

A three-dimensional transport-reaction model has been implemented to calculate the relative feasibility of the three proposed IET modes, hydrogen-MIET, formate-MIET and DIET. Two spherical acetogen and methanogen cells with a diameter of 1 µm each are positioned 5 µm apart and 5 µm from all boundaries of a rectangular domain of size $17 \times 11 \times 11$ µm^3 (figure 3.1). A 5 µm interspecies distance appears to occur frequently in experimental DIET systems (e.g., Summers et al.

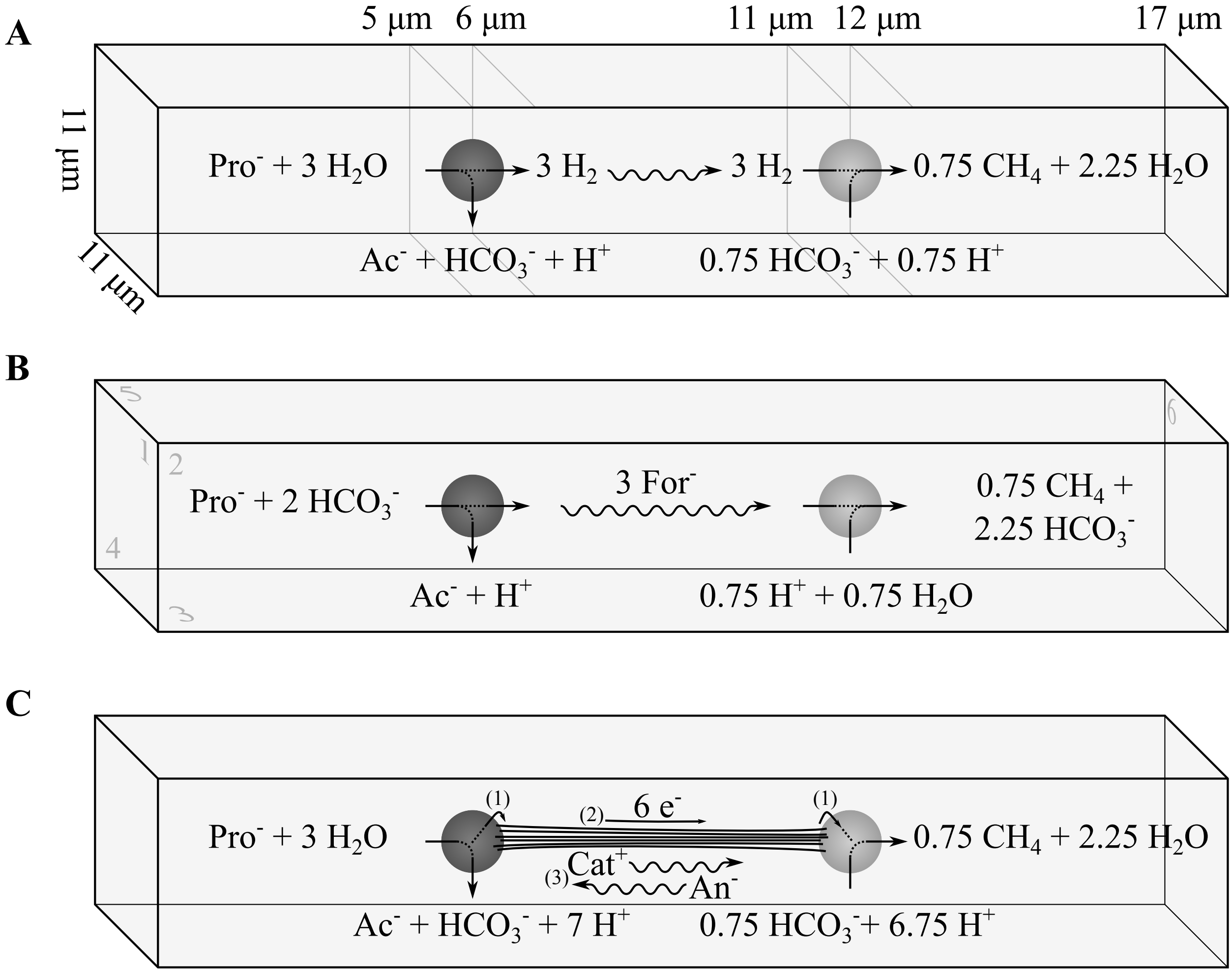

Figure 3.1: Model geometry, boundary conditions and reactions involved in the three described interspecies electron transfer mechanisms: (A) hydrogen-MIET, (B) formate-MIET and (C) DIET. In (B), on boundaries 1-6 a no-flux condition is set for mediators (H_2, For$^-$ and HFor) and fixed concentrations for all other components. Boundary concentration values (c_0) are stated in table 3.1. A zero-potential is set on boundary 6. In (C), numbers denote voltage losses for (1) redox factor activation losses, (2) nanowire resistance and (3) migration.

(2010); Malvankar et al. (2011); Malvankar and Lovley (2012); Malvankar et al. (2012b), although systems with smaller interspecies distances have been frequently observed as well (e.g., Franks et al. (2010); Bond et al. (2012); Stephen et al. (2014)) Spherical cells with identical diameters are used to eliminate effects the different cell geometries might have on substrate uptake rate. For DIET, it is assumed that multiple nanowires are formed between each cell pair (see e.g. figures in Malvankar et al. (2011)). A direct electric connection is made through the formation of 100 nanowires between each cell pair in the model. Many DIET parameters are not readily available. Therefore, some parameters are taken from experimental data for *Shewanella* and others for *Geobacter*, investigating the theoretical feasibility of the DIET mechanism, not of a single microbial species.

The solution consists of primary substrate, carbonate buffer, mediator and products. Due to the necessity to calculate local pH values, acid dissociation equilibria are included. The chemical components taken into account in the model are therefore protons (H^+), hydroxide (OH^-), potassium ion (K^+),

Table 3.1: Default model parameter values. The complete default parameter set with nomenclature is available in supplementary material as appendix B.

Symbol	Unit	Description	Default value	Reference and notes
Geometry				
A_{cell}	m^2	Surface area of cell	3.14×10^{-12}	Calculated from d_{cell}
d_{cell}	m	Diameter cell	1.00×10^{-6}	Acetogen and methanogen
Concentrations				
c_0	$\mathrm{mol\,m^{-3}}$	Fixed boundary concentration		
		Propionic acid	7.41×10^{-3}	
		Propionate	1.00	
		Acetic acid	5.75×10^{-3}	
		Acetate	1.00	
		Carbon dioxide	22.39	
		Bicarbonate	100	
		Methane	0.1438	From $p_{0,CH4} = 0.1$ bar
		Proton	1.00×10^{-4}	pH 7
		Hydroxide	1.01×10^{-4}	
		Chloride	1000	
		Potassium ion	1102	Closes charge balance
Thermodynamics and electrochemical				
$\Delta G'_{min}$	$\mathrm{J\,mol^{-1}}$	Min. req. $\Delta G'$ for cell anabolism, maintenance	-15.2×10^3	Boone & Bryant (1980)
V_{min}	V	Min. req. V for anabolism and maintenance	52.51×10^{-3}	Calculated as $-2\Delta G'_{min}/6F$
Butler-Volmer (DIET only)				
$A_{act,cell}$	m^2	Total area for redox complex activation for any cell	3.14×10^{-13}	Appendix C
c^s_{act}	$\mathrm{mol\,m^{-2}}$	Redox complex surface concentration	5.29×10^{-9}	Appendix C
k_0	s^{-1}	Standard redox complex activation rate constant	6000	Appendix D and Ly et al. (2013)
$N_{act,j}$		Number of redox complexes per nanowire for cell j		$N_{act,cell}/N_{nw,j}$
$N_{act,cell}$		Number of redox complexes per cell	1.0×10^4	Lower et al. (2007)
β	-	Symmetry factor	0.5	
Ohm's law (DIET only)				
A_{nw}	m^2	Cross-sectional area of a single nanowire	1.26×10^{-17}	Calculated from d_{nw}
d_{nw}	m	Diameter of single nanowire	4.00×10^{-9}	Malvankar et al. (2011)
L_{nw}	m	Length of single nanowire		
$N_{nw,j}$		Total number of nanowires connected to cell j		$N_{nw,pair}$ per connected cell k
$N_{nw,pair}$		Number of nanowires formed per cell pair	100	
ρ_{nw}	$\Omega\,\mathrm{m}$	Nanowire electrical resistivity	1.0	Malvankar et al. (2011)

chloride (Cl^-), propionate (Pro^-), propionic acid (HPro), bicarbonate (HCO_3^-), carbon dioxide (CO_2), hydrogen (H_2), formate (For^-), formic acid (HFor), acetate (Ac^-), acetic acid (HAc) and methane (CH_4).

3.2.2 Transport of solutes and charge balance

Transport of all chemical compounds in the solution (cells and surroundings) occurs only through diffusion (introducing diffusion coefficient D) and migration (charge z and migration potential field Φ_{mig}), as described by the steady state Nernst-Planck equation:

$$\nabla \cdot J_i = r_i \qquad \text{with flux} \qquad J_i = -D_i \nabla c_i - \frac{z_i D_i F}{RT} c_i \nabla \Phi_{mig} \tag{1.13}$$

With reaction rates r_i calculated as described in the next section, the unknowns in the system are the 14 concentrations c_i and the potential field gradient Φ_{mig} (15 unknowns per control element). Given equation 1.13 is applied for each component i (14 equations), the system is fully defined by setting the potassium ion concentration to satisfy the electroneutrality condition (via equation 1.16):

$$c_{K^+} = -\sum_{i \neq K^+} z_i c_i \tag{3.4}$$

In order to determine IET rates based only on cell metabolism, no-flux boundary conditions ($-\mathbf{n} \cdot Ji = 0$, where $\mathbf{n}$ is the normal vector) for the mediator and fixed concentrations ($c_i = c_{0,i}$) for all compounds are set at all domain boundaries. All boundaries are electrically insulated ($-\mathbf{n} \cdot F \sum_i z_i J_i = 0$ for faces 1-5 in figure 3.1B, where n is the normal vector), except one face of the domain (6 in figure 3.1B) for which the potential Φ_{mig} is set to a reference value ($\Phi_{mig} = 0$ V) to allow calculation of Φ_{mig} from $\nabla \Phi_{mig}$. Default parameter values are listed in table 3.1.

3.2.3 Reaction rates

For each compound i, the net volume-specific rate r_i in equation 1.13 includes contributions from biological conversions $r_{B,i}$ and acid dissociation $r_{A,i}$ (see subsection 1.2.3). Dissociation reactions occur throughout the entire domain, whereas biological conversions only take place in the cells. The net biological contributions, $r_{B,i} = \sum_j \nu_{ji} r_{X,j}$, are calculated with cell reaction rate $r_{X,j}$ and stoichiometry coefficients ν_{ji} specific for reactions occurring in each cell type as given in figure 3.1. Due to the cellular scale and thermodynamic restrictions, cell reaction rate can be completely regulated by a thermodynamic inhibition function that incorporates substrate, intermediate and product concentrations, such that empirical rate functions like the Monod equation (Batstone et al., 2006) can be omitted. The cell uptake rate (basis 1 mol propionate, 3 mol mediator, 6 mol equivalents) is given by the maximum rate (r_X^{max}), limited by inhibition factors $f_{inh,j}$ (constrained to $0 < f_{inh,j} < 1$):

$$r_{X,j} = \begin{cases} r_X^{max} f_{inh,MIET,j} & \text{for MIET} \\ r_X^{max} f_{inh,MIET,jk} & \text{for DIET, two-cell system} \end{cases} \tag{3.5}$$

For MIET, the only extracellular factor considered to limit the rate is thermodynamic inhibition, which is defined as in subsection 1.2.3:

$$f_{inh,MIET,j} = 1 - \exp\left(\left(\Delta G'_{r,j} - \Delta G'_{min}\right)/RT\right) \tag{3.6}$$

Equation 3.6 is equivalent to previously described inhibition functions such as Orcutt and Meile (2008). By using $f_{inh,MIET,j}$, the cell is limited only by the Gibbs free energy available for electron transport ($\Delta G'_{r,j} - \Delta G'_{min}$) generated by the catabolic reaction considered in each cell. $\Delta G'_{r,j}$ is a function of the surface-averaged concentration $\langle c_i \rangle_j$ (in $\mathrm{mol\,L^{-1}}$) or partial pressure (in bar, for H_2 and CH_4) of reactants and products i for cell j, expressed as:

$$\Delta G'_{r,j} = \Delta G^0_{r,j} + RT \ln Q \qquad \text{where } Q = \left(\prod_{i \neq \mathrm{H_2,CH_4}} \langle c_i \rangle_j^{\nu_{ji}} \prod_{i = \mathrm{H_2,CH_4}} \langle p_i \rangle_j^{\nu_{ji}} \right) \tag{3.7}$$

Equation 3.7 is the same as equation 1.4, written for the average concentration on the surface. Through equations 3.5-3.7, $r_{X,j}$ is completely regulated by $\langle c_i \rangle_j^{\nu_i}$, $\langle p_i \rangle_j^{\nu_i}$ and $\Delta G^0_{r,j}$. With r_X^{max} sufficiently high, an increase in r_X^{max} is compensated for by a small decrease in $f_{inh,MIET,j}$ via small changes in $\langle c_i \rangle_j^{\nu_i}$ and $\langle p_i \rangle_j^{\nu_i}$. r_X^{max} can therefore be set to an arbitrarily high value such that reactions proceed at their thermodynamic limit ($\Delta G'_{r,j} - \Delta G'_{min}$ approaches 0). Due to low mediator concentrations and the reaction stoichiometry, equation 3.7 is dominated by the mediator term ($\langle p_{\mathrm{H_2}} \rangle_j^{\nu_{\mathrm{H_2}}}$ or $\langle c_{\mathrm{For^-}} \rangle_j^{\nu_{\mathrm{For^-}}}$). A more detailed description of this thermodynamic inhibition function is given in subsection 1.2.3.

As stated above, $r_{X,j}$ is not governed by a kinetic function but it operates at the highest rate that is thermodynamically possible. The critical parameter is the minimum Gibbs free energy ($\Delta G'_{r_{min}}$), which has been estimated to be between -15 and -25 $\mathrm{kJ\,mol^{-1}}$ substrate (Stams and Plugge, 2009). Note that a larger (more negative) $\Delta G'_{min}$ will result in a lower rate, though both MIET and DIET will be uniformly impacted. Applying the model specifically to a propionate grown co-culture of *Syntrophobacter wolinii* and *Methanospirillum hungatei* (both capable of formate-MIET) growing on propionate (Boone and Bryant, 1980) and applying a growth yield ($Y_{S/X}$) of 0.15 $\mathrm{Cmol\,mol^{-1}}$ propionate, based on the observed growth rate and applied substrate concentrations (Boone and Bryant, 1980), it has been estimated that $\Delta G'_{min} = -15.2$ $\mathrm{kJ\,mol^{-1}}$ for both cell types (see Supplementary Figure 1). This value is applied to DIET and MIET.

The only difference between implementations for DIET and MIET is in the direct electron transfer component. In DIET, electrons are transferred between acetogen and methanogen through a conductive system driven by a voltage $V_{net,jk}$ between the two cells j and k. Electrons are produced through propionate metabolism by an oxidising cell, and then transferred to the reducing cells for carbon dioxide conversion (see figure 3.1C). Unlike with MIET, where the feasibility of the reaction is determined by the cell environment, the feasibility of the DIET reaction pair is determined on its paired basis. The net voltage available ($V_{net,jk}$) in the two-cell system is equal to the voltage available from the reaction given in 3.1C ($V_{r,jk}$) minus DIET-specific voltage losses for electron transfer between membrane bound redox complexes and nanowire (activation losses) at both cells j and k, nanowire resistance, and ion migration in the solution, as depicted by equation 3.8:

$$V_{net,jk} = V_{r,jk} - \eta_{act,j} - \eta_{act,k} - \eta_{nw,jk} - \eta_{mig,jk} \tag{3.8}$$

The voltages in equation 3.8, $V_{net,jk}$ and V_r, relate to Gibbs free energy changes via:

$$V = -\Delta G' / (F \nu_{e^-}) \tag{1.27}$$

where $\nu_{e^-} = 6$, the number of electrons involved in the catabolic half reaction. Therefore, $V_{r,jk}$ is calculated via the surface-averaged concentrations (using equation 3.7 and $\Delta G'_{r,jk} = \Delta G'_{r,j} + \Delta G'_{r,k}$). It was found that because no mediator is involved for DIET, none of the terms $\langle c_i \rangle_j^{\nu_i}$ and $\langle p_i \rangle_j^{\nu_i}$changes significantly with IET rate and as a result the voltage available from reaction is constant for all reported DIET rates ($V_{r,jk} = 52.93$ mV). Whereas MIET is regulated via the energy made available by the catabolic reaction ($\Delta G'_{r,j}$), DIET is controlled via the external electron transfer voltage losses (η). Because voltages V_{jk} and voltage losses η_{jk} in equation 3.8 are defined for the oxidising-reducing cell pair, the values observed by cell j are identical to those observed by its partner k (i.e., $V_{jk} = V_{kj}$ and $\eta_{jk} = \eta_{kj}$).

The electron transfer rate is limited by an inhibition function governed by the net and minimum voltage:

$$f_{inh,DIET,jk} = 1 - \exp\left(-F \nu_{\mathrm{e}^-} \left(V_{net,jk} - V_{min}\right) / RT\right) \tag{3.9}$$

There are two differences between the model for MIET and DIET. First, additional losses specific for DIET are taken into account (equation 3.8) and second, inhibition for cell j (equation 3.9) depends also directly on cell k ($V_{net,jk} = V_{net,kj}$, therefore $f_{inh,DIET,jk} = f_{inh,DIET,kj}$). Although equation 3.9 is expressed as voltage rather than free energy as in equation 3.6, the two regulation functions equation 3.6 and equation 3.9 are completely analogous as seen through the Gibbs-voltage relation given in equation 1.27.

The minimum voltage (V_{min}) can be calculated directly from equation 1.27 and $\Delta G'_{min}$, yielding $V_{min} = 52.51$ mV for any cell pair.

Cell conversion rates ($r_{X,j}$) are volume-specific and are referenced to the primary substrate. In order to express the rate per cell, the cell-specific electron transfer rate has been calculated as:

$$rate_{IET,j} = r_{X,j} \pi {d_{cell}}^3 N_A \tag{3.10}$$

with unit e$^-$/s, where N_A is Avagadro's number and 6 mol electrons are transferred per mol propionate consumed.

3.2.4 Redox complex activation losses

Activation losses occur each time an electron is transferred from the electron carrier associated with the membrane to the nanowire or *vice versa*. Both of these voltage losses ($\eta_{act,j}$ and $\eta_{act,k}$; (1) in figure 3.1C) are calculated using the Butler-Volmer equation assuming a one-step, single-electron transfer process (paragraph 1.2.3). The total current between the cells (I_{jk}) is the same in the electron producing and consuming cells ($I_{jk} = I_{kj} = rate_{IET,jk} F/N_A$), and this current is distributed evenly over the nanowires connecting the cells (analogous to an electrical circuit in parallel). The Butler-Volmer equation used to calculate the activation voltage loss ($\eta_{act,j}$) is as shown in equation 3.11:

$$I_{jk}/N_{nw,pair} = F A_{act,j} k_0 c^s_{act} \left(e^{(1-\beta)(F/RT)\eta_{act,j}} - e^{-\beta(F/RT)\eta_{act,j}} \right) \tag{3.11}$$

The number of nanowires present between the cell pair ($N_{nw,pair}$), symmetry factor (β), redox complex transfer rate constant (k_0) and activation complex concentration (c^s_{act}) have been taken as the same for electron producing and consuming cells. Given that the redox complex surface area available for activation ($A_{act,j}$) is calculated as described below, $\eta_{act,j}$ remains as the only unknown. The Butler-Volmer equation can therefore be solved implicitly to determine voltage losses $\eta_{act,j}$ and $\eta_{act,k}$ at which the current will be at its maximum.

To determine the total redox complex surface area per cell ($A_{act,cell}$), it was estimated that in total 10% of the cell surface area is available to transfer electrons to the nanowires, regardless of the number of nanowires. This estimate considers 10^4 redox complexes ($N_{act,j} = 10^4$) present on the cell surface of a *Shewanella* cell (Lower et al., 2007) and a redox complex diameter between 5 and 8 nm in diameter (Wigginton et al., 2007), using which the cytochrome coverage is calculated as around between 6 and 16% (appendix C). These values match well to estimates made by Okamoto et al. (2009). The available redox complex area per connection is calculated assuming that the total redox complex area available is distributed evenly over all nanowires connected to cell j ($A_{act,j} = A_{act,cell}/N_{nw,j}$). In a two-cell system this simplifies to $A_{act,j} = A_{act,k}$, such that activation losses are the same at both cells ($\eta_{act,j} = \eta_{act,k}$).

The redox complex transfer rate constant k_0 for redox complex-nanowire transfer is not readily available in literature. However, redox complex-electrode electron transfer rate constants have been reported. The heterogeneous rate constant for outer membrane cytochromes on *Shewanella* has been calculated as 150 s^{-1} (Okamoto et al., 2009). Using the redox complex concentration derived from $N_{act,cell}$, the surface concentration (c^s_{act}) is estimated to be 5.29×10^{-9} $\mathrm{mol\,m^{-2}}$. This matches well with the experimentally observed exchange current density (Bowden et al., 1982; Reed and Hawkridge, 1987), as shown in appendix D. Rates for electron transfer within a biofilm have been estimated to be 40 times faster than for transfer between biofilm and electrode (Ly et al., 2013). Therefore, for both the acetogen and methanogen, k_0 is assumed to be equal to 6000 s^{-1}. Further research could provide insight to the correctness of this estimate. Because no direct measurements have been done on Butler-Volmer parameters for system modelled in this work, a sensitivity assessment is conducted to test a range of parameters.

3.2.5 Nanowire ohmic losses

Ohmic conductivity for the nanowire is assumed because of recent experimental support (Malvankar et al., 2014) and as experimentally observed parameters can be found in literature (El-Naggar et al., 2010; Malvankar et al., 2011). The voltage loss due to nanowire resistance is calculated using Ohm's law. Because the current through each nanowire is inversely proportional to the number of nanowires, equation 1.30 is written as:

$$\eta_{nw,jk} = R_{nw,jk} I_{jk} / N_{nw,pair} = \rho_{nw} L_{nw,jk} I_{jk} / N_{nw,pair} A_{nw} \tag{3.12}$$

which is function of the IET rate, resistivity (ρ_{nw}), nanowire length ($L_{nw,jk}$) and nanowire cross-sectional area (A_{nw}). Parameters for nanowire losses are taken from measurements performed on *Geobacter sulfurreducens*. The nanowire length is set as the interspecies distance, 5 µm (figure 3.1). The nanowire diameter is $d_{nw} = 4$ nm and the electrical resistivity $\rho_{nw} = 1$ $\Omega\,\mathrm{m}$ (Malvankar et al., 2011).

3.2.6 Migration losses

The voltage loss due to extracellular ion migration in DIET, $\eta_{mig,jk}$, is related to an extracellular electric field (E) formed in the medium as a result of ion transport, equation 1.13. This electric field causes a potential field (related via $E = -\nabla\Phi$) resulting in an overall voltage loss $\eta_{mig,jk}$. A potential field is implicitly calculated in the modelling package used (and has been separately verified by calculation), from which $\eta_{mig,jk}$ is calculated as the difference between the average value of Φ_{mig} at the surfaces of methanogen and acetogen cells ($\eta_{mig,jk} = |\langle \Phi_{mig} \rangle_k - \langle \Phi_{mig} \rangle_j|$, the absolute value is taken such that $\eta_{mig,jk} = \eta_{mig,kj} > 0$ in equation 3.8).

Migration losses are only relevant for DIET because electrons are transferred separate from the ions. For mediated interspecies electron transfer, the electrons are bound to the reduced mediator compound (hydrogen, formate, *etc.*). Therefore, the uptake and production rates of charged chemical species at the microbial cells are balanced. For example, considering only charged compounds, a H_2-producing acetogen (reactions 3.1a) takes up one mol propionate (Pro^-) while producing one mol each of acetate (Ac^-), proton (H^+) and bicarbonate (${HCO_3}^-$), such that the total charge of compounds before the reaction is equal to the total charge of compounds after the reaction and the local charge balance remains. This is not true for direct IET (reactions 3.3a and 3.3b), where the electron is transferred separately from the other compounds. For direct IET, the acetogen takes up one mol of propionate (Pro^-) and produces one mol acetate (Ac^-), one mol bicarbonate (${HCO_3}^-$) and seven mol of protons (H^+), while transferring six mol electrons (e^-) through the nanowire. Although the global electroneutrality condition is still satisfied, the local electroneutrality balance is perturbed, as an excess of cations is present near the cell surface after the reaction. This causes anions to be transported to the cell surface as the system strives to satisfy the local electroneutrality condition (equation 1.16). The resulting net transport flux (J_i in equation 1.13) is then set by the local electroneutrality condition via the electric field ($E = -\nabla\Phi$) in the migration term.

3.2.7 Implementation of for a multicellular system

The MIET model can be directly implemented in a multicellular system without modification. When applying the DIET model to a larger cell community, the key complication is sharing of electrons between multiple pairs of donors and acceptors while maintaining a closed electron balance for all cell pairs. Proposed here is a method using an electron balancing factor, $f_{bal,jk}$, for each cell in a pair that limits the rate of faster reacting cells to the rate of its connected partners. The DIET rate equation 3.5 can be rewritten for a multicellular system:

$$r_{X,j} = \sum_k r_{X,jk} = r_X^{max} \sum_k \left(f_{inh,DIET,jk} f_{bal,jk} \right) \tag{3.13}$$

$f_{bal,jk}$ is a limiting factor ($0 \leq \sum_k f_{bal,jk} \leq 1$) introduced to satisfy the electron balance in the system and is needed when a cell forms connections with multiple other cells. When modelling a single cell pair with the same rXmax, rates are always balanced ($\sum_k f_{bal,jk} = \sum_k f_{bal,kj} = 1$) because the inhibition factor is the same for both cells (all terms in equation 3.9 are the same for j and k, so $f_{inh,DIET,jk} = f_{inh,DIET,kj}$), thereby reducing multicellular DIET rate equation 3.13 to two-cell system DIET rate equation 3.5.

The reason an extra factor $f_{bal,jk}$ must be introduced for a multicellular system is related to the redox complex area. As stated before, it is assumed that the total area of membrane-bound redox proteins $A_{act,cell}$ is the same for all cells and is shared evenly among the connected nanowires. For the multicellular system, one cell j can form a different number of nanowires than cell k, such that the redox complex area available to each nanowire connected to cell j, $A_{act,j}$, is no longer equal to $A_{act,k}$. The activation loss for j can thereby be limited in a different way than for cell k that is connected to a different number of cells ($N_{nw,j} \neq N_{nw,k}$, so $\eta_{act,j} \neq \eta_{act,k}$ as per equation 3.11), resulting in a different set of inhibition factors for cell j, k and their respective partners, consecutively requiring an extra rate balancing factor $f_{bal,jk} \neq f_{bal,kj}$ to close the electron conservation balance. $f_{bal,jk}$ is calculated for all cells and neighbours by maximising the total IET rate.

In order to investigate how electrons are shared according to the method described here and how sharing affects the total IET rate, a case study is set up involving twelve acetogens and twelve methanogens distributed randomly in a $30 \times 30 \times 30$ µm^3 domain. An average interspecies distance of 5 µm between a cell and its closest partner is enforced. 100 nanowires are taken to be present between an acetogen and each methanogen in a 10 µm radius (i.e., $N_{nw,pair}$ remains 100, but $N_{nw,jk} = \sum_k N_{nw,cell}$ can exceed 100).

3.2.8 Implementation

Both two-cell and multicellular models were implemented in COMSOL Multiphysics (COMSOL 4.4, COMSOL Inc., Burlington, MA) using the Nernst-Planck Equations module. Two Global ODEs and DAEs modules are set up and solved in parallel to determine the voltage losses for the Butler-Volmer and Ohm's law equations. For the multicellular model, the model geometry was defined in MATLAB and transferred via LiveLink (MATLAB 2014a, MathWorks, Natick, MA). $f_{bal,jk}$ is determined by minimising $\left(\sum_j rate_{IET,j}\right)^{-1}$ using a Sparse non-linear optimiser algorithm optimiser (Gill et al., 2005). Model code can be provided on request.

3.3 RESULTS AND DISCUSSION

3.3.1 Two-cell system

Results for single cell pair simulations show that MIET is controlled by hydrogen and formate/formic acid diffusion. The concentration along the centre of the domain changes by less than 0.01% of the mean concentration for all components except hydrogen, formate and formic acid (figure 3.2A). DIET rates are controlled by activation losses (93% of total voltage losses, see figure 3.2B), while solution resistance and diffusion limitation are insignificant ($\eta_{mig} << 1\%$ total voltage losses and the overall relative concentration differences for all components less than 0.01%). Formate-MIET (317×10^3 e$^-$/cp/s, figure 3.2C) is thermodynamically the most favourable IET mode, with the DIET rate 1 order of magnitude (44.9×10^3 e$^-$/cp/s) and the hydrogen-MIET rate 2 orders of magnitude lower (5.24×10^3 e$^-$/cp/s). Thus, considering external factors and with the baseline parameters chosen, DIET is more favourable than hydrogen-MIET, but substantially less favourable than formate MIET.

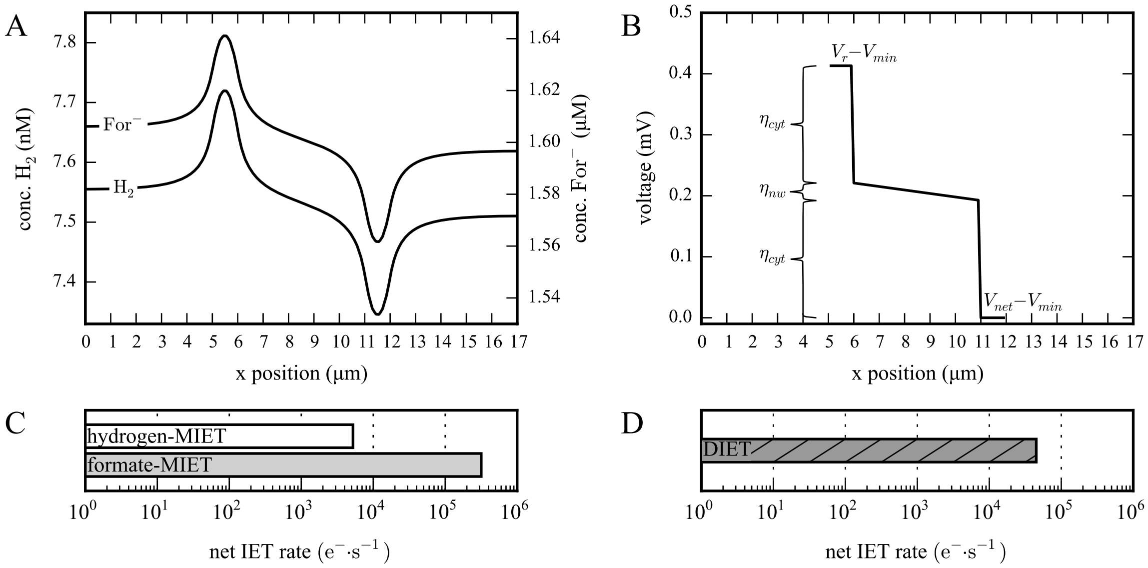

Figure 3.2: A: mediator profiles along the centre of the domain (x-axis at $L_y/2$, $L_z/2$) for formate- and hydrogen-MIET, for the default parameter set. B: DIET voltage and losses along the nanowire, default parameter set. Note that η_{mig} (solution resistance due to migration) is negligible compared to other losses. C and D: net IET rates for MIET and DIET, respectively, default parameter set.

The main reason formate-MIET allows a greater transfer rate than hydrogen-MIET (figure 3.2C) is because it allows a larger concentration gradient while maintaining feasible thermodynamics (figure 3.2A), despite the higher diffusion coefficient of hydrogen. This aligns well with previous analysis (Boone et al., 1989; Batstone et al., 2006).

Role of redox complex transfer rate

DIET activation losses are strongly dependent on multiple parameters which have limited literature support, likely the most arguable value being the redox complex transfer rate constant (k_0). Reducing k_0 by a factor 10 (e.g., if redox complex-nanowire transfer is not 40 but only 4 times faster than redox complex-electrode, or if k_0 is tenfold lower than reported by (Okamoto et al., 2009)) makes activation voltage losses even more dominant (99.2% of total voltage losses) and lowers the feasibility for DIET to a rate lower than hydrogen-MIET (figure 3.3, case 2). Doubling the redox complex transfer rate constant almost doubles the IET rate, with activation losses responsible for 87% of the total voltage losses. It is not until k_0 is increased tenfold (e.g. as reported by Hartshorne et al. (2007)) that redox complex activation is no longer the only governing loss (57% of the total voltage losses, the remaining 43% attributed to Ohmic losses in the nanowire) and that the DIET rate approaches the formate-MIET rate (to 90%).

Effect of cytochrome count and distribution

From equation 3.11 it can be seen that the same effects as in subsection 3.3.1 can be obtained by varying $A_{act,cell}$ or c_{act} with the same factor instead of k_0. An increase of $A_{act,cell}$ could be justified by assuming a different larger size of the redox complex (e.g., Edwards et al. (2014)), a decrease by

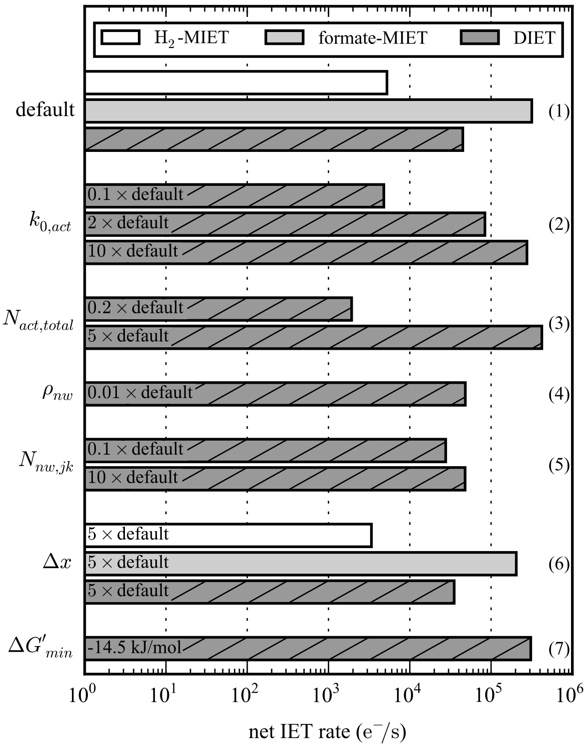

Figure 3.3: Sensitivity analysis for cell pair IET rates. The numbers on the right hand side indicate different parameter sensitivity studies (cases) and are referred to in the text. Note that case 1 shows the same data as figure 3.2C-D.

considering the cell surface not facing the other cell is unlikely to be used. Similarly, an increase in c_{act} is possible if redox complexes are preferentially located where electron transfer to nanowires occurs, instead of homogeneously distributed over the cell surface.

The amount of cytochromes on the cell surface ($N_{act,cell}$) governs both c_{act} and $A_{act,cell}$ and will therefore have an even stronger effect on the DIET rate than the same relative change in k_0, although the range through which $N_{act,cell}$ can be varied is smaller (for example, a tenfold increase in would result in an unrealistic 100% redox complex coverage). Reducing $N_{act,cell}$ by a factor 5 makes DIET less than half as feasible as hydrogen-MIET (figure 3.3, case 3), while increasing $N_{act,cell}$ by a factor 5 makes DIET thermodynamically more feasible than formate-MIET.

Nanowire resistivity

A small fraction of the total voltage losses for the default parameters is due to Ohmic losses in the nanowire. The resistivity (ρ_{nw}) used to determine Ohmic losses was measured for a biofilm (Malvankar et al., 2011), which means that the actual resistivity of an individual nanowire could be smaller. Reducing ρ_{nw} by 2 orders of magnitude (e.g., to the resistivity reported for individual nanowires in *Shewanella oneidensis* (El-Naggar et al., 2010)) causes a small increase in the DIET rate (figure 3.3, case 4), as the system is completely dominated by activation losses (99.9% of total voltage losses). Alternative nanowire conductivity models, such as electron hopping between redox components aligned along membrane vesicles as recently suggested to account for conduction in *Shewanella oneidensis* nanowires (Pirbadian et al., 2014) could be implemented in the model described here by considering a series of redox complex activation steps along the nanowire. The activation energy for a single step as calculated here, though, indicates that the standard activation rate constant k_0 for complex-complex transfer will need to be orders of magnitude higher than the k_0 used in this model for cytochrome hopping to be thermodynamically feasible.

Number of nanowires between a cell pair

The number of nanowires formed per cell pair ($N_{nw,pair}$) has a strong effect on the Ohmic loss (affecting the current per nanowire, $I_{jk}/N_{nw,pair}$, via equation 3.12) but no effect on activation losses (changes to the current per nanowire and $A_{act,j}$ cancel out), therefore a tenfold increase in $N_{nw,pair}$ will have the same effect as a tenfold decrease in ρ_{nw}. The range through which $N_{nw,pair}$ can be varied is different from the range for ρ_{nw}, however. The number of nanowires could be an order of magnitude lower or higher than the default value of 100. If 10 nanowires are formed per cell pair, the DIET rate changes to 60% of the original value, while 1000 nanowires per cell pair would result in an IET rate 107% of the default rate (figure 3.3, case 5) as the system is fully dominated by activation losses.

Interspecies distance (Δx)

Increasing interspecies distance (Δx) to 25 µm limits the DIET rate by increasing Ohmic losses but does not affect the redox complex activation losses, while for MIET the concentration gradient and thereby the diffusion flux is lowered. The model shows that a 5 times larger Δx attenuates MIET more than DIET, as DIET activation losses remain dominant (75% of the total voltage losses), resulting in a rate 80% of the original rate, while both MIET rates drop to 65% of the original rate (figure 3.3, case 6). This suggests DIET might be a thermodynamically more feasible alternative to MIET for disperse communities limited by diffusion, which is contrary to experimental observations where nanowire-DIET is commonly observed in dense aggregates (Summers et al., 2010; Rotaru et al., 2014a), possibly indicating that co-evolution and co-metabolism are more important than external limitations in this system. Use of non-organic conductive elements such as activated carbon (Liu et al., 2012) and magnetite (Cruz Viggi et al., 2014) could reduce resistivity, and leave only activation losses (though these will likely be increased), possibly making long-range transport even more feasible.

Importance of cell metabolism efficiency

The work done here only considers external limitations, and does not consider that there are energetic losses involved in translation of electrons to an electron mediator as assessed by (Nagarajan et al., 2013). Metabolic modelling indicated that the cell metabolism for DIET is more efficient than for MIET, justifying a less negative value for $\Delta G'_{min}$ (resulting in a smaller V_{min}). Comparing formate-MIET at a $\Delta G'_{min} = -15.2\ \mathrm{kJ\,mol^{-1}}$ per cell to DIET at a slightly less negative $\Delta G'_{min}$ values (e.g., $-14.5\ \mathrm{kJ\,mol^{-1}}$, see figure 3.3, case 7), suggests that for IET rates reported in this work ($10^4 - 10^5\ \mathrm{e^-/cp/s}$) a slightly more efficient metabolism for DIET is enough for the rate to match the formate-MIET rate. This result is important, since it suggests that comparative external electron transfer feasibility (sometimes resulting in order of magnitude different rates) can be compensated for by very slight advantages in cellular metabolism and hence cellular maintenance energy.

In conclusion, using the parameters estimated from literature published to date, the maximum rate for which thermodynamics are still feasible is considerably higher for formate-MIET than nanowire-DIET, which in turn is higher than hydrogen-MIET. A sensitivity analysis shows that for nanowire-DIET to be more feasible than formate-MIET, a slightly more efficient metabolism must be present, or the redox complex activation parameters must be considerably different from the baseline parameters used.

3.3.2 Multicellular system

The multicellular system was implemented to demonstrate application of the two-cell principles in a multicellular system, and identify whether a three-dimensional field with multiple sources and sinks would result in a different overall transfer rate. Experimentally observed systems analogous to this model include *Geobacter metallireducens/Methanosaeta harundinacea* (Rotaru et al., 2014b) and *Geobacter metallireducens/Methanosarcina barkeri* (Rotaru et al., 2014a), both of which degrade ethanol to methane, a conversion that is analogous to propionate oxidation but with more favourable thermodynamics.

Results are shown in figure 3.4 and represent simultaneously electron transfer rate between cells (coloured links), as well as overall migration potential field in two planes (coloured sections). While the migration potential field and the resulting losses $\eta_{mig,jk}$ are not limiting electron transfer, it does indicate that the potential field is governed mainly by interacting pairs. The results indicate that a multicellular system achieves slightly lower DIET rates per cell (on average 15% lower, $r_{X,j} = 38.2 \times 10^3$ versus 44.9×10^3 $e^- s^{-1}$). Rates depend strongly on the local species distribution. The highest IET rate is obtained by cell a in figure 3.4 (71.0×10^3 e^-/s). This is one of the methanogens surrounded by the most acetogens (six), which are all in turn connected to fewer methanogens. The lowest rate achieved is 13.4×10^3 e^-/s for cell b in figure 3.4, one of the acetogens connected to methanogen a, but no other methanogens. MIET rates are not affected by the larger community (the average rate is 2% higher than for the cell pair system).

The decrease in DIET rate is due to increased activation losses and electron balancing in the network. Despite the lower average IET rate, the average activation loss per cell pair increases (from 0.38 to 0.40 mV; 93% to 97% of total voltage losses), while Ohmic losses is almost 3 times lower due to the slightly lower IET rate and many additional nanowires formed per cell (on average, $N_{nw,j} = 291$ for the multicellular system, compared to $N_{nw,j} = N_{nw,pair} = 100$ for the cell pair system).

These results suggest communities capable of DIET achieve rates lower than the cell pair system, showing that formate-MIET remains thermodynamically more favourable compared to DIET for multicellular communities using the baseline parameter set chosen. It should be emphasised, however,

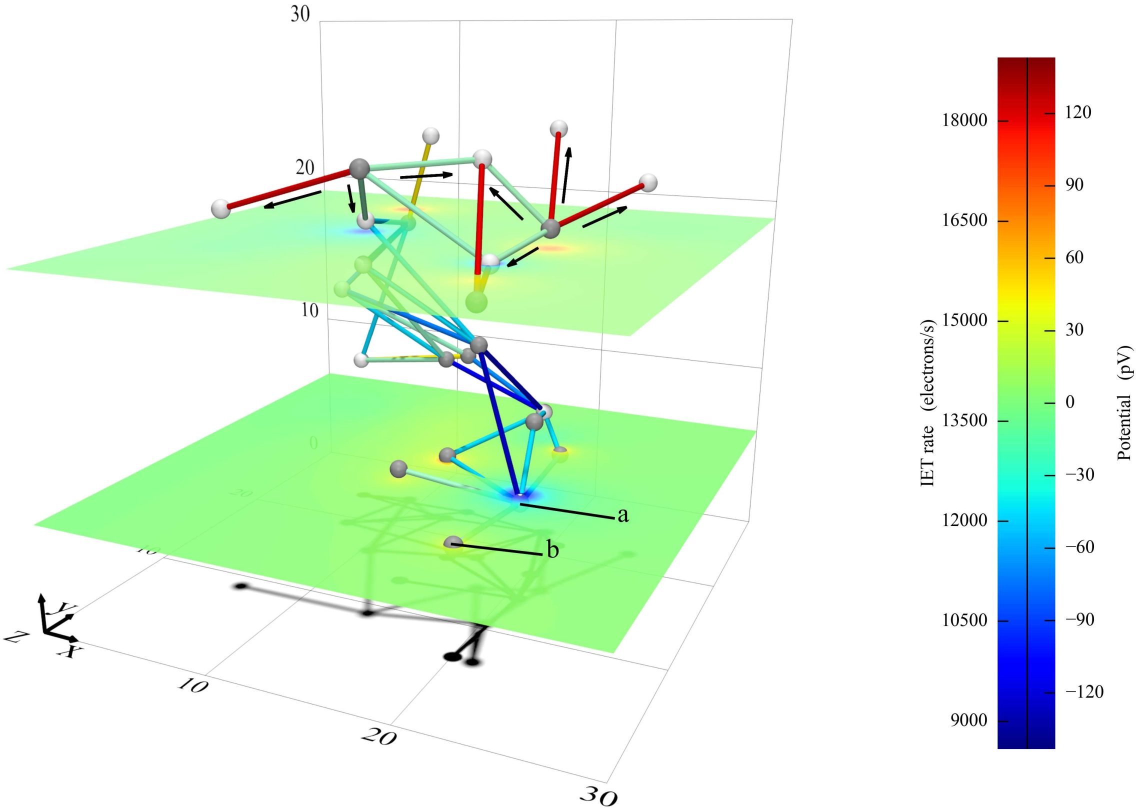

Figure 3.4: Cell positions (dark grey spheres are acetogens, light grey spheres methanogens), nanowires (lines, colour shows IET rate through nanowire in e^{-}/s) and potential field due to migration (planes, colour shows potential in pV). Cell a achieves the highest IET rate, cell b the lowest. Arrows denote the direction in which electrons flow. A movie showing cell positions and potential fields from different angles is available in the supplementary material as Supplementary movie 17.

that DIET rates in the multicellular system can exceed the cell pair rates if activation losses become less dominant. For example, increasing k_0 by a factor 10 (parameter set from figure 3.3, case 2, simulation 3) increases the average cell IET rate to 309×10^3 e^{-}/s (10% higher than cell pair DIET).

3.4 Conclusions

Investigation of extracellular losses suggests formate-MIET is thermodynamically more favourable than hydrogen-MIET (2 orders of magnitude maximum achievable rate difference) and DIET using nanowires (1 order of magnitude rate difference), with both MIET modes limited by diffusion flux and DIET limited by redox complex activation losses. In order for DIET to achieve rates comparable to or higher than formate-MIET, the true value for cell-nanowire redox complex transfer rate constant (k_0), cell redox complex concentratiFon (c_{act}), area ($A_{act,cell}$) or count ($N_{act,cell}$) must be 5-10 times higher than estimated from literature published to date. Cellular metabolism may also readily compensate for a decreased favourability in external transfer feasibility (Nagarajan et al., 2013) with differences on the order of less than a $\mathrm{kJ\,mol^{-1}}$ per cell compensating for electrochemical limitations in DIET.

Chapter 4

MODELLING OF SHELL-SHAPED AGGREGATES IN ZERO-VALENT SULFUR MEDIATED ANAEROBIC OXIDATION OF METHANE

ABSTRACT

The formation of shell-shaped ANME-2/DSS aggregates in anaerobic oxidation of methane coupled to sulfate reduction (AOM/SR) was investigated through mathematical modelling. Thermodynamic calculations and diffusion-reaction modelling of an AOM/SR aggregate was done to investigate the feasibility of a recently reported zero-valent sulfur-mediated syntrophic process. Results show that (i) the concentration changes by less than 20% of the bulk concentrations throughout the aggregate; (ii) thermodynamics are non-limiting due to low reaction rates, acid dissociation and polysulfide precipitation and (iii) the role of the DSS species might be non-mutualistic. Based on these findings, an individual-based mechanical modelling framework was applied to model the formation of shell-shaped aggregates from a small inoculum. It was found that experimentally observed aggregate morphologies are readily reproduced when (i) cell-cell links are formed in the ANME-2 core, but are weak enough in the outer DSS shell to allow displacement of individual cells and (ii) the inoculum is shell-shaped or cells are evenly distributed throughout the inoculum. These results suggest zero-valent sulfur-mediated AOM/SR is a viable reaction mechanism and provide an explanation as to how a thermodynamically less feasible morphology is formed in an already constrained system.

4.1 INTRODUCTION

Anaerobic oxidation of methane coupled to sulfate reduction (AOM/SR) is a common process in deep sea sediments, where methane released from vents is oxidised through a biological process:

$$\mathrm{CH_4(aq) + SO_4{}^{2-} \longrightarrow HS^- + HCO_3{}^- + H_2O} \tag{1.7}$$

Microscopy and cultivation experiments have shown that an anaerobic methanotroph (ANME) and species of the genus *Desulfosarcina* or *Desulfococcus*, or of the family Desulfobulbaceae (for simplicity all abbreviated to DSS) are present in the aggregates found to facilitate AOM/SR. It has generally been assumed that ammonium oxidation takes place at the ANME species and sulfate reduction occurs at the DSS. However, thermodynamic calculations and diffusion-reaction modelling (Orcutt and Meile, 2008; Alperin and Hoehler, 2010) as well as experimental results (Sø rensen et al., 2001; Nauhaus et al., 2002; Knittel and Boetius, 2009) have not been able to identify the redox mediator compound used by these species, as is discussed in more detail in subsection 1.2.2.

A radically different mechanism has recently been proposed for AOM/SR in deep sea sediments (Milucka et al., 2012). Strong evidence is available suggesting that ANME-2 cells are able to convert both methane and sulfate to produce zero-valent sulfur, which is believed to be bound to bisulfide (HS^-) to form hydrodisulfide (HS_2^-):

$$7\,CH_4(aq) + 8\,SO_4^{2-} + 5\,H^+ \longrightarrow 4\,HS_2^- + 7\,HCO_3^- + 11\,H_2O \tag{1.8}$$

The hydrodisulfide is taken up and disproportionated by the DSS cells:

$$4\,HS_2^- + 4\,H_2O \longrightarrow SO_4^{2-} + 7\,HS^- + 5\,H^+ \tag{1.9}$$

The thermodynamic feasibility of this process has not been studied in more detail than in the original paper (Milucka et al., 2012) and transport limitation of this mechanism (e.g., as in Orcutt and Meile (2008)) has not yet been investigated.

Furthermore, fluorescent in-situ hybridisation (FISH) microscopy has shown that 60 to 70% of the total biomass catalysing the AOM/SR reactions is contained in well-organised shell-shaped aggregates, with an distinct inner layer of ANME-2 and an outer layer of DSS (Orphan et al., 2002; Nauhaus et al., 2007; Boetius et al., 2000; Knittel and Boetius, 2009; Schreiber et al., 2010; Dekas and Orphan, 2010). Considering this is a suboptimal organisation for the exchange of mediator compounds (as quantified by Alperin and Hoehler (2010)), an explanation for the formation of these typical aggregate morphologies is of interest. Thus far, the organisation into these aggregate has only been investigated using a rule-based division numerical model (Nauhaus et al., 2007), which is limited in that (i) division rules are enforced on a natural system, (ii) the effect of thermodynamics is not considered and (iii) the morphology seems to change for aggregates larger than 5 µm in diameter.

The thermodynamic feasibility of reactions 1.8 and 1.9 is studied in more detail in this chapter to find out the range of concentrations for which the reactions are feasible. A diffusion-reaction based model using this novel mechanism is set up to analyse transport limitations for typical shell-shaped aggregates. Concentration profiles in the granules computed with this model are compared to the feasible concentration range identified using the thermodynamic model. This also allows investigation into the role of DSS cells in AOM/SR aggregates. Using the outcomes of the transport model, a mechanical model based on the methods described in chapter 2 is used to investigate how a shell-shaped aggregate can develop.

4.2 MODEL DESCRIPTION

4.2.1 Thermodynamic feasibility of zero-valent sulfur mediated AOM/SR

Based on the local activities of the compounds involved in the ANME-2 and DSS reactions, the Gibbs free energy of reaction is calculated. As in Milucka et al. (2012), the concentration is replaced by activity to take into account non-ideal behaviour of the compounds. Gaseous compounds are not involved in the reaction, allowing equation 1.4 to be simplified to:

$$\Delta G_r' = \Delta G_r^0 + RT \ln Q \qquad \text{where } Q = \prod_i \left(a_i / a_{ref}\right)^{\nu_i} \tag{4.1}$$

Here, i refers to any compound involved in the reactions 1.8 and 1.9. Default concentrations used in thermodynamic calculations are given in table 4.1.

Reactions are thermodynamically feasible if the value of $\Delta G_r'$ is negative, but in reality have a minimum value to account for cell maintenance and anabolic reactions, as discussed in subsection 1.2.3. This means there is a cut-off value above which the ANME-2 and DSS cells do not survive. This value is most likely less negative than the value reported in chapter 3 due to the adaptation to lower growth rates of ANME-2 and DSS cells.

The concentration range for which the AOM/SR mechanism is feasible can be determined with these calculations. By comparing this range to the concentration profiles determined using transport modelling, the role of thermodynamic limitation in shell-shaped granules can be evaluated.

Table 4.1: Activity and Gibbs free energy of formation for AOM/SR thermodynamic calculations (values adapted from Milucka et al. (2012) and Haynes (2014))

Compound	Symbol	a (mol L^{-1})	ΔG_f^0 (kJ mol^{-1})
methane	CH_4	1.74×10^{-3}	−34.39
sulfate	$SO_4{}^{2-}$	2.71×10^{-3}	−744.6
proton	H^+	3.16×10^{-8}	0
bicarbonate	$HCO_3{}^-$	1.14×10^{-2}	−586.8
bisulfide	HS^-	2.0×10^{-4}	12.05
hydrodisulfide	$HS_2{}^-$	9.5×10^{-6}	20.2
water	H_2O	0.982	−237.18

4.2.2 Diffusion-reaction model

A diffusion-reaction model is set up to calculate the concentration of the various substrates and products throughout the aggregate. Commonly found shell-shaped aggregates are around 25 µm in diameter (Boetius et al., 2000; Orphan et al., 2002; Nauhaus et al., 2007; Dekas et al., 2009). *In vitro* experiments have shown that the ANME-2 and DSS shells are roughly the same volume (Nauhaus et al., 2007), such that the radius of the inner ANME-2 core is 0.8 times the radius of the aggregate. A spherical boundary layer of 10 µm is assumed, corresponding to 1×10^8 aggregates per mL, each with a radius of roughly 3 µm (Treude et al., 2003; Knittel et al., 2003).

A schematically drawn section of a typical AOM/SR aggregate with an outer radius of 12.5 µm is shown in figure 4.1. The aggregate is spherically symmetrical and can therefore be modelled as a one-dimensional system using spherical coordinates along the line in the figure.

It is assumed that the concentration profiles are governed by Fick's second law of diffusion at steady state, equation 1.12, since convective transport would be strongly limited in the densely packed aggregate. The values for diffusion constants D_i are given in table 4.2. The volume-specific rate r_i in the equation is made up by a biological, an acid dissociation and a precipitation component ($r_i = r_{X,i} + r_{a,i} + r_{s,i}$).

Biochemical reactions

The biological rate r_X at which catabolic reactions 1.8 and 1.9 take place is derived from the specific growth rate (around $\mu = 0.003\,\text{day}^{-1}$) at a biomass yield of 0.01 Cmol biomass per mol CH_4 (Nauhaus

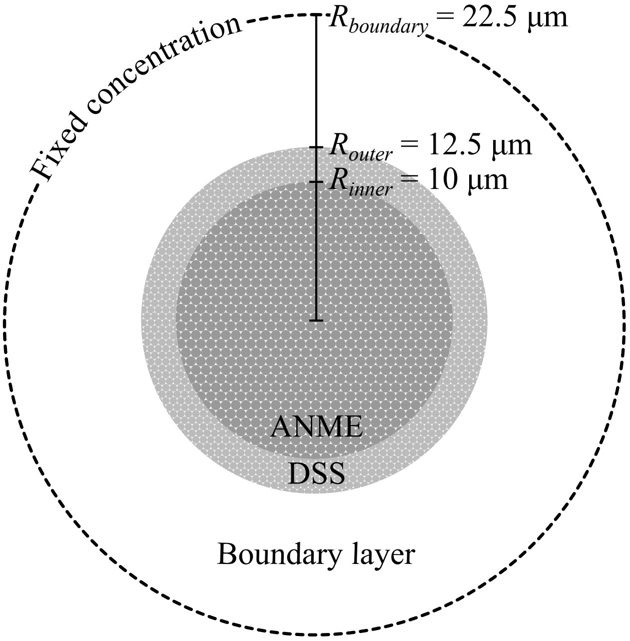

Figure 4.1: Schematic representation of a section along the centre of an aggregate with a radius 12.5 µm. The one-dimensional diffusion-reaction model is defined along the line. Note that individual cells drawn in the ANME and DSS shells are not to size.

Table 4.2: Model parameters for AOM/SR diffusion-reaction simulations. The full list of model parameters is available in appendix F.

Parameter	Symbol	Default value	Units	Reference
Boundary concentrations				
methane	$c_{0,\mathrm{CH_4}}$	1.50×10^{-3}	$\mathrm{mol\,L^{-1}}$	Table S3 in Milucka et al. (2012)
sulfate	$c_{0,\mathrm{SO_4}^{2-}}$	15.9×10^{-3}	$\mathrm{mol\,L^{-1}}$	Table S3 in Milucka et al. (2012)
proton	$c_{0,\mathrm{H^+}}$	1.00×10^{-7}	$\mathrm{mol\,L^{-1}}$	Table S3 in Milucka et al. (2012)
bicarbonate	$c_{0,\mathrm{HCO_3}^-}$	2.06×10^{-2}	$\mathrm{mol\,L^{-1}}$	Table S3 in Milucka et al. (2012)
bisulfide	$c_{0,\mathrm{HS^-}}$	8.40×10^{-4}	$\mathrm{mol\,L^{-1}}$	Calculated from acid diss. and spec.
hydrodisulfide	$c_{0,\mathrm{HS_2}^-}$	1.46×10^{-5}	$\mathrm{mol\,L^{-1}}$	Table S3 in Milucka et al. (2012)
Biomass properties				
specific growth rate	μ	–	$\mathrm{day^{-1}}$	via Monte-Carlo analysis
biomass yield	$Y_{X,S}$	0.01	$\mathrm{Cmol\,mol^{-1}}$	Nauhaus et al. (2007)
biomass concentration	c_X	30.4×10^3	$\mathrm{Cmol\,m^{-3}}$	
Aggregate geometry				
radius inner core	R_{inner}	$0.8 \times R_{outer}$	m	Nauhaus et al. (2007)
radius outer shell	R_{outer}	–	m	via Monte-Carlo analysis
radius boundary layer	$R_{boundary}$	$R_{outer} + 10\,\mathrm{\mu m}$	m	Treude et al. (2003); Knittel et al. (2003)
Acid dissociation constants				
carbon dioxide	$K_{a,\mathrm{CO_2}}$	4.47×10^{-7}	$\mathrm{mol\,L^{-1}}$	Haynes (2014)
hydrogen sulfide	$K_{a,\mathrm{H_2S}}$	1.48×10^{-7}	$\mathrm{mol\,L^{-1}}$	Schwarzenbach and Fischer (1960)
bisulfide	$K_{a,\mathrm{HS^-}}$	1.00×10^{-14}	$\mathrm{mol\,L^{-1}}$	Schwarzenbach and Fischer (1960)
hydrodisulfide	$K_{a,\mathrm{HS_2}^-}$	2.00×10^{-10}	$\mathrm{mol\,L^{-1}}$	Schwarzenbach and Fischer (1960)
Precipitation constants				
disulfide	$K_{s,\mathrm{S_2}^{2-}}$	3.47×10^{-12}	$\mathrm{mol\,L^{-1}}$	Kamyshny, Jr. et al. (2004)
Diffusion coefficients				
methane	$D_{\mathrm{CH_4}}$	1.84×10^{-9}	$\mathrm{m^2\,s^{-1}}$	Haynes (2014)
sulfate	$D_{\mathrm{SO_4}^{2-}}$	1.07×10^{-9}	$\mathrm{m^2\,s^{-1}}$	Haynes (2014)
proton	$D_{\mathrm{H^+}}$	9.31×10^{-9}	$\mathrm{m^2\,s^{-1}}$	Haynes (2014)
carbon dioxide	$D_{\mathrm{CO_2}}$	1.91×10^{-9}	$\mathrm{m^2\,s^{-1}}$	Haynes (2014)
bicarbonate	$D_{\mathrm{HCO_3}^-}$	1.19×10^{-9}	$\mathrm{m^2\,s^{-1}}$	Haynes (2014)
bisulfide	$D_{\mathrm{HS^-}}$	2.49×10^{-9}	$\mathrm{m^2\,s^{-1}}$	Wilke and Chang (1955); Albright (2008)
hydrodisulfide	$D_{\mathrm{HS_2}^-}$	1.70×10^{-9}	$\mathrm{m^2\,s^{-1}}$	Wilke and Chang (1955); Albright (2008)

et al., 2007). By taking cells to be spherical, the closest packing that can be achieved in aggregates is 74%, which with a biomass density of $1010\,\mathrm{kg\,m^{-3}}$ and a biomass composition of $CH_{1.8}O_{0.5}N_{0.2}$ gives a molar biomass concentration of $c_X = 30.4 \times 10^3\,\mathrm{Cmol\,m^{-3}}$. Given the specific growth rate, yield, biomass concentration and methane stoichiometry (via reaction 1.8), the catabolic rate in the ANME-2 shell can be calculated for any growth rate μ via $r_X = c_X\mu / \left(\nu_{ANME,\mathrm{CH_4}} Y_{X,S}\right)$. It is assumed that reaction 1.9 taking place at the DSS occurs at the same rate in the outer shell. Furthermore, the influence of anabolic substrates and products is disregarded and it is assumed that maintenance energy is already taken into account via the biomass yield.

Acid dissociation occurs throughout the entire domain. The rate at which these reactions occur is generally much higher than for biological reactions (order of seconds versus months). Therefore, it is assumed that acid dissociation reactions are at all times in equilibrium (as in chapter 3):

$$\mathrm{H_2S_n} \rightleftharpoons \mathrm{HS_n}^- + \mathrm{H}^+ \tag{4.2a}$$

$$\mathrm{HS_n}^- \rightleftharpoons \mathrm{S_n}^{2-} + \mathrm{H}^+ \tag{4.2b}$$

$$\mathrm{CO_2(aq)} + \mathrm{H_2O(l)} \rightleftharpoons \mathrm{HCO_3}^- + \mathrm{H}^+ \tag{4.2c}$$

S_n^{2-}, HS_n^- and H_2S_n denote (poly)sulfide, hydro(poly)sulfide and hydrogen (poly)sulfide, respectively, and can have between 1 and 8 sulfur atoms and ions (Kamyshny, Jr. et al., 2004). The polysulfide compounds ($n > 2$) are here distinguished from sulfide compounds, (sulfide S^{2-}, bisulfide HS^- and hydrogen sulfide H_2S). Sulfate (SO_4^{2-}) and sulfuric acid are excluded from the acid dissociation reactions because of the very low pK_a of sulfuric acid.

Besides acid dissociation, precipitation takes place in the aggregates and surrounding medium. The different polysulfides are in equilibrium with each other, as governed by the reaction (Kamyshny, Jr. et al., 2004):

$$\mathrm{HS}^- + \frac{(\mathrm{n}-1)}{8}\mathrm{S_8(s)} \rightleftharpoons \mathrm{S_n}^{2-} + \mathrm{H}^+ \tag{4.3}$$

Precipitation reactions are much faster than biological reactions, taking place in a number of seconds (Kamyshny, Jr. et al., 2003). Therefore, as with acid dissociation, equilibrium is assumed to be satisfied at all times in the model.

Model implementation

By simplifying the three-dimensional geometry in figure 4.1 to the one-dimensional spherical geometry, the computation time is reduced drastically, allowing a Monte-Carlo analysis to be conducted with 1000 simulations.

Based on these equilibrium reactions and assuming the concentrations for water and octasulfur ($S_8(s)$) are unity everywhere and do not change, the following equilibrium conditions are set for acid dissociation and precipitation:

$$r_{a,\mathrm{H_2S_n}} = r_{a,max}\left(1 - \frac{c_{\mathrm{HS_n}^-}c_{\mathrm{H^+}}}{K_{a,\mathrm{H_2S_n}}c_{\mathrm{H_2S_n}}}\right) \qquad \text{for } 1 \leq n \leq 8 \tag{4.4a}$$

$$r_{a,\mathrm{HS_n}^-} = r_{a,max}\left(1 - \frac{c_{\mathrm{S_n}^{2-}}c_{\mathrm{H^+}}}{K_{a,\mathrm{HS_n}^-}c_{\mathrm{HS_n}^-}}\right) \qquad \text{for } 1 \leq n \leq 8 \tag{4.4b}$$

$$r_{a,\mathrm{CO_2}} = r_{a,max}\left(1 - \frac{c_{\mathrm{HCO_3}^-}c_{\mathrm{H^+}}}{K_{a,\mathrm{CO_2}}c_{\mathrm{CO_2}}}\right) \tag{4.4c}$$

$$r_{a,\mathrm{S_n}^{2-}} = r_{s,max}\left(1 - \frac{c_{\mathrm{S_n}^{2-}}c_{\mathrm{H^+}}}{K_{s,\mathrm{S_n}^{2-}}c_{\mathrm{HS^-}}}\right) \qquad \text{for } 2 \leq n \leq 8 \tag{4.4d}$$

For $n = 1$, equation 4.3 is equivalent to acid dissociation reaction 4.2b, such that precipitation reactions only occur only for the polysulfides $n = 2$ through 8.

Rewriting Fick's second law (equation 1.12) to spherical coordinates, and taking the polar (θ) and azimuthal angle (ϕ) to be constant yields Fick's second law for a spherically symmetric system:

$$0 = r_i + D_i\left(\frac{1}{R^2}\frac{\partial\left(R^2\frac{\partial c}{\partial R}\right)}{\partial R}\right) \tag{4.5}$$

To solve this efficiently and implement it in the finite element analysis tool, the equation 4.5 is rewritten by multiplying with R^2:

$$0 = R^2 r_i + \frac{D_i\partial\left(R^2\frac{\partial c}{\partial R}\right)}{\partial R} \tag{4.6}$$

The numerical method is implemented using a finite element analysis software package (COMSOL Multiphysics 4.4, COMSOL Inc., Burlington, MA) and solved for steady state. Boundary concentrations as described by Milucka et al. (2012) are used, with the exception that the bisulfide concentration is calculated from the acid dissociation and polysulfide precipitation equilibrium reactions. Diffusion coefficients in the aggregate are assumed to be one fourth of those in water (Stewart, 2003). Diffusion coefficients for the polysulfides, hydropolysulfides and hydrogen polysulfides are not available in literature and are therefore calculated using the Wilke-Chang relation (Wilke and Chang, 1955), with the molar volume estimated using LeBas additive volumes method (Albright, 2008). The most important model parameters are given in table 4.2, the full list of parameters is available in the supplementary material (appendix F).

Monte-Carlo analysis

Both the radius of aggregates and the rate at which reactions occur can vary strongly for different aggregates and habitats (Knittel and Boetius, 2009). To take the combined effect of both variations into account, a Monte-Carlo analysis is conducted and the 95% prediction interval is determined for compounds involved in the reaction. Concentration profiles are estimated from 1000 simulations by varying the outer radius R_{outer} and growth rate μ in MATLAB (R2014b, The MathWorks, Natick, MA).

The distribution of the outer radius R_{outer} of the aggregate is modelled as an F-distribution and is scaled to a mode of 12.5 µm. While an outer radius of 75 µm has been reported in one study (Orphan et al., 2002), most literature reports that the largest aggregates observed are considerably smaller (e.g., (Boetius et al., 2000) reports the maximum cell count observed is around 10,000 cells, which would correspond to an aggregate with a radius of roughly 12 µm). It is therefore assumed that a radius of 75 µm is rare, and the degrees of freedom for the F-distribution are chosen such that the 99 percentile is at 75 µm.

The specific growth rate of the aggregate μ is believed to be around 0.003 day^{-1} (Nauhaus et al., 2007), with values as low as 0.001 day^{-1} and as high as 0.012 day^{-1} reported in literature (Dale et al., 2006; Zhang et al., 2014). It is assumed that the growth rates of ANME-2 and DSS are coupled (Milucka et al., 2012). Parameters for the F-distribution used to generate specific growth rates are chosen such that the mode is at 0.003 day^{-1} and the 90 percentile at 0.012 day^{-1}.

Both distributions with parameters for scale and degrees of freedom are shown in appendix G.

4.2.3 Individual-based mechanical model

Development of an AOM/SR aggregate is simulated using a three-dimensional mechanical model iteratively solving cell growth, division and relaxation of the individual cells, as shown in figure 2.2. The same method is used in this chapter, with changes made to the inoculum generation, cell-cell interactions and model parameters.

Inoculum

Individual ANME-2 cells in shell-type aggregates are usually found to be cocci (spherical cells) with a diameter around 0.5 µm (Boetius et al., 2000; Nauhaus et al., 2002, 2007). Most commonly, the DSS observed are cocci of 0.3-0.5 µm in diameter, or roughly one third to half the volume of the ANME cells (Nauhaus et al., 2007; Knittel and Boetius, 2009; Schreiber et al., 2010; Milucka et al., 2012). In the model, ANME cells are modelled as spheres with a minimum cell diameter $d_{min} = 0.44$ µm and a maximum $d_{max} = 0.55$ µm and DSS cells as spheres with a diameter of 0.35-0.44 µm, half the volume of an ANME cell. The cell mass is related to the diameter via the cell density and volume, as discussed in chapter 2.

The default inoculum consists of 6 ANME-2 and 12 DSS cells. The ANME-2 cells are randomly positioned within 0.7 µm of the centre, partially surrounded by the DSS cells 0.9 µm from the centre. The initial cell mass is chosen randomly such that the cell diameter is between d_{min} and d_{max}.

Table 4.3: Model parameters for AOM/SR mechanical model.

Parameter	Symbol	Default value	Units	Reference
Sticking links				
Spring constant ANME-ANME	$k_{s,s,ANME-ANME}$	1×10^{-12}	$\mathrm{N\,m^{-1}}$	
Spring constant ANME-DSS	$k_{s,s,ANME-DSS}$	1×10^{-15}	$\mathrm{N\,m^{-1}}$	
Spring constant DSS-DSS	$k_{s,s,DSS-DSS}$	1×10^{-15}	$\mathrm{N\,m^{-1}}$	
Formation limit	$d_{s,form}$	0.5	µm	
Stretch limit	$d_{s,break}$	1	µm	
Collission response				
Cell-cell collision spring constant	$k_{c,c}$	1×10^{-10}	$\mathrm{N\,m^{-1}}$	
Cell-substratum collision spring constant	$k_{c,s}$	1×10^{-10}	$\mathrm{N\,m^{-1}}$	
Other relaxation parameters				
Relaxation time step	Δt_{rel}	1	s	
Velocity damping coefficient	k_d	1×10^{-13}	$\mathrm{N\,s\,m^{-1}}$	
Cell geometry)				
Minimum cell diameter ANME	$d_{min,ANME}$	0.218	µm	
Maximum cell diameter ANME	$d_{max,ANME}$	0.275	µm	
Minimum cell diameter DSS	$d_{min,DSS}$	0.175	µm	
Maximum cell diameter DSS	$d_{max,DSS}$	0.220	µm	
Growth				
Growth time step	Δt_{growth}	1	week	
Growth rate coefficient for fil. form.	μ	0.003	$\mathrm{day^{-1}}$	
Growth rate coefficient for floc form.	μ	0.003	$\mathrm{day^{-1}}$	
Other parameters				
Biomass density	ρ	1010	$\mathrm{kg\,m^{-3}}$	
Cell count inoculum	$N_{cell,init}$	18	–	

Cell-cell forces

The forces taken into account for the AOM/SR system are:

- cell-cell sticking (EPS)
- cell-cell anti-collision
- velocity damping

Cell-cell sticking links (linear springs described by Hooke's law, equation 2.1) are formed when the distance between the cell surfaces is less than 0.1 µm and broken when the spring length exceeds the rest length by more than 0.5 µm. To account for the smaller cells compared to chapter 2, the spring constant for sticking links is decreased to $1 \times 10^{-12}\,\mathrm{N\,m^{-1}}$. In the default case, only ANME-ANME sticking links are formed. The full list of parameters is given in table 4.3.

4.3 RESULTS AND DISCUSSION

4.3.1 Thermodynamic feasibility of zero-valent sulfur mediated AOM/SR

Thermodynamic calculations show that only the bisulfide and hydrodisulfide activity can limit thermodynamics under reasonable assumptions. Methane or sulfate activity at the ANME would need to be in the 100 nM range to result in values close to the minimum Gibbs free energy threshold (Orcutt and Meile, 2008; Stams and Plugge, 2009), while even for a very high activity of bicarbonate hardly affects the feasibility of the reactions. A local p*H* less than 6 results in unfeasible thermodynamics for the DSS reaction, but previous work (e.g., chapter 3) suggests carbonate concentration is sufficient to buffer local p*H* changes, as confirmed by diffusion-reaction modelling presented later in this chapter. Furthermore, the p*H* used for these calculations is already lower than measured in many natural systems (Knittel and Boetius, 2009).

Bisulfide is not involved in the reaction taking place at the ANME-2 cell, but the bisulfide activity has a strong effect on the feasibility of the DSS and limits thermodynamics when it is increased to the 10 mM range (ten times the boundary concentration), as shown in figure 4.2. The concentration differences between the bulk and the DSS cell (black isolines) provide information on the maximum flux via Fick's first law, equation 1.10. The conditions assumed for thermodynamic calculations in Milucka et al. (2012) shows the reactions are thermodynamically moderately feasible, even if the concentration at the DSS is higher to account for the flux required to remove the produced bisulfide.

The activity of hydrodisulfide affects thermodynamic feasibility at the ANME and the DSS. As long as the activity of hydrodisulfide at the DSS remains lower than 0.1 mM (ten times the boundary concentration), the catabolic reaction taking place at the DSS is less feasible than the reaction at the ANME. For the DSS thermodynamics to become unfeasible, the hydrodisulfide activity must be less than 0.1 µM (one-hundredth of default), whereas the ANME reaction remains feasible even at higher hydrodisulfide concentrations, as shown in figure 4.3.

These thermodynamic calculations show that concentrations throughout the aggregate would need to vary by an order of magnitude for reactions 1.8 and 1.9 to become unfeasible.

The boundary concentrations for bisulfide and hydrodisulfide used by Milucka et al. (2012) do not satisfy the precipitation and acid dissociation equilibria defined by equations 4.2a, 4.2b and 4.3. If the bisulfide activity is taken from this paper ($2 \times 10^{-4}\,\mathrm{mol\,L^{-1}}$) and the hydrodisulfide concentration is adjusted to satisfy the equilibrium equations ($4.2 \times 10^{-6}\,\mathrm{mol\,L^{-1}}$), the thermodynamic feasibility of the DSS catabolism is reduced by 15% to $-45.7\,\mathrm{kJ\,mol^{-1}}$. If the hydrodisulfide activity is taken from the paper ($9.5 \times 10^{-6}\,\mathrm{mol\,L^{-1}}$) and the bisulfide concentration adjusted, the feasibility is reduced by 30% to $-36.4\,\mathrm{kJ\,mol^{-1}}$. Both values are expected to be sufficiently negative for the cell reactions to yield enough energy for maintenance and anabolism.

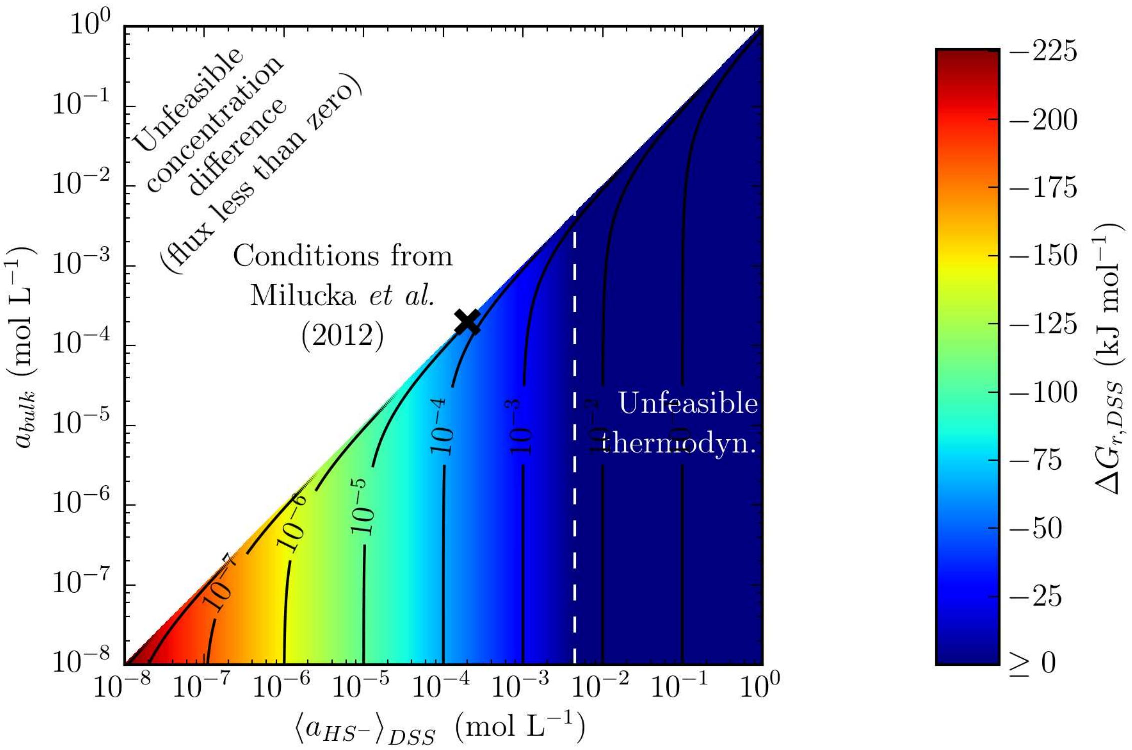

Figure 4.2: Thermodynamic feasibility of DSS reaction 1.9 over a range of bisulfide activities at the cell and bulk liquid. Black lines denote concentration difference (assuming activity *a* equals concentration *c*) and are proportional to flux via Fick's law, equation 1.10.

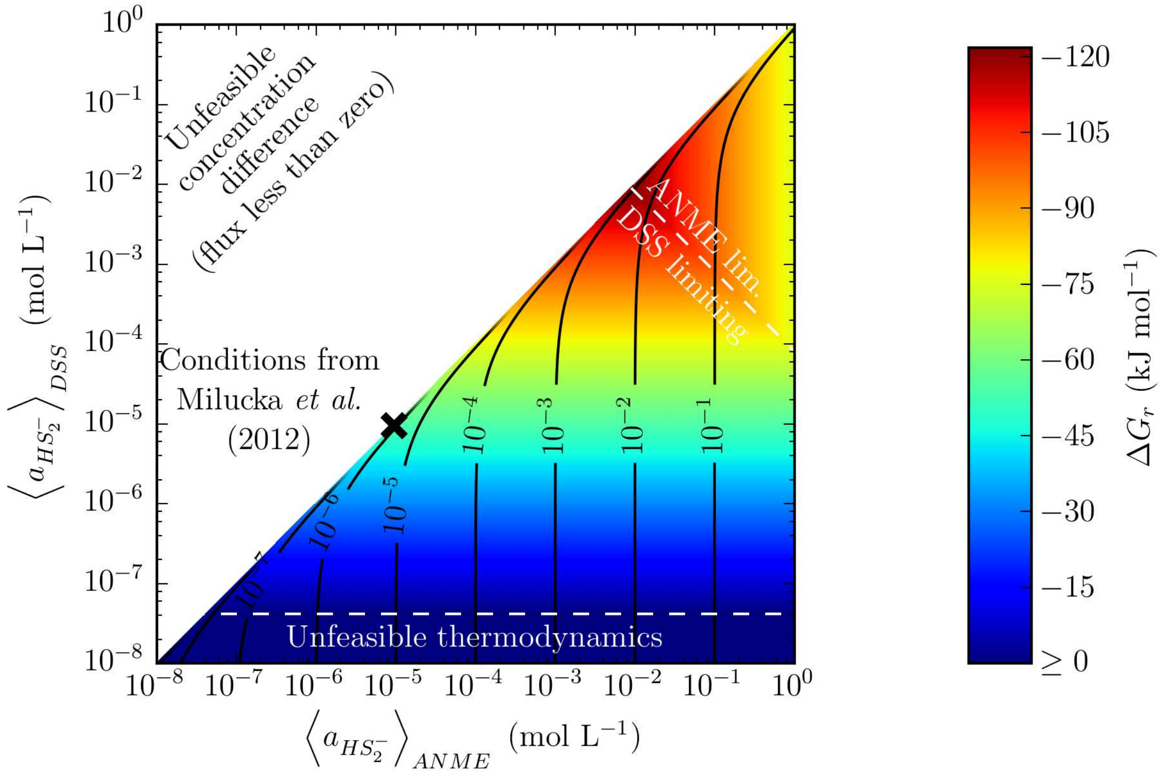

Figure 4.3: Thermodynamic feasibility of ANME and DSS reactions 1.8 and 1.9 over a range of hydrodisulfide activities. Colour denotes the least feasible reaction ($\min(\Delta G_{r,ANME}, \Delta G_{r,DSS})$). Black lines denote concentration difference and are proportional to flux via equation 1.10.

4.3.2 Chemical transport and reaction in AOM/SR aggregates

Using the reaction-diffusion model, it was found that concentration gradients are flat enough for all compounds involved in the AOM/SR reactions to be well within the thermodynamically feasible range reported in subsection 4.3.1 (see figure 4.4). The thermodynamic feasibility of the ANME-2 and DSS reactions is most sensitive to compounds of which the relative concentration changes strongly, as stated by the Gibbs free energy, equation 4.1. Compounds present at a the lowest concentration and used in the biological reaction are protons (H^+, pH), hydrodisulfide (HS_2^-) and bisulfide (HS^-), respectively, making these compounds of critical importance for the analysis. The pH is buffered by the high CO_2/HCO_3^- concentration in the system, leading to pH fluctuations of less than 0.05 throughout the domain (figure 4.4A) for 95% of the simulated cases. Similarly, precipitation and acid dissociation buffer the concentrations of hydrodisulfide and bisulfide so that concentration changes are less than 15% (figure 4.4B, C). Of the unbuffered compounds, methane is most likely to be limited based on reaction stoichiometry and boundary concentrations (reactions 1.8 and 1.9; table 4.2). In figure 4.4D and E it is shown that despite the lack of buffer reactions, the methane concentration profile for the default case does not change by more than 20% of the boundary concentration.

Role of DSS

Aggregates consisting only of ANME-2 have been observed as well (Orphan et al., 2002; Knittel and Boetius, 2009). A Monte-Carlo analysis without the outer shell has been conducted, showing that in the absence of the DSS shell (without changing the size of the ANME-2 core), the concentration gradient of all compounds throughout the aggregate is more flat (figure 4.4G, H and figure H.1). This suggests that the relation between both species is not of a purely mutualistic nature as presented in literature (e.g., Hoehler et al. (1994)), but that the presence of DSS cells in the aggregate might also have negative effects on the ANME-2 feasibility.

Although the DSS cells take up hydrodisulfide, the concentration of hydrodisulfide is lower when only ANME-2 cells are present in the aggregates (figure 4.4). The biological reaction at the DSS takes up 4 mol HS_2^- per mol reaction, simultaneously producing 7 mol HS^- (see equation 1.9) which via precipitation reaction 4.3 is converted to 7 mol polysulfide compounds, thereby producing a net amount of 3 mol polysulfides per mol reaction.

In order to further investigate the role of the DSS, the mechanism via which precipitation takes place must be further developed. Currently, the sulfur concentration is assumed to be constant (octasulfur is an infinite source/sink, i.e., the $S_8(s)$ concentration is constant). In the presence of DSS in the model, octasulfur is used to produce polysulfides from bisulfide. In the absence of DSS in the model, part of the produced hydrodisulfide precipitates to form octasulfur. In reality, the absence of DSS will result in accumulation of octasulfur near the ANME-2 species over time. By implementing precipitation modelling and modelling octasulfur as a finite reservoir, the exact nature of the symbiotic relationship between ANME-2 and DSS can be further quantified.

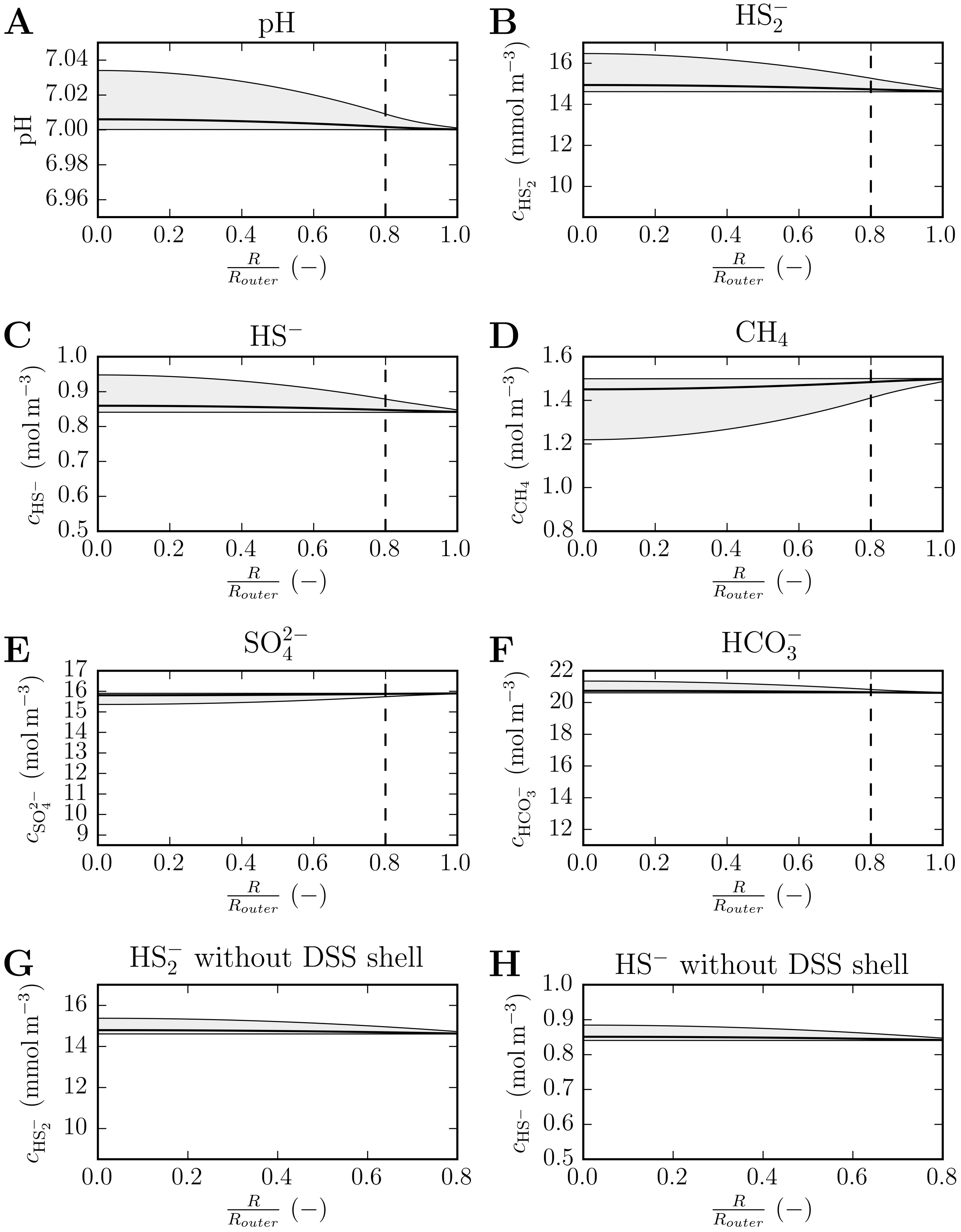

Figure 4.4: Average concentration profiles from the centre of the aggregate to the outer surface for the compounds involved in the AOM/SR reactions as determined by varying R_{outer} and μ using a Monte-Carlo analysis. (A-F) for the default case; (G-H) without an outer DSS shell. The dashed vertical line represents the boundary between the ANME-2 core and the DSS shell. The shaded area in the graphs represents the 95% prediction interval. The position along the radius R is normalised using R_{outer}.

Conclusions

The results obtained with the Monte-Carlo analysis suggest that diffusion limitation does not play an important role in aggregates that use zero-valent sulfur as an intermediate. Concentrations at the centre of the aggregates varies by less than 20% of the boundary concentrations as a result of extremely low reaction rates combined with acid dissociation and polysulfide precipitation reactions. This is in stark contrast to simulations done with other reaction mechanisms (Orcutt and Meile, 2008). Therefore, transport and thermodynamic limitations are not taken into account when calculating growth rates in the individual-based mechanical model to further investigate the formation of shell-shaped aggregates.

4.3.3 Mechanical modelling of shell-shaped aggregate formation

An ANME-2/DSS cell community is simulated using the method described in subsection 4.2.3, assuming growth rates of individual cells are randomly distributed around $0.003\,\mathrm{day}^{-1}$ with a standard deviation of 20%. Using an inoculum of 18 cells with an inner layer of ANME-2, an outer layer of DSS and only ANME-ANME sticking links, a shell-shaped aggregate develops consisting of an inner core of ANME-2 cells and a shell of DSS, as shown in figure 4.5A-F. The modelled aggregate morphology (J) shows the same distinct inner core consisting of ANME-2 cells, surrounded by an outer shell of DSS cells as observed using fluorescence *in-situ* hybridisation (FISH) microscopy, figure 4.5G. A shell-shaped aggregate is formed for all 15 simulations investigated, although holes in the outer shell can be larger towards the end of the simulation, similar to figure 4.5H and I.

The DSS cells initially (figure 4.5A) do not uniformly surround the ANME-2 cells, but the shell continues to envelop the core over time. Individual cells in the outer shell continue to grow and divide, thereby displacing new or existing DSS cells slightly in random directions (see methods in section 2.2). Simultaneously, the inner core increases in diameter, pushing DSS cells towards the outside of the aggregate and stimulating the formation of a thin and smooth outer shell. This mechanism also provides an explanation for the holes closing up towards the end of the simulation. The surface area of the inner core increases slower (with R^2) than the volume (with R^3), Therefore, with ANME-2 and DSS cells growing at equal rates, the surface covered by the DSS cells increases faster than the volume of the inner core.

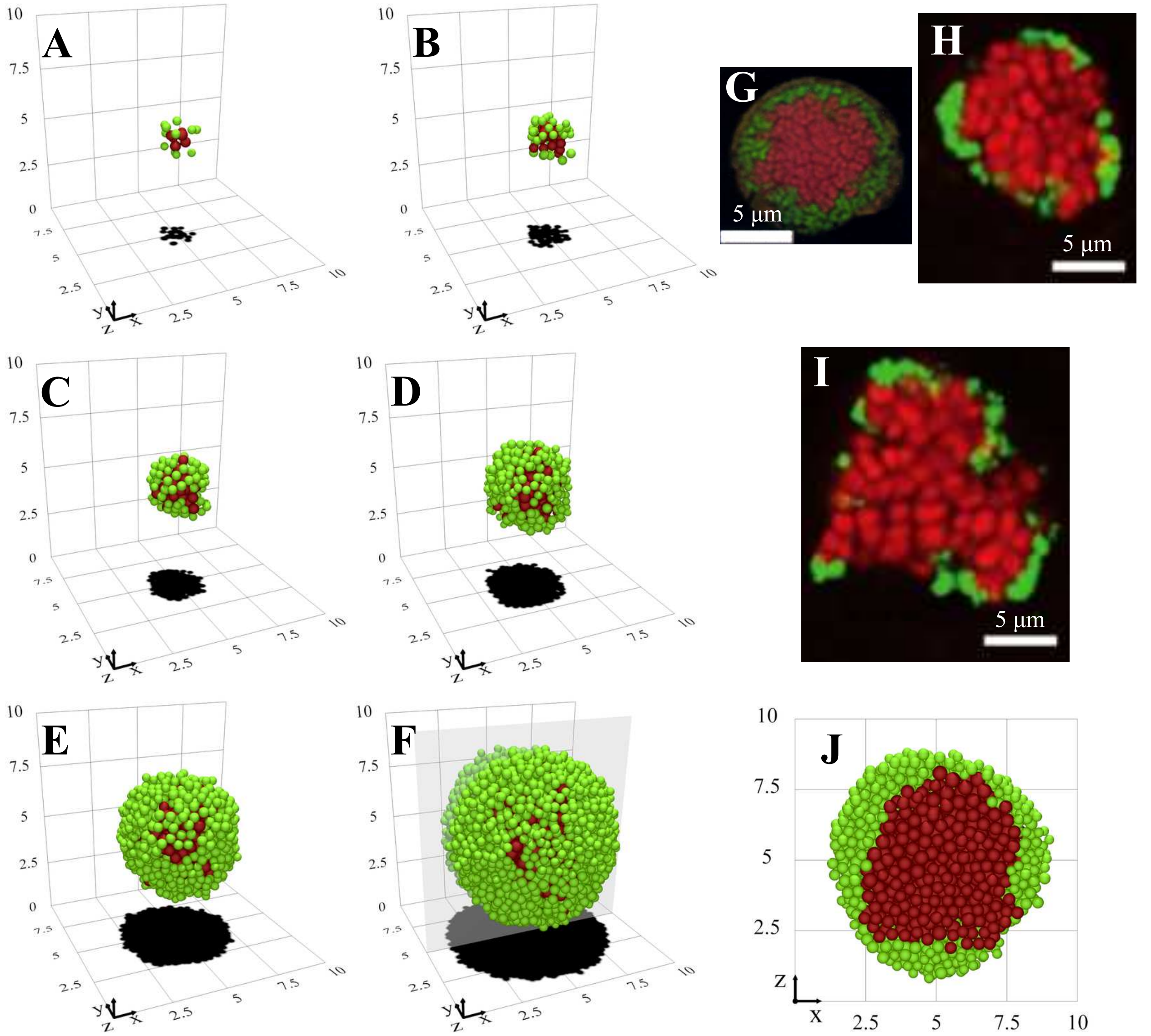

Figure 4.5: Development of a shell-shaped aggregate from an organised inoculum, with sticking links only forming between ANME-ANME cells (default case), with three micrographs of shell-shaped aggregates and a cut view of a simulated granule. Red spheres are ANME-2 cells, green spheres are DSS cells. Numbers denote the position in µm. Aggregate morphology is shown after (A) 0 weeks; (B) 50 weeks; (c) 100 weeks; (D) 150 weeks, (E) 200 weeks, (F) 250 weeks with cut section plane. (G-I) FISH micrographs of shell-shaped aggregates, (J) cut view of simulated granule aggregate after 250 weeks, the cut section plane is shown in F. Supplementary movies showing simulated aggregate formation over time are available in appendix A. G is adapted from Orphan et al. (2002), H and I from Knittel and Boetius (2009), used with permission.

Effect of cell-cell links

The mechanism describing the formation of shell-shaped aggregates also explains the importance of cell-cell sticking links observed using the model. ANME-2 cells form cell-cell sticking links, restricting ANME-2 cells to the inner core. The lack of strong ANME-2/DSS and DSS/DSS cell-cell links allows the cells to be displaced easily and be shaped into an outer shell. Similarly, EPS is excreted at different rates by various microbial species (Donot et al., 2012) and is known to cause cells to agglomerate. EPS is modelled here as cell-cell sticking links. Cells that produce considerable amounts of EPS easily stick together (strong sticking links with high spring constant $k_{s,s}$), whereas cells excreting less or no EPS form weaker links (weak sticking links with low $k_{s,s}$) or no links at all.

If the effect of EPS throughout the whole aggregate is negligible, the shell-shaped aggregate organisation is lost and a mixed morphology is developed, as shown in figure 4.6A. ANME-2 cells are not being contained in the inner core and blend with the outer shell of DSS cells, resulting in individual ANME-2 and DSS cells being located throughout the aggregate. In the default case (figure 4.5F, J), it is assumed that EPS excretion is negligible for DSS, such that sticking links are only formed within the inner ANME-2 core. If besides forming ANME-ANME links the ANME-2 cells excrete enough EPS to initiate links to DSS cells, the shell-shaped aggregate morphology is lost and a mixed aggregate develops (figure 4.6B). A cell-cell link is formed as an ANME-2 cell approaches a DSS cell, which causes the cells to remain in close proximity as the aggregate grows. Cells divide in random directions, but new cells are displaced instead of breaking existing cell-cell sticking links (for simulations with $k_{s,s} = 1 \times 10^{-12}$ the first links break after around 75-100 weeks). Inclusion of DSS-DSS links (i.e., all cells excrete EPS and can initiate new cell-cell links) results in the aggregate morphology becoming more organised and small clusters of cells to form (figure 4.6C). The ANME-2 and DSS clusters form cell-cell links and drag along groups of cells as the aggregate grows in size, resulting in an organisation where small, irregular clusters of ANME-2 or DSS dominate the aggregate. The segregation into inner core and outer shell is partially restored when the spring constants of the ANME-DSS and DSS-DSS links are lowered by an order of magnitude (figure 4.6D), causing cell-cell links to break after 50-75 weeks. The ANME-DSS and DSS-DSS links still cause some agglomeration, but the growing inner core is able to break up clumps of DSS cells as the ANME-2 core grows, resulting in the formation of a shell shaped aggregate similar to that of the default case. The movement of individual DSS cells is still impeded, however, which results in large holes in the outer shell. The shell envelops more of the inner core as the ANME-DSS and DSS-DSS spring constants are further decreased, until the morphology is similar to the default case (figure 4.6E and F), although links still start breaking after 50-75 weeks.

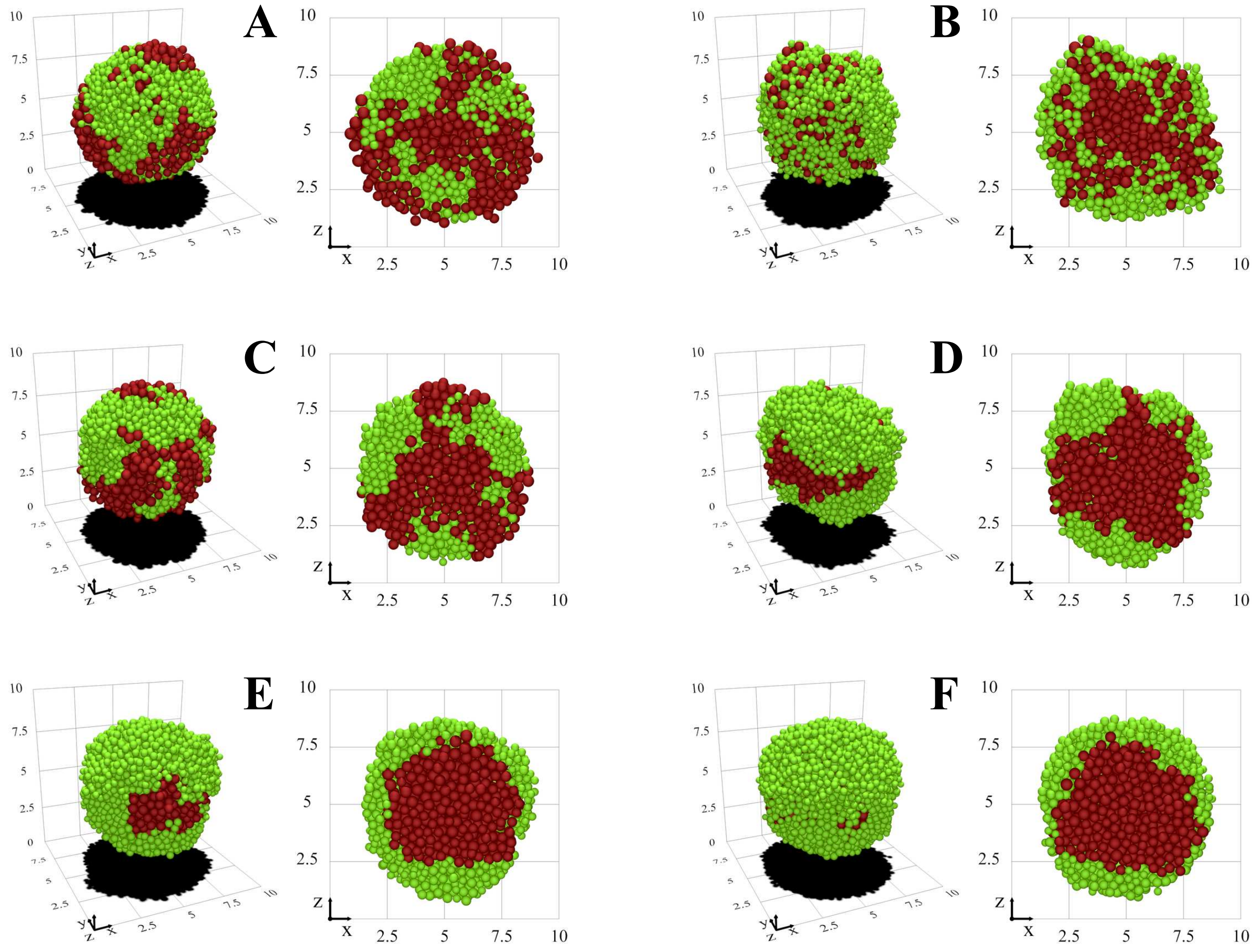

Figure 4.6: Perspective and cut view of aggregate morphology after 250 weeks, with sticking links formed between (A) none of the cells; (B) ANME-ANME and ANME-DSS with $k_{s,s,ANME-ANME} = k_{s,s,ANME-DSS} = 1 \times 10^{-12}\,\mathrm{N\,m^{-1}}$; (C-F) all cell types with $k_{s,s,ANME-ANME} = 1 \times 10^{-12}\,\mathrm{N\,m^{-1}}$, $k_{s,s,ANME-DSS}$ and $k_{s,s,DSS-DSS}$ set equal to: (C) $1 \times 10^{-12}\,\mathrm{N\,m^{-1}}$; (D) $1 \times 10^{-13}\,\mathrm{N\,m^{-1}}$; (E) $1 \times 10^{-14}\,\mathrm{N\,m^{-1}}$; (F) $1 \times 10^{-15}\,\mathrm{N\,m^{-1}}$. The inoculum is the same for all simulations and shown in figure 4.5A, the cut section plane is shown in figure 4.5F.

Effect of inoculum organisation

A structured inoculum readily forms shell-shaped aggregates if cell-cell sticking links are strong in the inner core and weak or absent in the outer shell. However, unstructured inocula (i.e., ANME-2 and DSS cells are positioned randomly throughout the initial aggregate) are expected to be present in *in vivo* and *in situ* systems as well. Simulations show that the inoculum plays an important role in the morphology of the mature aggregates. In figure 4.7 two typical aggregate morphologies growing from a random inoculum with a radius of 0.7 µm are shown (A and D). The randomly distributed inoculum consistently produces a DSS growing around an ANME-2 core (C and F), but the off-centre position of the ANME-2 core in the mature aggregate consistently results in the shell only partially enclosing the core and large holes to develop (B and E). For the organised aggregate (figure 4.5) the holes close as the aggregate develops. The off-centre cores in random aggregates form extrusions growing out of the aggregate. DSS cells that would otherwise be pushed over these holes instead collide with the extrusions and are displaced, preventing the holes from closing as the aggregate grows.

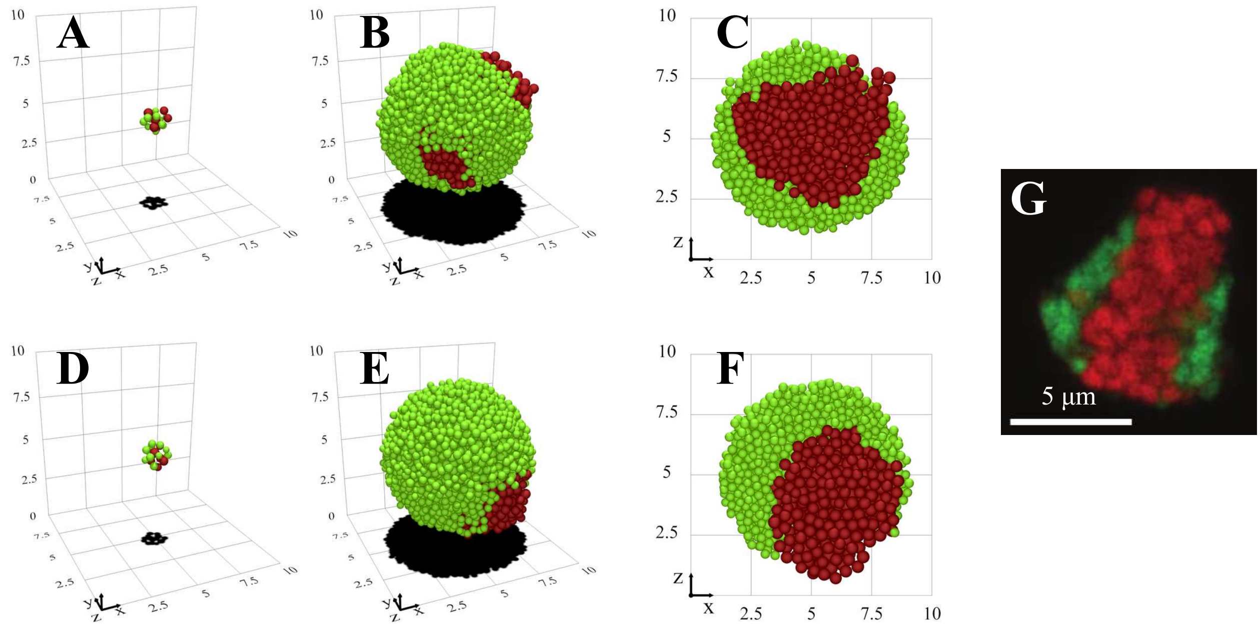

Figure 4.7: Aggregate morphology grown from (A and D) two different random inocula after 250 weeks, (B and E) perspective view and (C and F) cut view. G shows observed aggregate morphology adapted from Knittel and Boetius (2009), used with permission.

Although the random inocula do not develop in the clear shell-shaped aggregates shown in figure 4.5G and J, the non-spherical core, holes and extrusions shown in figure 4.7C are similar to experimentally observed aggregates figure 4.5H and I. The off-centre core shown in figure 4.7F results in a morphology different from the shell-shaped aggregates shown in figure 4.5, although similar morphologies have been observed in experiments (figure 4.7G).

4.4 CONCLUSIONS AND OUTLOOK

Thermodynamic calculations and diffusion-reaction modelling suggests that zero-valent sulfur is a feasible mechanism for coupling the anaerobic oxidation of methane (AOM) to sulfate reduction (SR) in shell-shaped aggregates. Acid dissociation, polysulfide precipitation and low biological reaction rates result in small (<20%) differences in the concentrations of reactive compounds and local p*H* throughout the aggregates. Given the effect of local concentrations on the biological rate is small, a mechanical model of the aggregate development is used to investigate is a purely mechanical explanation for the formation of shell-shaped aggregates exists. It was found that shell-shaped aggregates very similar to experimentally observed aggregates will develop if (i) only ANME-ANME sticking links or weak enough ANME-DSS and DSS-DSS links are formed and (ii) the inoculum initially has a shell-shaped morphology or has both species distributed uniformly over the inoculum.

The symbiotic relationship between ANME-2 and DSS is critically dependent on the role of the octasulfur reservoir in the reaction mechanism. This can be further investigated by implementing precipitation modelling into the diffusion-reaction system to investigate the polysulfide precipitation mechanism.

It has been suggested that ANME-2 cells fix nitrogen for DSS cells (Dekas et al., 2009, 2014). Considering the relationship between both species might be non-mutual as suggested by these results, an explanation as to for which purpose the ANME-2 cells fix an excess of nitrogen is of scientific interest. By extending the diffusion-reaction model, nitrogen fixation and ammonium concentration profiles can be investigated, which will provide insight into the relationship between ANME-2 and DSS in AOM/SR aggregates.

Another interesting extension to this study would be to investigate how inocula are formed as a result of cell-cell interactions. Work in this chapter suggests EPS production in ANME-2 and DSS cells plays an important role in the development of shell-shaped aggregates. If ANME-2 cells are found to indeed produce more EPS than DSS cells, free floating individual ANME-2 cells are more likely to agglomerate into small clusters. As the clusters grow bigger, the continued production of EPS allows free floating DSS cells to attach, forming small shell-shaped aggregates as shown in figure 4.5A. Aggregate formation starting with an inoculum of free floating individual cells can readily be modelled by extending the mechanical model to include Brownian motion of cells or forces exerted by medium flow.

Chapter 5

CONCLUSIONS AND RECOMMENDATIONS

5.1 CONCLUSIONS

Microbial interspecies interactions are ubiquitous in nature as well as various industrial processes and are known to play an important role in microbial communities present in these systems. Many systems exist where the role of interspecies interactions is not well understood and where a better fundamental understanding opens up options to enhance beneficial processes or limit detrimental effects caused by microorganisms.

Work presented in this thesis has focused on investigating mechanical and electrochemical interactions between microbes of different species present in various microbial communities. Through a mechanistic approach, the results presented have provided insight into how and why interspecies interactions affect processes that play an important role in the environment, industry and medicine. The work done contributes to the research fields by providing a better understanding of the fundamental biological, physical and (electro)chemical processes taking place in microbial communities. The tools that have been developed are also applicable to future research on these as well as other microbial systems.

Specifically, conclusions based on the work presented in this thesis are as follows:

Mechanical microbial interactions in biofilms and flocs

It was found that cell-substratum links can promote or impede the formation of biofilm mounds for a rod-shaped cell community. If anchoring links (link between cell and a fixed point on a surface) are formed when cells approach the substratum, multicellular layers are formed significantly faster than if instead gliding links are formed (link maintaining fixed distance between cell and surface) or if cell-substratum links are absent. Gliding links have the opposite effects, preventing cell stacking compared to the absence of cell-substratum links.

Head-tail cell-cell filial links formed during cell division cause a non-circular shape of the biofilm to develop as rod-shaped cells multiply. Initially, filial links maintain cell alignment as the biofilm develops, but as the cell count increases this effect becomes negligible.

In an activated sludge floc consisting of filament formers and floc formers, the relative growth rate of the microbial species has a strong effect on the morphology of the community. For a fast-growing floc former, dense flocs are formed that will readily settle. When the filament former grows relatively fast, a highly undesirable phenomenon called interfloc bridging can be reproduced using the mathematical model.

The presence of strong cell-cell sticking links in activated sludge flocs (for example, EPS) causes a compact floc to form with relatively few, but long external filaments. Weak sticking links causes sparse flocs to form that will poorly settle.

Compared to sticking link strength, cell-cell filial link stiffness has a weak effect on the morphology, resulting in similar floc morphologies for stiff and flexible links.

Random branching of filaments (e.g., as shown for Nocardia species in activated sludge flocs (Seviour and Nielsen, 2010)) results in fewer external filaments due in the microbial community to the shorter filament length and is therefore expected to impede interfloc bridging.

Spherical floc formers in activated sludge flocs do not readily capture filaments as well as their rod-shaped counterparts due to the formation of more compact clusters. This causes more filaments to escape the floc and thereby can result in an increased tendency of the sludge to display interfloc bridging.

Mediated versus direct interspecies electron transfer

Mathematical modelling shows that a novel interspecies electron (IET) transfer mode, direct IET through nanowires, is thermodynamically limited compared to formate-mediated IET for a cell pair converting propionate to methane. The maximum rate that can be obtained while maintaining feasible thermodynamics is about 9 times higher for direct IET than for hydrogen-mediated IET, but formate-mediated IET could achieve a rate 7 times higher than direct IET.

Based on parameters obtained from literature, direct IET is calculated to be strongly limited by activation losses, accounting for 93% of the total losses, with the remaining losses attributed to nanowire resistance and solution resistance. It is shown that the maximum rate is highly sensitive to the efficiency of the cell metabolism, with a $0.7\,\mathrm{kJ\,mol^{-1}}$ decrease in the minimum Gibbs free energy change of reaction sufficient for direct IET to outcompete formate-mediated IET in the modelled system. Alternatively, a factor 5 increase in the cytochrome count on the cell surface (resulting in a cytochrome coverage of 50%) allows direct IET to achieve similar rates as formate-mediated IET.

Multicellular modelling shows that the maximum rates for direct IET vary slightly from the cell pair system (between 15% lower and 10% higher depending on the parameter set).

Syntrophy and aggregate formation in marine methane oxidation

Thermodynamic calculations show that the zero-valent sulfur-mediated mechanism for anaerobic oxidation of methane (AOM) coupled to sulfate reduction (SR) is feasible over a wide range of concentrations, with the SR reaction being the least feasible reaction for most conditions. An order of magnitude difference in either the bisulfide (HS^-) or hydrodisulfide ($HS_2{}^-$) activity is needed to make the AOM/SR process thermodynamically unfeasible.

Because of the extremely low growth rates of ANME-2 and DSS cells facilitating anaerobic oxidation of methane, diffusion is non-limiting in AOM/SR systems. Acid dissociation and polysulfide precipitation buffer concentrations such that differences between the centre of the aggregate and the bulk liquid are less than 20%. These results suggest that thermodynamic limitation does not occur in the aggregate and that another interspecies interaction is responsible for the shell-shaped aggregates developing in these systems.

Modelling of AOM/SR aggregates without the outer DSS shell raises questions about the role of DSS cells, as elaborated upon in subsection 4.3.2. The presence of DSS cells prevents octasulfur from accumulating, but at the same time causes higher polysulfide concentrations at the ANME-2 cells. Further investigation into the precipitation mechanisms can provide insight into the symbiotic relationship between ANME-2 and DSS.

Mathematical modelling using the tool developed during the thesis shows that the formation of segregated layers in shell-shaped aggregates observed in experiments is controlled by the initial cell organisation and the formation of EPS links between cells. An inoculum with ANME-2 cells on the inside and DSS cells on the outside is required to consistently produce a shell-shaped aggregate. A random cell distribution can also result in shell-shaped aggregates, provided the distribution of cells throughout the inoculum is sufficiently uniform. If the inoculum is suitable and ANME-ANME links are strong enough to form a compact, smooth aggregate while ANME-DSS and DSS-DSS links are weak enough to be broken as the inner ANME-2 core grows, a shell-shaped aggregate is formed.

5.2 SIGNIFICANCE AND IMPLICATIONS OF RESEARCH FINDINGS

Biofilm modelling provides insight into the mechanisms that play a role in the formation of multilayered biofilms and point out the importance of various cell-cell and cell-substratum interactions. Understanding the mechanism through which biofilms are formed and the effect of various parameters on the morphology of the community is crucial in predicting problems in many fields. For example, a thin biofilm forming on medical equipment is difficult to detect and remove, while potentially having catastrophic consequences for patients (Donlan, 2001), while the formation of dense, uniform biofilms is desirable for granules used in for example granular sludge treatment processes (Xavier et al., 2007).

Activated sludge modelling shows how the formation of flocs that eventually play an important role in sludge bulking is affected by variables such as relative growth rate, abundance and strength of EPS sticking links and stiffness of filaments. The developed model allows visualisation of the development of activated sludge flocs and interspecies bridging, which is difficult to do in a non-invasive way in experiments or operational treatment facilities.

Furthermore, the mechanical model can reproduce real-world observations made in other biological systems, making it a valuable tool to predict the influence of various external parameters on the behaviour of microbial communities governed by mechanic interactions that cannot easily be determined experimentally. Through minor extensions to the existing modelling framework, the mechanical interactions in microbial communities can be studied.

Modelling of IET shows that the electron transfer step between cell and nanowire is strongly limiting the thermodynamic feasibility of direct IET through nanowires. This outcome defines the scope for future research, showing that in order for direct IET to be a thermodynamically more feasible alternative to formate-mediated IET, the more efficient metabolism for direct IET must play a role, a different cell-nanowire transfer mechanism must be present (e.g., Pirbadian et al. (2014)), or the rate constants or cytochrome concentrations estimated from literature are off by an order of magnitude. The developed model can readily be updated with new parameters obtained from experiments, allowing evaluation of alternative conductive matrices (Cruz Viggi et al., 2014) and different electroactive microbial species such as *Methanosarcina barkeri* (Rotaru et al., 2014a).

Results presented for ANME-2/DSS granules facilitating the anaerobic oxidation of methane demonstrate that diffusion-based transport is not expected to be limiting the ability of cells to take up substrate and remove products for the conditions reported by Milucka et al. (2012). The development of a thermodynamically suboptimal microbial community configuration can be explained by mechanical interactions between cells and the initial seed of the community in the medium, providing insight to the development of deep-sea microbial communities that are extremely difficult to study *in situ* or *in vitro*. Similarly, it is possible that other unusual microbial aggregate morphologies occurring in nature are determined by underlying physical mechanisms.

5.3 OUTLOOK AND FUTURE WORK

Multidisciplinary research on microbial community interactions has been presented in this thesis. Physical modelling techniques have been applied to microbiological systems to study the effect of mechanical intra- and intercellular interactions on microbial biofilms and flocs in chapter 2. Electrochemical and thermodynamic studies have been conducted and transport phenomena models have been applied in chapter 3 to investigate extracellular limitations of classical and novel interspecies electron transfer modes. In chapter 4, the thermodynamics, transport limitations and mechanical interactions in a microbial community facilitating the anaerobic oxidation of methane has been investigated through a combination of the techniques presented in chapters 2 and 3.

The methods and results published in this thesis allow a number of follow-up studies to be conducted, especially for the mechanical modelling framework presented in chapter 2. Because cells are modelled as independent entities, the mechanical modelling tool is very suitable for applications in fields where properties of individual cells are important, such as interspecies interactions and microbial ecology. The tool is developed in Java, which makes it fast, allows for integration with existing finite element methods (e.g., COMSOL) and makes it readily available to multiple computer architectures. The source code of the individual-based model has been made available under the MIT License at github.com/tomasstorck/diatomas. It is available for anyone to use and redistribute provided the original work is acknowledged, for example by referring to the original paper (Storck et al., 2014). All this makes the modelling tool available to other researchers to use and extend.

Possible extensions to the studies described in chapter 2-4 are discussed in the remainder of this chapter. A number of extensions discussed have been investigated by Mr. Bas Cockx and Dr. Cristian Picioreanu, as part of a MSc thesis at TU Delft (Cockx, 2014). Parts of the methods presented in chapter 2 are currently being implemented in a larger mathematical model as part of a PhD study at the Technical University of Denmark and the University of Birmingham.

A manuscript based on the research presented in chapter 4 is currently in preparation for submission to the journal of Environmental Microbiology or the journal of Applied and Environmental Microbiology.

5.3.1 Numerical optimisation of mechanical modelling tool for modelling more complex systems

The results presented in chapter 2 taken from the paper Storck et al. (2014) are limited by the computational time required for the relaxation step, resulting in communities consisting of hundreds to several thousands of cells. Significant improvements in performance have been achieved by implementing a more efficient ordinary differential equation solver described in subsection 2.2.3, allowing communities of up to 25,000 cells to be simulated in about 65 hours of computation time (see for example figure 2.3). Much greater improvements in computational speed can be achieved by parallelisation of the relaxation step, allowing multiple interactions to be calculated simultaneously. Cockx (2014) has performed parallelisation of the Java code used in the relaxation step leading to significant increases in the computation speed, as shown in figure 5.1. Cell communities consisting of up to 100,000 cells have been simulated with the parallelised code. An activated sludge floc demonstrating the size of communities that can be simulated with the optimised code is shown in figure 5.2.

Besides parallelisation, there are various aspects of the model that can be sped up by making improvements to the code, for example:

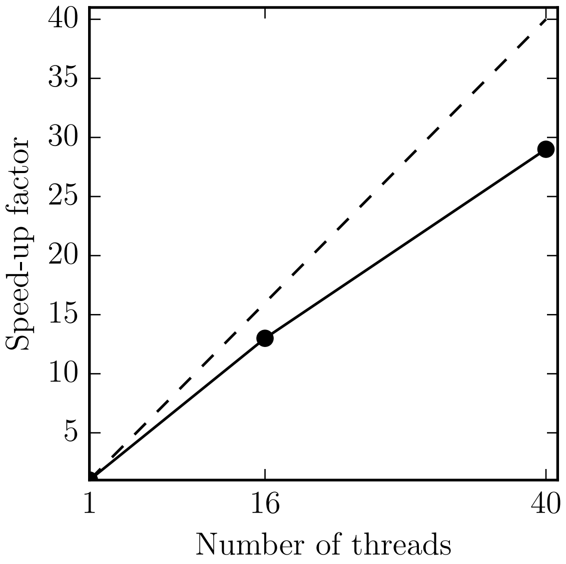

Figure 5.1: Increase in computation speed as a function of the number of process threads used. The dotted line represents a linear speed-up. Adapted from Cockx (2014) and redrawn, used with permission.

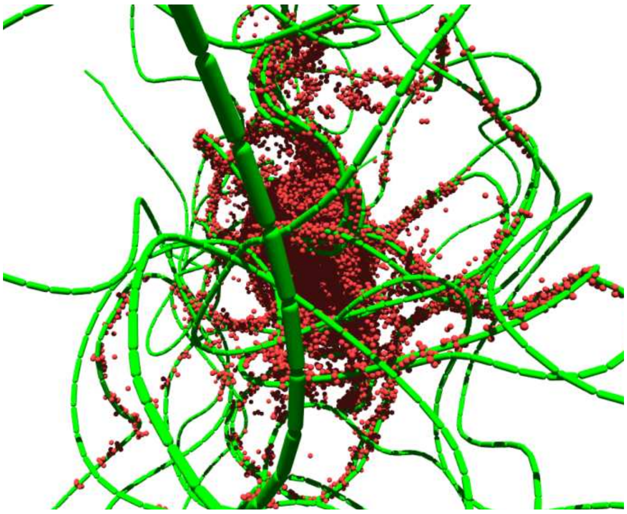

Figure 5.2: Activated sludge floc showing excessive external filament growth, simulated using the parallelised relaxation method. Note that parameters used are not the same as in chapter 2 and that a cell attachment mechanism is used. Adapted from Cockx (2014), used with permission.

- Optimisations to binary space partitioning during the relaxation step can minimise the number of calculations done for each cell by only computing mechanical interactions for cells that are in close proximity.
- Some systems can be modelled as a two-dimensional system, greatly reducing the number of cells in the system and the complexity of the relaxation step.
- Model parameters (e.g., spring constants) can be optimised to reduce numerical stiffness.
- Although the various ODE solvers included in the Apache Commons Mathematics Library (version 3.3, The Apache Software Foundation; see commons.apache.org/proper/commons-math/userguide/ode.html) have been tested, there are many solvers available that could be better suited for modelling this system of equations.

By improving the computational speed of the model, systems containing more cells and interactions can be simulated, creating opportunities to model more complex systems.

5.3.2 Verification of mechanical modelling tool using *in vivo* systems

In section 5.1 a number of conclusions is presented stating how physical variables affect the modelled aggregate morphology. These findings have an impact on the microbial communities that develops *in vivo*, which can be verified with experiments. Here, some examples of experiments that could verify the modelling results are briefly discussed.

The type of cell-substratum links is reported to have an effect on the thickness of the biofilm. This can be reproduced experimentally by growing similar inocula of cells on different types of planes. The topographical (e.g., roughness), hydrophobic and electrostatic properties of the substratum affect the cell-substratum links without impacting the cell-cell links, which is of vital importance in these experiments. A rough, unequal surface will provide support for cell appendages to hold on to, simulating the anchoring links in the simulations. A smooth, electrostatically charged surface would promote electrostatic forces that cause the biofilm to maintain a certain distance from the surface, thereby promoting the formation of gliding links. Similarly, a smooth, strongly hydrophobic surface should make it harder for the hydrophilic cells to attach, simulating the absence of cell-substratum links.

The importance of filial links can be quantified by growing two inocula of pure culture rod-shaped cells with a similar cell morphology on a smooth substratum, one able to form filial links and one unable.

It is expected that cell-cell sticking links in the model fulfil the same role as EPS in experimental systems. The strength of EPS links can be lowered using various biocidal compounds targeting these compounds, allowing the correlation between sticking link strength and aggregate morphology to be investigated.

Filament branching is expected to influence activated sludge floc morphology and thereby settleability. Through growing similar inocula *in vivo*, some dominated with a branching species and some with non-branching species, further insight can be obtained.

Other findings reported in this chapter serve more as model verification than novel findings. The improved settleability of compact sludge flocs is a well-known phenomenon, which is made of use in aerobic granular sludge treatment processes (de Kreuk et al., 2010). Similarly, the importance of relative growth rates of floc formers and filament formers is well described in existing literature (Seviour and Nielsen, 2010).

5.3.3 Application of mechanical modelling tool to *in vivo* microbial systems

The mechanical model presented in chapter 2 has been applied to an *E. coli* biofilm, activated sludge flocs and AOM/SR aggregates (chapters 2 and 4), but can be applied to other systems where mechanical interactions are expected to dominate the aggregate morphology without major modifications to the functionality of the model.

Possibly the most important field in which the model can be applied is microbial ecology. The properties of the individual cells can be modified to a great extent, allowing cell communities of different morphologies or capable of forming various links to be investigated. This information can be invaluable where biomass properties cannot readily be adjusted in experiments or where observational methods are limited. Although some modelling tools already exist (see the overview in subsection 1.2.3), the simplicity, extendability and availability of the framework presented in the thesis makes it an interesting addition to the field of ecology.

A general example where the modelling framework could provide better insight to the ecology of a microbial community is where properties inherent to EPS are linked and difficult to separate. If cell-cell and cell-substratum links are both inherently a result of EPS secreted by the cell, it could be difficult to determine if these two effects are advantageous, detrimental or a combination of both for a particular system. In the model the two effects are easily investigated separately, which could show that one type of link is beneficial while the other has a negative impact on the system. Therefore, eliminating one type of link in the actual system - although difficult to do - would be worth investing time and money in.

Another readily available application of the modelling tool is to predict the importance of strong cell-cell and cell-substratum interaction forces versus weaker interactions to cultures not investigated in chapter 2. Cockx (2014) has *Staphylococcus* species. The role of these forces on the development of ordered cell community morphologies has been investigated (figure 5.3; see Cockx (2014)). The development of dental plaque biofilms has been modelled by growing a mixed microbial community of cocci and bacilli cells on a planar substratum. The resulting biofilm was found to be of a similar morphology as biofilms observed in experiments (figure 5.4, Cockx (2014); Walker and Sedlacek

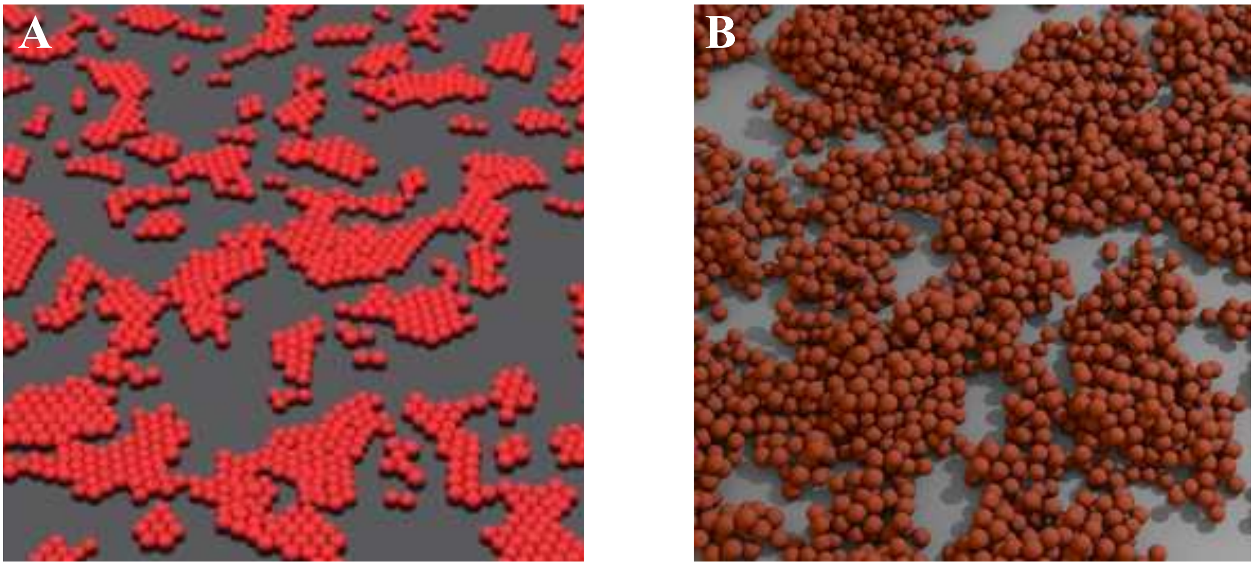

Figure 5.3: Morphology of *Staphylococcus* communities with (A) strong cell-cell and cell-substratum attractive forces and (B) weak cell-cell and cell-substratum attractive forces. Adapted from Cockx (2014), used with permission.

(2007)).

Although currently only mechanical interactions are modelled, the individual cell-based approach used makes the model readily available to take into account other cell-cell interactions on an individual cell level, combining mechanical interactions with interactions such as gene transfer ((Seoane et al., 2011; Rudge et al., 2012)). Work on combining the model for mechanical interactions with a model for horizontal gene transfer has been commenced at the Technical University of Denmark and the University of Birmingham by Mr. Bas Cockx.

Implementation of microbial motility (Picioreanu et al., 2007; Janulevicius et al., 2010; Harvey et al., 2011) in the mechanical model will allow simulation of swarming microbial communities combined

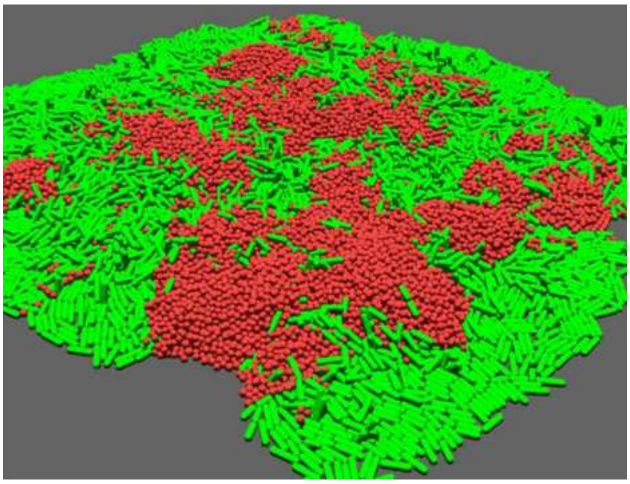

Figure 5.4: Modelled morphology of a mixed community dental plaque biofilm. Adapted from Cockx (2014), used with permission.

with cell growth and division. For example, the flexibility of rod-shaped cells as modelled by (Janulevicius et al., 2010) can be reproduced by modelling individual cells as multiple particles connected by multiple intracellular springs of variable stiffness ($K_{s,s}$).

Cell-cell communication and quorum sensing (Nadell et al., 2008, 2010; Melke et al., 2010) can be readily implemented in the model as algorithms calculating the cell proximity are already present in the model (collision detection, Ericson (2005)). Alternatively, by computing the concentration field of various signalling molecules, a computationally less efficient but more accurate solution can be obtained.

The flexibility of the mechanical model can be extended greatly through the implementation of a finite element analysis or finite difference analysis tool. Functionality to interact with a finite element analysis package (COMSOL Multiphysics, version 4.4, COMSOL Inc., Burlington, MA) is already implemented in the model but not applied to work included in the thesis. Some possible applications of the mechanical model combined with an finite element analysis tool are given below:

Through calculation of stresses acting on cells, cell detachment similar to Bottero et al. (2013) and Tierra et al. (2015) can be modelled, but with the viscoelastic properties of the biomass determined by cell-cell interactions on an individual cell level. Through the individual-based properties of the biomass a realistic behaviour of multispecies systems, inhomogeneous biomass densities and reattachment of chunks of biomass detached by sloughing events can be modelled.

Another extension utilising finite element analysis is diffusion-migration-reaction modelling in order to investigate microbial communities growing via mediated or direct interspecies electron transfer, based on methods described in chapter 3. Because intercellular distances are important to the diffusive flux that can be achieved for mediated interspecies electrons transfer but not for direct interspecies electron transfer which is limited by activation losses, the effect of the electron transfer mode on the morphology of the resulting microbial aggregates can be readily predicted.

Through evolution-based modelling, the interplay of cell properties such as cell size, cell aspect ratio, mechanical cell-cell interactions, substrate affinity and maximum rate can be studied. By randomly imposing mutations to newly formed cells via slight modifications of these cell properties, minimal changes to the model will be needed besides implementing selection pressure criteria (e.g., cell maintenance, medium outflow or biocidal compounds (Chambless, 2006)).

Extensions made to the mechanical model as discussed in chapter 4 have made the tool suitable to model dense cell communities on an individual cell level and can be used to predict the morphology of the aggregate. Further studies can be done based on granule formation mechanisms without the need to implement additional features in the model, either on ANME/SR aggregates or on other granules. For example, the model can readily be applied to model the mechanical interactions in dense granules such as in upflow anaerobic sludge blanket reactors (Schmidt and Ahring, 1996).

Through a simple extension, sarcina-like structures observed for ANME-2 cells (Nauhaus et al., 2007;

Knittel and Boetius, 2009) can be modelled using this tool. Through implementation of a division plane this cell division mechanism can be reproduced and the effect on the aggregate morphology can be investigated.

By implementing Brownian motion into the mechanical model, the formation of initial cell-shaped aggregates from free floating individual cells can be investigated. EPS production in ANME-2 cells can initiate the formation of small ANME-2 clumps. As more EPS is produced, the attachment of floating DSS cells can result in a DSS shell surrounding the ANME-2 core, which readily develops into large, shell-shaped communities as shown in chapter 4.

5.3.4 Verification of interspecies electron transfer model

The outcomes of the study presented in chapter 3 are closely tied to the values used for DIET parameters. Based on literature published to date, estimates are made for these values. The case studies quantify how sensitive the results are to changes of the different parameters studied.

While parameters for hydrogen- and formate-MIET models are well described, the DIET model is highly sensitive to values that dictate the activation losses (transfer rate constant k_0, redox complex count $N_{act,cell}$) and minimum Gibbs free energy of reaction ($\Delta G'_{min}$).

Experimental investigation is required to get better estimates of values for these parameters. These experiments often use state-of-the-art microscopy and electrochemical techniques. Based on the defined scope for experimental work in section 5.2, it would be of interest to re-evaluate the feasibility of the various IET mechanisms using the methods presented in chapter 3 when more accurate estimates of electron transfer parameters are obtained experimentally.

Values for k_0 for heterogeneous DEET are estimated from Okamoto et al. (2009) and more recently Okamoto et al. (2011) using cyclic voltammetry. A very useful extension could be made to the model if the value for k_0 can be derived for DIET, but the microscopic scale at which these interactions take place makes such an experiment extremely difficult and might require combination with other techniques more readily applicable to these systems (e.g., atomic force microscopy). The value for $N_{act,cell}$ was determined in Lower et al. (2007) using force spectroscopy (atomic force microscopy). With improvements made to atomic force microscopes over the past ten years, a higher resolution and thereby a more accurate estimate of this parameter should be achievable. In the current model, DIET parameters are obtained from systems with various microbial species and grown on different substrates. Evaluation of these parameters for a standard microbiological system would provide better insight to the validity of these parameters and feasibility of the DIET mechanism.

The model used in this thesis takes into account acetate production but not acetoclastic methanogenesis, as the latter is thermodynamically less limiting than methanogenesis using hydrogen and formate. Acetate uptake is expected to play an important role in DIET (Nagarajan et al., 2013). The acetate metabolism is not expected to have a strong effect on the relative feasiblity of the IET modes, but it will be important for the total methane production rate and therefore should be implemented when verifying the metabolic rates of the acetogen/methanogen system.

5.3.5 Application of interspecies electron transfer model

The direct interspecies electron transfer (IET) model presented in chapter 3 has currently been applied only to metallic-like conductivity nanowire systems (figure 5.5), as believed to be present between *Geobacter* species (Malvankar et al., 2014). For *Shewanella* species, flavin diffusion are responsible for 75% of the transfer rate (Marsili et al., 2008; Kotloski and Gralnick, 2013), and the role of nanowires is still being investigated. According to some studies, transport through *Shewanella* nanowires occurs via electron hopping or electron tunnelling (Leung et al., 2013; Malvankar et al., 2014). In electron hopping, electrons are transferred from reduced to oxidised molecules which need to be spatially positioned in a way that the hopping step is feasible (Malvankar and Lovley, 2014). The rate at which transfer occurs is governed by a rate constant k_{hop} and can be modelled using the method described by Pirbadian and El-Naggar (2012). In electron tunnelling, the wave nature of electrons is exploited to transfer electrons through the conductor/insulator barriers via quantum tunnelling, as described using Schrödinger's equation. By implementing an electron hopping or tunnelling mechanism to model electron transport through the nanowire, direct IET involving a *Shewanella*-like species can be simulated to investigate the thermodynamic feasibility of electron hopping and tunnelling. Different mechanisms are responsible for transport along the nanowire than for metallic-like conductivity, which means losses during electron transport will be different. Furthermore, because *Shewanella* nanowires are extruded from the cell as explained by Pirbadian et al. (2014) and paragraph 1.2.1, it is possible that activation losses encountered by these species are different in than modelled in this work.

The model can readily be applied to investigate the relative feasibility of the IET mechanisms with other substrates (e.g., butyrate (Stams and Dong, 1995) or ethanol (Rotaru et al., 2014a)) and intermediates (e.g., comparing feasibility of flavin diffusion and DIET (Marsili et al., 2008; Kotloski and Gralnick, 2013)).

Various interspecies distance for multicellular systems have been reported in literature (see subsection 3.2.1). Average interspecies distances smaller than 5 µm have not been investigated in chapter 3 because transport through the cell interior will start to dominate the system. Because of the various barriers in the cell (transfer across cell wall and membrane, transport through cytoplasm, etc.), external diffusion will no longer dominate the mediated IET transport rates. By extending the transport model to include the cell interior, an accurate estimate of the feasibility of IET at smaller interspecies distances can be investigated.

Nagarajan et al. (2013) described intracellular limitations of direct IET through metabolic modelling and has shown that the metabolism of direct IET is more efficient than that of mediated IET. It was

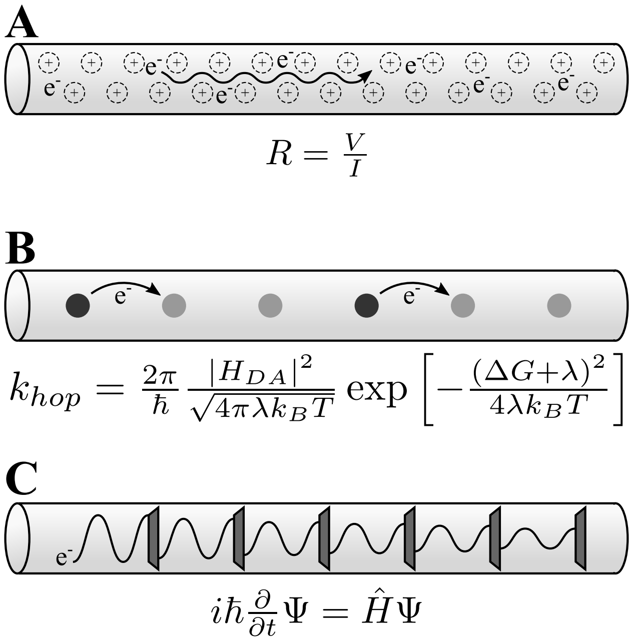

Figure 5.5: Electron transport mechanisms proposed for direct IET with their governing equations, (A) metallic-like conductivity, where electrons are not associated with a single atom (denoted by $+$) but are shared by the ions, described by Ohm's law; (B) cytochrome hopping, where electrons hop from discrete reduced molecules (dark) to oxidised molecules (light), governed by the rate constant k_{hop}; (C) cytochrome tunnelling, where the wave nature of electrons allows them to tunnel through barriers. The quantum state of the electron is described by Schrödinger's equation.

shown in chapter 3 that a small metabolic advantage for direct IET results in a thermodynamically more feasible process. By combining the method described by Nagarajan et al. (2013) with the IET model, the metabolic advantage can be calculated and effects of both intracellular and extracellular limitations can be investigated. Alternatively, research has been done by the same group on quantifying the maintenance energy required by *Geobacter sulfurreducens*. By implementing the effect of these calculations on the minimum Gibbs free energy requirements for direct IET, the estimate used for $\Delta G'_{r,min}$ in chapter 3 can be adjusted.

The model presented in chapter 3 can be applied to investigate the feasibility of microbial fuel cells. Extracellular losses occurring during electron transfer and transport between cells and electrodes are analogous to extracellular losses encountered in the IET model. Extracellular electron transfer via nanowires (nanowire-DEET) can readily be modelled by changing parameters to describe heterogeneous (cell-electrode) transfer instead of homogeneous (cell-cell) transfer (Ly et al., 2013).

5.3.6 Application of anaerobic oxidation of methane/sulfate reduction diffusion-reaction models

The diffusion-reaction model presented in chapter 4 is able to accurately model concentration profiles in granules while taking into account acid-base and precipitation equilibria. Through simplification of the diffusion-reaction equations, the three-dimensional aggregate geometry is accurately described using a one-dimensional spherically symmetrical model, speeding up calculations significantly while increasing the resolution and stability of the model. This makes the model readily applicable for modelling diffusion limitation in aggregates of other AOM/SR mechanisms proposed over the past years as part of a Monte-Carlo analysis (Sø rensen et al., 2001; Nauhaus et al., 2005; Moran et al., 2008; Alperin and Hoehler, 2010). The thermodynamic feasibility calculations presented in chapter 4 can easily be implemented in the model as well. The computational efficiency of the model also opens up possibilities to implement this method in macroscopic advection-diffusion-reaction models, such as AOM at hydrothermal vents (Knittel and Boetius, 2009) and individual granule concentration profiles in granular sludge reactors (Xavier et al., 2007).

Work presented in chapter 4 and Milucka et al. (2012) has raised questions as to the role of the DSS species in AOM/SR. Milucka et al. (2012) has suggested the DSS cells obtain energy by disproportionating hydrodisulfide via reaction 1.9. While this can have a positive effect on the thermodynamic feasibility of ANME reaction 1.8 by taking up 4 mol of HS_2^-, the DSS produces 7 mol of HS^- which via precipitation reaction 4.3 is converted back to 7 mol HS_n^-. Because in this manner a net amount of sulfide compounds is produced by the DSS, the thermodynamic feasibility of the ANME-2 reaction is reduced by the presence of the DSS cells. On the other hand, the DSS cells prevent octasulfur from accumulating at the ANME-2 cells, which would make the presence of DSS cells beneficial for the ANME-2. By further developing the precipitation mechanism in the model through implementation of a finite octasulfur pool and modelling the diffusion and precipitation mechanisms, the effect of the DSS cells on the ANME-2 cells can be quantified.

REFERENCES

Albright, L. F., ed. (2008). Albright's Chemical Engineering Handbook. CRC Press/Taylor and Francis, Boca Raton, FL.

Alperin, M. J. and Hoehler, T. M. (2010). Anaerobic methane oxidation by archaea/sulfate-reducing bacteria aggregates: 1. Thermodynamic and physical constraints. American Journal of Science *309*, 869–957.

Alpkvist, E. and Klapper, I. (2007a). A multidimensional multispecies continuum model for heterogeneous biofilm development. Bulletin of mathematical biology *69*, 765–89.

Alpkvist, E. and Klapper, I. (2007b). Description of mechanical response including detachment using a novel particle model of biofilm/flow interaction. Water Science & Technology *55*, 265.

Alpkvist, E., Picioreanu, C., van Loosdrecht, M. C. M. and Heyden, A. (2006). Three-dimensional biofilm model with individual cells and continuum EPS matrix. Biotechnology and bioengineering *94*, 961–979.

Bard, A. and Faulkner, L. (1980). Electrochemical methods: fundamentals and applications. 2nd ed. edition, Wiley, New York.

Batstone, D. J., Keller, J., Angelidaki, I., Kalyuzhnyi, S. V., Pavlostathis, S. G., Rozzi, A., Sanders, W. T. M., Siegrist, H. and Vavilin, V. A. (2002). Anaerobic Digestion Model No. 1. First edit edition, IWA Publishing, London.

Batstone, D. J., Picioreanu, C. and van Loosdrecht, M. C. M. (2006). Multidimensional modelling to investigate interspecies hydrogen transfer in anaerobic biofilm. Water research *40*, 3099–3108.

Bitton, G. (2011). Wastewater Microbiology. 4th ed. edition, Wiley-Blackwell, Hoboken, NJ.

Bockris, J. O. and Nagy, Z. (1973). Symmetry Factor and Transfer Coefficient. Journal of Chemical Education *50*, 839–843.

Boetius, A., Ravenschlag, K., Schubert, C. J., Rickert, D., Widdel, F., Gieseke, A., Amann, R., Jø rgensen, B. B., Witte, U. and Pfannkuche, O. (2000). A marine microbial consortium apparently mediating anaerobic oxidation of methane. Nature *407*, 623–6.

Bond, D. R., Takács, I., Tender, L. M. and Torres, C. I. (2012). On Electron Transport through Geobacter Biofilms. ChemSusChem *5*, 1099–105.

Boone, D. R. and Bryant, M. P. (1980). Propionate-Degrading Bacterium, Syntrophobacter wolinii sp. nov. gen. nov., from Methanogenic Ecosystems. Appl. Envir. Microbiol. *40*, 626–632.

Boone, D. R., Johnson, R. L. and Liu, Y. (1989). Diffusion of the Interspecies Electron Carriers H2 and Formate in Methanogenic Ecosystems and Its Implications in the Measurement of Km for H2 or Formate Uptake. Applied Environmental Microbiology *55*, 1735–1741.

Bottero, S., Storck, T., Heimovaara, T. J., van Loosdrecht, M. C. M., Enzien, M. V. and Picioreanu, C. (2013). Biofilm development and the dynamics of preferential flow paths in porous media. Biofouling *29*, 1–18.

Bowden, E. F., Hawkridge, F. M., Chlebowski, J. F., Bancroft, E. E., Thorpe, C. and Blount, H. N. (1982). Cyclic voltammetry and derivative cyclic voltabsorptometry of purified horse heart cytochrome c at tin-doped indium oxide optically transparent electrodes. Journal of the American Chemical Society *104*, 7641–7644.

Bridgham, S. D., Cadillo-Quiroz, H., Keller, J. K. and Zhuang, Q. (2013). Methane emissions from wetlands: Biogeochemical, microbial, and modeling perspectives from local to global scales. Global Change Biology *19*, 1325–1346.

Burdman, S. and Jurkevitch, E. (1998). Aggregation in Azospirillum brasilense: effects of chemical and physical factors and involvement of extracellular components. Microbiology *144*, 1989–1999.

Celler, K., Hödl, I., Simone, a., Battin, T. J. and Picioreanu, C. (2014). A mass-spring model unveils the morphogenesis of phototrophic Diatoma biofilms. Scientific reports *4*, 3649.

Chambless, J. (2006). A three-dimensional computer model of four hypothetical mechanisms protecting biofilms from antimicrobials. Applied and environmental microbiology *72*, 2005–2013.

Cockx, B. (2014). Efficient modeling of mechanical interactions in microbial community development. Msc thesis TU Delft.

Cruz Viggi, C., Rossetti, S., Fazi, S., Paiano, P., Majone, M. and Aulenta, F. (2014). Magnetite particles triggering a faster and more robust syntrophic pathway of methanogenic propionate degradation. Environmental science & technology *48*, 7536–7543.

Dale, A. W., Regnier, P. and Cappellen, P. V. A. N. (2006). Bioenergetic controls on anaerobic oxidation of methane (AOM) in coastal marine sediments: A theoretical analysis. American Journal of Science *306*, 246–294.

de Jong, I. G., Beilharz, K., Kuipers, O. P. and Veening, J.-W. (2011). Live Cell Imaging of Bacillus subtilis and Streptococcus pneumoniae using Automated Time-lapse Microscopy. Journal of Visualized Experiments *e3145*, 1–6.

de Kreuk, M. K., Kishida, N., Tsuneda, S. and van Loosdrecht, M. C. M. (2010). Behavior of polymeric substrates in an aerobic granular sludge system. Water Research *44*, 5929–5938.

Dekas, A. E., Chadwick, G. L., Bowles, M. W., Joye, S. B. and Orphan, V. J. (2014). Spatial distribution of nitrogen fixation in methane seep sediment and the role of the ANME archaea. Environmental microbiology *16*, 3012–3029.

Dekas, A. E. and Orphan, V. J. (2010). Identification of diazotrophic microorganisms in marine sediment via fluorescence in situ hybridization coupled to nanoscale secondary ion mass spectrometry (FISH-NanoSIMS), vol. 486,. Elsevier Inc.

Dekas, A. E., Poretsky, R. S. and Orphan, V. J. (2009). Deep-sea archaea fix and share nitrogen in methane-consuming microbial consortia. Science (New York, N.Y.) *326*, 422–6.

Dillon, R., Fauci, L., Fogelson, A. and Gaver III, D. (1996). Modeling Biofilm Processes Using the Immersed Boundary Method. Journal of Computational Physics *129*, 57–73.

Donlan, R. M. (2001). Biofilm formation: a clinically relevant microbiological process. Clinical infectious diseases : an official publication of the Infectious Diseases Society of America *33*, 1387–1392.

Donot, F., Fontana, A., Baccou, J. C. and Schorr-Galindo, S. (2012). Microbial exopolysaccharides: Main examples of synthesis, excretion, genetics and extraction. Carbohydrate Polymers *87*, 951–962.

Edwards, M. J., Baiden, N. A., Johs, A., Tomanicek, S. J., Liang, L., Shi, L., Fredrickson, J. K., Zachara, J. M., Gates, A. J., Butt, J. N., Richardson, D. J. and Clarke, T. A. (2014). The X-ray crystal structure of Shewanella oneidensis OmcA reveals new insight at the microbe-mineral interface. FEBS letters *588*, 1886–1890.

El-Naggar, M. Y., Wanger, G., Leung, K. M., Yuzvinsky, T. D., Southam, G., Yang, J., Lau, W. M., Nealson, K. H. and Gorby, Y. a. (2010). Electrical transport along bacterial nanowires from Shewanella oneidensis MR-1. Proceedings of the National Academy of Sciences of the United States of America *107*, 18127–18131.

Ericson, C. (2005). Real Time Collision Detection. Real-time Collision Detection, 2nd ed. edition, Morgan Kaufmann Publishers, San Francisco.

Evans, L., ed. (2000). Biofilms: Recent Advances in their Study and Control. Harwood Academic Publishers, Amsterdam.

Franks, A. E., Malvankar, N. and Nevin, K. P. (2010). Bacterial biofilms: the powerhouse of a microbial fuel cell. Biofuels *1*, 589–604.

Gill, P. E., Murray, W. and Saunders, M. A. (2005). SNOPT: An SQP Algorithm for Large-Scale Constrained Optimization. SIAM Review *47*, 99–131.

Gorby, Y. A., Yanina, S., McLean, J. S., Rosso, K. M., Moyles, D., Dohnalkova, A., Beveridge, T. J., Chang, I. S., Kim, B. H., Kim, K. S., Culley, D. E., Reed, S. B., Romine, M. F., Saffarini, D. A., Hill, E. A., Shi, L., Elias, D. A., Kennedy, D. W., Pinchuk, G., Watanabe, K., Ishii, S., Logan, B., Nealson, K. H. and Fredrickson, J. K. (2006). Electrically conductive bacterial nanowires produced by Shewanella oneidensis strain MR-1 and other microorganisms. Proceedings of the National Academy of Sciences *103*, 11358–11363.

Hartshorne, R. S., Jepson, B. N., Clarke, T. a., Field, S. J., Fredrickson, J., Zachara, J., Shi, L., Butt, J. N. and Richardson, D. J. (2007). Characterization of Shewanella oneidensis MtrC: a cell-surface decaheme cytochrome involved in respiratory electron transport to extracellular electron acceptors. Journal of biological inorganic chemistry *12*, 1083–94.

Harvey, C. W., Morcos, F., Sweet, C. R., Kaiser, D., Chatterjee, S., Liu, X., Chen, D. Z. and Alber, M. (2011). Study of elastic collisions of Myxococcus xanthus in swarms. Physical biology *8*, 026016.

Harvey, R. J., Marr, A. G. and Painter, P. R. (1967). Kinetics of growth of individual cells of Escherichia coli and Azotobacter agilis. Journal of bacteriology *93*, 605–17.

Haynes, W. M., ed. (2014). CRC Handbook of Chemistry and Physics. 94 (intern edition, CRC Press/Taylor and Francis, Boca Raton, FL.

Hedderich, R. and Whitman, W. B. (2013). Physiology and Biochemistry of the Methane-Producing Archaea. In The Prokaryotes, (Rosenberg, E., DeLong, E. F., Lory, S., Stackebrandt, E. and Thompson, F., eds), chapter 18, pp. 635–662. Springer Berlin Heidelberg Berlin, Heidelberg.

Heijnen, J. and Kleerebezem, R. (2009). Bioenergetics of microbial growth. In Encyclopedia of Bioprocess Technology pp. 1–24.

Heijnen, J. J. (2010). Impact of thermodynamic principles in systems biology. Advances in biochemical engineering/biotechnology *121*, 139–62.

Hermansson, M. (1999). The DLVO theory in microbial adhesion. Colloids and Surfaces B: Biointerfaces *14*, 105–119.

Hoehler, T. M., Alperin, M. J., Albert, D. B., Martens, S. and Field, A. (1994). Field and laboratory studies of methane oxidation in an anoxic marine sediment ' Evidence for a methanogen-sulfate reducer consortium that methanogens and. Global biogeochemical cycles *8*, 451–463.

Hoh, C. Y. and Cord-Ruwisch, R. (1996). A practical kinetic model that considers endproduct inhibition in anaerobic digestion processes by including the equilibrium constant. Biotechnology and bioengineering *51*, 597–604.

Hunter, J. D. (2007). Matplotlib: A 2D graphic environment. Computing in Science & Engineering *9*, 90–95.

Inoue, K., Leang, C., Franks, A. E., Woodard, T. L., Nevin, K. P. and Lovley, D. R. (2011). Specific localization of the c-type cytochrome OmcZ at the anode surface in current-producing biofilms of Geobacter sulfurreducens. Environmental Microbiology Reports *3*, 211–217.

Izaguirre, J. A., Chaturvedi, R., Huang, C., Cickovski, T., Coffland, J., Thomas, G., Forgacs, G., Alber, M., Hentschel, G., Newman, S. A. and Glazier, J. A. (2004). CompuCell, a multi-model framework for simulation of morphogenesis. Bioinformatics (Oxford, England) *20*, 1129–37.

Janulevicius, A., van Loosdrecht, M. C. M., Simone, A. and Picioreanu, C. (2010). Cell flexibility affects the alignment of model myxobacteria. Biophysical journal *99*, 3129–3138.

Kamyshny, Jr., A., Goifman, A., Gun, J., Rizkov, D. and Lev, O. (2004). Equilibrium Distribution of Polysulfide Ions in Aqueous Solutions at 25 ÂřC: A New Approach for the Study of Polysulfides' Equilibria. Environmental Science & Technology *38*, 6633–6644.

Kamyshny, Jr., A., Goifman, A., Rizkov, D. and Lev, O. (2003). Kinetics of Disproportionation of Inorganic Polysulfides in Undersaturated Aqueous Solutions at Environmentally Relevant Conditions. Aquatic Geochemistry *9*, 291–304.

Képès, F. (1986). The cell cycle of Escherichia coli and some of its regulatory systems. FEMS Microbiology Letters *32*, 225–246.

Knittel, K. and Boetius, A. (2009). Anaerobic oxidation of methane: progress with an unknown process. Annual review of microbiology *63*, 311–34.

Knittel, K., Boetius, A., Lemke, A., Eilers, H., Lochte, K., Pfannkuche, O., Linke, P. and Amann, R. (2003). Activity, Distribution, and Diversity of Sulfate Reducers and Other Bacteria in Sediments above Gas Hydrate (Cascadia Margin, Oregon). Geomicrobiology Journal *20*, 269–294.

Koch, A. L. and Wang, C. H. (1982). How close to the theoretical diffusion limit do bacterial uptake systems function? Archives of microbiology *131*, 36–42.

Kolenbrander, P. E. (2000). Oral microbial communities: biofilms, interactions, and genetic systems. Annual review of microbiology *54*, 413–37.

Kotloski, N. J. and Gralnick, J. A. (2013). Flavin electron shuttles dominate extracellular electron transfer by Shewanella oneidensis. mBio *4*, 10–13.

Kreft, J.-U., Booth, G. and Wimpenny, J. W. (1998). BacSim, a simulator for individual-based modelling of bacterial colony growth. Microbiology *144 (Pt 1*, 3275–87.

Kreft, J.-U., Picioreanu, C., Wimpenny, J. W. and van Loosdrecht, M. C. M. (2001). Individual-based modelling of biofilms. Microbiology *147*, 2897–2912.

Kurnikova, M. G., Coalson, R. D., Graf, P. and Nitzan, a. (1999). A lattice relaxation algorithm for three-dimensional Poisson-Nernst-Planck theory with application to ion transport through the gramicidin A channel. Biophysical journal *76*, 642–56.

Lardon, L. A., Merkey, B. V., Martins, S., Dötsch, A., Picioreanu, C., Kreft, J.-U. and Smets, B. F. (2011). iDynoMiCS: next-generation individual-based modelling of biofilms. Environmental microbiology *13*, 2416–2434.

Lau, A. O., Strom, P. F. and Jenkins, D. (1984). Growth kinetics of Sphaerotilus natans and a floc former in pure and dual continuous culture. Water Pollution Control Federation Journal *56*, 41–51.

Le-Clech, P., Chen, V. and Fane, T. a. G. (2006). Fouling in membrane bioreactors used in wastewater treatment. Journal of Membrane Science *284*, 17–53.

Leang, C., Qian, X., Mester, T. and Lovley, D. R. (2010). Alignment of the c-type cytochrome OmcS along pili of Geobacter sulfurreducens. Applied and Environmental Microbiology *76*, 4080–4084.

Leung, K. M., Wanger, G., El-Naggar, M. Y., Gorby, Y., Southam, G., Lau, W. M. and Yang, J. (2013). Shewanella oneidensis MR-1 bacterial nanowires exhibit p-type, tunable electronic behavior. Nano Letters *13*, 2407–2411.

Levar, C. E., Chan, C. H., Mehta-kolte, M. G. and Bond, D. R. (2014). High Redox Potential Extracellular Electron Acceptors. *5*, 1–9.

Liu, F., Rotaru, A.-E., Shrestha, P. M., Malvankar, N. S., Nevin, K. P. and Lovley, D. R. (2012). Promoting direct interspecies electron transfer with activated carbon. Energy & environmental science *5*, 8982–8989.

Liu, Y., Wang, Z., Liu, J., Levar, C., Edwards, M. J., Babauta, J. T., Kennedy, D. W., Shi, Z., Beyenal, H., Bond, D. R., Clarke, T. a., Butt, J. N., Richardson, D. J., Rosso, K. M., Zachara, J. M., Fredrickson, J. K. and Shi, L. (2014). A trans-outer membrane porin-cytochrome protein complex for extracellular electron transfer by Geobacter sulfurreducens PCA. Environmental Microbiology Reports *6*, 776–785.

Lovley, D. R. (2012). Electromicrobiology. Annual review of microbiology *66*, 391–409.

Lower, B. H., Shi, L., Yongsunthon, R., Droubay, T. C., McCready, D. E. and Lower, S. K. (2007). Specific bonds between an iron oxide surface and outer membrane cytochromes MtrC and OmcA from Shewanella oneidensis MR-1. Journal of bacteriology *189*, 4944–52.

Ly, H. K., Harnisch, F., Hong, S.-F., Schröder, U., Hildebrandt, P. and Millo, D. (2013). Unraveling the interfacial electron transfer dynamics of electroactive microbial biofilms using surface-enhanced Raman spectroscopy. ChemSusChem *6*, 487–492.

Madigan, M. T., Martinko, J. M., Stahl, D. A. and Clark, D. P. (2009). Brock Biology of Microorganisms. Brock Biology of Microorganisms, 13th ed. edition, Benjamin Cummings, San Francisco.

Malvankar, N. S., King, G. M. and Lovley, D. R. (2015). Centimeter-long electron transport in marine sediments via conductive minerals. The ISME Journal *9*, 527–531.

Malvankar, N. S. and Lovley, D. R. (2012). Microbial nanowires: a new paradigm for biological electron transfer and bioelectronics. ChemSusChem *5*, 1039–46.

Malvankar, N. S. and Lovley, D. R. (2014). Microbial nanowires for bioenergy applications. Current Opinion in Biotechnology *27*, 88–95.

Malvankar, N. S., Tuominen, M. T. and Lovley, D. R. (2012a). Comment on "On electrical conductivity of microbial nanowires and biofilms" by S. M. Strycharz-Glaven, R. M. Snider, A. Guiseppi-Elie and L. M. Tender, Energy Environ. Sci., 2011, 4, 4366. Energy & Environmental Science *5*, 6247.

Malvankar, N. S., Tuominen, M. T. and Lovley, D. R. (2012b). Lack of cytochrome involvement in long-range electron transport through conductive biofilms and nanowires of Geobacter sulfurreducens. Energy & Environmental Science *5*, 8651.

Malvankar, N. S., Vargas, M., Nevin, K. P., Franks, A. E., Leang, C., Kim, B.-C., Inoue, K., Mester, T., Covalla, S. F., Johnson, J. P., Rotello, V. M., Tuominen, M. T. and Lovley, D. R. (2011). Tunable metallic-like conductivity in microbial nanowire networks. Nature nanotechnology *6*, 573–579.

Malvankar, N. S., Yalcin, S. E., Tuominen, M. T. and Lovley, D. R. (2014). Visualization of charge propagation along individual pili proteins using ambient electrostatic force microscopy. Nature nanotechnology *9*, 1012–1017.

Marsili, E., Baron, D. B., Shikhare, I. D., Coursolle, D., Gralnick, J. a. and Bond, D. R. (2008). Shewanella secretes flavins that mediate extracellular electron transfer. Proceedings of the National Academy of Sciences of the United States of America *105*, 3968–3973.

Martins, A. M. P., Pagilla, K., Heijnen, J. J. and van Loosdrecht, M. C. M. (2004). Filamentous bulking sludge - a critical review. Water research *38*, 793–817.

Matsumoto, S., Katoku, M., Saeki, G., Terada, A., Aoi, Y., Tsuneda, S., Picioreanu, C. and van Loosdrecht, M. C. M. (2010). Microbial community structure in autotrophic nitrifying granules characterized by experimental and simulation analyses. Environmental microbiology *12*, 192–206.

Mehta, T., Coppi, M. V., Childers, S. E. and Lovley, D. R. (2005). Outer membrane c-type cytochromes required for Fe(III) and Mn(IV) oxide reduction in Geobacter sulfurreducens. Applied and environmental microbiology *71*, 8634–8641.

Melke, P., Sahlin, P., Levchenko, A. and Jönsson, H. (2010). A cell-based model for quorum sensing in heterogeneous bacterial colonies. PLoS computational biology *6*, e1000819.

Merkey, B. V., Rittmann, B. E. and Chopp, D. L. (2009). Modeling how soluble microbial products (SMP) support heterotrophic bacteria in autotroph-based biofilms. Journal of theoretical biology *259*, 670–83.

Milucka, J., Ferdelman, T. G., Polerecky, L., Franzke, D., Wegener, G., Schmid, M., Lieberwirth, I., Wagner, M., Widdel, F. and Kuypers, M. M. M. (2012). Zero-valent sulphur is a key intermediate in marine methane oxidation. Nature *491*, 541–6.

Moran, J. J., Beal, E. J., Vrentas, J. M., Orphan, V. J., Freeman, K. H. and House, C. H. (2008). Methyl sulfides as intermediates in the anaerobic oxidation of methane. Environmental Microbiology *10*, 162–173.

Morita, M., Malvankar, N. S., Franks, A. E., Summers, Z. M., Giloteaux, L., Rotaru, A.-E., Rotaru, C. and Lovley, D. R. (2011). Potential for direct interspecies electron transfer in methanogenic wastewater digester aggregates. mBio *2*, e00159–11.

Myers, C. R. and Myers, J. M. (2002). MtrB is required for proper incorporation of the cytochromes OmcA and OmcB into the outer membrane of Shewanella putrefaciens MR-1. Applied and Environmental Microbiology *68*, 5585–5594.

Myers, J. M. and Myers, C. R. (2000). Role of the tetraheme cytochrome CymA in anaerobic electron transport in cells of Shewanella putrefaciens MR-1 with normal levels of menaquinone. Journal of Bacteriology *182*, 67–75.

Nadell, C. D., Foster, K. R. and Xavier, J. B. (2010). Emergence of spatial structure in cell groups and the evolution of cooperation. PLoS computational biology *6*, e1000716.

Nadell, C. D., Xavier, J. B., Levin, S. a. and Foster, K. R. (2008). The evolution of quorum sensing in bacterial biofilms. PLoS biology *6*, e14.

Nagarajan, H., Embree, M., Rotaru, A.-E., Shrestha, P. M., Feist, A. M., Palsson, B. O., Lovley, D. R. and Zengler, K. (2013). Characterization and modelling of interspecies electron transfer mechanisms and microbial community dynamics of a syntrophic association. Nature communications *4*, 2809.

Nauhaus, K., Albrecht, M., Elvert, M., Boetius, A. and Widdel, F. (2007). In vitro cell growth of marine archaeal-bacterial consortia during anaerobic oxidation of methane with sulfate. Environmental microbiology *9*, 187–96.

Nauhaus, K., Boetius, A., Krüger, M. and Widdel, F. (2002). In vitro demonstration of anaerobic oxidation of methane coupled to sulphate reduction in sediment from a marine gas hydrate area. Environmental microbiology *4*, 296–305.

Nauhaus, K., Treude, T., Boetius, A. and Krüger, M. (2005). Environmental regulation of the anaerobic oxidation of methane: a comparison of ANME-I and ANME-II communities. Environmental microbiology *7*, 98–106.

Nikonenko, V. V., Kovalenko, A. V., Urtenov, M. K., Pismenskaya, N. D., Han, J., Sistat, P. and Pourcelly, G. (2014). Desalination at overlimiting currents: State-of-the-art and perspectives. Desalination *342*, 85–106.

Noren, D. and Hoffman, M. (2005). Clarifying the ButlerâĂŞVolmer equation and related approximations for calculating activation losses in solid oxide fuel cell models. Journal of Power Sources *152*, 175–181.

Okabe, S., Satoh, H. and Watanabe, Y. (1999). In situ analysis of nitrifying biofilms as determined by in situ hybridization and the use of microelectrodes. Applied and environmental microbiology *65*, 3182–3191.

Okamoto, A., Nakamura, R. and Hashimoto, K. (2011). In-vivo identification of direct electron transfer from Shewanella oneidensis MR-1 to electrodes via outer-membrane OmcAâĂŞMtrCAB protein complexes. Electrochimica Acta *56*, 5526–5531.

Okamoto, A., Nakamura, R., Ishii, K. and Hashimoto, K. (2009). In vivo electrochemistry of C-type cytochrome-mediated electron-transfer with chemical marking. Chembiochem : a European journal of chemical biology *10*, 2329–2332.

Orcutt, B. and Meile, C. (2008). Constraints on mechanisms and rates of anaerobic oxidation of methane by microbial consortia: process-based modeling of ANME-2 archaea and sulfate reducing bacteria. Biogeosciences Discussions *5*, 1587–1599.

Orphan, V. J., House, C. H., Hinrichs, K.-u., McKeegan, K. D. and Delong, E. F. (2001). Methane-consuming archaea revealed by directly coupled isotopic and phylogenetic analysis. Science *293*, 484–487.

Orphan, V. J. V., House, C. H., Hinrichs, K.-U., McKeegan, K. D. and Delong, E. F. (2002). Multiple archaeal groups mediate methane oxidation in anoxic cold seep sediments. Proceedings of the National Academy of Sciences of the United States of America *99*, 7663–7668.

Pfeffer, C., Larsen, S., Song, J. and Dong, M. (2012). Filamentous bacteria transport electrons over centimetre distances. Nature *491*, 218–221.

Picioreanu, C., Head, I. M., Katuri, K. P., van Loosdrecht, M. C. M. and Scott, K. (2007). A computational model for biofilm-based microbial fuel cells. Water research *41*, 2921–2940.

Picioreanu, C., Kreft, J.-U. and van Loosdrecht, M. C. M. (2004). Particle-Based Multidimensional Multispecies Biofilm Model. Applied and environmental microbiology *70*, 3024–3040.

Picioreanu, C., Van Loosdrecht, M. C. and Heijnen, J. J. (2000). Effect of diffusive and convective substrate transport on biofilm structure formation: a two-dimensional modeling study. Biotechnology and bioengineering *69*, 504–515.

Picioreanu, C. and van Loosdrecht, M. C. M. (2002). A Mathematical Model for Initiation of Microbiologically Influenced Corrosion by Differential Aeration. Journal of The Electrochemical Society *149*, B211.

Picioreanu, C., van Loosdrecht, M. C. M., Curtis, T. P. and Scott, K. (2010). Model based evaluation of the effect of pH and electrode geometry on microbial fuel cell performance. Bioelectrochemistry *78*, 8–24.

Pierucci, O. (1978). Dimensions of Escherichia coli at various growth rates: model for envelope growth. Journal of bacteriology *135*, 559–74.

Pirbadian, S., Barchinger, S. E., Leung, K. M., Byun, H. S., Jangir, Y., Bouhenni, R. a., Reed, S. B., Romine, M. F., Saffarini, D. a., Shi, L., Gorby, Y. a., Golbeck, J. H. and El-Naggar, M. Y. (2014). Shewanella oneidensis MR-1 nanowires are outer membrane and periplasmic extensions of the extracellular electron transport components. Proceedings of the National Academy of Sciences *111*, 12883–12888.

Pirbadian, S. and El-Naggar, M. Y. (2012). Multistep hopping and extracellular charge transfer in microbial redox chains. Physical chemistry chemical physics : PCCP *14*, 13802–8.

Pitts, K. E., Dobbin, P. S., Reyes-Ramirez, F., Thomson, A. J., Richardson, D. J. and Seward, H. E. (2003). Characterization of the Shewanella oneidensis MR-1 decaheme cytochrome MtrA: Expression in Escherichia coli confers the ability to reduce soluble FE(III) chelates. Journal of Biological Chemistry *278*, 27758–27765.

Popławski, N., Shirinifard, A., Swat, M. and Glazier, J. A. (2008). Simulation of single-species bacterial-biofilm growth using the Glazier-Graner-Hogeweg model and the CompuCell3D modeling environment. Mathematical biosciences and engineering *5*, 355–388.

Press, W. H., Teukolskky, S. A., Vetterling, W. T. and Flannery, B. P. (2007). Numerical Recipes: The Art of Scientific Computing. 3 edition, Cambridge University Press.

Qian, X., Reguera, G., Mester, T. and Lovley, D. R. (2007). Evidence that OmcB and OmpB of Geobacter sulfurreducens are outer membrane surface proteins. FEMS Microbiology Letters *277*, 21–27.

Reed, D. E. and Hawkridge, F. M. (1987). Direct electron transfer reactions of cytochrome c at silver electrodes. Analytical chemistry *59*, 2334–2339.

Reguera, G., McCarthy, K. D., Mehta, T., Nicoll, J. S., Tuominen, M. T. and Lovley, D. R. (2005). Extracellular electron transfer via microbial nanowires. Nature *435*, 1098–1101.

Rotaru, A.-E., Shrestha, P. M., Liu, F., Markovaite, B., Chen, S., Nevin, K. and Lovley, D. (2014a). Direct Interspecies Electron Transfer Between Geobacter metallireducens and Methanosarcina barkeri. Applied and environmental microbiology *80*, 4599–4605.

Rotaru, A.-E., Shrestha, P. M., Liu, F., Shrestha, M., Shrestha, D., Embree, M., Zengler, K., Wardman, C., Nevin, K. P. and Lovley, D. R. (2014b). A new model for electron flow during anaerobic digestion: direct interspecies electron transfer to Methanosaeta for the reduction of carbon dioxide to methane. Energy & environmental science *7*, 408–415.

Rothfield, L. I. and Zhao, C. R. (1996). How do bacteria decide where to divide? Cell *84*, 183–186.

Rudge, T. J., Steiner, P. J., Phillips, A. and Haseloff, J. (2012). Computational Modeling of Synthetic Microbial Biofilms. ACS synthetic biology *1*, 345–352.

Schmidt, J. E. and Ahring, B. K. (1996). Granular sludge formation in upflow anaerobic sludge blanket (UASB) reactors. Biotechnology and Bioengineering *49*, 229–246.

Schreiber, L., Holler, T., Knittel, K., Meyerdierks, A. and Amann, R. (2010). Identification of the dominant sulfate-reducing bacterial partner of anaerobic methanotrophs of the ANME-2 clade. Environmental microbiology *12*, 2327–40.

Schwarzenbach, G. and Fischer, A. (1960). Die Aciditat der Sulfane und die Zusammensetzung wasseriger Polysulfidlosungen. Helvetica Chimica Acta *241*, 1365–1390.

Seoane, J., Yankelevich, T., Dechesne, A., Merkey, B. V., Sternberg, C. and Smets, B. F. (2011). An individual-based approach to explain plasmid invasion in bacterial populations. FEMS microbiology ecology *75*, 17–27.

Seviour, R. J. and Nielsen, P. H. r., eds (2010). Microbial ecolog of Activated Sludge. First edit edition, IWA Publishing, London.

Sezgin, M., Jenkins, D. and Parker, D. S. (1978). A unified theory of filamentous activated sludge bulking. Journal of the Water Pollution Control Federation *50*, 362–381.

Shapiro, J. A. (1987). Organization of developing Escherichia coli colonies viewed by scanning electron microscopy. Journal of bacteriology *169*.

Shapiro, J. A. and Hsu, C. (1989). Escherichia coli K-12 cell-cell interactions seen by time-lapse video. Journal of Bacteriology *171*, 5963–5974.

Shi, L., Richardson, D. J., Wang, Z., Kerisit, S. N., Rosso, K. M., Zachara, J. M. and Fredrickson, J. K. (2009). The roles of outer membrane cytochromes of Shewanella and Geobacter in extracellular electron transfer. Environmental Microbiology Reports *1*, 220–227.

Shi, L., Squier, T. C., Zachara, J. M. and Fredrickson, J. K. (2007). Respiration of metal (hydr)oxides by Shewanella and Geobacter: A key role for multihaem c-type cytochromes. Molecular Microbiology *65*, 12–20.

Shrestha, P. M., Rotaru, A.-E., Aklujkar, M., Liu, F., Shrestha, M., Summers, Z. M., Malvankar, N., Flores, D. C. and Lovley, D. R. (2013). Syntrophic growth with direct interspecies electron transfer as the primary mechanism for energy exchange. Environmental microbiology reports *5*, 904–910.

Skarke, A., Ruppel, C., Kodis, M., Brothers, D. and Lobecker, E. (2014). Widespread methane leakage from the sea floor on the northern US Atlantic margin. Nature Geoscience *7*, 657–661.

Smith, J. M., Van Ness, H. C. and Abbott, M. M. (2001). Introduction to Chemical Engineering Thermodynamics, vol. 27,. 6th editio edition, McGraw-Hill.

Sø rensen, K. B., Finster, K. and Ramsing, N. B. (2001). Thermodynamic and Kinetic Requirements in Anaerobic Methane Oxidizing Consortia Exclude Hydrogen, Acetate, and Methanol as Possible Electron Shuttles. Microbial ecology *42*, 1–10.

Stams, A. J., De Bok, F. A. M., Plugge, C. M., van Eekert, M. H. A., Dolfing, J. and Schraa, G. (2006). Exocellular electron transfer in anaerobic microbial communities. Environmental Microbiology *8*, 371–382.

Stams, A. J. and Dong, X. (1995). Role of formate and hydrogen in the degradation of propionate and butyrate by defined suspended cocultures of acetogenic and methanogenic bacteria. Antonie van Leeuwenhoek *68*, 281–4.

Stams, A. J. and Plugge, C. M. (2009). Electron transfer in syntrophic communities of anaerobic bacteria and archaea. Nat Rev Micro *7*, 568–577.

Stephen, C. S., LaBelle, E. V., Brantley, S. L. and Bond, D. R. (2014). Abundance of the Multiheme c-Type Cytochrome OmcB Increases in Outer Biofilm Layers of Electrode-Grown Geobacter sulfurreducens. PloS one *9*, e104336.

Stewart, E. J., Madden, R., Paul, G. and Taddei, F. (2005). Aging and death in an organism that reproduces by morphologically symmetric division. PLoS biology *3*, 295–300.

Stewart, P. S. (2003). Diffusion in biofilms. Journal of bacteriology *185*, 1485–1491.

Storck, T., Picioreanu, C., Virdis, B. and Batstone, D. J. (2014). Variable Cell Morphology Approach for Individual-Based Modeling of Microbial Communities. Biophysical Journal *106*, 2037–2048.

Strycharz-Glaven, S. M., Snider, R. M., Guiseppi-Elie, A. and Tender, L. M. (2011). On the electrical conductivity of microbial nanowires and biofilms. Energy & Environmental Science *4*, 4366.

Strycharz-Glaven, S. M. and Tender, L. M. (2012). Reply to the ’Comment on "On electrical conductivity of microbial nanowires and biofilms"’ by N. S. Malvankar, M. T. Tuominen and D. R. Lovley, Energy Environ. Sci., 2012, 5, DOI: 10.1039/c2ee02613a. Energy & Environmental Science *5*, 6250.

Summers, Z. M., Fogarty, H. E., Leang, C., Franks, A. E., Malvankar, N. S. and Lovley, D. R. (2010). Direct Exchange of Electrons Within Aggregates of an Evolved Syntrophic Coculture of Anaerobic Bacteria. Science *330*, 1413–1415.

Tamulonis, C., Postma, M. and Kaandorp, J. (2011). Modeling filamentous cyanobacteria reveals the advantages of long and fast trichomes for optimizing light exposure. PloS one *6*, e22084.

Tierra, G., Pavissich, J. P., Nerenberg, R., Xu, Z. and Alber, M. S. (2015). Multicomponent model of deformation and detachment of a biofilm under fluid flow. Journal of the Royal Society Interface *12*, 1–13.

Treude, T., Boetius, a., Knittel, K., Wallmann, K. and Barker Jørgensen, B. (2003). Anaerobic oxidation of methane above gas hydrates at Hydrate Ridge, NE Pacific Ocean. Marine Ecology Progress Series *264*, 1–14.

van Loosdrecht, M. C. M., Eikelboom, D., Gjaltema, A., Tijhuis, L. and Heijnen, J. J. (1995). Biofilm structures. Water science & technology *32*, 35–43.

Vargas, M., Malvankar, N. S., Tremblay, P.-L., Leang, C., Smith, J. A., Patel, P., Synoeyenbos-West, O., Nevin, K. P. and Lovley, D. R. (2013). Aromatic Amino Acids Required for Pili Conductivity and Long-Range Extracellular Electron Transport in Geobacter sulfurreducens. mBio *4*, e00105–13.

Veazey, J. P., Reguera, G. and Tessmer, S. H. (2011). Electronic properties of conductive pili of the metal-reducing bacterium Geobacter sulfurreducens probed by scanning tunneling microscopy. Physical Review E - Statistical, Nonlinear, and Soft Matter Physics *84*, 1–4.

Virdis, B., Harnisch, F., Batstone, D. J., Rabaey, K. and Donose, B. C. (2012). Non-invasive characterization of electrochemically active microbial biofilms using confocal Raman microscopy. Energy Environ. Sci. *5*, 7017–7024.

Virdis, B., Millo, D., Donose, B. C. and Batstone, D. J. (2014). Real-time measurements of the redox states of c-type cytochromes in electroactive biofilms: a confocal resonance Raman Microscopy study. PloS one *9*, e89918.

Volle, C., Ferguson, M. and Aidala, K. (2009). Physical Properties of Native Biofilm Cells Explored by Atomic Force Microscopy. Biophysical Journal *96*, 398a.

Walker, C. and Sedlacek, M. J. (2007). An in vitro biofilm model of subgingival plaque. Oral Microbiology and Immunology *22*, 152–161.

Wanner, O. and Gujer, W. (1986). A multispecies biofilm model. Biotechnology and bioengineering *28*, 314–28.

Wigginton, N. S., Rosso, K. M., Lower, B. H., Shi, L. and Hochella, M. F. (2007). Electron tunneling properties of outer-membrane decaheme cytochromes from Shewanella oneidensis. Geochimica et Cosmochimica Acta *71*, 543–555.

Wilke, C. R. and Chang, P. (1955). Correlation of diffusion coefficients in dilute solutions. AIChE Journal *1*, 264–270.

Windisch, B., Bray, D. and Duke, T. (2006). Balls and chains–a mesoscopic approach to tethered protein domains. Biophysical journal *91*, 2383–2392.

Wood, B. D. and Whitaker, S. (1998). Diffusion and reaction in biofilms. Chemical engineering science *53*, 397–425.

Xavier, J. B., De Kreuk, M. K., Picioreanu, C. and Van Loosdrecht, M. C. M. (2007). Multi-scale individual-based model of microbial and bioconversion dynamics in aerobic granular sludge. Environmental science & technology *41*, 6410–6417.

Xavier, J. B. and Foster, K. R. (2007). Cooperation and conflict in microbial biofilms. Proceedings of the national academy of sciences of the United States of America *104*, 876–881.

Xavier, J. B., Picioreanu, C. and van Loosdrecht, M. C. M. (2005a). A general description of detachment for multidimensional modelling of biofilms. Biotechnology and bioengineering *91*, 651–669.

Xavier, J. B., Picioreanu, C. and van Loosdrecht, M. C. M. (2005b). A framework for multidimensional modelling of activity and structure of multispecies biofilms. Environmental microbiology *7*, 1085–1103.

Xie, B., Dai, X.-C. and Xu, Y.-T. (2007). Cause and pre-alarm control of bulking and foaming by Microthrix parvicella - A case study in triple oxidation ditch at a wastewater treatment plant. Journal of hazardous materials *143*, 184–191.

Yang, Y., Xu, M., Guo, J. and Sun, G. (2012). Bacterial extracellular electron transfer in bioelectrochemical systems. Process Biochemistry *47*, 1707–1714.

Zhang, Y., Maignien, L., Stadnitskaia, A., Boeckx, P., Xiao, X. and Boon, N. (2014). Stratified community responses to methane and sulfate supplies in mud volcano deposits: insights from an in vitro experiment. PloS one *9*, e113004.

APPENDICES

APPENDIX A SUPPLEMENTARY MATERIAL AVAILABLE ONLINE

Chapter 2

Supplementary movie 1: Animation of E. coli biofilm growth without anchoring links, without filial links, without DLVO forces (IbM version 2015)

Supplementary movie 2: Animation of E. coli biofilm growth without anchoring links, without filial links, with DLVO forces (IbM version 2015)

Supplementary movie 3: Animation of E. coli biofilm growth without anchoring links, without filial links, with DLVO forces (IbM version 2014)

Supplementary movie 4: Animation of E. coli biofilm growth with anchoring links, without filial links, with DLVO forces (IbM version 2014)

Supplementary movie 5: Animation of E. coli biofilm growth without anchoring links, with filial links, with DLVO forces (IbM version 2014)

Supplementary movie 6: Animation of E. coli biofilm growth with anchoring links, without filial links, with DLVO forces (IbM version 2015)

Supplementary movie 7: Animation of E. coli biofilm growth with gliding cell-substratum links, without filial links, with DLVO forces (IbM version 2015)

Supplementary movie 8: Animation of activated sludge aggregate growth, low substrate concentration (default case) (IbM version 2014)

Supplementary movie 9: Animation of activated sludge aggregate growth, high substrate concentration (IbM version 2014)

Supplementary movie 10: Animation of activated sludge aggregate growth, low substrate concentration, stiff filial links (IbM version 2014)

Supplementary movie 11: Animation of activated sludge aggregate growth, low substrate concentration, flexible filial links (IbM version 2014)

Supplementary movie 12: Animation of activated sludge aggregate growth, low substrate concentration, strong sticking links (IbM version 2014)

Supplementary movie 13: Animation of activated sludge aggregate growth, low substrate concentration, weak sticking links (IbM version 2014)

Supplementary movie 14: Animation of floc growth resulting in interfloc bridging, low substrate concentration (IbM version 2015)

Supplementary movie 15: Animation of activated sludge aggregate growth, low substrate concentration, with 30% chance of filament branching (IbM version 2014)

Supplementary movie 16: Animation of activated sludge aggregate growth, low substrate concentration, with sphere-shaped floc former (IbM version 2014)

Movies are available on UQ eSpace:
espace.uq.edu.au
Movies based on IbM version 2014 are also available via the Biophysical Journal website:
www.biophysj.org/biophysj/supplemental/S0006-3495(14)00291-4.

Chapter 3

Supplementary movie 17: Three-dimensional view of cell positions and potential field for the multicellular direct IET system. The colour bar and scale is the same as in figure 3.4.

Movies are available on UQ eSpace:
espace.uq.edu.au

Chapter 4

Supplementary movie 18: AOM/SR aggregate development for sticking links between ANME-ANME cells only, $k_{s,s,ANME-ANME} = 1 \times 10^{-12}\,\mathrm{N\,m^{-1}}$, organised inoculum (default).

Supplementary movie 19: AOM/SR aggregate development without sticking links, organised inoculum.

Supplementary movie 20: AOM/SR aggregate development for sticking links between ANME-ANME and ANME-DSS cells, $k_{s,s,ANME-ANME} = k_{s,s,ANME-DSS} = 1 \times 10^{-12}\,\mathrm{N\,m^{-1}}$, organised inoculum.

Supplementary movie 21: AOM/SR aggregate development for sticking links between all cell types, $k_{s,s,ANME-ANME} = k_{s,s,ANME-DSS} = k_{s,s,DSS-DSS} = 1 \times 10^{-12}\,\mathrm{N\,m^{-1}}$, organised inoculum.

Supplementary movie 22: AOM/SR aggregate development for sticking links between all cell types, $k_{s,s,ANME-ANME} = 1 \times 10^{-12}\,\mathrm{N\,m^{-1}}$, $k_{s,s,ANME-DSS} = k_{s,s,DSS-DSS} = 1 \times 10^{-13}\,\mathrm{N\,m^{-1}}$, organised inoculum.

Supplementary movie 23: AOM/SR aggregate development for sticking links between all cell types, $k_{s,s,ANME-ANME} = 1 \times 10^{-12}\,\mathrm{N\,m^{-1}}$, $k_{s,s,ANME-DSS} = k_{s,s,DSS-DSS} = 1 \times 10^{-14}\,\mathrm{N\,m^{-1}}$, organised inoculum.

Supplementary movie 24: AOM/SR aggregate development for sticking links between all cell types, $k_{s,s,ANME-ANME} = 1 \times 10^{-12}\,\mathrm{N\,m^{-1}}$, $k_{s,s,ANME-DSS} = k_{s,s,DSS-DSS} = 1 \times 10^{-15}\,\mathrm{N\,m^{-1}}$, organised inoculum.

Supplementary movie 25: AOM/SR aggregate development for sticking links between ANME-ANME cells only, $k_{s,s,ANME-ANME} = 1 \times 10^{-12}\,\mathrm{N\,m^{-1}}$, random inoculum with seed A.

Supplementary movie 26: AOM/SR aggregate development for sticking links between ANME-ANME cells only, $k_{s,s,ANME-ANME} = 1 \times 10^{-12}\,\mathrm{N\,m^{-1}}$, random inoculum with seed B.

Movies are available on UQ eSpace:
espace.uq.edu.au

APPENDIX B NOMENCLATURE AND DEFAULT PARAMETER VALUES FOR INTERSPECIES ELECTRON TRANSFER MODEL

Table B.1: Nomenclature and default parameter values for interspecies electron transfer model

Symbol	Unit	Description	Default value	Reference and notes
Subscripts				
A		Acid dissociation		As in Batstone et al. (2002)
act		Redox complex activation		Used for DIET only
B		Biological (component-specific)		
bal		Balancing		Used for DIET only
$cell$		Any cell (same for all cells)		
i		Chemical component		
IET		Interspecies electron transfer		
inh		Inhibition		
j		Specific biological cell (different for other cell)		
jk		Specific cell pair (different for other cell pair)		Used for DIET only
k		Biological cell connected to j		Used for DIET only
mig		(Due to) migration		Used for DIET only
min		Minimum		
net		After losses		Used for DIET only
nw		Nanowire		Used for DIET only
$pair$		Any cell pair (same for all cell pairs)		Used for DIET only
r		Reaction (gross, before losses)		
X		Biomass (cell-specific)		

Table B.1 (continued): Nomenclature and default parameter values for interspecies electron transfer model

Symbol	Unit	Description	Default value	Reference and notes
Geometry				
A_{cell}	m^2	Surface area of cell	3.14×10^{-12}	Calculated from d_{cell}
d_{cell}	m	Diameter of cell (acetogen, methanogen)	1.00×10^{-6}	
L	m	Length or dimension		
		Length (x) of domain - two-cell system	17.0×10^{-6}	
		Depth (y) of domain - two-cell system	11.0×10^{-6}	
		Height (z) of domain - two-cell system	11.0×10^{-6}	
		Length (x) of domain - multicellular	30.0×10^{-6}	
		Depth (y) of domain - multicellular	30.0×10^{-6}	
		Height (z) of domain - multicellular	30.0×10^{-6}	
c	$mol\,m^{-3}$	Local concentration		
$\langle c\rangle$	$mol\,m^{-3}$	Average cell surface concentration		
c_0	$mol\,m^{-3}$	Fixed boundary concentration		
		Propionic acid	7.41×10^{-3}	
		Propionate	1.00	
		Acetic acid	5.75×10^{-3}	
		Acetate	1.00	
		Carbon dioxide	22.39	
		Bicarbonate	100	
		Methane	0.1438	Calculated from p0,CH4
		Proton	$1.00\times10-4$	pH 7
		Hydroxide	$1.01\times10-4$	
		Chloride	1000	

Table B.1 (continued): Nomenclature and default parameter values for interspecies electron transfer model

Symbol	Unit	Description	Default value	Reference and notes
		Potassium ion	1102	Closes charge balance
H	$\mathrm{mol\,m^{-3}\,Pa^{-1}}$	Henry coefficient		
		Hydrogen	$0.795\times10-5$	Haynes (2014)
		Methane	$1.44\times10-5$	Haynes (2014)
p	Pa	Local partial pressure		
p_0	Pa	Fixed boundary partial pressure		
		Methane	1.00×104	
<u>Nernst-Planck</u>				
D	$\mathrm{m^2\,s^{-1}}$	Diffusion coefficient		At 298 K
		Hydrogen	5.11×10^{-9}	Haynes (2014)
		Formic acid	1.50×10^{-9}	Cussler (1997)
		Formate	1.45×10^{-9}	Haynes (2014)
		Propionic acid	1.06×10^{-9}	Cussler (1997)
		Propionate	0.953×10^{-9}	Haynes (2014)
		Acetic acid	1.29×10^{-9}	Haynes (2014)
		Acetate	1.09×10^{-9}	Haynes (2014)
		Carbon dioxide	1.91×10^{-9}	Haynes (2014)
		Bicarbonate	1.19×10^{-9}	Haynes (2014)
		Methane	1.84×10^{-9}	Haynes (2014)
		Proton	9.31×10^{-9}	Haynes (2014)
		Hydroxide	5.27×10^{-9}	Haynes (2014)
		Chloride	2.03×10^{-9}	Haynes (2014)
		Potassium ion	1.96×10^{-9}	Haynes (2014)

Table B.1 (continued): Nomenclature and default parameter values for interspecies electron transfer model

Symbol	Unit	Description	Default value	Reference and notes
F	$\mathrm{C\,mol^{-1}}$	Faraday's constant	96485	
J	$\mathrm{mol\,m^{-2}\,s^{-1}}$	Flux		
R	$\mathrm{J\,mol^{-1}\,K^{-1}}$	Ideal gas constant	8.3145	
T	K	Temperature	298	
z	–	Charge of ion		
Reaction rate				
f_{bal}	–	Scaling factor for electron balancing		Used for DIET only
f_{inh}	–	Limitation or inhibition factor		
K	–	Reaction quotient		
r	$\mathrm{mol\,m^{-3}\,s^{-1}}$	Volume-specific reaction rate		
r_X^{max}	$\mathrm{mol\,m^{-3}\,s^{-1}}$	Maximum biomass conversion rate		Arbitrarily chosen to be much greater than r_X
$rateIET$	$\mathrm{e^-/s}$	Absolute electron transfer rate		
$Y_{X/S}$	$\mathrm{Cmol\,mol^{-1}}$	Yield biomass over substrate	0.15	Supplementary Figure 1
ν	–	Stoichiometry in reaction		
Acid dissociation				
pK_a	–	-log10 acid diss. constant		At 298 K
		Formic acid	3.75	Haynes (2014)
		Propionic acid	4.87	Haynes (2014)
		Acetic acid	4.76	Haynes (2014)
		Carbon dioxide	6.35	Haynes (2014)
		Water	14.0	Haynes (2014)
Thermodynamics				

Table B.1 (continued): Nomenclature and default parameter values for interspecies electron transfer model

Symbol	Unit	Description	Default value	Reference and notes
ΔG^0_{form}	$\mathrm{J\,mol^{-1}}$	Gibbs free energy change of formation (standard conditions, pH 0)		Haynes (2014)
$\Delta G'_r$	$\mathrm{J\,mol^{-1}}$	Free energy change available from biological reaction in cell		Function of $\langle ci \rangle_j$ and ν_{ji} for all involved i
$\Delta G' min$	$\mathrm{J\,mol^{-1}}$	Min. req. $\Delta G'$ for cell anabolism, maintenance	-15.2×10^3	Boone and Bryant (1980), based on formate-MIET
Electrochemical (DIET only)				
c_{act}	$\mathrm{mol\,m^{-2}}$	Redox complex surface concentration	5.29×10^{-9}	Calculated from A_{cell} and $N_{act,cell}$
E	$\mathrm{V\,m^{-1}}$	Electric field		
V	V	Potential difference		
V_{min}	V	Min. V req. for anabolism and maintenance	52.51×10^{-3}	
η	V	Voltage drop or potential loss		
Φ	V	Potential field		
Butler-Volmer (DIET only)				
$A_{act,cell}$	$\mathrm{m^2}$	Total area for redox complex activation for any cell	3.14×10^{-13}	10% of A_{cell}, Appendix C
k_0	$\mathrm{s^{-1}}$	Standard activation rate constant	6000	Appendix C
$N_{act,j}$		Number of redox complexes per nanowire for cell j		$N_{act,cell}/N_{nw,j}$
$N_{act,cell}$		Number of redox complexes per cell	1.0×10^4	Lower et al. (2007)
β	–	Symmetry factor	0.5	
Ohm's law (DIET only)				
A_{nw}	$\mathrm{m^2}$	Cross-sectional area of single nanowire	1.26×10^{-17}	Calculated from d_{nw}
d_{nw}	m	Diameter of single nanowire	4.00×10^{-9}	Malvankar et al. (2011)
L_{nw}	m	Length of single nanowire		Equal to interspecies distance
$N_{nw,j}$		Total number of nanowires connected to cell j		$N_{nw,pair}$ per connected cell k
$N_{nw,pair}$		Number of nanowires formed per cell pair	100	

Table B.1 (continued): Nomenclature and default parameter values for interspecies electron transfer model

Symbol	Unit	Description	Default value	Reference and notes
$R_{nw,jk}$	Ω	Ohmic resistance of nanowire		
ρ_{nw}	$\Omega\,\mathrm{m}$	Electrical resistivity of nanowire	1.0	Malvankar et al. (2011)

APPENDIX C CALCULATION OF CYTOCHROME COVERAGE AND CONCENTRATION FROM PUBLISHED EXPERIMENTAL DATA (LOWER ET AL., 2007; WIGGINTON ET AL., 2007)

Table C.1: An Excel sheet with these calculations is available as supplementary material of the paper, see section Peer-reviewed papers.

Parameter	Value range		Unit	Reference
	Lower	Upper		
Avogadro's constant	6.02×10^{23}	6.02×10^{23}	mol^{-1}	
Cytochromes per cell for DEET	1.00×10^{4}	1.00×10^{4}	–	Lower et al. (2007)
Diameter of cytochrome	5	8	nm	Wigginton et al. (2007)
Projected surface area of single cyt.	2.0×10^{-17}	5.0×10^{-17}	m^2	
Diameter of cell	1	1	µm	
Surface area of single cell	3.1×10^{-12}	3.1×10^{-12}	m^2	
Relative cytochrome coverage DEET	6.25%	16.00%	$\mathrm{m}^2\ \mathrm{cyt}\,(\mathrm{m}^2\ \mathrm{cell})^{-1}$	
Cytochrome concentration	5.29×10^{-9}	5.29×10^{-9}	$\mathrm{mol\,m}^{-2}$	

APPENDIX D COMPARISON OF CALCULATED HETEROGENEOUS EXCHANGE CURRENT DENSITY TO PUBLISHED EXPERIMENTAL DATA (REED & HAWKRIDGE, 1987; BOWDEN *et al.*, 1982)

Table D.1: An Excel sheet with these calculations is available as supplementary material of the published paper, see Peer-reviewed papers.

c_{act} mol m^{-3}	c^s_{act} mol m^{-2}	$k_{0,vol}$ m s^{-1}	k_0 s^{-1}	i_0 A m^{-2}	Reference
0.199		1.50×10^{-5}		0.288	Reed and Hawkridge (1987)
0.199		9.10×10^{-6}		0.175	Reed and Hawkridge (1987)
0.091		6.00×10^{-6}		0.0527	Reed and Hawkridge (1987)
0.091		4.70×10^{-6}		0.0413	Reed and Hawkridge (1987)
0.181		2.80×10^{-6}		0.0489	Reed and Hawkridge (1987)
0.181		3.70×10^{-6}		0.0646	Reed and Hawkridge (1987)
0.098		1.60×10^{-5}		0.151	Reed and Hawkridge (1987)
0.098		1.60×10^{-5}		0.151	Reed and Hawkridge (1987)
0.051		2.20×10^{-5}		0.108	Reed and Hawkridge (1987)
0.038		4.90×10^{-5}		0.180	Bowden et al. (1982)
0.073		1.70×10^{-5}		0.120	Bowden et al. (1982)
0.3		8.10×10^{-6}		0.234	Bowden et al. (1982)
0.073		1.00×10^{-6}		0.00704	Bowden et al. (1982)
	5.29×10^{-9}		150	0.0766	Appendix C, Okamoto et al. (2009)

APPENDIX E DERIVATION OF MINIMUM GIBBS FREE ENERGY REQUIREMENT FOR FORMATE-MIET

The minimum Gibbs free energy change required for IET is approximated by adjusting $\Delta G'_{min}$ to obtain an IET rate close to the value estimated from literature. The equations describing the IET rate were given in subsection 3.2.3:

$$r_{X,j} = \begin{cases} r_X^{max} f_{inh,MIET,j} & \text{for MIET} \\ r_X^{max} f_{inh,MIET,jk} & \text{for DIET, two-cell system} \end{cases} \tag{3.5}$$

$$f_{inh,MIET,j} = 1 - \exp\left(\Delta G'_{r,j} - \Delta G'_{min}/RT\right) \tag{3.6}$$

$$rate_{IET,j} = r_{X,j} \pi {d_{cell}}^3 N_A \tag{3.10}$$

In order to estimate $rate_{IET}$, the first data points of an OD-600 absorbance spectrometry experiment described by Boone and Bryant (1980) is analysed. The growth rate μ during the exponential growth phase can be estimated by fitting a function $m = m_0 e^{\mu t}$ to the first three data points (see figure E.1). The best fit was obtained using $\mu = 0.20\ \mathrm{d}^{-1}$. Assuming a yield $Y_{X/S} = 0.15\ \mathrm{Cmol\,mol}^{-1}$ and knowing 6 mol electrons is transferred per mol substrate consumed, the IET rate is calculated using equation E.1:

$$rate_{IET} = \frac{6\mu\,(vol_X \rho_X)}{Y_{s/x} MW_X} N_A \tag{E.1}$$

The resulting IET rate is around $300 \times 10^3\ \mathrm{e}^-/\mathrm{s}$. A summary of this method is given in figure E.1.

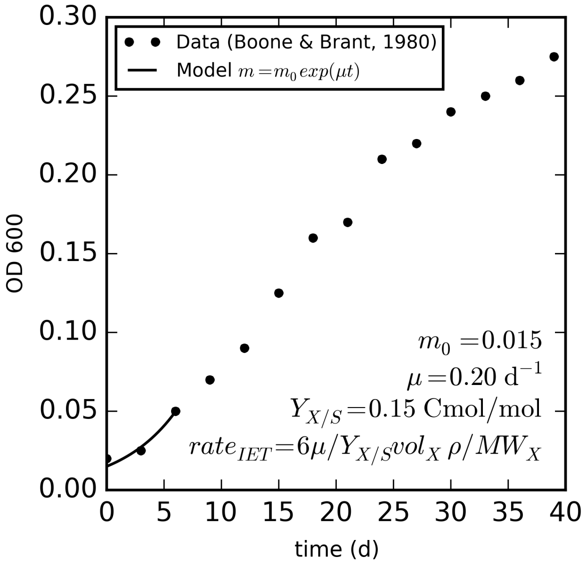

Figure E.1: Summary of method to estimate $\Delta G'_{min}$ from literature

APPENDIX F MODEL PARAMETERS AOM/SR DIFFUSION-REACTION MODEL

Table F.1: Model parameters for AOM/SR diffusion-reaction model

Parameter	Symbol	Default value	Units	Reference
Boundary concentrations				
methane	$c_{0,\mathrm{CH_4}}$	1.50×10^{-3}	$\mathrm{mol\,L^{-1}}$	Table S3 in Milucka et al. (2012)
sulfate	$c_{0,\mathrm{SO_4}^{2-}}$	15.9×10^{-3}	$\mathrm{mol\,L^{-1}}$	Table S3 in Milucka et al. (2012)
proton	$c_{0,\mathrm{H^+}}$	1.00×10^{-7}	$\mathrm{mol\,L^{-1}}$	Table S3 in Milucka et al. (2012)
bicarbonate	$c_{0,\mathrm{HCO_3}^-}$	2.06×10^{-2}	$\mathrm{mol\,L^{-1}}$	Table S3 in Milucka et al. (2012)
hydrogen sulfide	$c_{0,\mathrm{H_2S}}$	5.68×10^{-4}	$\mathrm{mol\,L^{-1}}$	Calculated from acid diss. and spec.
bisulfide	$c_{0,\mathrm{HS^-}}$	8.40×10^{-4}	$\mathrm{mol\,L^{-1}}$	Calculated from acid diss. and spec.
sulfide	$c_{0,\mathrm{S2-}}$	8.40×10^{-11}	$\mathrm{mol\,L^{-1}}$	Calculated from acid diss. and spec.
hydrogen disulfide	$c_{0,\mathrm{H_2S_2}}$	1.46×10^{-7}	$\mathrm{mol\,L^{-1}}$	Calculated from acid diss. and spec.
hydrodisulfide	$c_{0,\mathrm{HS_2}^-}$	1.46×10^{-5}	$\mathrm{mol\,L^{-1}}$	Table S3 in Milucka et al. (2012)
disulfide	$c_{0,\mathrm{S_2}^{2-}}$	2.91×10^{-8}	$\mathrm{mol\,L^{-1}}$	Calculated from acid diss. and spec.
hydrogen trisulfide	$c_{0,\mathrm{H_2S_3}}$	1.53×10^{-9}	$\mathrm{mol\,L^{-1}}$	Calculated from acid diss. and spec.
hydrotrisulfide	$c_{0,\mathrm{HS_3}^-}$	9.65×10^{-7}	$\mathrm{mol\,L^{-1}}$	Calculated from acid diss. and spec.
trisulfide	$c_{0,\mathrm{S_3}^{2-}}$	3.05×10^{-7}	$\mathrm{mol\,L^{-1}}$	Calculated from acid diss. and spec.
hydrogen tetrasulfide	$c_{0,\mathrm{H_2S_4}}$	2.11×10^{-10}	$\mathrm{mol\,L^{-1}}$	Calculated from acid diss. and spec.
hydrotetrasulfide	$c_{0,\mathrm{HS_4}^-}$	3.34×10^{-7}	$\mathrm{mol\,L^{-1}}$	Calculated from acid diss. and spec.
tetrasulfide	$c_{0,\mathrm{S_4}^{2-}}$	1.68×10^{-6}	$\mathrm{mol\,L^{-1}}$	Calculated from acid diss. and spec.
hydrogen pentasulfide	$c_{0,\mathrm{H_2S_5}}$	4.51×10^{-11}	$\mathrm{mol\,L^{-1}}$	Calculated from acid diss. and spec.
hydropentasulfide	$c_{0,\mathrm{HS_5}^-}$	1.43×10^{-7}	$\mathrm{mol\,L^{-1}}$	Calculated from acid diss. and spec.
pentasulfide	$c_{0,\mathrm{S_5}^{2-}}$	2.85×10^{-6}	$\mathrm{mol\,L^{-1}}$	Calculated from acid diss. and spec.
hydrogen hexasulfide	$c_{0,\mathrm{H_2S_6}}$	1.16×10^{-15}	$\mathrm{mol\,L^{-1}}$	Calculated from acid diss. and spec.
hydrohexasulfide	$c_{0,\mathrm{HS_6}^-}$	1.16×10^{-8}	$\mathrm{mol\,L^{-1}}$	Calculated from acid diss. and spec.
hexasulfide	$c_{0,\mathrm{S_6}^{2-}}$	1.84×10^{-6}	$\mathrm{mol\,L^{-1}}$	Calculated from acid diss. and spec.
hydrogen heptasulfide	$c_{0,\mathrm{H_2S_7}}$	4.83×10^{-21}	$\mathrm{mol\,L^{-1}}$	Calculated from acid diss. and spec.
hydroheptasulfide	$c_{0,\mathrm{HS_7}^-}$	4.83×10^{-14}	$\mathrm{mol\,L^{-1}}$	Calculated from acid diss. and spec.
heptasulfide	$c_{0,\mathrm{S_7}^{2-}}$	4.83×10^{-7}	$\mathrm{mol\,L^{-1}}$	Calculated from acid diss. and spec.
hydrogen octasulfide	$c_{0,\mathrm{H_2S_8}}$	1.36×10^{-21}	$\mathrm{mol\,L^{-1}}$	Calculated from acid diss. and spec.
hydrooctasulfide	$c_{0,\mathrm{HS_8}^-}$	1.36×10^{-14}	$\mathrm{mol\,L^{-1}}$	Calculated from acid diss. and spec.
octasulfide	$c_{0,\mathrm{S_8}^{2-}}$	1.36×10^{-7}	$\mathrm{mol\,L^{-1}}$	Calculated from acid diss. and spec.
Biomass properties				

Table F.1 (continued): Model parameters for AOM/SR diffusion-reaction model

Parameter	Symbol	Default value	Units	Reference
specific growth rate	μ	–	day^{-1}	via Monte-Carlo analysis
biomass yield	$Y_{X,S}$	0.01	$\mathrm{Cmol\,mol}^{-1}$	Nauhaus et al. (2007)
Aggregate geometry				
radius inner core	R_{inner}	$0.8 \times R_{outer}$	m	Nauhaus et al. (2007)
radius outer shell	R_{outer}	–	m	via Monte-Carlo analysis
radius boundary layer	$R_{boundary}$	$R_{outer} + 10\,\mu\mathrm{m}$	m	
Acid dissociation constants				
carbon dioxide	$K_{a,\mathrm{CO_2}}$	4.47×10^{-7}	$\mathrm{mol\,L}^{-1}$	Haynes (2014)
hydrogen sulfide	$K_{a,\mathrm{H_2S}}$	1.48×10^{-7}	$\mathrm{mol\,L}^{-1}$	Schwarzenbach and Fischer (1960)
bisulfide	K_{a,HS^-}	1.00×10^{-14}	$\mathrm{mol\,L}^{-1}$	Schwarzenbach and Fischer (1960)
hydrogen disulfide	$K_{a,\mathrm{H_2S_2}}$	1.00×10^{-5}	$\mathrm{mol\,L}^{-1}$	Schwarzenbach and Fischer (1960)
hydrodisulfide	$K_{a,\mathrm{HS_2}^-}$	2.00×10^{-10}	$\mathrm{mol\,L}^{-1}$	Schwarzenbach and Fischer (1960)
hydrogen trisulfide	$K_{a,\mathrm{H_2S_3}}$	6.31×10^{-5}	$\mathrm{mol\,L}^{-1}$	Schwarzenbach and Fischer (1960)
hydrotrisulfide	$K_{a,\mathrm{HS_3}^-}$	3.16×10^{-8}	$\mathrm{mol\,L}^{-1}$	Schwarzenbach and Fischer (1960)
hydrogen tetrasulfide	$K_{a,\mathrm{H_2S_4}}$	1.58×10^{-4}	$\mathrm{mol\,L}^{-1}$	Schwarzenbach and Fischer (1960)
hydrotetrasulfide	$K_{a,\mathrm{HS_4}^-}$	5.01×10^{-7}	$\mathrm{mol\,L}^{-1}$	Schwarzenbach and Fischer (1960)
hydrogen pentasulfide	$K_{a,\mathrm{H_2S_5}}$	3.16×10^{-4}	$\mathrm{mol\,L}^{-1}$	Schwarzenbach and Fischer (1960)
hydropentasulfide	$K_{a,\mathrm{HS_5}^-}$	2.00×10^{-6}	$\mathrm{mol\,L}^{-1}$	Schwarzenbach and Fischer (1960)
hydrogen hexasulfide	$K_{a,\mathrm{H_2S_6}}$	1	$\mathrm{mol\,L}^{-1}$	Assumed
hydrohexasulfide	$K_{a,\mathrm{HS_6}^-}$	1.58×10^{-5}	$\mathrm{mol\,L}^{-1}$	Schwarzenbach and Fischer (1960)
hydrogen heptasulfide	$K_{a,\mathrm{H_2S_7}}$	1	$\mathrm{mol\,L}^{-1}$	Assumed
hydroheptasulfide	$K_{a,\mathrm{HS_7}^-}$	1	$\mathrm{mol\,L}^{-1}$	Assumed
hydrogen octasulfide	$K_{a,\mathrm{H_2S_8}}$	1	$\mathrm{mol\,L}^{-1}$	Assumed
hydrooctasulfide	$K_{a,\mathrm{HS_8}^-}$	1	$\mathrm{mol\,L}^{-1}$	Assumed
Precipitation constants				
disulfide	$K_{s,\mathrm{S_2}^{2-}}$	3.47×10^{-12}	$\mathrm{mol\,L}^{-1}$	Kamyshny, Jr. et al. (2004)
trisulfide	$K_{s,\mathrm{S_3}^{2-}}$	3.63×10^{-11}	$\mathrm{mol\,L}^{-1}$	Kamyshny, Jr. et al. (2004)
tetrasulfide	$K_{s,\mathrm{S_4}^{2-}}$	2.00×10^{-10}	$\mathrm{mol\,L}^{-1}$	Kamyshny, Jr. et al. (2004)
pentasulfide	$K_{s,\mathrm{S_5}^{2-}}$	3.39×10^{-10}	$\mathrm{mol\,L}^{-1}$	Kamyshny, Jr. et al. (2004)
hexasulfide	$K_{s,\mathrm{S_6}^{2-}}$	2.19×10^{-10}	$\mathrm{mol\,L}^{-1}$	Kamyshny, Jr. et al. (2004)
heptasulfide	$K_{s,\mathrm{S_7}^{2-}}$	5.75×10^{-11}	$\mathrm{mol\,L}^{-1}$	Kamyshny, Jr. et al. (2004)
octasulfide	$K_{s,\mathrm{S_8}^{2-}}$	1.62×10^{-11}	$\mathrm{mol\,L}^{-1}$	Kamyshny, Jr. et al. (2004)
Diffusion coefficients				
methane	$D_{\mathrm{CH_4}}$	1.84×10^{-9}	$\mathrm{m^2\,s}^{-1}$	Haynes (2014)

Table F.1 (continued): Model parameters for AOM/SR diffusion-reaction model

Parameter	Symbol	Default value	Units	Reference
sulfate	$D_{{SO_4}^{2-}}$	1.07×10^{-9}	$m^2\,s^{-1}$	Haynes (2014)
proton	D_{H^+}	9.31×10^{-9}	$m^2\,s^{-1}$	Haynes (2014)
carbon dioxide	D_{CO_2}	1.91×10^{-9}	$m^2\,s^{-1}$	Haynes (2014)
bicarbonate	$D_{{HCO_3}^-}$	1.19×10^{-9}	$m^2\,s^{-1}$	Haynes (2014)
hydrogen sulfide	D_{H_2S}	2.32×10^{-9}	$m^2\,s^{-1}$	Wilke and Chang (1955); Albright (2008)
bisulfide	D_{HS^-}	2.49×10^{-9}	$m^2\,s^{-1}$	Wilke and Chang (1955); Albright (2008)
sulfide	$D_{{S_2}^-}$	2.70×10^{-9}	$m^2\,s^{-1}$	Wilke and Chang (1955); Albright (2008)
hydrogen disulfide	$D_{H_2S_2}$	1.64×10^{-9}	$m^2\,s^{-1}$	Wilke and Chang (1955); Albright (2008)
hydrodisulfide	$D_{{HS_2}^-}$	1.70×10^{-9}	$m^2\,s^{-1}$	Wilke and Chang (1955); Albright (2008)
disulfide	$D_{{S_2}^{2-}}$	1.78×10^{-9}	$m^2\,s^{-1}$	Wilke and Chang (1955); Albright (2008)
hydrogen trisulfide	$D_{H_2S_3}$	1.32×10^{-9}	$m^2\,s^{-1}$	Wilke and Chang (1955); Albright (2008)
hydrotrisulfide	$D_{{HS_3}^-}$	1.36×10^{-9}	$m^2\,s^{-1}$	Wilke and Chang (1955); Albright (2008)
trisulfide	$D_{{S_3}^{2-}}$	1.40×10^{-9}	$m^2\,s^{-1}$	Wilke and Chang (1955); Albright (2008)
hydrogen tetrasulfide	$D_{H_2S_4}$	1.13×10^{-9}	$m^2\,s^{-1}$	Wilke and Chang (1955); Albright (2008)
hydrotetrasulfide	$D_{{HS_4}^-}$	1.15×10^{-9}	$m^2\,s^{-1}$	Wilke and Chang (1955); Albright (2008)
tetrasulfide	$D_{{S_4}^{2-}}$	1.18×10^{-9}	$m^2\,s^{-1}$	Wilke and Chang (1955); Albright (2008)
hydrogen pentasulfide	$D_{H_2S_5}$	0.995×10^{-9}	$m^2\,s^{-1}$	Wilke and Chang (1955); Albright (2008)
hydropentasulfide	$D_{{HS_5}^-}$	1.01×10^{-9}	$m^2\,s^{-1}$	Wilke and Chang (1955); Albright (2008)
pentasulfide	$D_{{S_5}^{2-}}$	1.03×10^{-9}	$m^2\,s^{-1}$	Wilke and Chang (1955); Albright (2008)
hydrogen hexasulfide	$D_{H_2S_6}$	0.897×10^{-9}	$m^2\,s^{-1}$	Wilke and Chang (1955); Albright (2008)
hydrohexasulfide	$D_{{HS_6}^-}$	0.909×10^{-9}	$m^2\,s^{-1}$	Wilke and Chang (1955); Albright (2008)
hexasulfide	$D_{{S_6}^{2-}}$	0.922×10^{-9}	$m^2\,s^{-1}$	Wilke and Chang (1955); Albright (2008)
hydrogen heptasulfide	$D_{H_2S_7}$	0.821×10^{-9}	$m^2\,s^{-1}$	Wilke and Chang (1955); Albright (2008)
hydroheptasulfide	$D_{{HS_7}^-}$	0.831×10^{-9}	$m^2\,s^{-1}$	Wilke and Chang (1955); Albright (2008)
heptasulfide	$D_{{S_7}^{2-}}$	0.841×10^{-9}	$m^2\,s^{-1}$	Wilke and Chang (1955); Albright (2008)
hydrogen octasulfide	$D_{H_2S_8}$	0.760×10^{-9}	$m^2\,s^{-1}$	Wilke and Chang (1955); Albright (2008)
hydrooctasulfide	$D_{{HS_8}^-}$	0.768×10^{-9}	$m^2\,s^{-1}$	Wilke and Chang (1955); Albright (2008)
octasulfide	$D_{{S_8}^{2-}}$	0.776×10^{-9}	$m^2\,s^{-1}$	Wilke and Chang (1955); Albright (2008)

APPENDIX G F-DISTRIBUTIONS USED FOR MONTE-CARLO ANALYSIS OF AOM/SR DIFFUSION-REACTION MODEL

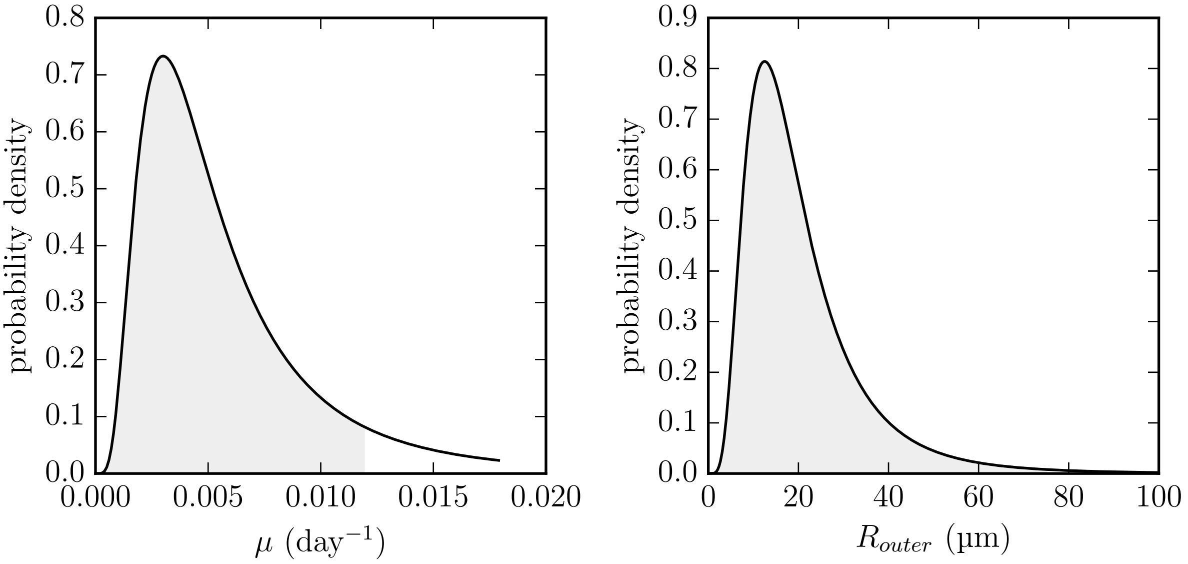

Figure G.1: The F-distribution used for μ and r_{outer} in subsection 4.3.2. The F-distribution for μ is generated using $V_1 = 15$, $V_2 = 7$ degrees of freedom and scaled by $0.003/0.674$ to obtain a distribution with mode $\mu = 0.003\,\mathrm{h}^{-1}$. The 90%-ile is located at $\mu = 0.012\,\mathrm{h}^{-1}$ and marked in grey. The F-distribution for r_{outer} is generated using $V_1 = 15$, $V_2 = 11$ and scaled by $12.5/0.733$ to mode $r_{outer} = 12.5\,\mu\mathrm{m}$. The 99%-ile is located at $r_{outer} = 75\,\mu\mathrm{m}$ and marked in grey.

Appendix H Concentration profiles for diffusion-reaction model of AOM/SR aggregates without outer DSS shell

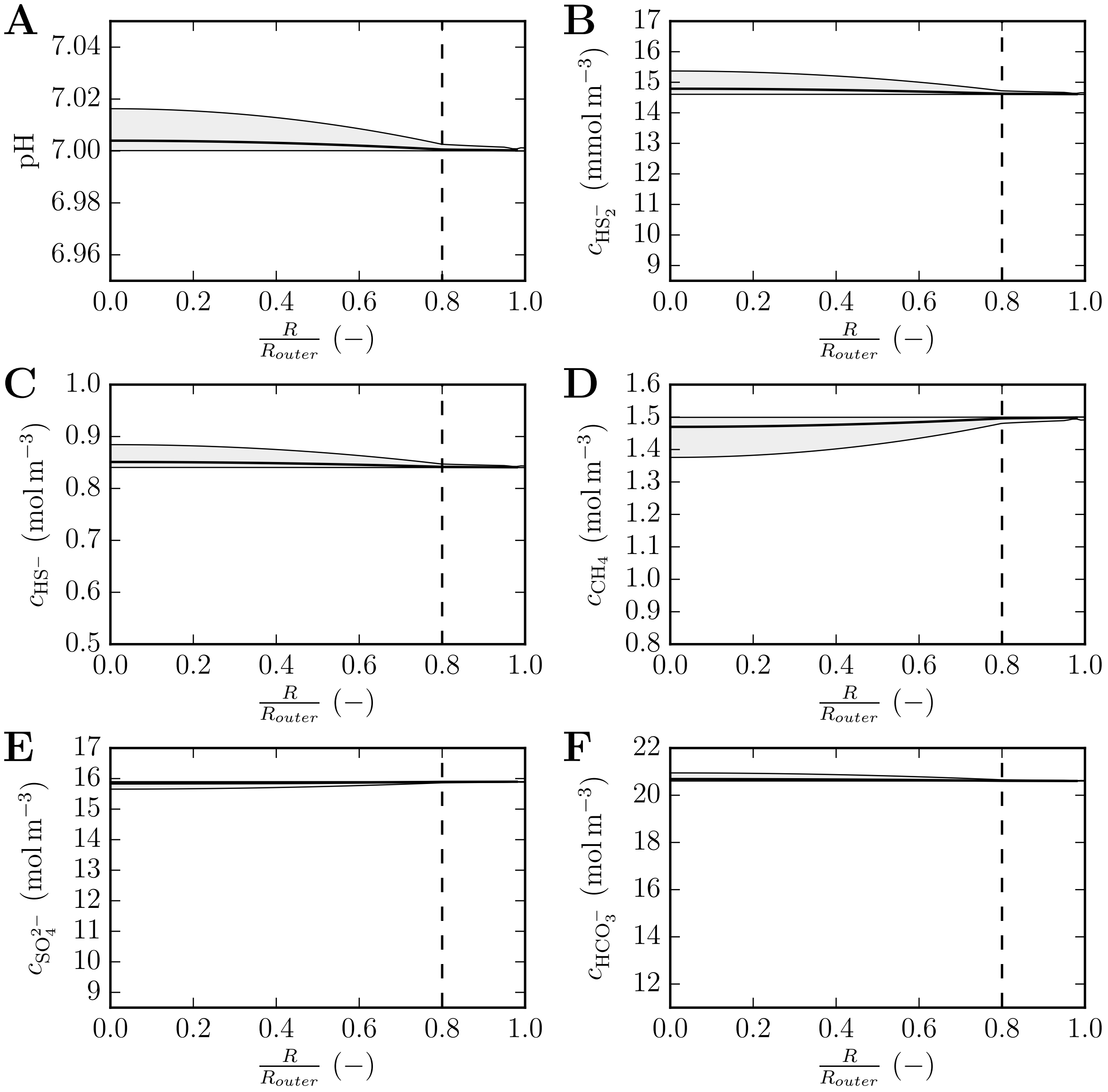

Figure H.1: Average concentration profiles without outer DSS shell, from the centre of the aggregate to the outer surface for the compounds involved in the AOM/SR reactions. Generated by varying R_{outer} and μ using a Monte-Carlo analysis with 100 generated samples. The outer DSS shell has been removed such that equation equation 1.9 does not occur. The shaded area in the graphs represents the 95% prediction interval. The position along the radius R is normalised using R_{outer}.

APPENDIX I ORIGINAL PEER-REVIEWED PAPERS SUBMITTED

In this appendix the papers implemented in this thesis are included:

- **Storck, T.**, Picioreanu, C., Virdis, B., and Batstone, D. J. (2014). Variable cell morphology approach for individual-based modelling of microbial communities. Biophysical Journal *106*, 2037–2048. doi:10.1016/j.bpj.2014.03.015
- **Storck, T.**, Virdis, B., and Batstone, D. J. Modelling extracellular limitations for mediated versus direct interspecies electron transfer. *Accepted for publication in The ISME Journal*

For the paper in The ISME Journal, the manuscript PDF generated by the journal is included. The only modification is a typographic error that has been rectified in this appendix (the value for k_0 in the table).

Biophysical Journal Volume 106 May 2014 2037–2048

Variable Cell Morphology Approach for Individual-Based Modeling of Microbial Communities

Tomas Storck,[†] Cristian Picioreanu,[‡] Bernardino Virdis,[†§] and Damien J. Batstone[†*]
[†]Advanced Water Management Centre, The University of Queensland, Brisbane, Australia; [‡]Department of Biotechnology, Delft University of Technology, Delft, The Netherlands; and [§]Centre for Microbial Electrosynthesis, The University of Queensland, St. Lucia, Brisbane, Australia

ABSTRACT An individual-based, mass-spring modeling framework has been developed to investigate the effect of cell properties on the structure of biofilms and microbial aggregates through Lagrangian modeling. Key features that distinguish this model are variable cell morphology described by a collection of particles connected by springs and a mechanical representation of deformable intracellular, intercellular, and cell-substratum links. A first case study describes the colony formation of a rod-shaped species on a planar substratum. This case shows the importance of mechanical interactions in a community of growing and dividing rod-shaped cells (i.e., bacilli). Cell-substratum links promote formation of mounds as opposed to single-layer biofilms, whereas filial links affect the roundness of the biofilm. A second case study describes the formation of flocs and development of external filaments in a mixed-culture activated sludge community. It is shown by modeling that distinct cell-cell links, microbial morphology, and growth kinetics can lead to excessive filamentous proliferation and interfloc bridging, possible causes for detrimental sludge bulking. This methodology has been extended to more advanced microbial morphologies such as filament branching and proves to be a very powerful tool in determining how fundamental controlling mechanisms determine diverse microbial colony architectures.

INTRODUCTION

Modeling of microbial interactions in biological aggregates (e.g., microbial biofilms, granules, and flocs) is a very powerful method to analyze the role of fundamental controlling factors in defining relations between structure and function in mixed microbial populations. Numerical models help predict different structural and functional aspects, such as shape and size of the aggregate, development of a certain spatial distribution of microbial populations and extracellular polymeric substances (EPS), or the impact of specific mechanisms such as gene transfer, microbial motility, or cell-cell signaling.

The two basic approaches taken for modeling microbial aggregates are based on a continuum or on an individual representation of the microbial community. Continuum-based models use a volume-averaged description of the biomass composing the biofilm. Starting from the now widely applied 1D continuum models (1), more complex 2D and 3D continuum multispecies biofilm models have been proposed (see, e.g., Alpkvist and Klapper (2) and Merkey et al. (3)). Alternatively, in individual-based models (IbM), biofilms are represented as a collection of individual microbes or functional elements (agents), whereas substrate transport/reaction and hydraulic flow are solved separately in a continuum field (see, e.g., Kreft et al. (4) and Lardon et al. (5)). Models combining continuum (for EPS) with individual (for microbial cells) representations have also been developed (6). Both approaches are suitable for investigating mixed-population aggregates, with IbMs generally being superior for investigating the impact of interactions at microbe level, whereas the continuum-based approach is still more applicable at larger geometric scales (7).

IbM of microbial populations has allowed the spatial investigation of the role of intra- and extracellular polymer substances (5,8,9), gene transfer (10,11), cell-cell communication and quorum sensing (12–14), microbial motility (15–17), antibiotic resistance and survival of persister cells (18), and substrate transfer effects on many different microbial ecology interactions (competition, mutualism, parasitism, toxicity, cross-feeding, etc.) (19–22). Inclusion of solute reaction-transport models also allows for detailed analysis of the impact of fundamental constraints, such as thermodynamic substrate and product concentration limits, or diffusive flux on larger aggregates and engineered and environmental systems as a whole (20).

A key challenge in IbM has been determining how the positions of the agents change over time, which at a higher level determines how the microbial colonies spread and change in shape, size, and microbial ecology. In approaching this essential mechanical problem, the existing microbial community models are often limited in their complexity in one or more of the following ways.

1. Only simple microbial geometries are applied, either spheres or cylinders.
2. Structural properties of the aggregate are not determined by the actions of individual agents, but are imposed on a collection of agents.
3. Rigid connections are used for intra- or intercellular links.

Submitted October 30, 2013, and accepted for publication March 13, 2014.

*Correspondence: damienb@awmc.uq.edu.au

Editor: Sean Sun.

0006-3495/14/05/2037/12 $2.00

http://dx.doi.org/10.1016/j.bpj.2014.03.015

Microbial morphology consists of essentially two elements: primary morphology refers to cell shape (e.g., cocci are spherical cells, bacilli are rod-shaped, etc.), whereas secondary morphology is related to division mode and subsequent sibling connections (e.g., strings of streptococci, grapelike staphylococci colonies, sarcina tetrads, filamentous bacilli, branched filamentous streptomyces, etc.). The simplest shape (i.e., a sphere in 3D or a circle in 2D) for a microbial cell allows for ready computation of division and anticollision (4,23), but it brings serious limitations when describing a series of other aspects numerically, as it can be easily observed that cells have a wide variety of morphologies (24). For example, bacilli (rod-shaped cells) may have a different response to substrate concentrations compared to cocci (sphere-shaped cells), as rods have a larger surface/volume ratio than spheres. Rod-shaped cells also transfer genes differently when they are positioned side by side than when they are perpendicular to each other (10). Interspecies or microbe-surface electron transfer can also be influenced by cell shape and the way cells connect in a filamentous microcolony (25). It is also hypothesized that specific coaggregation between cells with different morphology (e.g., filamentous actinomycetes with streptococci or lactobacilli) is essential in the formation of complex food webs, such as in dental plaque (26)). Cell morphology also strongly affects the shape of the aggregate. For example, an array of filamentous rod-shaped cells can form a longer, more slender, and more rigid filament than the equivalent number of spherical cells. Therefore, understanding how filamentous microorganisms influence aggregates is very important in the development of activated sludge flocs used in water treatment (27,28). Real-world functionality of morphology infers that different cell shapes should also be included in agent-based modeling, particularly where interactions between individual cells are being investigated.

In a coarse-grain representation of the biofilm microbial structure, grouping of cells as a collection (cluster) and modeling only the interactions between different clusters would remove interactions between individual cells that could otherwise have a crucial effect on the aggregate structure. Nitrifying biofilms are one typical example where clustering is important, with ammonium- and nitrite-oxidizing organisms typically organized in spherical clusters (6,29). This clustering would be more easily modeled using structural elements (e.g., strong adhesion forces between sibling cells).

In a mechanical model of microbial aggregates, the function of extracellular polymers is mainly to act as an elastic link between particles. Including biofilm structural components such as EPS as hard spherical objects (5,30,31) or rigid links (32) may introduce artifacts related to the volumetric occupation and to the actual rheological properties of the polymeric matrix. Rather, in concordance with the particle-spring representation of microbial cells, the EPS matrix could be described by a collection of springs connecting a series of cells.

In-depth numerical methods for simulating microbial growth and the resulting structures at the cell and cluster levels (e.g., the cellular Potts model (32,33)) are readily available in the literature. Particle-spring approaches have long been used in chemistry to model molecular interactions, for example, in proteins using amino acid subunits (34). Particle-spring models have been used for maintaining an elastic cell shape and allowing for deformable cell-cell and cell-particulate connections in biofilms (17,35). More recently, these models have been constructed to explain patterns developed during the social movement of myxobacteria (16,17), where populations of flexible, gliding rod-shaped cells were shown to form specific patterns as a function of the various forces acting on each bacterial body as it is subjected to multiple cell-cell interactions. By a similar method, large populations of long, flexible filamentous cells of gliding cyanobacteria were modeled and the effectiveness of photophobic responses in this population was quantified (36). Recently, growth and colony formation of zigzagged Diatoma chains in contrasting flow environments have also been modeled with a particle-spring model (37). However, the approach of modeling heterogeneous biofilms with growing microorganisms of variable morphology has not been previously addressed.

To address some of the restrictions in existing IbMs, we have developed a variable-morphology physics-based approach for modeling microbial communities. The cell shape, as well as the cell aggregate morphology, is provided by a particle-spring approach in an overall Lagrangian approach, allowing inheritance of morphological and other properties. This approach has been applied to simple single- and mixed-population systems.

MODEL DESCRIPTION

The numerical model is designed to simulate formation of complex microbial community structures (e.g., biofilms, biological flocs) based on mechanical interactions between cells with variable primary, secondary, and tertiary morphology (e.g., cocci, bacilli, and filaments). This section describes the modeling approach for the elemental components (subcellular agents) as well as for primary (cellular), secondary (cell-descendants), and tertiary (intercellular/environmental) relationships between microbial cells.

Components and structure

Elemental components: particles and springs

The basic model elements are particles (mass agents) connected by massless springs. Each particle is characterized by three state variables: mass (m), velocity ($\mathbf{v}$), and position ($\mathbf{p}$). Springs join particles to each other or to fixed reference points (e.g., a biofilm substratum) and have a characteristic spring constant, k_s, and a rest length, L_s^{rest}. A microbial cell can consist of one particle (in the case of spherical cells) or of multiple particles connected by intracellular springs (for rods and more complicated geometries). Cells can also be linked by intercellular springs into filaments. Further links connect cells and filaments into higher-level structures such as aggregates, biofilms, or flocs.

All springs used in this model are linearly elastic, following Hooke's Law. Equation 1 describes the force in a spring connecting two particles:

$$\mathbf{F}_s = k_s \frac{\mathbf{L}_s}{L_s}\left(L_s - L_s^{rest}\right), \tag{1}$$

where $\mathbf{F}_s$ is the force acting on particle a, k_s is the spring constant, $\mathbf{L}_s$ is a vector describing the relative position of particle a with respect to the position of particle b (i.e., $\mathbf{L}_s = \mathbf{p}_b - \mathbf{p}_a$), L_s is the length (norm) of vector $\mathbf{L}_s$, and L_s^{rest} is the rest length of the spring. The force acting on particle b is $-\mathbf{F}_s$.

Primary structures: cell types

The primary structure defines the shape of individual cells. Different cellular geometries can be defined by connecting particles with springs. Cocci are spherical microbes, represented in the model by single particles with diameter D_s. Bacilli are rod-shaped cells, represented by two particles with fixed diameter, D_r, connected by a stiff spring with variable rest length, $L_{s,i}^{rest}$ (see Fig. 1 *A*). If flexible cell bodies or other shapes (e.g., bacteria with different aspect ratios L_r/D_r, helical bacteria, spirochetes, etc.) are of interest, these could be modeled by multiple particles connected by different settings of elastic and angular springs (16,17,34).

Microbial cells have an inherent density, ρ, but their mass changes during cell growth, leading to a change in cell shape or size. The spherical cell diameter, D_s, can be calculated as $D_s = \sqrt[3]{6m/\pi\rho}$. Rod-shaped cells are assumed to have a diameter D_r that does not change as the cell grows and an internal spring rest length that changes as a function of the current microbial mass, so that the cell density remains constant. A rod-shaped cell consists of two half-spheres and an open-ended cylinder, so that the internal spring rest length is set by the mass via $L_{s,i}^{rest} = 4m/(\rho\pi D_r^2) - 2D_r/3$. A stiff internal spring (high $k_{s,i}$ value) keeps the actual spring length ($L_{s,i}$) approximately at the desired spring length ($L_{s,i}^{rest}$), so that the cell length can be described by $L_r = L_{s,i}^{rest} + D_r$.

Secondary structures: filial links

The secondary structure defines microbial assemblies related by filial links between immediate siblings. Examples include diplococci and diplobacilli (pairs of spheres or rods), streptococci and streptobacilli (filaments of spheres or rods through division along a single plane), and sarcina and tetrads (square and cubic structures formed by division of cocci along two and three planes, respectively (38)). Less structured links lead to staphylococci clusters (grapelike structures) and palisade bacilli. In this article, only modeling of straight and branched rod filaments is illustrated, but filaments of spherical cells can easily be implemented using sets of filial springs.

Straight filaments of rods can be created in several ways. Short head-to-tail springs ensure that cells will remain connected by inducing the elastic force, $\mathbf{F}_{s,f,short}$ (a function of $k_{s,f,short}$ and $\mathbf{L}_{s,f,short}$; see Eq. 1 and Fig. 1 *B*). The angle between cells can be controlled by adding longer-range springs with the elastic force $\mathbf{F}_{s,f,long}$. By changing the difference in rest length of the two springs, the filament rigidity (i.e., the resistance to chain bending) and the gap between two bacilli in a filament can be readily controlled. The rest length for filament springs between two cells A and B is a function of the internal spring rest lengths of the cells ($L_{s,i,A}^{rest}$ and $L_{s,i,B}^{rest}$) and diameter D_r. In addition, spring length

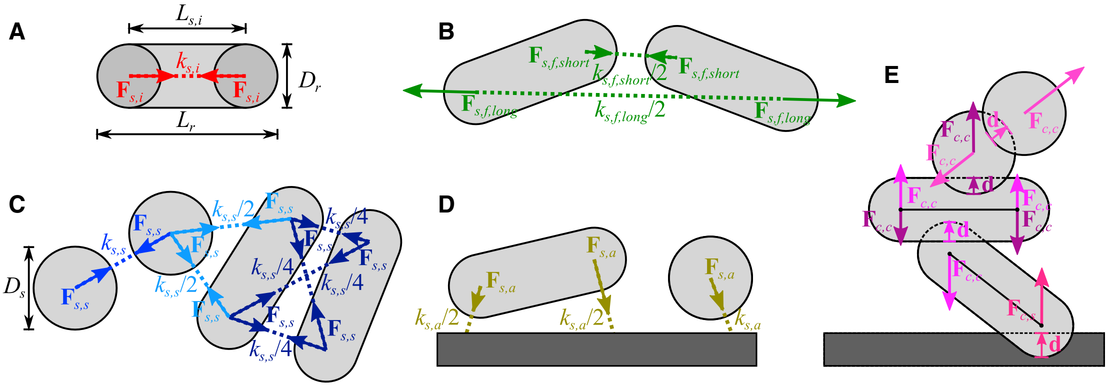

FIGURE 1 Forces acting on the mass particles. (*A*) Internal spring forces, $\mathbf{F}_{s,i}$, in rod-shaped cells. (B) Short and long filial spring forces, $\mathbf{F}_{s,f}$, in rod-shaped cells. (*C*) Sticking spring forces, $\mathbf{F}_{s,s}$, using four springs between rod-shaped cells, two springs between a rod-shaped and a spherical cell, and one spring between spherical cells. (*D*) Anchoring forces, $\mathbf{F}_{s,a}$. (*E*) Collision response forces between rod-shaped cells, spherical cells, and rod-shaped and spherical cells, $\mathbf{F}_{c,c}$, and between cell and substratum, $\mathbf{F}_{c,s}$. In addition to the forces shown in the figure, drag acts on all particles opposing the direction of movement. Force vectors are added to a resultant force vector for each mass particle. Spring constants (k_s) are scaled for the number of springs in that link. To see this figure in color, go online.

factors ($l_{s,short}$ and $l_{s,long}$) control the size of the gap between cells. For straight filaments, the rest length is given by $L^{rest}_{s,f,short} = l_{s,f,short}D_r$ and $L^{rest}_{s,f,long} = l_{s,f,long}D_r + L^{rest}_{s,i,A} + L^{rest}_{s,i,B}$.

Filament branching is implemented in a similar way. In a branch joint, two sets of springs are created from newly branched cell *A* to neighboring cells *B* and *C*. The joint between cell *A* and cell *B* is described by a set of springs with rest lengths $L^{rest}_{s,f,short} = l_{s,f,branch}D_r$ and $L^{rest}_{s,f,long} = l_{s,f,branch}$ $\sqrt{(L^{rest}_{s,i,A} + 0.5L^{rest}_{s,f,short})^2 + (L^{rest}_{s,i,B} + \sqrt{0.75}L^{rest}_{s,f,short})^2}$, where $l_{s,f,branch} = 0.5(l_{s,f,short} + l_{s,f,long})$. By substituting the internal spring rest length of cell *C* for that of *B*, the springs in the joint between *A* and *C* can be described.

The set of a short and a long spring is very similar to the use of an angular spring. By setting the relative spring length, the stiffness of the filaments and branches can be maintained, thus allowing a high versatility in defining and maintaining secondary structures.

Tertiary structures: sticking and anchoring links

In this model, nonfilial cell-cell and cell-substratum links are called tertiary links and include sticking and anchoring connections for cell-cell and cell-substratum links, respectively. These links may describe the adhesive forces created by EPS (see Burdman et al. (39) and references therein), thus enabling aggregation of biomass.

Sticking links form an elastic matrix by creating cell-cell bonds with the number of springs depending on cell morphology. One spring is needed for sphere-to-sphere, two springs for sphere-to-rod, and four springs for rod-to-rod connections (Fig. 1 *C*) to fully satisfy geometric degrees of freedom. This approach allows for implicit modeling of elasticity and strength of the sticking-link matrix, without actually defining the mass of the EPS. Tertiary structure linear springs generate forces $\mathbf{F}_{s,s}$ with rest length defined by $L^{rest}_{s,s}$ (Eq. 1). The spring constants, $k_{s,s}$, are scaled for the number of springs involved in the link ($k_{s,s}/N_{s,s}$).

Cell-substratum bonds play an important role in the tertiary biofilm structure. These links are modeled using anchoring forces $\mathbf{F}_{s,a}$, characterized by $k_{s,a}/N_{s,a}$ and $L^{rest}_{s,a}$. A sphere is fixed using a single spring, whereas rods require two springs to be immobilized so that all rotational degrees of freedom are eliminated (Fig. 1 *D*). The locations on the substratum at which the springs are fixed are determined by projecting the position of the cell particles along the vertical axis onto the horizontal plane.

Collision response

During growth and division, cells will collide with each other and with the substratum. To avoid overlapping cells, a collision detection mechanism was implemented, and collision response forces are applied on overlapping particles.

Collision detection is handled by factorial checking of all cell pairs, with proximity and factorial elimination used to minimize checks. Routines detect collision events (40) by calculating the distance, $\boldsymbol{\delta}$, for point-point (two spherical cells), line-segment-point (a spherical and a rod-shaped cell), line-segment-line-segment (two rod-shaped cells), and point-plane (particle-substratum). For two cells *A* and *B*, the collision detection functions return the overlap vector $\mathbf{d} = (D_A + D_B)/2 - \boldsymbol{\delta}$, which provides distance and direction of overlap. Collision response is based on elastic repulsion of colliding objects, by adding forces $\mathbf{F}_{c,c} = k_{c,c}\,\mathbf{d}$ whenever overlap is detected, where $k_{c,c}$ is the cell-cell collision coefficient. For spherical cells, the collision response force, $\mathbf{F}_{c,c}$, will act in the sphere center. For rod-shaped cells, $\mathbf{F}_{c,c}$ is distributed proportionally between the two particles according to the inverse of the distance between collision point and particle (Fig. 1 *E*).

In a similar way, for cell-substratum collision, the force $\mathbf{F}_{c,s}$ is introduced with a coefficient $k_{c,s}$.

DLVO force

Cells in proximity to a planar substratum encounter an attractive van der Waals force ($F_{vdW} \propto -d^{-2}$, where *d* is the distance between cell surface and substratum) and a repulsive electrostatic force ($F_R \propto \kappa e^{-\kappa d}$, where κ is the inverse Debye length) (41). The combination of the van der Waals and electrostatic force is called the DLVO force ($\mathbf{F}_{DLVO} = C_{ES}\kappa e^{-\kappa\mathbf{d}} - C_{vdW}\mathbf{d}^{-2}$, with key constants C_{ES} and C_{vdW}), after the surname initials of the researchers who independently formulated the theory (Derjaguin and Landau, Verwey and Overbeek). DLVO forces allow cells to maintain a fixed stable distance from the substratum, usually on the order of a few nanometers (reversible adhesion). If a cell overcomes the repulsive force and further approaches the substratum, the attractive force becomes dominant again and pulls the cell onto the substratum (irreversible adhesion). Because other forces in the model operate on the micrometer scale, the DLVO forces can make the numerical model stiff. To minimize model stiffness, the norm of $\mathbf{d}$ in the DLVO force is set to have a lower limit of $6/\kappa$, even if the actual distance between cell surface and substratum is smaller.

Model processes

The major processes included in the model are i), cell growth and division, and ii), particle movement and link reorganization to achieve mechanical relaxation. When needed, other processes could be introduced in this framework (see Discussion).

Cell growth

In the model, increase in cell size is driven by an increase in cell mass, assuming constant cell density. Spherical cells can only grow in diameter, whereas rod-shaped cells grow only in length, maintaining a fixed diameter (46,47).

Mass change for a single cell is the result of specific microbial growth rate (μ) (48), so that the increase in mass is described by $\mathrm{d}m/\mathrm{d}t = \mu m$. For rod-shaped cells, the mass is distributed equally over the two particles comprising a cell. For this study, the specific growth rate is generated randomly for each growth step and for each cell, following a normal distribution around the mean with a standard deviation (see Table 1). Because the scope of this framework is the microbial community structure, other factors affecting the net growth rate are not taken into account in this study (e.g., biomass decay and starvation that lead to cell mass decrease, substrate limitation, and product/substrate inhibition, etc.).

Cell division

Division is biochemically a very complex process, with one of the key issues being the division plane (24). Prokaryotic bacilli such as *Escherichia coli* will normally divide longitudinally along a plane in the central cross section of the rod, whereas cocci may divide into one, two, three, or any number of planes to form filaments, tetrads, sarcina, or staph structures, respectively (38). For rods, the division plane is inherent in the geometry of the cell.

In the model, a cell divides when a critical mass has been reached. Apart from determining divisional plane and cell-sibling orientation, the other major issue is sharing of links in secondary and tertiary structures. Secondary links are redistributed to maintain a straight filament by inserting newly formed cells in the array (branching excluded), whereas tertiary links are distributed between mother and daughter according to the proximity of the cell.

Mechanical relaxation

The initial collection of cells is made of a system of particles and springs in mechanical equilibrium. When new cells are formed as a result of microbial growth and division, this equilibrium is perturbed. The model takes a physics-based approach to compute the new location for each particle by relaxing the momentum balances toward the equilibrium of forces:

$$\frac{\mathrm{d}\mathbf{v}}{\mathrm{d}t} = \frac{\sum_j \mathbf{F}_j}{m}, \qquad (2)$$

where $\mathbf{v} = [v_x, v_y, v_z]$ is the particle velocity and $\Sigma \mathbf{F}_j$ the sum of all forces acting on the particle. Position $\mathbf{p} = [p_x, p_y, p_z]$ is then calculated from velocity:

$$\frac{\mathrm{d}\mathbf{p}}{\mathrm{d}t} = \mathbf{v}. \qquad (3)$$

Each particle will contribute with six equations (Eqs. 2 and 3 in a three-dimensional Cartesian coordinate system) to the system of ordinary differential equations, which describes the redistribution of the microbial community.

Included in the model presented here are elastic forces, $\mathbf{F}_s$, due to intracellular, intercellular, or cell-substratum springs, and collision-response forces, $\mathbf{F}_c$. In addition, velocity-damping forces $\mathbf{F}_d = -k_d\mathbf{v}$ prevent large oscillations and stabilize the movement of particles toward the mechanical equilibrium. For simulations involving a planar substratum, the DLVO force and normal forces act on cells as well.

During each time step of mechanical relaxation, cell-cell and cell-substratum distances are checked and tertiary links are formed or broken. Formation of a new set of springs between two cells A and B (a sticking link) occurs when the distance, d, between the cell center (for a spherical cell) or the cell axis (for rod-shaped cells) and the center or axis of the other cell is $d < d_{s,form}$. An existing link is broken when the actual spring length exceeds the maximum length, $L_{s,s} > L_{s,s}^{rest} + d_{s,break}$. In a similar way, anchoring links are formed and broken, with d the distance between cell and substratum. The spring constants are set such that the springs are stiff enough for the cell structures to be rigid under weak stress and to mitigate overall model stiffness. Intracellular springs have relatively high stiffness compared to intercellular springs, as also suggested in literature (49). Values for spring constants, formation, and stretch limits are given in Table 1.

Model implementation and solution

As cell growth and division are orders of magnitude slower than the mechanical relaxation (minutes/hours versus seconds (50)), it is computationally advantageous to use a model solution that splits the time-stepping algorithm into two phases. During the growth phase, executed with time steps on the order of hours, cell masses increase. When the cell mass exceeds a critical value after the growth step, the cell divides. Filial links may be created between the involved cells. In a second phase, a partially relaxed state is calculated by moving the particles according to the ordinary differential equation momentum balances (Eqs. 2 and 3), solved over a much shorter time interval. Sticking and anchoring links can be created or removed during this phase. A Dormand-Prince Runge-Kutta ordinary differential equation solver (51) is used to determine relaxation. For the small-size microbial aggregates simulated, 1 s of mechanical relaxation was in general sufficient.

After relaxation, the state variables for each particle and cell links are stored, and a new growth/division phase begins.

The model solution algorithm has been implemented as object-oriented Java code. Through the JMatIO library (December 2012, http://sourceforge.net/projects/jmatio/), MATLAB (R2012b, The MathWorks, Natick, MA) was used to preprocess for rendering in POV-Ray (3.7 Beta, http://www.povray.org/, Persistence of Vision Pty., Williamstown, Victoria, Australia).

TABLE 1 Model parameters

Parameter	Symbol	Default value	Units	Reference
Internal springs				
Spring constant	$k_{s,i}$	5×10^{-11}	N m^{-1}	
Filial links (*E. coli*)				
Short spring spring constant	$k_{s,f,short}$	5×10^{-13}	N m^{-1}	
Long spring spring constant	$k_{s,f,long}$	5×10^{-13}	N m^{-1}	
Stretch limit	$d_{f,break}$	1	μm	
Short spring relative length	$l_{f,short}$	0.5	—	
Long spring relative length	$l_{f,long}$	1.7	—	
Filial links (activated sludge)				
Short spring spring constant	$k_{s,f,short}$	2×10^{-11}	N m^{-1}	
Long spring spring constant	$k_{s,f,long}$	2×10^{-11}	N m^{-1}	
Stretch limit	$d_{f,break}$	2	μm	
Short spring relative length	$l_{f,short}$	0.5	—	
Long spring relative length	$l_{f,long}$	1.7	—	
Sticking links (activated sludge)				
Spring constant	$k_{s,s}$	1×10^{-11}	N m^{-1}	
Formation limit	$d_{s,form}$	0.5	μm	
Stretch limit	$d_{s,break}$	1	μm	
Anchoring links (*E. coli*)				
Spring constant	$k_{s,a}$	1×10^{-11}	N m^{-1}	
Formation limit	$d_{a,form}$	0.5	μm	
Stretch limit	$d_{a,break}$	1	μm	
DLVO forces (*E. coli*)				
Electrostatic force grouped constants	C_{ES}	1×10^{-22}	N m	
Van der Waals force grouped constants	C_{vdW}	1×10^{-31}	N m^{2}	
Inverse Debye length	κ	5×10^{7}	m^{-1}	
Collision response				
Cell-cell collision spring constant	$k_{c,c}$	1×10^{-10}	N m^{-1}	
Cell-substratum collision spring constant	$k_{c,s}$	1×10^{-10}	N m^{-1}	
Other forces				
Velocity damping coefficient	k_d	1×10^{-13}	N s m^{-1}	
Bacilli geometry (*E. coli*)				
Cell diameter	D_r	0.75 ± 0.0375	μm	(42)
Initial cell length	$L_{r,0}$	3	μm	
Final cell length	$L_{r,div}$	5.75	μm	(42)
Cell mass at division	$m_{r,div}$	2.45×10^{-15}	kg	
Filament-former geometry (activated sludge)				
Cell diameter	D_r	0.5	μm	(43)
Initial cell length	$L_{r,0}$	1.67	μm	
Final cell length	$L_{r,div}$	4	μm	(43)
Cell mass at division	$m_{r,div}$	3.70×10^{-15}	kg	
Floc former geometry (activated sludge)				
Cell diameter	D_r	0.35	μm	(43)
Initial cell length	$L_{r,0}$	0.317	μm	
Final cell length	$L_{r,div}$	1.1	μm	(43)
Cell mass at division	$m_{r,div}$	6.09×10^{-16}	kg	
Growth (*E. coli*)				
Growth rate coefficient for bacilli	μ	1.23 ± 0.277	h^{-1}	(44,45)
Growth (activated sludge, low O_2 concentration)				
Growth rate coefficient for fil. form.	μ	0.217 ± 0.0434	h^{-1}	
Growth rate coefficient for floc form.	μ	0.153 ± 0.0306	h^{-1}	
Growth (activated sludge, high O_2 concentration)				
Growth rate coefficient for fil. form.	μ	0.271 ± 0.0542	h^{-1}	(43)
Growth rate coefficient for floc form.	μ	0.383 ± 0.0766	h^{-1}	(43)
Other parameters				
Biomass density	ρ	1010	kg m^{-3}	

RESULTS AND DISCUSSION

Two case studies are discussed to illustrate the potential of this modeling approach. The first case is a simulation of colony growth of rod-shaped cells (e.g., *E. coli*, *Bacillus subtilis*, etc.) on a planar surface. In the second case, a mix of two cell morphologies is used (spherical cells and chains of rod-shaped cells) to simulate communities of floc-forming and filamentous bacteria in mixed population systems, as encountered in activated sludge flocs and anaerobic biofilms.

Rod-shaped cells on a planar surface

Growth of a pure culture containing rod-shaped cells is simulated on a planar substratum, which may represent an agar surface. Cell diameter and final length are taken from earlier experimental work (42), assuming *E. coli* growth on glucose. When a cell is formed, its diameter is determined by random sampling from a normal distribution with a standard deviation of 5% of the mean diameter (Table 1). The cell diameter remains constant for the rest of the simulation and the cell length is set to satisfy the equations described in the section Primary structures: cell types. The specific growth rate of a cell is generated randomly at each time step from a normal distribution, with parameters as found in Koch and Wang (44) and Képès (45). The cell is modeled by two particles connected by a stiff spring. Primarily, collision response, DLVO, and velocity-damping forces act on the cells. Additional forces are introduced when investigating the effect of cell-substratum (anchoring) and filial links. Ten simulations with different initial states are run for each case.

Colony formation without anchoring and filial links

Without anchoring links to bind the cells to the substratum, cells can move along the surface and encounter only a drag force relative to the cell velocity (introduced as damping in this model). Although the differences in diameter cause cells to displace each other slightly in the vertical dimension, DLVO forces prevent cells from stacking for an average of 3.8 h (Fig. 2 *A*, Fig. 3 *B*, and Movie S1 in the Supporting Material). By fitting an ellipse to enclose all cells, the mean area of the biofilm at which stacking occurs is for this particular case found to be 730 ± 80 μm^2 (95% confidence interval).

Simulation results suggest that the cells remain aligned during colony expansion, as observed in Fig. 2 *A*. The overall orientation of cells in the colony can be quantified with the orientation correlation coefficient (16), $C(t) = (1/K)\sum_{j\neq k}^{K}(2\cos^2\theta(\mathbf{o}_j(t),\mathbf{o}_k(t)) - 1)$, where $\mathbf{o}$ is the orientation vector for the cell (equivalent to $\mathbf{L}_{s,i}$).

From a parallel alignment of cells in the early stage of colony formation, a more random orientation develops over time (see Fig. 3 *A*). The initial parallel positioning can be explained by the cell division mechanism. Directly after division, both cells are aligned head to tail. The internal springs then relax, displacing the cells slightly while maintaining strong alignment. After several division and relaxation steps, the alignment is lost.

The spread of different generations throughout the biofilm can be observed by labeling the first four generations of cells with different colors. After 70 divisions (4.67 h), cell generations are generally grouped (i.e., phase separation occurs, Fig. 2 *A*), but some cell clusters have moved into cell collections of a different generation.

These simulations suggest that when rod-shaped cells with parameters as in Table 1 grow on a flat, smooth substratum to which no EPS links can be formed, the biofilm may grow as a monolayer for a limited period of time. The simulated colony formation is very similar to the experimental observations of *E. coli* growth presented as time lapse microscopy movies by Stewart et al. (52). Also, colonies of *B. subtilis* have been observed to develop the same morphology (53).

Effect of anchoring to substratum

Observational work also shows that multiple layers of cells can form when rod-shaped bacteria grow on a planar substratum (46). The underlying mechanism for this mounding of cells is not well understood, and one factor that can contribute to cell stacking is anchoring between cells and the substratum, which would impede the movement along the substratum. In this way, the newly formed cells could meet more resistance to movement along the substratum plane and be forced to escape toward the top of the colony. The anchoring links can be seen as strong cell bonds with substratum due to pili, or as a result of sticky EPS.

During simulations of this scenario, cell-substratum links are formed, stretched, broken, and formed again as new cells displace their neighbors. Simulations show that initially the colony can expand along the plane, similar to two-dimensional development without anchoring forces. However, as the colony increases in size, the amount of opposing force met by a cell growing far from the colony edge increases until DLVO and anchoring forces are overcome, the cell is pushed up into the third dimension and the anchoring link is broken. If the cell is close enough to the substratum, a new cell-substratum link is formed, but this link is quickly broken as well because of the excessive upward force. This process repeats until eventually the cell is pushed too far from the substratum to form new anchoring links, and where DLVO force is weaker, thereby escaping the substratum (Fig. 2 *B* and Movie S2). Cells not anchored to the substratum continue to grow freely and eventually form stacks and mounds. Similar to experimental observations (46), this mound is highest around the colony center. The first cells that break away from the substratum are positioned around the middle of the colony, where the forces required to displace neighboring cells are the highest.

The model biofilm thickness (colony height) has been quantified and compared to that of a biofilm without anchoring links (Fig. 3 *B*). Without anchoring links, the biofilm can remain flat for almost 4 h. Including cell anchoring leads to three-dimensional colonies after on average of 2.9 h for the set of parameters described in Table 1. The mean surface area at which cell stacking is first observed is 210 ± 30 μm^2. This area is much smaller than the default case due to anchoring links limiting the horizontal expansion of the biofilm, as well as a lower cell count at which cells first stack.

By increasing or decreasing the strength of the anchoring links (via $d_{a,break}$), the moment at which stacking occurs can be advanced or delayed. For example, setting $d_{a,break}$ to

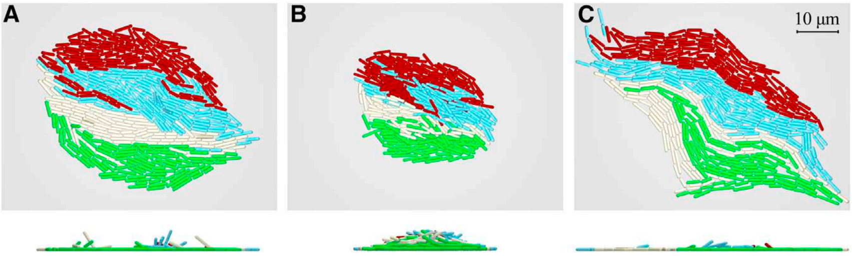

FIGURE 2 Colony development for a pure culture of rod-shaped cells on a planar substratum (top and lateral views) after 4.67 h, with no anchoring and no filial links (*A*), with cell-substratum anchoring (*B*), and with filial links only (*C*). Colors denote the first four cell generations: red, yellow, blue, and green, respectively. Animations of these simulations are presented in Movies S1–S3 in the Supporting Material. To see this figure in color, go online.

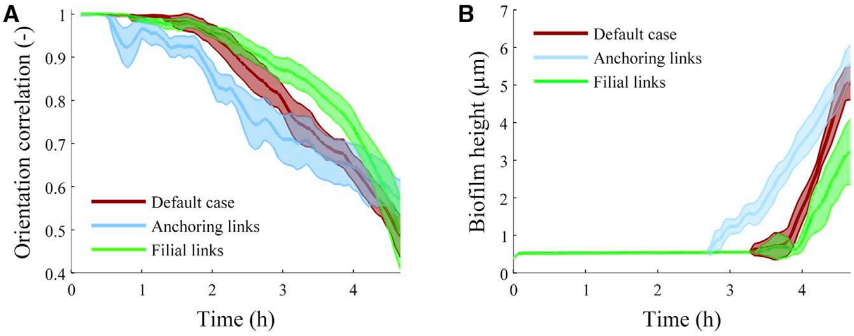

FIGURE 3 (*A*) Orientation correlation coefficient. (*B*) Biofilm thickness, for simulated colonies of rod-shaped cells growing on a planar substratum. The shaded regions represent the 95% confidence interval for the mean, based on 10 simulations (two-tailed *t*-test). To see this figure in color, go online.

twice the default length causes cells to stack after 1.9 h on average, whereas halving $d_{a,break}$ results in cell stacking after 3.08 h.

Cell-substratum links also appear to disrupt the parallel alignment of rod-shaped cells in the biofilm. Anchored cells respond to displacement with an opposing force, pushing away other cells in different directions, eventually causing the biofilm to lose the parallel cell alignment (i.e., the orientation correlation quickly decreases; see Fig. 3 *A*).

In conclusion, it is expected that biofilms able to form cell-substratum connections will become thicker and much less spread out than biofilms less able to bind to a substratum. This can be investigated experimentally by inoculating substrata with different surface roughness and observing the biofilm spread and thickness through microscopy. An extension of this case study is the inclusion of a slime capsule cell-substratum link (17). Although both approaches maintain a constant distance between cell and substratum, the slime allows the cells to freely glide along the plane, whereas anchoring links exert force and eventually break when cells are displaced horizontally. Simulation results suggest, as expected, that gliding prevents cells from stacking (results not shown).

Effect of filial links

Independent of the presence of anchoring links, the model consistently produces colonies with rounded edges (Fig. 2, *A* and *B*), in contrast to some experimental observations (52,53), which show also elongated or irregularly shaped colonies. One possible explanation is that elongated colonies could be the result of cells maintaining a head-to-tail connection after division, which was implemented in the model through the use of filial links.

Simulations with filial links and no anchoring to substratum indeed resulted in irregularly shaped monolayer colonies, with less circularity (Fig. 2 *C* and Movie S3). Initially, the alignment of cells is better maintained in the presence of filial links, but near the end of the simulation (3.67 h), the alignment is lost completely (Fig. 3 *A*).

It can be seen in Fig. 3 *B* that filial links have no significant effect on the moment at which cell stacking first occurs (4.02 h with filial links). For these simulations, the area of the biofilm at the time mound formation is first observed is 1100 ± 200 μm^2, much larger than in the default case. A possible explanation for this increase is that due to the decreased colony roundness a larger ellipse is needed to envelop the cells.

The simulations show that the colony roundness can be largely determined by the ability of the species to form head-to-tail connections: cells capable of forming chains show more irregularity in their colony shape. A relation between mound formation and filial links was not observed. One way to further assess this is to compare biofilm morphology for species that have similar cell morphology but differ in their ability to form filial links (either through manipulation or strain selection). Through image processing, the effect of filial links on cell orientation can be quantified experimentally.

Activated sludge floc structure and bulking

Wastewater treatment involves extensive use of activated sludge processes, where the microorganisms aggregated in flocs are retained in the treatment system by use of gravity clarifiers. One of the main problems of this technology is that bulking of sludge causes flocs with poor settleability and dewaterability. Sludge bulking is a result of the shape and low density of flocs, often caused by excessive and long filament formers (24,28). In activated sludge floc formation, a distinction can be made between two groups of microorganisms: floc formers, which grow in densely packed, quasispherical aggregates, and filament formers, which grow in long structured chains of cells (28). It is generally believed that by maintaining a healthy balance between both groups, the floc structure formed can be optimized to minimize bulking (54). Ideal flocs would have an internal filamentous matrix to provide structure. However, growth of filaments outside of the floc should be prevented to limit interfloc bridging, poor settling, and compressibility (filamentous bulking sludge (28)).

The analysis here focuses on the balance between two characteristic organisms, the filament former *Sphaerotilus natans* and a floc former from the *Citrobacter* genus, growing together in the same floc. *S. natans* is a rod-shaped organism known to form relatively rigid filaments and is widely found in wastewater treatment plants that have bulking sludge problems (55). Growth parameters are readily available for both pure culture (56) and growth in coculture with a floc former (43). For the sake of simplicity, variation in rod cell diameters has been neglected. By varying some of the microbial properties (e.g., relative growth rates, filament stiffness, sticking strength, presence of branching, floc former cell shape), effects on the structure of the resulting flocs can be investigated.

Relative growth rate of floc and filament formers

Compared to filament formers, floc formers have a higher maximum growth rate but a lower affinity for both oxygen and soluble carbon (28). Therefore, at low substrate concentrations the filament formers can dominate the floc. Although the model currently does not calculate substrate concentration fields, the ratio of the average growth rates of both species can be scaled by assuming fixed bulk concentrations. Two sets of parameters were used (Table 1), corresponding to low and high oxygen concentration. In the initial floc, the same total mass of floc and filament formers was taken. That is, the inoculum contains six times as many floc former cells as filament former cells due to the different cellular masses of the two cell types (Fig. 4 *A*).

At low concentrations, starting from an initial state (Fig. 4 *A*), the filament former grows faster than the floc former (Fig. 4 *B*). The developed floc is disperse, with small colonies of floc formers attached at different positions to filaments extending freely into the bulk liquid. This behavior has frequently been reported in the literature (see, e.g., Martins et al. (27) and references therein). The faster filament growth quickly puts filament formers out of reach of floc formers, which mainly occupy the floc interior. The chains of filament formers can then quickly expand into the bulk liquid and form interfloc bridges, in turn making sludge bulking possible (as experimentally visualized by Xie et al. (57); see Fig. 5 *F*).

The model predicts that at high substrate concentrations (starting from the same initial state), an ideal floc is formed (28). The filaments are present inside the floc but do not extend into the bulk liquid because they are captured by the floc formers before they escape from the floc (Fig. 4 *C*). The dividing filamentous cells are very likely to connect through sticking springs with the more abundant floc formers that grow faster at high O_2 concentrations, preventing the filament from growing away from the dense floc kernel. In time, however, the filaments will still be able to escape the floc (Movie S5), pushing other cells away and breaking cell-cell links as they grow away from the floc.

Stiffness of filaments

Filament stiffness (resistance to filament buckling) can be tuned by changing relative spring rest lengths for filial links, e.g., a shorter $l_{s,f,short}$ and longer $l_{s,f,long}$ lead to stiffer filaments. Three parameter sets were used here for ($l_{s,f,short}$, $l_{s,f,long}$): standard (0.5, 1.7), flexible (0.9, 1.3), and stiff (0.1, 2.1), together with the low-concentration growth parameters (Table 1). The gap size between cells is identical for these parameter sets.

The simulation results suggest that filial-link stiffness in the range tested does not play a major role in interfloc bridging, as all three cases resulted in a similar floc structure (Fig. 4, *B*, *D*, and *E*). Note that the stretch limit $d_{f,break}$ was not increased with increasing stiffness, so filaments already under tension (stiff) could break under a lower force than flexible filaments. For these parameters, however, filament link breakage occurred only rarely.

Strength of sticking links

The influence of sticking links on floc formation (e.g., due to different EPS strength) was investigated by varying the sticking-spring stretch limit ($d_{s,break}$) among normal (1 μm), strong (5 μm), and weak (0.2 μm) limits. It was

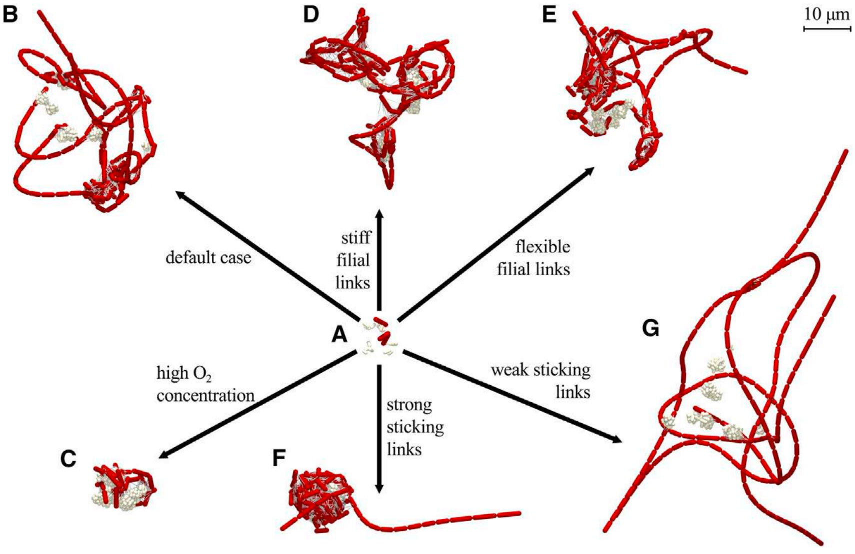

FIGURE 4 Simulated activated sludge floc structures made of floc-former (*gray*) and filament-former (*red*) rod-shaped cells, showing the effect of different types of intercellular links. (*A*) Initial state for all simulated flocs. (*B*) The standard case (low O_2 concentration ($l_{s,f,short}$ = 0.5, $l_{s,f,long}$ = 1.7), and $d_{s,break}$ = 1 μm). (*C*) Increased relative floc-former growth rate (high O_2 concentration parameter set from Table 1). (*D* and *E*) Different filament stiffness is generated by changing ($l_{s,f,short}$, $l_{s,f,long}$) to (0.1, 2.1) for stiff filaments (*D*) and (0.9, 1.3) for flexible filaments. (*E*). (*F* and *G*) Sticking-link strength is adjusted by changing $d_{s,break}$ to 5 μm for strong sticking (*F*) and 0.2 μm for weak sticking (*G*). States *A*, *B*, and *D–G* are shown after 16.80 h (369 cells), and state *C* after 7.67 h (362 cells). Animations of aggregate development for all simulations can be seen in Movies S4–S9. To see this figure in color, go online.

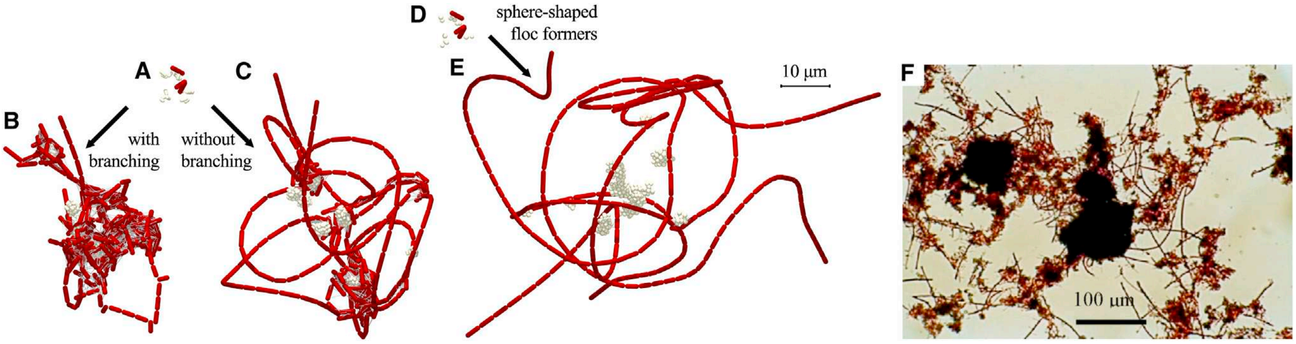

FIGURE 5 Simulated activated sludge floc structures showing the effects of filament branching and spherical floc formers. (*A*) Initial state for a rod-shaped floc former. (*B* and *C*) Rod-shaped floc former with 30% filament branching (*B*) and in a strictly straight (nonbranching) configuration. (*D*) Initial state for spherical floc former. (*E*) Spherical floc former. (*F*) Interfloc bridging observed in a Gram-stained visible light micrograph (from Xie et al. (57)). Simulation results are shown after 19.65 h. Animations of aggregate development resulting in structures *B*, *C*, and *E* can be viewed in Movies S10, S4, and S11, respectively. To see this figure in color, go online.

found that sticking springs play an essential role in the formation of floc structure and therefore in interfloc bridging (Fig. 4, *B*, *F*, and *G*). Strong sticking links allow floc formers to capture and maintain links with filament formers, resulting in a compact floc with few outreaching filaments (Fig. 4 *F*). For weaker sticking links, the floc breaks up as it grows (Fig. 4 *G*), resulting in a very disperse structure. These simulations suggest that the strength of EPS in activated sludge communities is a major factor in sludge bulking. It is even possible that by adding chemicals to degenerate EPS, sludge bulking can increase where EPS structure is weakened instead of broken down completely. This is a challenge to assess by means of simple experiments, since methods to reduce EPS strength (e.g., ion exchange resins or EDTA) also can have an impact on environmental factors.

Branching of filaments

Although the modeled organism *S. natans* does not show true branching, many other filament formers do (e.g., *Nocardia* (56)). To model filament branching effects on floc bridging, a 30% chance is set to form a new branch at division instead of inserting the new cell in the straight filament. Model simulations show how the branching filament former sprouts numerous side chains, at the expense of filament length (Fig. 5 *B*). In the floc with filament branching, the filaments are not long enough to extend far into the bulk liquid. The density of such a floc is therefore greater than that of a floc made of straight filaments growing at a similar rate (Fig. 5 *C*), thereby attenuating the bulking tendency of filamentous sludge, as also observed experimentally (50).

Sphere-shaped versus rod-shaped floc formers

Although for this study most simulations included rod-shaped floc formers, spherical cells are also widespread in activated sludge (56). Simulations have been run to investigate the effect of floc former morphology on floc structure. All parameters (i.e., mass, growth rate, and spring constants) for spherical cells were the same as those for rod-shaped floc formers, except for the maximum diameter, which was set to obtain the same maximum mass ($D_{s,div} = 0.52\ \mu$m). The same initial number of cells and a similar initial cell distribution were created (compare Fig. 5, *A* and *D*).

Simulated flocs including spherical floc formers (Fig. 5 *E*) were more disperse than those created with rod-shaped cells (Fig. 5 *C*). The most notable difference is that the spherical cells do not capture filaments as well as the rod-shaped cells. The denser packing of spherical cells in a colony leads to a smaller cluster volume for the spherical floc formers. This means that the chance to encounter a filament former is smaller for spherical floc formers than for rod-shaped cells, resulting in less dense flocs.

Context and applications

Although both simple (single-population) and more complex (mixed-population and mixed-morphology) applications have been demonstrated here on a largely physical basis, the method allows for obvious extension to applications where substrate fields are also solved (i.e., solute transport and reaction are included). This would allow more realistic growth based on substrate and product concentration fields and would make the model available to investigate biochemical phenomena such as interspecies electron transfer on an aggregate scale.

Another key application is physical dynamics in the presence of a convective field, with two-way coupling through computational fluid dynamics (58). Rather than imposing a specific geometry and set of mechanical properties on the biofilm, these can be dynamically developed in the presence of the flow field. The model proposed here is well suited to this application due to its fundamental mechanical basis.

There is a wide range of possible extensions, including microbial motility, implementation of inert and substrate particles, and imposition of planar axes and division rules that allow formation of packets such as tetrads. The main negative of this approach is the computational requirements, particularly with large numbers of agents, but this can be addressed in a number of ways, including solver optimization and code parallelization.

Another key issue is experimental or observational verification of model-based analysis. In this article, we have largely focused on development and application of a variable morphology technique and this has identified possible controlling mechanisms on a basic level that drive apparently complex colony behavior. This highlights the application of model-based analysis to develop experimental hypotheses that then can be further investigated, with application to both simple and complex systems. One of the strengths of identifying experiments based on model analysis is that specific experiments can be observed and modeled under dynamic conditions to provide a complete picture of how morphology is derived from basic properties.

CONCLUSIONS

Application of a variable morphology model allows for better understanding of how the geometric and mechanical properties of elemental agents (microbes and EPS) can influence larger aggregates. Specifically, we showed here that for both uniform populations (e.g., of bacilli), as well as complex mixed cultures (in flocs), larger aggregates are strongly influenced by the shape of the microbe, as well as by physical characteristics of filial and EPS connections. This approach can be extended to a wide range of potential systems, with particular applicability to problems where mechanical properties of the aggregate are important or coupled to the growth environment.

SUPPORTING MATERIAL

Eleven animations of simulated microbial community development are available at http://www.biophysj.org/biophysj/supplemental/S0006-3495(14)00291-4.

This project was supported under the Australian Research Council's (ARC) Discovery Projects funding scheme (project number DP0985000). Dr. Damien Batstone is the recipient of an ARC Research Fellowship. The work of Dr. Cristian Picioreanu was funded by the Netherlands Organization for Scientific Research (NWO, VIDI grant 864.06.003). Dr. Bernardino Virdis is supported by strategic funding for the Centre for Microbial Electrosynthesis (UQ).

REFERENCES

1. Wanner, O., and W. Gujer. 1986. A multispecies biofilm model. *Biotechnol. Bioeng.* 28:314–328.
2. Alpkvist, E., and I. Klapper. 2007. A multidimensional multispecies continuum model for heterogeneous biofilm development. *Bull. Math. Biol.* 69:765–789.
3. Merkey, B. V., B. E. Rittmann, and D. L. Chopp. 2009. Modeling how soluble microbial products (SMP) support heterotrophic bacteria in autotroph-based biofilms. *J. Theor. Biol.* 259:670–683.
4. Kreft, J.-U., C. Picioreanu, …, M. C. M. van Loosdrecht. 2001. Individual-based modelling of biofilms. *Microbiology.* 147:2897–2912.
5. Lardon, L. A., B. V. Merkey, …, B. F. Smets. 2011. iDynoMiCS: next-generation individual-based modelling of biofilms. *Environ. Microbiol.* 13:2416–2434.
6. Alpkvist, E., C. Picioreanu, …, A. Heyden. 2006. Three-dimensional biofilm model with individual cells and continuum EPS matrix. *Biotechnol. Bioeng.* 94:961–979.
7. Wood, B. D., and S. Whitaker. 1998. Diffusion and reaction in biofilms. *Chem. Eng. Sci.* 53:397–425.
8. Xavier, Jde. B., C. Picioreanu, and M. C. M. van Loosdrecht. 2005. A general description of detachment for multidimensional modelling of biofilms. *Biotechnol. Bioeng.* 91:651–669.
9. Xavier, J. B., and K. R. Foster. 2007. Cooperation and conflict in microbial biofilms. *Proc. Natl. Acad. Sci. USA.* 104:876–881.
10. Seoane, J., T. Yankelevich, …, B. F. Smets. 2011. An individual-based approach to explain plasmid invasion in bacterial populations. *FEMS Microbiol. Ecol.* 75:17–27.
11. Rudge, T. J., P. J. Steiner, …, J. Haseloff. 2012. Computational modeling of synthetic microbial biofilms. *ACS Synth. Biol.* 1:345–352.
12. Nadell, C. D., K. R. Foster, and J. B. Xavier. 2010. Emergence of spatial structure in cell groups and the evolution of cooperation. *PLOS Comput. Biol.* 6:e1000716.
13. Nadell, C. D., J. B. Xavier, …, K. R. Foster. 2008. The evolution of quorum sensing in bacterial biofilms. *PLoS Biol.* 6:e14.
14. Melke, P., P. Sahlin, …, H. Jönsson. 2010. A cell-based model for quorum sensing in heterogeneous bacterial colonies. *PLOS Comput. Biol.* 6:e1000819.
15. Picioreanu, C., I. M. Head, …, K. Scott. 2007. A computational model for biofilm-based microbial fuel cells. *Water Res.* 41:2921–2940.
16. Janulevicius, A., M. C. M. van Loosdrecht, …, C. Picioreanu. 2010. Cell flexibility affects the alignment of model myxobacteria. *Biophys. J.* 99:3129–3138.
17. Harvey, C. W., F. Morcos, …, M. Alber. 2011. Study of elastic collisions of *Myxococcus xanthus* in swarms. *Phys. Biol.* 8:026016.
18. Chambless, J. D., S. M. Hunt, and P. S. Stewart. 2006. A three-dimensional computer model of four hypothetical mechanisms protecting biofilms from antimicrobials. *Appl. Environ. Microbiol.* 72:2005–2013.
19. Picioreanu, C., J.-U. Kreft, and M. C. M. Van Loosdrecht. 2004. Particle-based multidimensional multispecies biofilm model. *Appl. Environ. Microbiol.* 70:3024–3040.
20. Batstone, D. J., C. Picioreanu, and M. C. M. van Loosdrecht. 2006. Multidimensional modelling to investigate interspecies hydrogen transfer in anaerobic biofilms. *Water Res.* 40:3099–3108.
21. Xavier, J. B., M. K. De Kreuk, …, M. C. M. Van Loosdrecht. 2007. Multi-scale individual-based model of microbial and bioconversion dynamics in aerobic granular sludge. *Environ. Sci. Technol.* 41:6410–6417.
22. Picioreanu, C., M. C. M. van Loosdrecht, …, K. Scott. 2010. Model based evaluation of the effect of pH and electrode geometry on microbial fuel cell performance. *Bioelectrochemistry.* 78:8–24.
23. Kreft, J.-U., G. Booth, and J. W. Wimpenny. 1998. BacSim, a simulator for individual-based modelling of bacterial colony growth. *Microbiology.* 144:3275–3287.
24. Clark, D., P. Dunlap, …, J. Martinko. 2009. Brock Biology of Microorganisms, 13th ed. Benjamin Cummings, San Francisco.
25. Pfeffer, C., S. Larsen, …, L. P. Nielsen. 2012. Filamentous bacteria transport electrons over centimetre distances. *Nature.* 491:218–221.
26. Kolenbrander, P. E. 2000. Oral microbial communities: biofilms, interactions, and genetic systems. *Annu. Rev. Microbiol.* 54:413–437.
27. Martins, A. M. P., K. Pagilla, …, M. C. M. van Loosdrecht. 2004. Filamentous bulking sludge—a critical review. *Water Res.* 38:793–817.
28. Seviour, R. J. 2010. Factors affecting the bulking and foaming filamentous bacteria in activated sludge. *In* Microbial Ecology of Activated

Sludge. R. J. Seviour and P. H. Nielsen, editors. International Water Association, London, pp. 139–167.

29. Okabe, S., H. Satoh, and Y. Watanabe. 1999. In situ analysis of nitrifying biofilms as determined by in situ hybridization and the use of microelectrodes. *Appl. Environ. Microbiol.* 65:3182–3191.

30. Xavier, J. B., C. Picioreanu, and M. C. M. van Loosdrecht. 2005. A framework for multidimensional modelling of activity and structure of multispecies biofilms. *Environ. Microbiol.* 7:1085–1103.

31. Matsumoto, S., M. Katoku, …, M. C. van Loosdrecht. 2010. Microbial community structure in autotrophic nitrifying granules characterized by experimental and simulation analyses. *Environ. Microbiol.* 12: 192–206.

32. Popławski, N. J., A. Shirinifard, …, J. A. Glazier. 2008. Simulation of single-species bacterial-biofilm growth using the Glazier-Graner-Hogeweg model and the CompuCell3D modeling environment. *Math. Biosci. Eng.* 5:355–388.

33. Izaguirre, J. A., R. Chaturvedi, …, J. A. Glazier. 2004. CompuCell, a multi-model framework for simulation of morphogenesis. *Bioinformatics.* 20:1129–1137.

34. Windisch, B., D. Bray, and T. Duke. 2006. Balls and chains—a mesoscopic approach to tethered protein domains. *Biophys. J.* 91:2383–2392.

35. Dillon, R., L. Fauci, …, D. Gaver, III. 1996. Modeling biofilm processes using the immersed boundary method. *J. Comput. Phys.* 129: 57–73.

36. Tamulonis, C., M. Postma, and J. Kaandorp. 2011. Modeling filamentous cyanobacteria reveals the advantages of long and fast trichomes for optimizing light exposure. *PLoS ONE.* 6:e22084.

37. Celler, K., I. Hödl, …, C. Picioreanu. 2014. A mass-spring model unveils the morphogenesis of phototrophic Diatoma biofilms. *Sci. Rep.* 4:3649.

38. Rothfield, L. I., and C. R. Zhao. 1996. How do bacteria decide where to divide? *Cell.* 84:183–186.

39. Burdman, S., E. Jurkevitch, …, Y. Okon. 1998. Aggregation in *Azospirillum brasilense*: effects of chemical and physical factors and involvement of extracellular components. *Microbiology.* 144:1989–1999.

40. Ericson, C. 2005. Real Time Collision Detection, 2nd ed. Morgan Kaufmann, San Francisco.

41. Hermansson, M. 1999. The DLVO theory in microbial adhesion. *Colloids Surf. B Biointerfaces.* 14:105–119.

42. Pierucci, O. 1978. Dimensions of *Escherichia coli* at various growth rates: model for envelope growth. *J. Bacteriol.* 135:559–574.

43. Lau, A. O., P. F. Strom, and D. Jenkins. 1984. Growth kinetics of *Sphaerotilus natans* and a floc former in pure and dual continuous culture. *J. Water Pollut. Control Fed.* 56:41–51.

44. Koch, A. L., and C. H. Wang. 1982. How close to the theoretical diffusion limit do bacterial uptake systems function? *Arch. Microbiol.* 131:36–42.

45. Képès, F. 1986. The cell cycle of *Escherichia coli* and some of its regulatory systems. *FEMS Microbiol. Lett.* 32:225–246.

46. Shapiro, J. A., and C. Hsu. 1989. *Escherichia coli* K-12 cell-cell interactions seen by time-lapse video. *J. Bacteriol.* 171:5963–5974.

47. Stewart, P. S. 2003. Diffusion in biofilms. *J. Bacteriol.* 185:1485–1491.

48. Harvey, R. J., A. G. Marr, and P. R. Painter. 1967. Kinetics of growth of individual cells of *Escherichia coli* and *Azotobacter agilis*. *J. Bacteriol.* 93:605–617.

49. Volle, C., M. Ferguson, and K. Aidala. 2009. Physical properties of native biofilm cells explored by atomic force microscopy. *Biophys. J.* 96 (*Supplement*):398a, Abstract.

50. Picioreanu, C., M. C. Van Loosdrecht, and J. J. Heijnen. 2000. Effect of diffusive and convective substrate transport on biofilm structure formation: a two-dimensional modeling study. *Biotechnol. Bioeng.* 69:504–515.

51. Press, W. H., S. A. Teukolskky, …, B. P. Flannery. 2007. Numerical Recipes: The Art of Scientific Computing, 3rd ed. Cambridge University Press, Cambridge, United Kingdom.

52. Stewart, E. J., R. Madden, …, F. Taddei. 2005. Aging and death in an organism that reproduces by morphologically symmetric division. *PLoS Biol.* 3:e45.

53. de Jong, I. G., K. Beilharz, …, J.-W. Veening. 2011. Live cell imaging of *Bacillus subtilis* and *Streptococcus pneumoniae* using automated time-lapse microscopy. *J. Vis. Exp.* 3145:1–6.

54. Sezgin, M., D. Jenkins, and D. S. Parker. 1978. A unified theory of filamentous activated sludge bulking. *J. Water Pollut. Control Fed.* 50: 362–381.

55. Bitton, G. 2011. Wastewater Microbiology, 4th ed. Wiley-Blackwell, Hoboken, NJ.

56. Seviour, E. M., S. McIlroy, and R. J. Seviour. 2010. Descriptions of activated sludge organisms. *In* Microbial Ecology of Activated Sludge. R. J. Seviour and P. H. Nielsen, editors. International Water Association, London, pp. 453–487.

57. Xie, B., X.-C. Dai, and Y.-T. Xu. 2007. Cause and pre-alarm control of bulking and foaming by *Microthrix parvicella*—a case study in triple oxidation ditch at a wastewater treatment plant. *J. Hazard. Mater.* 143:184–191.

58. Alpkvist, E., and I. Klapper. 2007. Description of mechanical response including detachment using a novel particle model of biofilm/flow interaction. *Water Sci. Technol.* 55:265–273.

Modelling extracellular limitations for mediated versus direct interspecies electron transfer

Tomas Storck[†], Bernardino Virdis[†‡], Damien J. Batstone[†]*

[†] Advanced Water Management Centre, The University of Queensland, Australia

[‡] Centre for Microbial Electrochemical Systems, The University of Queensland, Australia

* Corresponding author:

Damien J. Batstone

Level 4, Gehrmann Laboratories Building (60)

Cooper Road, St. Lucia, QLD 4072, Australia

Ph.: +61 7 334 69051

Email: damienb@awmc.uq.edu.au

ABSTRACT

Interspecies electron transfer (IET) is important for many anaerobic processes, but is critically dependent on mode of transfer. In particular, direct interspecies electron transfer (DIET) has been recently proposed as a metabolically advantageous mode compared to mediated interspecies electron transfer (MIET) via hydrogen or formate. We analyse relative feasibility of these IET modes by modelling external limitations using a reaction-diffusion-electrochemical approach in a 3D domain. For otherwise identical conditions, external electron transfer rates per cell pair (cp) are considerably higher for formate-MIET (317×10^3 $e^-\cdot cp^{-1}$ s^{-1}) compared with DIET (44.9×10^3 $e^-\cdot cp^{-1}$ s^{-1}) or hydrogen-MIET (5.24×10^3 $e^-\cdot cp^{-1}$ s^{-1}). MIET is limited by the mediator concentration gradient at which reactions are still thermodynamically feasible, while DIET is limited through redox cofactor (*e.g.*, cytochromes) activation losses. Model outcomes are sensitive to key parameters for external electron transfer including cofactor transfer rate constant and redox cofactor area, concentration or count per cell, but formate-MIET is generally more favourable for reasonable parameter ranges. Extending the analysis to multiple cells shows that the size of the network does not strongly influence relative or absolute favourability of IET modes. Similar electron transfer rates for formate-MIET and DIET can be achieved in our case with a slight (0.7 kJ mol^{-1}) thermodynamic advantage for DIET. This indicates that close to thermodynamic feasibility, external limitations can be compensated for by improved metabolic efficiency when using direct electron transfer.

Keywords: bioelectrochemical system / direct interspecies electron transfer / interspecies formate transfer / interspecies hydrogen transfer / mediated interspecies electron transfer / nanowire

Category: Microbe-microbe and microbe-host interactions

INTRODUCTION

Interspecies electron transfer (IET) is a mechanism whereby different microbial species in a community share reducing equivalents. IET plays an important role in bio-electrochemical systems and in other thermodynamically limited processes, such as syntrophic organic acid and ethanol oxidation in anaerobic environments (Boone & Bryant, 1980; Nagarajan *et al.*, 2013).

Mediated interspecies electron transfer (MIET) is the most frequently described mode of IET, whereby an electron-carrying compound (mediator) is transported by diffusion from mediator-producing cells to mediator-consuming cells along a concentration gradient. The mediator diffusion rate is limited by the concentration gradient at which oxidation and reduction reactions are thermodynamically feasible (Boone *et al.*, 1989; Batstone *et al.*, 2006). Hydrogen-mediated interspecies electron transfer (hydrogen-MIET) has been generally proposed as the dominant transfer mechanism for syntrophic propionate oxidation via acetogenesis and methanogenesis, but alternative IET modes such as formate-MIET have since been suggested as an alternative, allowing an increased electron transfer rate due to a higher intercellular mediator concentration gradient (Boone *et al.*, 1989; Batstone *et al.*, 2006). While many methanogenic archaea encode for genes important to formate utilisation, they fail to utilise formate in pure culture (Hedderich & Whitman, 2013), leaving hydrogen as default, presumably the less favourable electron transfer mode.

Direct interspecies electron transfer (DIET) has been recently proposed to describe cell-cell electron transfer. DIET is analogous to direct extracellular electron transfer (DEET), which describes electron transfer between cells and solid-state electron acceptors (*e.g.*, iron or manganese oxides, electrodes). DEET research has revolved mainly around studies of bacteria belonging to the genera *Shewanella* and *Geobacter* (Stams *et al.*, 2006), which have proved as highly efficient in engaging with solid extracellular electron acceptors. Cell-to-cell DIET has been observed mainly in defined co-culture IET systems of these organisms (*e.g.*, for *Geobacter metallireducens* and *G. sulfurreducens*) (Summers *et al.*, 2010; Liu *et al.*, 2012; Shrestha *et al.*, 2013), as well as in *Geobacter* dominated mixed-culture performing ethanol oxidation (Morita *et al.*, 2011). Recently, it was shown that DIET can occur in methanogenic systems and between microbial species commonly found in environmental biological aggregates (*e.g.*, between *Methanosaeta* and *Geobacter* species) (Rotaru, Shrestha, Liu, Shrestha, *et al.*, 2014). Use of DIET over MIET can even enhance the metabolic capability of methanogens such as *Methanosarcina barkeri* to allow methanogenesis simultaneously from CO_2 reduction and acetate cleavage (Rotaru, Shrestha, Liu, Markovaite, *et al.*, 2014). Although bacteria belonging to the genus *Shewanella* have been frequently reported to transfer electrons to electrodes or Fe(III) or Mn(IV) oxides, their role in interspecies interaction remains to be reported.

Transcriptomic and proteomic data, together with phenotypes of gene deletion mutants suggested that DIET in syntrophic co-cultures can occur through electrical connections using pili with metallic-like conductivity (Malvankar *et al.*, 2011; Vargas *et al.*, 2013; Malvankar *et al.*, 2014). Outer membrane cytochromes play an important role in extracellular electron transfer to insoluble minerals such as Fe(III) oxides in *Geobacter* (Mehta *et al.*, 2005), as well as in *Shewanella* species (Shi *et al.*, 2009; Okamoto *et al.*, 2011). If electrons during DIET follow a pathway similar to that observed in respiration of Fe(III)/Mn(IV) oxides, then reduced intracellular redox carriers such as NADH would transfer electrons through the extracellular environment via *c*-type cytochromes and conductive pili (Lovley, 2012). At the receiving end of the conductive pili, electrons needs to be transferred to the methanogen via another redox complex.

Metabolic modelling of *Geobacter*-mediated ethanol oxidation with sulphate as terminal electron acceptor has suggested that DIET has a metabolic advantage over MIET (hydrogen or formate) (Nagarajan *et al.*, 2013). However, the analysis considered only intracellular metabolism, without taking into account external voltage losses inherent to long-range electron transport. Although DIET does not depend on a mediator to transfer electrons (and is therefore less likely to be limited by diffusion), transport of electrons between the cells through a conductive matrix results in multiple electrochemical losses unique to DIET. These include (1) activation losses (overpotentials) for transfer from a terminal membrane-bound redox complex to the nanowire (and the inverse), (2) electrical resistance of the nanowire and (3) solution resistance caused by migration of ions between the cells. Indirect, secondary limitations may also develop due to development of a pH gradient caused by saline ion migration, and due to accumulation of non-mediator intermediates. A single factor may control, or multiple factors may combine in order to govern feasibility of DIET.

External limitations in nanowire-DIET have not been previously analysed, particularly in relation to well-understood MIET systems. In this work, we propose a mechanistic framework that enables direct assessment of the relative feasibility of DIET and MIET in a thermodynamically restricted syntrophic system (specifically, propionate conversion to acetate and methane).

MODEL DESCRIPTION

Model geometry and components

A three-dimensional transport-reaction model has been implemented to calculate the relative feasibility of the three proposed IET modes, hydrogen-MIET, formate-MIET and DIET. Two spherical acetogen and methanogen cells with a diameter of 1 μm each are positioned 5 μm apart and 5 μm from all boundaries of a rectangular domain of size 17×11×11 μm^3 (Figure 1). For DIET, it is assumed that a direct electric connection is made through the formation of 100 nanowires between each cell pair.

The solution consists of primary substrate, carbonate buffer, mediator and products. Due to the necessity to calculate local pH values, acid dissociation equilibria are included. The chemical components taken into account in the model are therefore protons (H^+), hydroxide (OH^-), potassium ion (K^+), chloride (Cl^-), propionate (Pro^-), propionic acid (HPro), bicarbonate (HCO_3^-), carbon dioxide (CO_2), hydrogen (H_2), formate (For^-), formic acid (HFor), acetate (Ac^-), acetic acid (HAc) and methane (CH_4).

Transport of solutes and charge balance

Transport of all chemical compounds in the solution (cells and surroundings) occurs only through diffusion (introducing diffusion coefficient D) and migration (charge z and migration potential field Φ_{mig}), as described by the steady state Nernst-Planck equations:

$$\nabla \cdot J_i = r_i \qquad \text{with flux} \qquad J_i = -D_i \nabla c_i - \frac{z_i D_i F}{RT} c_i \nabla \Phi_{mig} \qquad (1a)$$

With reaction rates r_i calculated as described in the next section, the unknowns in the system are the 14 concentrations c_i and the potential field gradient $\nabla\Phi_{mig}$ (15 unknowns per control element). Given equation (1a) is applied for each component i (14 equations), the system is fully defined by setting the potassium ion concentration to satisfy the electroneutrality condition:

$$c_{\mathrm{K}^+} = -\sum_{i \neq \mathrm{K}^+} z_i c_i \tag{1b}$$

In order to determine IET rates based only on cell metabolism, no-flux boundary conditions ($-\mathbf{n} \cdot J_i = 0$, where **n** is the normal vector) for the mediator and fixed concentrations ($c_i = c_{0,i}$) for all compounds are set at all domain boundaries. All boundaries are electrically insulated ($-\mathbf{n} \cdot F \sum_i z_i J_i = 0$ for faces 1-5 in Figure 1B), except one face of the domain (6 in Figure 1B) for which the potential Φ_{mig} is set to a reference value ($\Phi_{mig} = 0$ V) to allow calculation of Φ_{mig} from $\nabla\Phi_{mig}$. Default parameter values are listed in Table 1.

Reaction rates

For each compound *i*, the net volume-specific rate r_i in equation (1a) includes contributions from biological conversions $r_{B,i}$ and acid dissociation $r_{A,i}$ (Batstone *et al.*, 2002). Dissociation reactions occur throughout the entire domain, whereas biological conversions only take place in the cells. The net biological contributions, $r_{B,i} = \sum_j \nu_{ji} r_{X,j}$, are calculated with cell reaction rate $r_{X,j}$ and stoichiometry coefficients ν_{ji} specific for reactions occurring in each cell type as given in Figure 1. Due to the cellular scale and thermodynamic restrictions, cell reaction rate can be completely regulated by a thermodynamic inhibition function that incorporates substrate, intermediate and product concentrations, such that empirical rate functions like the Monod equation (Batstone *et al.*, 2006) can be omitted. The cell uptake rate (basis 1 mole propionate, 3 mol mediator, 6 mol e^- equivalents) is given by the maximum rate ($r_X^{\max}$), limited by inhibition factors $f_{inh,j}$ (constrained to $0 < f_{inh,j} < 1$):

$$r_{X,j} = \begin{cases} r_X{}^{\max} f_{inh,MIET,j} & \text{for MIET} \quad (2a) \\ r_X{}^{\max} f_{inh,DIET,jk} & \text{for DIET, two-cell system} \quad (2b) \end{cases}$$

For MIET, the only extracellular factor considered to limit the rate is thermodynamic inhibition:

$$f_{inh,MIET,j} = 1 - \exp\left(\left(\Delta G'_{r,j} - \Delta G'_{min}\right)/RT\right) \tag{3}$$

Equation (3) is equivalent to previously described inhibition functions (Hoh & Cord-Ruwisch, 1996; Batstone *et al.*, 2006), but with the inclusion of a minimum Gibbs free energy change term ($\Delta G'_{min}$) that defines the threshold energy required for cell maintenance and anabolism. By using $f_{inh,MIET,j}$, the cell is limited only by the Gibbs free energy available for electron transport ($\Delta G'_{r,j}$ - $\Delta G'_{min}$) generated by the catabolic reaction considered in each cell. $\Delta G'_{r,j}$ is a function of the surface-averaged concentration $\langle c_i \rangle_j$ (in mol L^{-1}) or partial pressure (in bar, for H_2 and CH_4) of reactants and products *i* for cell *j*, expressed as:

$$\Delta G'_{r,j} = \Delta G^0{}_{r,j} + RT \ln\left(\prod_{i \neq \mathrm{H_2, CH_4}} \langle c_i \rangle_j{}^{\nu_{ji}} \prod_{i = \mathrm{H_2, CH_4}} \langle p_i \rangle_j{}^{\nu_{ji}} \right) \tag{4}$$

Through equations (2)-(4), $r_{X,j}$ is completely regulated by $\langle c_i \rangle_j{}^{\nu_{ji}}$, $\langle p_i \rangle_j{}^{\nu_{ji}}$ and $\Delta G^0{}_{r,j}$. With $r_X^{\max}$ sufficiently high, an increase in $r_X^{\max}$ is compensated for by a small decrease in $f_{inh,MIET,j}$ via small changes in $\langle c_i \rangle_j{}^{\nu_{ji}}$ and $\langle p_i \rangle_j{}^{\nu_{ji}}$. $r_X{}^{max}$ can therefore be set to an arbitrarily high value so that reactions proceed at their thermodynamic limit ($\Delta G'_{r,j}$ - $\Delta G'_{min}$ approaches 0). Due to low mediator concentrations and the reaction stoichiometry, equation (4) is dominated by the mediator term ($\langle p_{H_2} \rangle_j^{\nu_{j,H_2}}$ or $\langle c_{For^-} \rangle_j^{\nu_{j,For^-}}$).

As stated above, $r_{X,j}$ is not governed by a kinetic function but it operates at the highest rate that is thermodynamically possible. The critical parameter is the minimum Gibbs free energy ($\Delta G'_{min}$), which has been estimated to be between -15 and -25 kJ mol^{-1} substrate (Stams &

Plugge, 2009). Note that a larger (more negative) $\Delta G'_{min}$ will result in a lower rate, though both MIET and DIET will be uniformly impacted. Applying our model specifically to a propionate grown co-culture of *Syntrophobacter wolinii* and *Methanospirillum hungatei* (both capable of formate-MIET) growing on propionate (Boone & Bryant, 1980) and applying a growth yield ($Y_{S/X}$) of 0.15 Cmol mol^{-1} propionate, based on the observed growth rate and applied substrate concentrations (Boone & Bryant, 1980), we estimate $\Delta G'_{min}$ = -15.2 kJ mol^{-1} for both cell types (see Supplementary Figure 1). This value is applied to DIET and MIET.

The only difference between implementations for DIET and MIET is in the direct electron transfer component. In DIET, electrons are transferred between acetogen and methanogen through a conductive system driven by a voltage $V_{net,jk}$ between the two cells *j* and *k*. Electrons are produced through propionate metabolism by an oxidising cell, and then transferred to the reducing cells for carbon dioxide conversion (see Figure 1C). Unlike with MIET, where the feasibility of the reaction is determined by the cell environment, the feasibility of the DIET reaction pair is determined on its paired basis. The net voltage available ($V_{net,jk}$) in the two-cell system is equal to the voltage available from the reaction given in Figure 1C ($V_{r,jk}$) minus DIET-specific voltage losses for electron transfer between membrane bound redox cofactors and nanowire (activation losses) at both cells *j* and *k*, nanowire resistance, and ion migration in the solution, as depicted by equation (5):

$$V_{net,jk} = V_{r,jk} - \eta_{cyt,j} - \eta_{cyt,k} - \eta_{nw,jk} - \eta_{mig,jk} \tag{5}$$

The voltages in equation (5), $V_{net,jk}$ and V_r, relate to Gibbs free energy changes via $V = -\Delta G' / \left(F \nu_{e^-}\right)$ (where $\nu_{e^-} = 6$, the number of electrons involved in the catabolic half reaction), so that $V_{r,jk}$ is calculated via the surface-averaged concentrations (using equation (4) and $\Delta G'_{r,jk} = \Delta G'_{r,j} + \Delta G'_{r,k}$). We found that because no mediator is involved for DIET, none of the terms $\left\langle c_i \right\rangle_j^{\nu_{ji}}$ and $\left\langle p_i \right\rangle_j^{\nu_{ji}}$ changes significantly with IET rate and as a result the voltage available from reaction is constant for all reported DIET rates ($V_{r,jk}$ = 52.93 mV). Whereas MIET is regulated via the energy made available by the catabolic reaction ($\Delta G'_{r,j}$), DIET is controlled via the external electron transfer voltage losses (η). Because voltages V_{jk} and voltage losses η_{jk} in equation (5) are defined for the oxidising-reducing cell pair, the values observed by cell j are identical to those observed by its partner k (i.e., $V_{jk} = V_{kj}$ and $\eta_{jk} = \eta_{kj}$).

The electron transfer rate is limited by an inhibition function governed by the net and minimum voltage:

$$f_{inh,DIET,jk} = 1 - \exp\left(-F\nu_e\left(V_{net,jk} - V_{min}\right)/RT\right) \tag{6}$$

There are two differences between the model for MIET and DIET. First, additional losses specific for DIET are taken into account (equation (5)) and second, inhibition for cell j (equation (6)) depends also directly on cell k ($V_{net,jk} = V_{net,kj}$, therefore $f_{inh,DIET,jk} = f_{inh,DIET,kj}$). Although equation (6) is expressed as voltage rather than free energy as in equation (3), the two regulation functions (3) and (6) are completely analogous as seen through the voltage-Gibbs free energy relation above.

The minimum voltage (V_{min}) can be calculated directly from the voltage-Gibbs relation and $\Delta G'_{min}$, yielding V_{min} = 52.51 mV for any cell pair.

Cell conversion rates ($r_{X,j}$) are volume-specific and are referenced to the primary substrate. In order to express the rate per cell, the cell-specific electron transfer rate has been calculated as $rate_{IET,j} = r_{X,j} \pi d_{cell}^{3} N_A$ (where N_A is Avagadro's number and 6 mol electrons are transferred per mol propionate consumed), with unit $e^{-} \cdot s^{-1}$.

Redox cofactor activation losses

Activation losses occur each time an electron is transferred from the electron carrier associated with the membrane to the nanowire or *vice versa*. Both of these voltage losses ($\eta_{act,j}$ and $\eta_{act,k}$; (1) in Figure 1C) are calculated using the Butler-Volmer equation assuming a one-step, single-electron transfer process. The total current between the cells (I_{jk}) is the same in the electron producing and consuming cells ($I_{jk} = I_{kj} = rate_{IET,jk} F / N_A$), and this current is distributed evenly over the nanowires connecting the cells (analogous to an electrical circuit in parallel). The Butler-Volmer equation used to calculate the activation voltage loss ($\eta_{act,j}$) is as shown in equation (7) (Bard & Faulkner, 1980; Noren & Hoffman, 2005):

$$I_{jk} / N_{nw,pair} = FA_{act,j} k_0 c_{act} \left(e^{(1-\beta)(F/RT)\eta_{act,j}} - e^{-\beta(F/RT)\eta_{act,j}} \right) \qquad (7)$$

The number of nanowires present between the cell pair ($N_{nw,pair}$), symmetry factor (β), cofactor transfer rate constant (k_0) and activation cofactor concentration (c_{act}) have been taken as the same for electron producing and consuming cells. Given that the redox cofactor surface area available for activation ($A_{act,j}$) is calculated as described below, $\eta_{act,j}$ remains as the only unknown. The Butler-Volmer equation can therefore be solved implicitly to determine voltage losses $\eta_{act,j}$ and $\eta_{act,k}$ at which the current will be at its maximum.

To determine the total redox cofactor surface area per cell ($A_{act,cell}$), it was estimated that in total 10% of the cell surface area is available to transfer electrons to the nanowires, regardless of the number of nanowires. This estimate considers 10^4 redox cofactors ($N_{act,j} = 10^4$) present on the cell surface of a *Shewanella* cell (Lower *et al.*, 2007) and a redox cofactor diameter between 5 and 8 nm in diameter (Wigginton *et al.*, 2007), using which the cytochrome coverage is calculated as around between 6 and 16% (Supplementary Table 2). These values match well to estimates made by Okamoto et al. (2009). The available redox cofactor area per connection is calculated assuming that the total redox cofactor area available is distributed evenly over all nanowires connected to cell *j* ($A_{act,j} = A_{act,cell} / N_{nw,j}$). In a two-cell system this simplifies to $A_{act,j} = A_{act,k}$, such that activation losses are the same at both cells ($\eta_{act,j} = \eta_{act,k}$).

The cofactor transfer rate constant k_0 for redox cofactor-nanowire transfer is not readily available in literature. However, redox cofactor-electrode electron transfer rate constants have been reported. The heterogeneous rate constant for outer membrane cytochromes on *Shewanella* has been calculated as 150 s^{-1} (Okamoto *et al.*, 2009). Using the redox cofactor concentration derived from $N_{act,cell}$, the surface concentration (c_{act}) is estimated to be 5.29×10^{-9} mol m^{-2}. This matches well with the experimentally observed exchange current density (Bowden *et al.*, 1982; Reed & Hawkridge, 1987), as shown in Supplementary Table 3. Rates for electron transfer within a biofilm have been estimated to be 40 times faster than for transfer between biofilm and electrode (Ly *et al.*, 2013). Therefore, for both the acetogen and methanogen, we consider k_0 as equal to 6000 s^{-1}. Further research could provide insight to the correctness of this estimate. Because no direct measurements have been done on Butler-Volmer parameters for system modelled in our work, we also provide a sensitivity assessment to test a range of parameters.

Nanowire ohmic losses

Ohmic conductivity for the nanowire is assumed because of recent experimental support (Malvankar *et al.*, 2014) and as experimentally observed parameters can be found in literature (El-Naggar *et al.*, 2010; Malvankar *et al.*, 2011). The voltage loss due to nanowire resistance is calculated using Ohm's law, expressed for this system as:

$$\eta_{nw,jk} = R_{nw,jk} I_{jk} \big/ N_{nw,pair} = \rho_{nw} L_{nw,jk}\, I_{jk} \big/ N_{nw,pair}\, A_{nw} \tag{8}$$

which is function of the IET rate, resistivity (ρ_{nw}), nanowire length ($L_{nw,jk}$) and nanowire cross-sectional area (A_{nw}). Parameters for nanowire losses are taken from measurements performed on *Geobacter sulfurreducens*. The nanowire length is set as the interspecies distance, 5 um (Figure 1). The nanowire diameter is d_{nw} = 4 nm and the electrical resistivity ρ_{nw} = 1 Ω m (Malvankar *et al.*, 2011).

Migration losses

The voltage loss due to extracellular ion migration in DIET, $\eta_{mig,jk}$, is related to an extracellular electric field (*E)* formed in the medium as a result of ion transport, equations (1a and b). This electric field causes a potential field (related via $E = -\nabla\Phi$) resulting in an overall voltage loss $\eta_{mig,jk}$. A potential field is implicitly calculated in the modelling package used (and has been separately verified by calculation), from which $\eta_{mig,jk}$ is calculated as the difference between the average value of Φ_{mig} at the surfaces of methanogen and acetogen cells ($\eta_{mig,jk} = \left| \langle \Phi_{mig} \rangle_k - \langle \Phi_{mig} \rangle_j \right|$, the absolute value is taken such that $\eta_{mig,jk} = \eta_{mig,kj} > 0$ in equation (5)). This loss is only relevant for DIET because electrons are transferred separate from the ions.

Implementation of for a multicellular system

The MIET model can be directly implemented in a multicellular system without modification. When applying the DIET model to a larger cell community, the key complication is sharing of electrons between multiple pairs of donors and acceptors while maintaining a closed electron balance for all cell pairs. We propose here a method using an electron balancing factor, $f_{bal,jk}$, for each cell in a pair that limits the rate of faster reacting cells to the rate of its connected partners. The DIET rate equation (2b) can be rewritten for a multicellular system:

$$r_{X,j} = \sum_k r_{X,jk} = r_X^{\max} \sum_k \left(f_{inh,DIET,jk} \, f_{bal,jk} \right) \quad \text{for DIET, multicellular system} \tag{9}$$

$f_{bal,jk}$ is a limiting factor ($0 \le \sum_k f_{bal,jk} \le 1$) introduced to satisfy the electron balance in the system and is needed when a cell forms connections with multiple other cells. When modelling a single cell pair with the same r_X^{max}, rates are always balanced ($\sum_k f_{bal,jk} = \sum_j f_{bal,kj} = 1$) because the inhibition factor is the same for both cells (all terms in equation (6) are the same for j and k, so $f_{inh,DIET,jk} = f_{inh,DIET,kj}$), thereby reducing multicellular DIET rate equation (9) to two-cell system DIET rate equation (2b).

The reason an extra factor $f_{bal,jk}$ must be introduced for a multicellular system is related to the redox cofactor area. As stated before, it is assumed that the total area of membrane-bound redox proteins $A_{act,cell}$ is the same for all cells and is shared evenly among the connected nanowires. For the multicellular system, one cell j can form a different number of nanowires than cell k, so that the redox cofactor area available to each nanowire connected to cell j, $A_{act,j}$, is no longer equal to $A_{act,k}$. The activation loss for j can thereby be limited in a different way than for cell k that is connected to a different number of cells ($N_{nw,j} \neq N_{nw,k}$, so $\eta_{act,j} \neq \eta_{act,k}$ as per equation (7)), resulting in a different set of inhibition factors for cell j, k and their respective partners, consecutively requiring an extra rate balancing factor $f_{bal,jk} \neq f_{bal,kj}$ to close the electron conservation balance. $f_{bal,jk}$ is calculated for all cells and neighbours by maximising the total IET rate.

In order to investigate how electrons are shared according to the method described here and how sharing affects the total IET rate, a case study is set up involving twelve acetogens and twelve methanogens distributed randomly in a 30×30×30 μm^3 domain. An average interspecies distance of 5 µm between a cell and its closest partner is enforced and 100 nanowires are taken to be present between an acetogen and each methanogen in a 10 µm radius (*i.e.*, $N_{nw,pair}$ remains 100, but $N_{nw,j} = \sum_k N_{nw,cell}$ can exceed 100).

Implementation

Both two-cell and multicellular models were implemented in COMSOL Multiphysics (COMSOL 4.4, COMSOL Inc., Burlington, MA) using the Nernst-Planck Equations module.

Two Global ODEs and DAEs modules are set up and solved in parallel to determine the voltage losses for the Butler-Volmer and Ohm's law equations. For the multicellular model, the model geometry was defined in MATLAB and transferred via LiveLink (MATLAB 2014a, MathWorks, Natick, MA). $f_{bal,jk}$ is determined by minimising $\left(\sum_j rate_{IET,j}\right)^{-1}$ using a SNOPT algorithm optimiser (Gill *et al.*, 2005). Model code can be provided by the corresponding author on request.

RESULTS AND DISCUSSION

Two-cell system

Results for single cell pair simulations show that MIET is controlled by hydrogen and formate/formic acid diffusion. The concentration along the centre of the domain changes by less than 0.01% of the mean concentration for all components except hydrogen, formate and formic acid (Figure 2A). DIET rates are controlled by activation losses (93% of total voltage losses, see Figure 2B), while migration losses and diffusion limitation are insignificant (η_{mig} << 1% total voltage losses and the overall relative concentration differences for all components less than 0.01%). Formate-MIET (317×10^3 $e^-\cdot cp^{-1}$ s^{-1}, Figure 2C) is thermodynamically the most favourable IET mode, with the DIET rate 1 order of magnitude (44.9×10^3 $e^-\cdot cp^{-1}$ s^{-1}) and the hydrogen-MIET rate 2 orders of magnitude lower (5.24×10^3 $e^-\cdot cp^{-1}$ s^{-1}). Thus, considering external factors and with the baseline parameters chosen, DIET is more favourable than hydrogen-MIET, but substantially less favourable than formate MIET.

The main reason formate-MIET allows a greater transfer rate than hydrogen-MIET (Figure 2C) is because it allows a larger concentration gradient while maintaining feasible thermodynamics (Figure 2A), despite the higher diffusion coefficient of hydrogen. This aligns well with previous analysis (Boone *et al.*, 1989; Batstone *et al.*, 2006).

DIET activation losses are strongly dependent on multiple parameters which have limited literature support, likely the most arguable value being the cofactor transfer rate constant (k_0). Reducing k_0 by a factor 10 (*e.g.*, if redox cofactor-nanowire transfer is not 40 but only 4 times faster than redox cofactor-electrode, or if k_0 is tenfold lower than reported in Okamoto et al (2009)) makes activation voltage losses even more dominant (99.2% of total voltage losses) and lowers the feasibility for DIET to a rate lower than hydrogen-MIET (Figure 3, case 2). Doubling the cofactor transfer rate constant almost doubles the IET rate, with activation losses responsible for 87% of the total voltage losses. It is not until k_0 is increased tenfold that redox cofactor activation is no longer the only governing loss (57% of the total voltage losses, the remaining 43% attributed to Ohmic losses in the nanowire) and that the DIET rate approaches the formate-MIET rate (to 90%). From equation (7) it can be seen that the same effects can be obtained by varying $A_{act,cell}$ or c_{act} with the same factor instead of k_0. An increase of $A_{act,cell}$ could be justified by assuming a different larger size of the redox cofactor (*e.g.*, Edwards et al. (2014)), a decrease by considering the cell surface not facing the other cell is unlikely to be used. Similarly, an increase in c_{act} is possible if redox cofactors are preferentially located where electron transfer to nanowires occurs, instead of homogeneously distributed over the cell surface.

The amount of cytochromes on the cell surface ($N_{act,cell}$) governs both c_{act} and $A_{act,cell}$ and will therefore have an even stronger effect on the DIET rate than the same relative change in k_0, although the range through which $N_{act,cell}$ can be varied is smaller (for example, a tenfold increase in would result in an unrealistic 100% redox cofactor coverage). Reducing $N_{act,cell}$ by a factor 5 makes DIET less than half as feasible as hydrogen-MIET (Figure 3, case 3), while increasing $N_{act,cell}$ by a factor 5 makes DIET thermodynamically more feasible than formate-MIET.

A small fraction of the total voltage losses for the default parameters is due to Ohmic losses in the nanowire. The resistivity (ρ_{nw}) used to determine Ohmic losses was measured for a biofilm (Malvankar *et al.*, 2011), which means that the actual resistivity of an individual nanowire could be smaller. Reducing ρ_{nw} by 2 orders of magnitude (*e.g.*, to the resistivity reported for individual nanowires in *Shewanella oneidensis* (El-Naggar *et al.*, 2010)) causes a small increase the in the DIET rate (Figure 3, case 4), as the system is completely dominated by activation losses (99.9% of total voltage losses). Alternative nanowire conductivity models, such as electron hopping between redox components aligned along membrane vesicles as recently suggested to account for conduction in *Shewanella oneidensis* nanowires (Pirbadian *et al.*, 2014) could be implemented in the model described here by considering a series of redox cofactor activation steps along the nanowire. The activation energy for a single step as calculated here, though, indicates that the standard activation rate constant k_0 for cofactor-cofactor transfer will need to be orders of magnitude higher than the k_0 used in this model for cytochrome hopping to be thermodynamically feasible.

The number of nanowires formed per cell pair ($N_{nw,pair}$) has a strong effect on the Ohmic loss (affecting the current per nanowire, $I_{jk}/N_{nw,pair}$, via equation (8)) but no effect on activation losses (changes to the current per nanowire and $A_{act,j}$ cancel out), therefore a tenfold increase in $N_{nw,pair}$ will have the same effect as a tenfold decrease in ρ_{nw}. The range through which $N_{nw,pair}$ can be varied is different from the range for ρ_{nw}, however. The number of nanowires could be an order of magnitude lower or higher than the default value of 100. If 10 nanowires are formed per cell pair, the DIET rate changes to 60% of the original value, while 1000 nanowires per cell pair would result in an IET rate 107% of the default rate (Figure 3, case 5) as the system is fully dominated by activation losses.

Increasing interspecies distance (Δx) to 25 μm limits the DIET rate by increasing Ohmic losses but does not affect the redox cofactor activation losses, while for MIET the concentration gradient and thereby the diffusion flux is lowered. The model shows that a 5 times larger Δx attenuates MIET more than DIET, as DIET activation losses remain dominant (75% of the total voltage losses), resulting in a rate 80% of the original rate, while both MIET rates drop to 65% of the original rate (Figure 3, case 6). This suggests DIET might be a thermodynamically more feasible alternative to MIET for disperse communities limited by diffusion, which is contrary to experimental observations where nanowire-DIET is commonly observed in dense aggregates (Summers *et al.*, 2010; Rotaru, Shrestha, Liu, Markovaite, *et al.*, 2014), possibly indicating that co-evolution and co-metabolism are more important than external limitations in this system. We also note that use of non-organic conductive elements such as activated carbon (Liu *et al.*, 2012) and magnetite (Cruz Viggi *et al.*, 2014) could reduce resistivity, and leave only activation losses (though these will likely be increased), possibly making long-range transport even more feasible.

The work done here only considers external limitations, and does not consider that there are energetic losses involved in translation of electrons to an electron mediator as assessed by (Nagarajan *et al.*, 2013). Metabolic modelling indicated that the cell metabolism for DIET is more efficient than for MIET, justifying a less negative value for $\Delta G'_{min}$ (resulting in a smaller V_{min}). Comparing formate-MIET at a $\Delta G'_{min}$ = -15.2 kJ mol^{-1} per cell to DIET at a slightly less negative $\Delta G'_{min}$ values (*e.g.*, -14.5 kJ mol^{-1}, see Figure 3, case 7), suggests that for IET rates reported in this work (10^4-10^5 $e^{-}\cdot cp^{-1}\cdot s^{-1}$) a slightly more efficient metabolism for DIET is enough for the rate to match the formate-MIET rate. This result is important, since it suggests that comparative external electron transfer feasibility (sometimes resulting in order of magnitude different rates) can be compensated for by very slight advantages in cellular metabolism and hence cellular maintenance energy.

Multicellular system

The multicellular system was implemented to demonstrate application of the two-cell principles in a multicellular system, and identify whether a 3D field with multiple sources and sinks would result in a different overall transfer rate. Experimentally observed systems analogous to this model include *Geobacter metallireducens/Methanosaeta harundinacea* (Rotaru, Shrestha, Liu, Shrestha, *et al.*, 2014) and *Geobacter metallireducens/Methanosarcina barkeri* (Rotaru, Shrestha, Liu, Markovaite, *et al.*, 2014), both of which degrade ethanol to methane, a conversion that is analogous to propionate oxidation but with more favourable thermodynamics.

Results are shown in Figure 4 and represent simultaneously electron transfer rate between cells (coloured links), as well as overall migration potential field in two planes (coloured sections). While the migration potential field and the resulting losses $\eta_{mig,jk}$ are not limiting electron transfer, it does indicate that the potential field is governed mainly by interacting pairs. The results indicate that a multicellular system achieves slightly lower DIET rates per cell (on average 15% lower, $r_{X,j}$ = 38.2×10^3 versus 44.9×10^3 e$^-$·s^{-1}). Rates depend strongly on the local species distribution. The highest IET rate is obtained by cell *a* in Figure 4 (71.0×10^3 e$^-$·s^{-1}), a methanogen surrounded by six acetogens, all in turn connected to fewer methanogens. The lowest rate achieved is 13.4×10^3 e$^-$·s^{-1} for cell b in Figure 4, one of the acetogens connected to methanogen *a*, but no other methanogens. MIET rates are not affected by the larger community (the average rate is 2% higher than for the cell pair system).

The decrease in DIET rate is due to increased activation losses and electron balancing in the network. Despite the lower average IET rate, the average activation loss per cell pair increases (from 0.38 to 0.40 mV; 93% to 97% of total voltage losses), while Ohmic losses is almost 3 times lower due to the slightly lower IET rate and many additional nanowires formed per cell (on average, $N_{nw,j}$ = 291 for the multicellular system, compared to $N_{nw,j}$ = $N_{nw,pair}$ = 100 for the cell pair system).

These results suggest communities capable of DIET achieve rates lower than the cell pair system, showing that formate-MIET remains thermodynamically more favourable compared to DIET for multicellular communities using the baseline parameter set chosen. It should be emphasised, however, that DIET rates in the multicellular system can exceed the cell pair rates if activation losses become less dominant. For example, increasing k_0 by a factor 10 (parameter set from Figure 3, case 2, simulation 3) increases the average cell IET rate to 309×10^3 $e^-\cdot s^{-1}$ (10% higher than cell pair DIET).

CONCLUSIONS

Investigation of extracellular losses suggests formate-MIET is thermodynamically more favourable than hydrogen-MIET (2 orders of magnitude rate difference) and DIET using nanowires (1 order of magnitude rate difference), with both MIET modes limited by diffusion flux and DIET limited by redox cofactor activation losses. In order for DIET to achieve rates comparable to or higher than formate-MIET, the true value for cell-nanowire cofactor transfer rate constant (k_0), cell redox cofactor concentration (c_{act}), area ($A_{act,cell}$) or count ($N_{act,cell}$) must be 5-10 times higher than estimated from literature published to date. Cellular metabolism may also readily compensate for a decreased favourability in external transfer feasibility (Nagarajan *et al.*, 2013) with differences on the order of less than a kJ mol^{-1} per cell compensating for electrochemical limitations in DIET.

Supplementary information is available at The ISME Journal's website

ACKNOWLEDGEMENTS

This project was supported under Australian Research Council's Discovery Projects funding scheme (project number DP0985000). Dr. Bernardino Virdis is supported by strategic funding for the Centre for Microbial Electrochemical Systems (UQ). Dr. Damien Batstone is the recipient of an Australian Research Fellowship.

CONFLICT OF INTEREST

The authors declare no conflict of interest

REFERENCES

Bard A, Faulkner L. (1980). Electrochemical methods: fundamentals and applications. 2nd ed. Wiley: New York.

Batstone DJ, Keller J, Angelidaki I, Kalyuzhnyi S V., Pavlostathis SG, Rozzi A, *et al.* (2002). Anaerobic Digestion Model No. 1. First edit. IWA Publishing: London.

Batstone DJ, Picioreanu C, van Loosdrecht MCM. (2006). Multidimensional modelling to investigate interspecies hydrogen transfer in anaerobic biofilm. *Water Res* **40**:3099–3108.

Boone DR, Bryant MP. (1980). Propionate-Degrading Bacterium, Syntrophobacter wolinii sp. nov. gen. nov., from Methanogenic Ecosystems. *Appl Envir Microbiol* **40**:626–632.

Boone DR, Johnson RL, Liu Y. (1989). Diffusion of the Interspecies Electron Carriers H2 and Formate in Methanogenic Ecosystems and Its Implications in the Measurement of Km for H2 or Formate Uptake. *Appl Environ Microbiol* **55**:1735–1741.

Bowden EF, Hawkridge FM, Chlebowski JF, Bancroft EE, Thorpe C, Blount HN. (1982). Cyclic voltammetry and derivative cyclic voltabsorptometry of purified horse heart cytochrome c at tin-doped indium oxide optically transparent electrodes. *J Am Chem Soc* **104**:7641–7644.

Cruz Viggi C, Rossetti S, Fazi S, Paiano P, Majone M, Aulenta F. (2014). Magnetite particles triggering a faster and more robust syntrophic pathway of methanogenic propionate degradation. *Environ Sci Technol* **48**:7536–7543.

Edwards MJ, Baiden NA, Johs A, Tomanicek SJ, Liang L, Shi L, *et al.* (2014). The X-ray crystal structure of Shewanella oneidensis OmcA reveals new insight at the microbe-mineral interface. *FEBS Lett* **588**:1886–1890.

El-Naggar MY, Wanger G, Leung KM, Yuzvinsky TD, Southam G, Yang J, *et al.* (2010). Electrical transport along bacterial nanowires from Shewanella oneidensis MR-1. *Proc Natl Acad Sci U S A* **107**:18127–18131.

Gill PE, Murray W, Saunders MA. (2005). SNOPT: An SQP Algorithm for Large-Scale Constrained Optimization. *SIAM Rev* **47**:99–131.

Hedderich R, Whitman WB. (2013). Physiology and Biochemistry of the Methane-Producing Archaea. In:*The Prokaryotes*, Rosenberg, E, DeLong, EF, Lory, S, Stackebrandt, E, & Thompson, F (eds), Springer Berlin Heidelberg: Berlin, Heidelberg, pp. 635–662.

Hoh CY, Cord-Ruwisch R. (1996). A practical kinetic model that considers endproduct inhibition in anaerobic digestion processes by including the equilibrium constant. *Biotechnol Bioeng* **51**:597–604.

Liu F, Rotaru A-E, Shrestha PM, Malvankar NS, Nevin KP, Lovley DR. (2012). Promoting direct interspecies electron transfer with activated carbon. *Energy Environ Sci* **5**:8982–8989.

Lovley DR. (2012). Electromicrobiology. *Annu Rev Microbiol* **66**:391–409.

Lower BH, Shi L, Yongsunthon R, Droubay TC, McCready DE, Lower SK. (2007). Specific bonds between an iron oxide surface and outer membrane cytochromes MtrC and OmcA from Shewanella oneidensis MR-1. *J Bacteriol* **189**:4944–52.

Ly HK, Harnisch F, Hong S-F, Schröder U, Hildebrandt P, Millo D. (2013). Unraveling the interfacial electron transfer dynamics of electroactive microbial biofilms using surface-enhanced Raman spectroscopy. *ChemSusChem* **6**:487–492.

Malvankar NS, Vargas M, Nevin KP, Franks AE, Leang C, Kim B-C, *et al.* (2011). Tunable metallic-like conductivity in microbial nanowire networks. *Nat Nanotechnol* **6**:573–579.

Malvankar NS, Yalcin SE, Tuominen MT, Lovley DR. (2014). Visualization of charge propagation along individual pili proteins using ambient electrostatic force microscopy. *Nat Nanotechnol* **9**:1012–1017.

Mehta T, Coppi M V., Childers SE, Lovley DR. (2005). Outer membrane c-type cytochromes required for Fe(III) and Mn(IV) oxide reduction in Geobacter sulfurreducens. *Appl Environ Microbiol* **71**:8634–8641.

Morita M, Malvankar NS, Franks AE, Summers ZM, Giloteaux L, Rotaru A-E, *et al.* (2011). Potential for direct interspecies electron transfer in methanogenic wastewater digester aggregates. *MBio* **2**:e00159–11.

Nagarajan H, Embree M, Rotaru A-E, Shrestha PM, Feist AM, Palsson BØ, *et al.* (2013). Characterization and modelling of interspecies electron transfer mechanisms and microbial community dynamics of a syntrophic association. *Nat Commun* **4**:2809.

Noren DA, Hoffman MA. (2005). Clarifying the Butler–Volmer equation and related approximations for calculating activation losses in solid oxide fuel cell models. *J Power Sources* **152**:175–181.

Okamoto A, Nakamura R, Hashimoto K. (2011). In-vivo identification of direct electron transfer from Shewanella oneidensis MR-1 to electrodes via outer-membrane OmcA–MtrCAB protein complexes. *Electrochim Acta* **56**:5526–5531.

Okamoto A, Nakamura R, Ishii K, Hashimoto K. (2009). In vivo electrochemistry of C-type cytochrome-mediated electron-transfer with chemical marking. *Chembiochem* **10**:2329–2332.

Pirbadian S, Barchinger SE, Leung KM, Byun HS, Jangir Y, Bouhenni R a., *et al.* (2014). Shewanella oneidensis MR-1 nanowires are outer membrane and periplasmic extensions of the extracellular electron transport components. *Proc Natl Acad Sci* **111**:12883–12888.

Reed DE, Hawkridge FM. (1987). Direct electron transfer reactions of cytochrome c at silver electrodes. *Anal Chem* **59**:2334–2339.

Rotaru A-E, Shrestha PM, Liu F, Markovaite B, Chen S, Nevin K, *et al.* (2014). Direct Interspecies Electron Transfer Between Geobacter metallireducens and Methanosarcina barkeri. *Appl Environ Microbiol* **80**:4599–4605.

Rotaru A-E, Shrestha PM, Liu F, Shrestha M, Shrestha D, Embree M, *et al.* (2014). A new model for electron flow during anaerobic digestion: direct interspecies electron transfer to Methanosaeta for the reduction of carbon dioxide to methane. *Energy Environ Sci* **7**:408–415.

Shi L, Richardson DJ, Wang Z, Kerisit SN, Rosso KM, Zachara JM, *et al.* (2009). The roles of outer membrane cytochromes of Shewanella and Geobacter in extracellular electron transfer. *Environ Microbiol Rep* **1**:220–227.

Shrestha PM, Rotaru A-E, Aklujkar M, Liu F, Shrestha M, Summers ZM, *et al.* (2013). Syntrophic growth with direct interspecies electron transfer as the primary mechanism for energy exchange. *Environ Microbiol Rep* **5**:904–910.

Stams AJM, De Bok FAM, Plugge CM, van Eekert MHA, Dolfing J, Schraa G. (2006). Exocellular electron transfer in anaerobic microbial communities. *Environ Microbiol* **8**:371–382.

Stams AJM, Plugge CM. (2009). Electron transfer in syntrophic communities of anaerobic bacteria and archaea. *Nat Rev Micro* **7**:568–577.

Summers ZM, Fogarty HE, Leang C, Franks AE, Malvankar NS, Lovley DR. (2010). Direct Exchange of Electrons Within Aggregates of an Evolved Syntrophic Coculture of Anaerobic Bacteria. *Science (80-)* **330**:1413–1415.

Vargas M, Malvankar NS, Tremblay P-L, Leang C, Smith JA, Patel P, *et al.* (2013). Aromatic Amino Acids Required for Pili Conductivity and Long-Range Extracellular Electron Transport in Geobacter sulfurreducens. *MBio* **4**:e00105–13.

Wigginton NS, Rosso KM, Lower BH, Shi L, Hochella MF. (2007). Electron tunneling properties of outer-membrane decaheme cytochromes from Shewanella oneidensis. *Geochim Cosmochim Acta* **71**:543–555.

FIGURE LEGENDS

Figure 1: Model geometry, boundary conditions and reactions involved in the three described interspecies electron transfer mechanisms: (A) hydrogen-MIET, (B) formate-MIET

and (C) DIET. In (B), on boundaries 1-6 a no-flux condition is set for mediators (H_2, For^- and HFor) and fixed concentrations for all other components. Boundary concentration values ($c_{0,i}$) are stated in Table 1. A zero-potential is set on boundary 6. In (C), numbers denote voltage losses for (1) redox factor activation losses, (2) nanowire resistance and (3) migration.

Figure 2: A: mediator profiles along the centre of the domain (x-axis at $L_y/2$, $L_z/2$) for formate- and hydrogen-MIET, for the default parameter set. B: DIET voltage and losses along the nanowire, default parameter set. Note that η_{mig} is negligible compared to other losses. C and D: net IET rates for MIET and DIET, respectively, default parameter set.

Figure 3: Sensitivity analysis for cell pair IET rates. The numbers on the right hand side indicate different parameter sensitivity studies (cases) and are referred to in the text. Note that case 1 shows the same data as Figure 2C-D.

Figure 4: Cell positions (dark grey spheres are acetogens, light grey spheres methanogens), nanowires (lines, colour shows IET rate through nanowire in $e^-\cdot s$) and potential field due to migration (planes, colour shows potential in pV). Cell a achieves the highest IET rate, cell b the lowest. Arrows denote the direction in which electrons flow. A movie showing cell positions and potential fields from different angles is available in the supplementary material as Supplementary Movie 1.

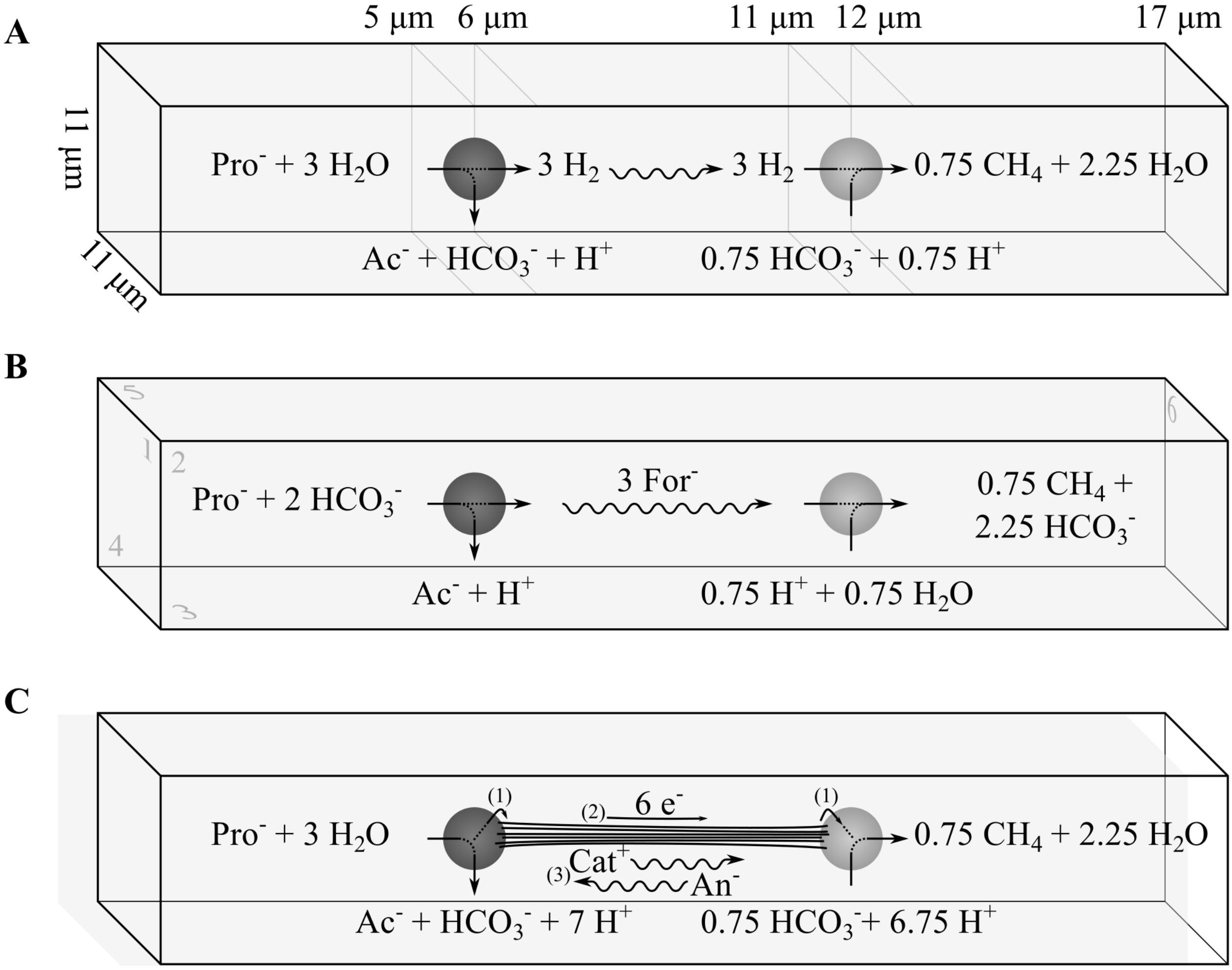
A
5 µm
6 µm
11 µm
12 µm
17 µm
11 µm
11 µm
Pro⁻ + 3 H₂O
3 H₂
3 H₂
0.75 CH₄ + 2.25 H₂O
Ac⁻ + HCO₃⁻ + H⁺
0.75 HCO₃⁻ + 0.75 H⁺
B
5
6
1
2
4
3
Pro⁻ + 2 HCO₃⁻
3 For⁻
0.75 CH₄ +
2.25 HCO₃⁻
Ac⁻ + H⁺
0.75 H⁺ + 0.75 H₂O
C
(1)
(2)
6 e⁻
(1)
Pro⁻ + 3 H₂O
0.75 CH₄ + 2.25 H₂O
Cat⁺
(3)
An⁻
Ac⁻ + HCO₃⁻ + 7 H⁺
0.75 HCO₃⁻+ 6.75 H⁺

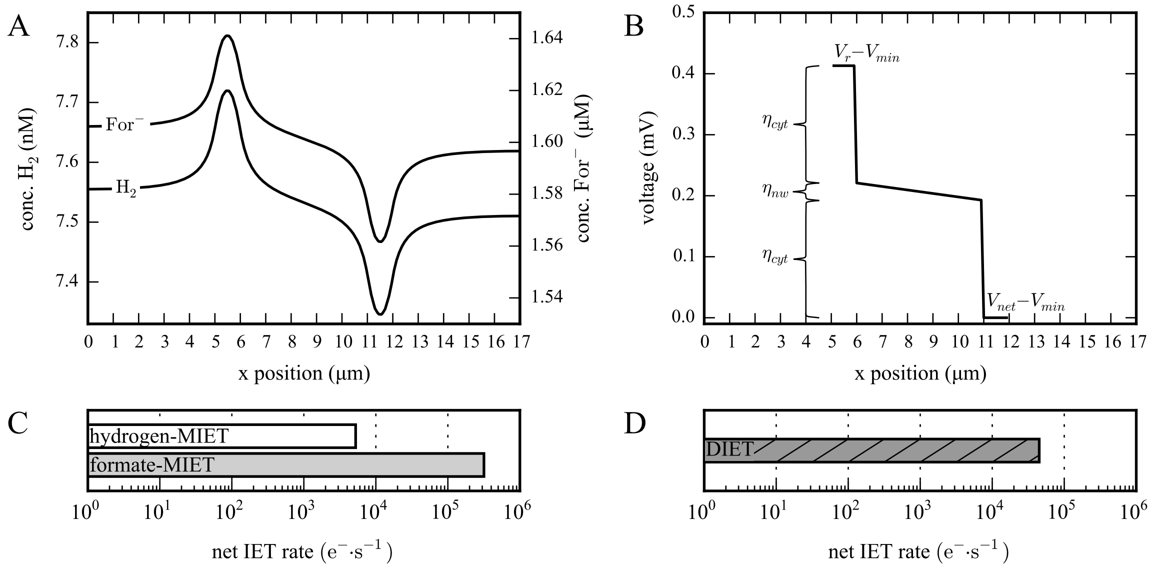
A
B
C
D
conc. H_2 (nM)
conc. For^- (µM)
For^-
H_2
x position (µm)
voltage (mV)
$V_r - V_{min}$
$V_{net} - V_{min}$
η_{cyt}
η_{nw}
η_{cyt}
hydrogen-MIET
formate-MIET
DIET
net IET rate ($e^- \cdot s^{-1}$)
7.4
7.5
7.6
7.7
7.8
1.54
1.56
1.58
1.60
1.62
1.64
0.0
0.1
0.2
0.3
0.4
0.5
0 1 2 3 4 5 6 7 8 9 10 11 12 13 14 15 16 17
10^0 10^1 10^2 10^3 10^4 10^5 10^6

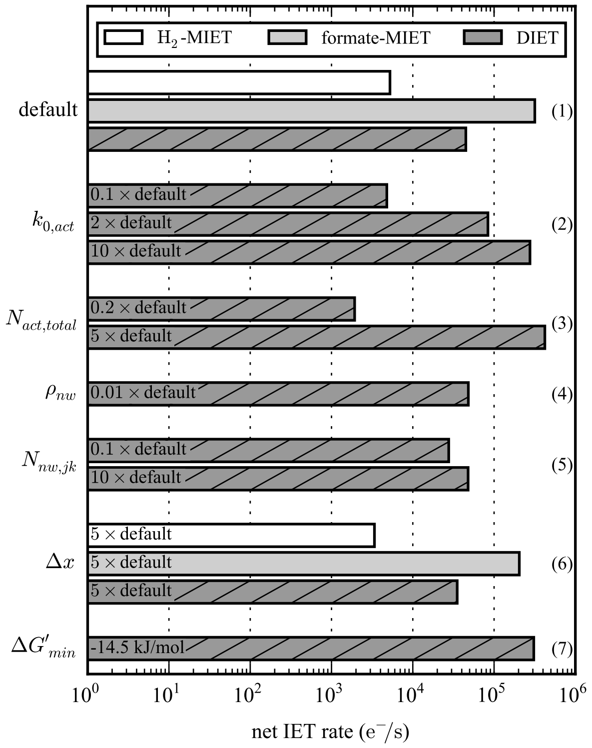
H$_2$-MIET
formate-MIET
DIET
default
(1)
$k_{0,act}$
0.1 × default
2 × default
10 × default
(2)
$N_{act,total}$
0.2 × default
5 × default
(3)
ρ_{nw}
0.01 × default
(4)
$N_{nw,jk}$
0.1 × default
10 × default
(5)
Δx
5 × default
5 × default
5 × default
(6)
$\Delta G'_{min}$
-14.5 kJ/mol
(7)
10^0
10^1
10^2
10^3
10^4
10^5
10^6
net IET rate (e$^-$/s)

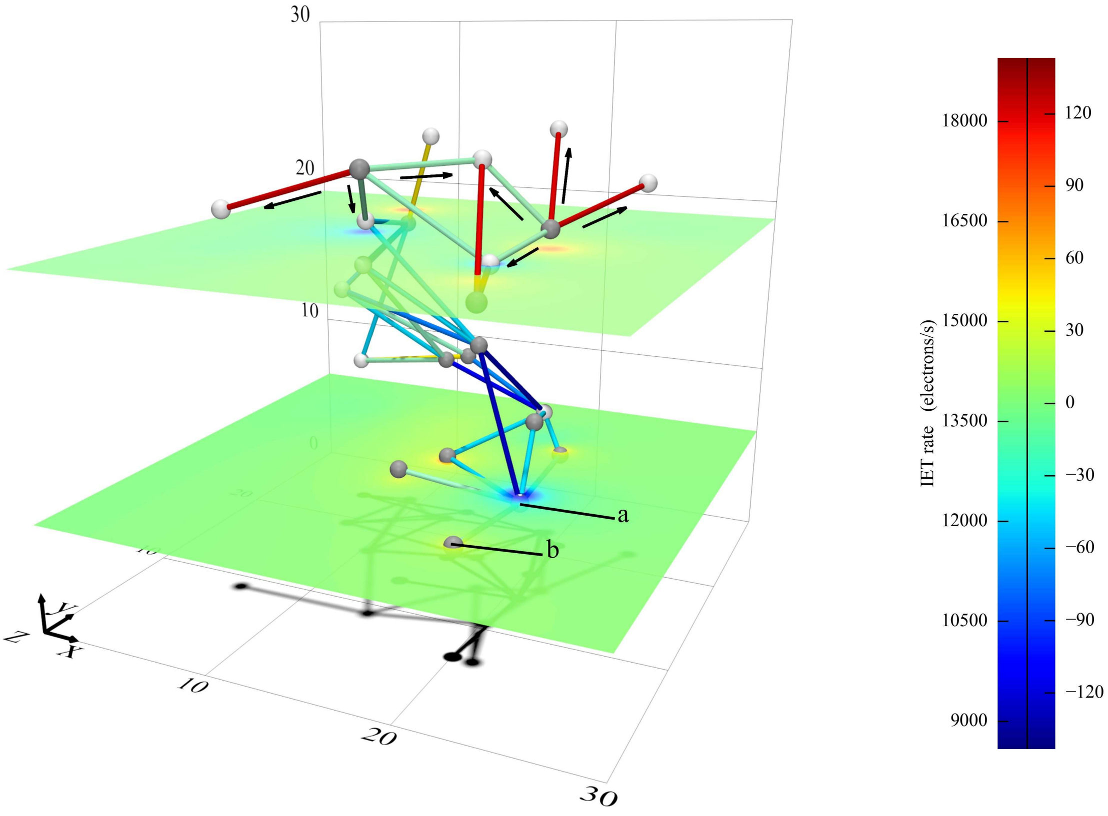
30
20
10
0
a
b
Y
Z
X
10
20
30
IET rate (electrons/s)
18000
16500
15000
13500
12000
10500
9000
Potential (pV)
120
90
60
30
0
−30
−60
−90
−120

Symbol	*Unit*	*Description*	*Default value*	*Reference and notes*
Geometry				
A_{cell}	m^2	Surface area of cell	3.14×10^{-12}	Calculated from d_{cell}
d_{cell}		Diameter cell (acetogen, methanogen)	1.00×10^{-6}	
Concentrations				
c_0	mol m^{-3}	Fixed boundary concentration		
		Propionic acid	7.41×10^{-3}	
		Propionate	1.00	
		Acetic acid	5.75×10^{-3}	
		Acetate	1.00	
		Carbon dioxide	22.39	
		Bicarbonate	100	
		Methane	0.1438	Calculated from $p_{0,CH4}$ = 0.1 bar
		Proton	1.00×10^{-4}	pH 7
		Hydroxide	1.01×10^{-4}	
		Chloride	1000	
		Potassium ion	1102	Closes charge balance
Thermodynamics and electrochemical				
$\Delta G'_{min}$	J mol^{-1}	Min. req. $\Delta G'$ for cell anabolism, maintenance	-15.2×10^{3}	Boone & Bryant (1980)
V_{min}	V	Min. req. V for anabolism and maintenance	52.51×10^{-3}	Calculated as $-2\Delta G'_{min}/6F$
Butler-Volmer (DIET only)				
$A_{act,cell}$	m^2	Total area for redox cofactor activation for any cell	3.14×10^{-13}	10% of A_{cell}, Supplementary Table 2
c_{act}	mol m^{-2}	Redox cofactor surface concentration	5.29×10^{-9}	Supplementary Table 2
k_0	s^{-1}	Standard redox cofactor activation rate constant	6000	Supp. Table 3, Ly *et al.* (2013)
$N_{act,j}$		Number of redox cofactors per nanowire for cell j		$N_{act,cell}/N_{nw,j}$
$N_{act,cell}$		Number of redox cofactors per cell	1.0×10^{4}	Lower *et al.* (2007)
β	-	Symmetry factor	0.5	
Ohm's law (DIET only)				
A_{nw}	m^2	Cross-sectional area of a single nanowire	1.26×10^{-17}	Calculated from d_{nw}
d_{nw}	m	Diameter of single nanowire	4.00×10^{-9}	Malvankar *et al.* (2011)
L_{nw}	m	Length of single nanowire		
$N_{nw,j}$		Total number of nanowires connected to cell j		(Number of connected cells k) × $N_{nw,pair}$
$N_{nw,pair}$		Number of nanowires formed per cell pair	100	
ρ_{nw}	Ω m	Electrical resistivity of nanowire	1.0	Malvankar *et al.* (2011)